MICROCOPY RESOLUTION TEST CHART

NATIONAL BUREAU OF STANDARDS 1963-A

DTIC FILE COPY

Characterization of Accelerating Pipe Flow

Paul J. Lefebvre
Launcher & Missile Systems Department

AD-A193 065

DTIC
ELECTE
MAR 2 4 1988
S D

Naval Underwater Systems Center
Newport, Rhode Island / New London, Connecticut

88 3 24 050

PREFACE

This document represents the author's
doctoral dissertation submitted for the degree
of Doctor of Philosophy in Mechanical Engineering
from the University of Rhode Island.   This study
was funded by the NUSC IR/IED Program.

REVIEWED AND APPROVED: 1 MARCH 1988

W.A. McNally
Head, Launcher & Missile Systems Department

REPORT DOCUMENTATION PAGE

1a. REPORT SECURITY CLASSIFICATION UNCLASSIFIED	1b RESTRICTIVE MARKINGS
2a. SECURITY CLASSIFICATION AUTHORITY	3 DISTRIBUTION/AVAILABILITY OF REPORT Approved for public release; distribution unlimited.
2b DECLASSIFICATION/DOWNGRADING SCHEDULE	

4 PERFORMING ORGANIZATION REPORT NUMBER(S) TD 6666	5 MONITORING ORGANIZATION REPORT NUMBER(S)

6a. NAME OF PERFORMING ORGANIZATION Naval Underwater Systems Ctr	6b OFFICE SYMBOL (If applicable) Code 8322	7a. NAME OF MONITORING ORGANIZATION

6c. ADDRESS (City, State, and ZIP Code) Newport Laboratory Newport, Rhode Island 02841	7b ADDRESS (City, State, and ZIP Code)

8a. NAME OF FUNDING/SPONSORING ORGANIZATION	8b OFFICE SYMBOL (If applicable)	9. PROCUREMENT INSTRUMENT IDENTIFICATION NUMBER

8c. ADDRESS (City, State, and ZIP Code)	10 SOURCE OF FUNDING NUMBERS			
	PROGRAM ELEMENT NO	PROJECT NO	TASK NO	WORK UNIT ACCESSION NO

11 TITLE (Include Security Classification)

CHARACTERIZATION OF ACCELERATING PIPE FLOW

12 PERSONAL AUTHOR(S)
Lefebvre, Paul J.

13a. TYPE OF REPORT Final	13b TIME COVERED FROM ___ TO ___	14 DATE OF REPORT (Year, Month, Day) 88-03-01	15 PAGE COUNT 241

16 SUPPLEMENTARY NOTATION

17 COSATI CODES			18. SUBJECT TERMS (Continue on reverse if necessary and identify by block number)
FIELD	GROUP	SUB-GROUP	Pipe Flow Velocity Profile.
20	04		Turbulence
19			Flow Loop

19 ABSTRACT (Continue on reverse if necessary and identify by block number)

A unique series of experiments was conducted to determine the effects of constant acceleration on the flow in a 5-cm-diameter pipe. These experiments, which differed substantially from those of previous researchers, investigated such phenomena as transition to turbulence and the general physics of the effect acceleration has on various flow parameters such as wall shear stress, velocity profile, and turbulence intensity profile. The experiments were conducted in the Naval Underwater Systems Center Flow Loop Facility, which was designed and built for this study. This facility provided the capability of programmed acceleration via a control system that uses the position of a downstream control valve for transient flow control. Based on the data collected during the experiments along with a linear momentum analysis, it was determined that hot-film wall shear stress sensors can be accurately used in transient flows up to at least 1 g acceleration.

20 DISTRIBUTION/AVAILABILITY OF ABSTRACT ☐ UNCLASSIFIED/UNLIMITED ☒ SAME AS RPT ☐ DTIC USERS	21 ABSTRACT SECURITY CLASSIFICATION UNCLASSIFIED	
22a NAME OF RESPONSIBLE INDIVIDUAL Paul J. Lefebvre	22b TELEPHONE (Include Area Code) (401) 841-1905	22c OFFICE SYMBOL Code 8322

DD FORM 1473, 84 MAR   83 APR edition may be used until exhausted
All other editions are obsolete

A

TABLE OF CONTENTS

i

TABLE OF CONTENTS (Cont'd)

LIST OF ILLUSTRATIONS

x

LIST OF ILLUSTRATIONS (Cont'd)

LIST OF TABLES

LIST OF SYMBOLS

A,B,C,D,F	Constants
a	Area
D	Test section diameter
D_e-2	Beam diameter
d_f	Fringe spacing for axial velocity
d_m	LDV measuring volume length
dP/dx	Axial pressure gradient
d_Z	Fringe spacing for radial velocity
E	Instantaneous hot-film anemometer output voltage
$\bar{E}$	Time-mean hot-film anemometer output voltage
f	Focal length
f_c	Low pass cutoff frequency
f	Instantaneous friction factor
$\bar{f}$	Time-mean friction factor
f_d	Doppler frequency
f_{du}	Doppler frequency for axial velocity component
f_{dv}	Doppler frequency for radial velocity component
$f_{pedestal}$	Doppler frequency of LDV pedestal signal
f_{so}	Minimum LDV frequency shift for V = 0
f_{sv}	Minimum LDV frequency shift for V-component
I(t)	Instantaneous value of some variable I
⟨I(t)⟩	Ensemble average of quantity I at time t
⟨I(t)$_{RMS}$⟩	RMS of the fluctuations of I about its ensemble average at time of t

J_0	Bessel function of the first kind
K	Convective acceleration parameter
K_a	Local acceleration parameter
$K_{a,tr}$	Local acceleration parameter at transition
L	Length over which pressure measurements are taken or length of control volume
l_m	LDV measuring volume length
M	Number of repeat tests used in ensemble averaging
N	Number of valid data points obtained during the sampling time
N_{FR}	Number of fringes
P	Pressure
Q	Volumetric flowrate
R	Pipe radius
$\overline{Re}$	Time-mean Reynolds number
Re	Instantaneous Reynolds number
Re_{cl}	Reynolds number based on centerline velocity
Re_D	Pipe Reynolds number
Re_{tr}	Reynolds number at transition
Re_δ	Boundary layer thickness Reynolds number
r	Radial distance from pipe centerline
r^*	Dimensionless radial position $= r/R$
T	Fluid temperature in °C
t	Time

$t*$	Dimensionless time $= vt/R^2$
t_{tr}	Time to transition from $t = 0$
t_{tr}^*	Dimensionless time at transition, from start of transition
U	Instantaneous local axial velocity
$\overline{U}$	Time-mean local axial velocity
U^+	Wall function velocity coordinate $= U/u*$
U_{cl}	Instantaneous centerline velocity
$\overline{U}_{cl}$	Time-mean centerline velocity
$\overline{U}_m$	Time-mean cross-sectional averaged velocity
U_m	Instantaneous, cross-sectional averaged velocity
U_{max}	Steady-state centerline velocity
$\overline{U}_{mf}$	Final time-mean cross-sectional averaged velocity
$\overline{U}_{m0}$	Initial time-mean, cross-sectional averaged velocity
$U_{m,tr}$	Cross-sectional averaged velocity at transition
$u*$	Friction velocity
u'	Instantaneous fluctuation in the axial velocity
$\sqrt{u'^2}$	RMS of axial velocity fluctuations
V	Radial component of velocity
$\vec{V}$	Velocity vector
Ψ	Volume
v'	Instantaneous fluctuation in the radial velocity
$\ddot{X}$	Average acceleration during test run
x	Axial distance

Y	Distance from wall
Y^+	Wall function distance coordinate $= Yu*/\nu$
β_D	Bandwidth of Doppler signal spectrum
ΔP	Differential pressure
ΔT	Temperature difference between the wall shear stress sensor and the fluid
δ	Boundary layer thickness
δ_{tr}	Boundary layer thickness at transition
κ	Focusing lens half angle
κ'	Constant ($= 0.4$) in equation (IV-3)
λ	Laser light wavelength
λ_N	Roots of the Bessel function
μ	Dynamic viscosity
ρ	Mass density
$\overline{\rho u'v'}$	Reynolds stress
τ_w	Instantaneous wall shear stress
$\overline{\tau_w}$	Time-mean wall shear stress
$\tau_{w,tr}$	Wall shear stress at transition
ν	Kinematic viscosity

ACKNOWLEDGMENTS

xviii

I. INTRODUCTION

PROBLEM STATEMENT

Accelerating shear flows and other time-dependent laminar and turbulent shear flows are encountered in many applications of aero-dynamics and hydrodynamics. Examples include the startup of a closed conduit flow, a train suddenly entering a tunnel, flow over turbine blades, emergency cooling of a nuclear reactor, maneuvering submarines and aircraft, and the highly transient launch of a missile or torpedo.

Currently available approaches used in the analysis of accelerating flows include the testing of a full-scale prototype or scale model, and the creation of a quasi-steady numerical simulation, which incorporates a number of simplifying assumptions. Common simplifying assumptions include the substitution of steady-state values of friction factor, Reynolds stress, transition Reynolds number, and velocity profile for their transient counterpart. Presently, there is such a scarcity of knowledge about the details of transient or accelerating shear flow phenomena that the errors arising from making these assumptions can only be estimated for a few specific transient flows.

In addition to the practical aspects of unsteady flows, there is

1

considerable interest in expanding the state-of-the-art regarding the
fundamental physics associated with laminar, turbulent, and transition-
al accelerating flows to better understand general transient flow
phenomena. After considering some correlations that can be made to
date between turbulent steady-state flows and accelerating transient
flows, it is also conceivable that a study of accelerating flows could
substantially contribute to the understanding of general turbulent
flows.

To define the basic structure of the transient flow as influenced
by the instantaneous flow conditions (and also the past history), a
very basic flow (that in a long, circular pipe and under constant
acceleration) was selected. Unlike previous transient pipe flow
studies, this study had the unique advantage of constant acceleration
over a large flow range. This flow was provided by a flow loop
facility designed and built for this study at the Naval Underwater
Systems Center (NUSC). In the facility, tests were conducted over a
large range of accelerations and pipe Reynolds numbers.

LITERATURE REVIEW

The complex nature of unsteady laminar, turbulent, and transition-
al pipe flow has proven to be very difficult to characterize
experimentally or solve analytically. Since little is known about the
physics of unsteady flows, numerical solutions of other than laminar
flows are questionable at best.

The classical, exact analytical solution for accelerating laminar

2

pipe flow was derived by Szymanski [1] in 1932, i.e., flow started
from rest with a constant pressure gradient dP/dX suddenly applied.
The solution of the time-dependent, instantaneous velocity U at
radialposition from the centerline r is in the form of a Bessel
function and given as

$$\frac{U(r,t)}{U_{max}} = (1 - r*^2) - \sum_{n=1}^{\infty} \frac{8J_0(\lambda_n r*)}{\lambda_n^3 J_1(\lambda_n)} e^{(-\lambda_n^2 t*)} \qquad (I-1)$$

where

$$t* = \frac{vt}{R^2} , \qquad (I-2)$$

$$r* = \frac{r}{R} , \qquad (I-3)$$

$$U_{max} = (-dp/dx) R^2/4\mu , \qquad (I-4)$$

and v is the kinematic viscosity, μ is the dynamic viscosity, t is
time, R is the pipe radius, U_{max} is the steady-state centerline
velocity, J_0 is the Bessel function of the first kind, and λ_n
are the roots of the Bessel function.

Figure I-1 gives the resulting time-dependent velocity profiles up
to the point when the steady-state profile is developed. Figure I-2
shows the instantaneous cross-sectional averaged velocity U_m as a
function of non-dimensionalized time t*. The initial portion of the
curve exhibits a constant acceleration followed by an exponential
decay in acceleration.

Other special cases in laminar flow for which a theory has been
developed include the work of Chambre et al. [2], who extended
Szymanski's solution for the case of general time dependence of the

3
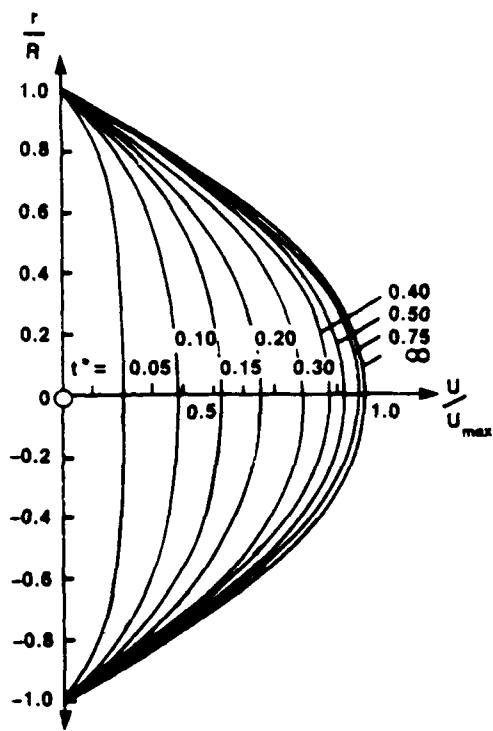
Figure I-1. Time-Dependent Velocity Profiles
from Szymanski's Solution
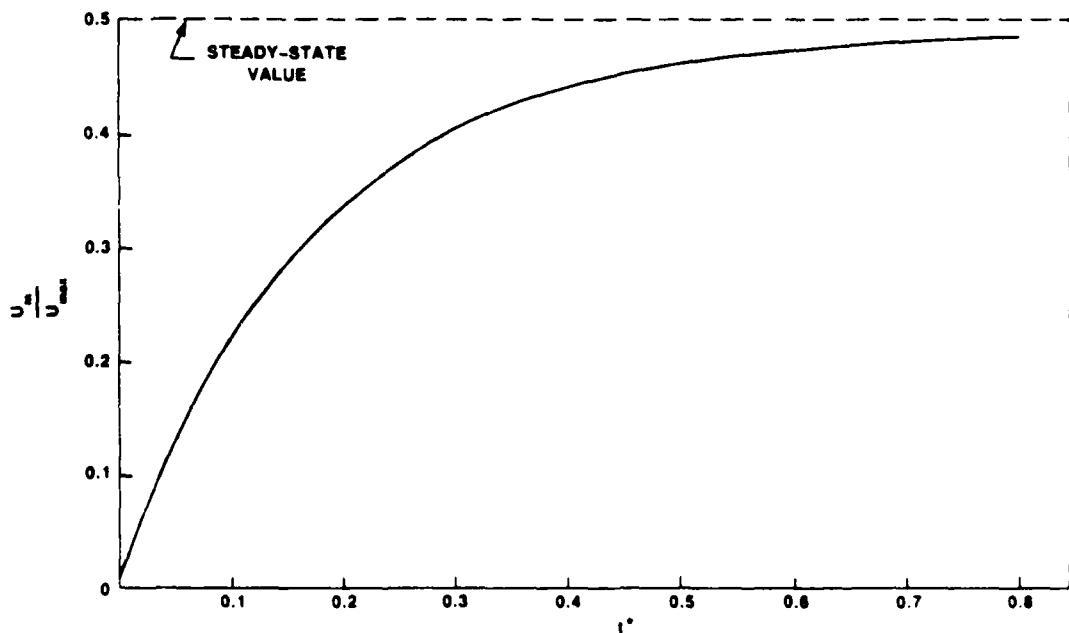
Figure I-2. Cross-Sectional Averaged Velocity vs Time
from Szymanski's Solution

4

pressure gradient. Also, Zielke [3] derived an equation for the frequency dependent friction in laminar flow as related to the instantaneous, cross-sectional averaged velocity and its weighted history. No theory exists for transient turbulent flow.

A numerical solution of Szymanski's flow was recently developed by Tapply et al. [4]. The finite volume method was applied to the unsteady Navier-Stokes equation, which was discritized to an elliptic form for the solution at each time step. Excellent agreement with Szymanski's exact solution was obtained. Additionally, the method was applied to a laminar flow, initially at rest, having a constant, cross-sectional averaged acceleration. Even though the results were limited to a pipe Reynolds number of 100, the numerical approach was shown to be a viable means of numerically simulating unsteady flows at higher pipe Reynolds numbers and possibly even in the turbulent regime should a suitable turbulence model be incorporated.

Numerical solutions to unsteady turbulent flow problems have been reported by many including Kawamura [5] for accelerating and decelerating turbulent flows and Ohmi et al. [6] for pulsating turbulent pipe flow. Most studies used quasi-steady turbulence models without any real justification.

Experimental studies were also very limited in flow conditions and in type of data acquired. The majority of flow conditions inc_ _ed: (1) pulsating flow, (2) suddenly applied, constant pressure gradient, and (3) suddenly applied, stepwise change in flow rate.

In general, results for pulsating flow studies are only

applicable for the specific cases being studied and give little insight into the underlying physics associated with the general class of unsteady flows. This is mainly a consequence of the additional complexity of pulsating flows where phase variations exist between velocity and pressure across the entire pipe diameter. Therefore, the effects of the acceleration portion of the transient influence the flow during the deceleration portion and vice versa. In addition, the acceleration and rate of change of acceleration--two parameters that greatly influence the flow--are constantly changing, making it impossible to determine their influence on the flow.

Controlled, pulsating pipe flow is relatively easy to obtain in air and liquid flow facilities. This is probably one of the major reasons for the many studies that have been reported. Laminar pulsating flow studies have been conducted as early as 1929 by Richardson and Tyler [7] with more recent studies by Linford et al. [8] and Denison [9]. Results showed that cross-sectional averaged velocity lags the pressure by 90°, while the velocity near the wall lags pressure by 45°.

The earliest pulsating turbulent pipe flow studies known to the author are those of Schultz-Grunow [10] in 1940. Relatively crude measurements of pressure loss and velocity distribution using a liquid manometer were made. The most comprehensive set of experiments conducted to date with sophisticated instrumentation are those of Mizushina et al. [11,12] in 1975 and Ramaprian and Tu [13] in 1982.

Mizushina et al. conducted their experiments in an aqueous

6

solution at an average pipe Reynolds number of 10,000 with peak

oscillations of 40 percent of the mean flow and a pulsation frequency

between 0.13 and 4 Hz. They measured pressure gradients and used

electrochemical sensors to measure wall shear stress and axial

velocity at several radial positions. Ramaprian and Tu conducted

their experiments in water at a mean pipe Reynolds number of 50,000

and frequencies of 0.5 and 3.6 Hz with peak oscillations of 65 and 15

percent of the mean flow, respectively.

They measured wall shear stress with flush-mounted, hot-film

sensors and instantaneous, axial, local velocity with a laser Doppler

velocimeter (LDV). In both studies, turbulence intensity was obtained

by ensemble averaging the data. Reynolds stress was estimated

indirectly from the wall shear stress and velocity profile data by

using an integral momentum equation.

The combined results from these studies show that the pulsations

play a significant part in turbulent flow when the oscillation

frequencies approach and exceed the critical frequency, which was

defined as the steady-state bursting frequency. The data also suggest

the existence of an inflection point in the time-mean velocity profile

very near the wall. Neither the time-mean nor the ensemble-averaged

velocity profiles followed the universal log law. At lower pulsation

frequencies, the ensemble-averaged velocity profiles were strongly

distorted and had an inflection point. At higher frequencies, the

distortion was confined to a thin, near-wall region with the remainder

of the profile remaining smooth. The ensemble-averaged turbulence

7

intensity and Reynolds shear stress were also significantly affected by the pulsations. In addition, Ramaprian and Tu developed a finite volume numerical solution, which incorporated a quasi-steady turbulence model (Prandtl energy model). The simulation erroneously predicted the negligible effect of the pulsations on the time-mean flow and was unable to follow the detailed turbulence history through the cycle.

Unsteady flow studies, more similar to the one conducted under the present study, were those which investigated accelerating pipe flow with either a suddenly applied, constant pressure gradient or stepwise increase in flow rate. One of the earliest such studies was that of Daily et al [14] in 1956. The apparatus consisted of a 2.54-cm diameter circular test section with a length of 99 pipe diameters. This section was mounted vertically between two pneumatically pressurized reservoir tanks. The test fluid was water and the acceleration was controlled via the time-controlled flow of compressed air in either or both of the reservoir tanks. Maximum pipe Reynolds number was 500,000 and accelerations ranged from 4.6 to 12.2 m/s/s. The acceleration throughout the run was not constant and the previously stated accelerations were the maximum observed during a run. The instantaneous flow rate was measured with a nozzle placed upstream of the test section. The accuracy of this measurement was not provided but is most probably highly inaccurate. Pressure gradient was also measured along the length of the test section. Wall shear stress was calculated by using the linear momentum equation.

8

Since the acceleration continuously changed during a test run, the validity of using this equation is questionable. Results from this study were minimal and only showed that the unsteady wall shear stress was slightly greater than its steady-state counterpart. No transition information was obtainable from the data.

In 1959, Carstens et al. [15] conducted some relatively crude experiments on an accelerating flow with a suddenly applied, constant pressure gradient. The facility consisted of a constant head tank that fed a horizontal, 1.27-cm diameter test section whose exit was open to the atmosphere. Accelerations and pipe Reynolds numbers were not given but it appears that both were low.

Instantaneous, cross-sectional averaged flow rate was determined by analysis of a 35-mm motion picture record of the configuration of the free jet at the test section outlet. No accuracy was estimated for this measurement. Pressure gradient was also measured over 95 pipe diameters of the test section. Wall shear stress was calculated using the linear momentum equation.

As with Daily's results, the only information obtained was that the quasi-steady wall shear stress was a good approximation of the unsteady shear stress in turbulent flows.

Denisov [16] conducted a series of experiments in 1970 in which the instantaneous flow rate was varied by pumping an additional amount of water into the 1-cm diameter test section via a special flow rate control. This control was in the form of a cylinder with a piston set in motion in a prescribed manner using a cam mechanism. Instantan-

9

eous, cross-sectional averaged flow rate was measured with an induction flowmeter and pressure gradient was monitored along the 244 pipe diameter test section. The flowmeter accuracy was not given nor was any mention made as to whether the meter's main purpose was for steady-state measurements or whether it was specially designed for transient application.

Tests were initiated from initial velocities of 0.7 to 1.3 m/s to a final velocity of 2.7 m/s. The acceleration changed constantly during a run and reached a maximum of between 8 and 140 m/s/s, depending on the particular run. Like the previous experiments, instantaneous wall shear stress was calculated from the linear momentum equation. It was concluded that the wall shear stress depends not only on the instantaneous acceleration but also on the time rate of change of acceleration. In addition, the unsteady shear stress can vary from the steady-state value by up to 20 percent for the accelerations tested.

In 1975, Kataoka et al. [17] reported a much more sophisticated experimental study of a startup flow via a step input of constant flow rate. A closed system with an aqueous solution for the test fluid and a centrifugal pump and solenoid valve for rapid startup was used. The test section was 2.8 cm in diameter and 165 pipe diameters long. Electrochemical sensors were used for the measurements of instantaneous, local velocity and wall shear stress. Tests were conducted at suddenly applied flow rates corresponding to pipe Reynolds numbers of 6230 and 11,900. The final flow rate was reached in approximately 0.5

seconds. Transition was observed anywhere between 7.5 and 14 seconds from the start of the acceleration for pipe Reynolds numbers of 6230 and between 2.5 and 9 seconds for the 11,900 pipe Reynolds number tests. For each pipe Reynolds number, a fully developed profile was reached after approximately 30 seconds.

An interesting observation was that the flow rate remained constant until transition, after which the flow gradually decreased to another steady-state flow rate. During the acceleration portion of the tests, an annular jet effect was also noted. That is, the velocity reached a peak in an annular region at the edge of the boundary layer of the developing flow. The peculiar velocity profile was attributed to the non-uniformity of acceleration of the central core. Absolute values of wall shear stress were not presented nor were comparisons made with quasi-steady values.

In 1976, Marayama et al. [18] also conducted some experiments on the stepwise change in flow rate from an initial pipe Reynolds number of 5000 to a final pipe Reynolds number of 10,000. The facility was a closed-loop system where a by-pass line was equipped with a solenoid valve and a sluice valve. Stepwise changes in flow rate were obtained by quickly opening a solenoid valve while the magnitude of the change in flow rate was controlled by the sluice valve. The test section was a 5.1-cm diameter pipe with a length of 235 pipe diameters. The test fluid was an aqueous solution. Instantaneous, local velocity and wall shear stress were measured with electrochemical sensors. The tests were repeated 50 times to ensemble average the data. This number was

chosen to avoid slight changes in both initial and final conditions during the series of experiments. However, the 50 repeats were not enough for the ensemble average of turbulence intensity. The ensemble-averaged values were further smoothed, therefore, by using the two adjacent results in the sampling period.

Results showed that the new flow rate was established in approximately 0.25 second. However, it took about 7 seconds to reach a new steady-state velocity profile. Reynolds stress, as calculated from an integral momentum equation, and the wall shear stress and velocity profile data, started to increase at approximately 2.4 seconds with subsequent rapid increase to 3.0 seconds coming close to the final steady-state values. The turbulence intensity in the near-wall region was shown to initially increase rapidly above the final steady-state value. This was followed by a decrease of the excess and by a less rapid increase in the core region until the steady-state profile was reached.

Two series of transient pipe flow experiments were reported by van de Sande et al [19] in 1980. These experiments were of the startup flow of water in both a 2-cm and a 5-cm diameter test section with a suddenly applied, constant pressure gradient. The test section was located between two constant head tanks. A quick-opening valve initiated a test run. In the first series of experiments using the 5-cm diameter test section, the flow was accelerated to a final pipe Reynolds number of 60,500. Unfortunately, the average acceleration was relatively low at approximately 0.3 m/s/s. A LDV was used to

12

obtain local axial velocity at 20 locations across the test section diameter. Two test runs were conducted at each of the LDV measurement locations to assure reproduciblity. The second series of tests used a 2-cm diameter test section upon which hydrogen-bubble flow visualization experiments were conducted. The final pipe Reynolds number for this series of tests ranged from 2500 to 21,600.

Results for the LDV tests showed a delayed transition from laminar to turbulent flow at a pipe Reynolds number of approximately 57,500. All of the 40 test runs showed transition within 0.1 second of each other. Velocity profiles showed that total redistribution of momentum took place soon after the initiation of turbulence. Within 0.6 second after transition, the final profile had been approached. The conclusion was drawn that accelerations are of a stable character. Prior to transition and until minor losses in the system caused the pressure gradient to deviate from its initial constant value, velocity profiles followed those obtained by Szymanski. The frictional losses during the transient, as deduced from the measured velocity profiles, were substantially lower than the corresponding quasi-steady values.

The flow visualization experiments showed that initially plug flow existed in the test section until about 2 seconds into the run when boundary layers were first noticed to develop. The onset of turbulence, as evidenced by instabilities in the shape of the velocity profile and the origination of turbulent eddies, only took place almost at the end of the acceleration.

In summary, experimental studies conducted to date were, for the most part, limited to low pipe Reynolds numbers. Severe limitations on the amount of useful information obtained from these data resulted since acceleration and time rate of change of acceleration changed continuously over any one test run. This precluded extrapolating results to any flows other than those tested. In addition, except for very short durations, the accelerations tested were all of very low values. Analytical solutions are extremely limited with little hope of any new developments in the near future. Numerical solutions are limited to quasi-steady approximations with little or no substantiation of the assumptions.

OBJECTIVE AND SCOPE

This study is a detailed experimental investigation of the structure of accelerating flows. Constantly accelerating flow in a long circular pipe of 5-cm diameter was selected as the most suitable flow due to the basic nature of the corresponding steady-state flow field and the relatively long duration of constant acceleration during the transient. Even though it was felt that both the instantaneous acceleration and its rate of change with time greatly influence the flow, only constant acceleration flows were considered for this study due to the already large extent of the study. Future studies were envisioned to investigate the effect of time rate of change of acceleration on the flow.

14

The major objective of this study was to define the characteristics of the structure and predominant phenomena of accelerating pipe flows. The intent was to obtain a better understanding not only of the subject flow, but also of more general transient flows and, to a lesser degree, of steady-state turbulence in general. The flow phenomena to be investigated as a function of acceleration included:

- Wall shear stress (friction factor)

- Pressure gradient

- Velocity profile

- Reynolds stress

- Transition pipe Reynolds number.

A second objective of this study was to determine the suitability of using the generally accepted, quasi-steady assumptions in analyzing accelerating flows.

Specifically, the overall scope of the present study can be summarized in the following paragraphs.

Testing was conducted on the NUSC Flow Loop Facility. The test section was a 5-cm diameter circular pipe, 606 pipe diameters long, through which the flow was accelerated at constant accelerations ranging from 1.8 to 11.8 m/s/s. The flow was either started from rest to investigate laminar and transitional flows or from a fully developed, turbulent flow (at approximately 1 m/s, cross-sectional averaged velocity) to investigate accelerating turbulent flows. The flow was accelerated to a maximum, cross-sectional averaged velocity of either 8.8 or 11.3 m/s.

Experimental data were obtained throughout the transient and included measurement of instantaneous, cross-sectional averaged velocity via a transient flowmeter; instantaneous local velocity and Reynolds stress from a two-component LDV; instantaneous wall shear stress using flush-mounted, hot-film sensors; and instantaneous wall pressure from small diaphragm high frequency-response, flush-mounted pressure transducers. The wall shear stress and pressure sensors were distributed along the length of the test section to observe some of the overall spatial characteristics of the flow.

The data were reduced and presented in a manner whereby not only the flow characteristics and the implications of using quasi-steady assumptions were defined, but also in a way that is conducive to the future development of turbulence models suitable for transient flows.

16

II. EXPERIMENTAL APPARATUS AND CALIBRATION

The experimental apparatus for this study consisted of an accelerating pipe flow facility and the instrumentation and data acquisition system used to measure the various flow parameters during transient and preliminary steady-state tests. The NUSC Flow Loop Facility, which was designed and built specifically for transient flow tests, was used for this study, the initial one conducted on the facility. The NUSC facility has provisions for a range of different size and shape test sections and for user-defined transient flows such as constant or exponential acceleration or constant time rate of change of acceleration. This programmed acceleration is provided via a novel control system, which was designed specifically for the NUSC facility. The flowing fluid was city water. The facility is described in detail by Lefebvre [20]. The next section of this report describes only the major features of the facility as they pertain to the present study.

FLOW LOOP FACILITY

A diagram of the facility as configured for the present study is shown in figure II-1; photographs of the facility are presented in appendix A. The following description considers the components as they appear in the downstream flow direction.

The facility is a recirculating flow loop with a 30,000-liter, constant head reservoir where the water surface was exposed to the
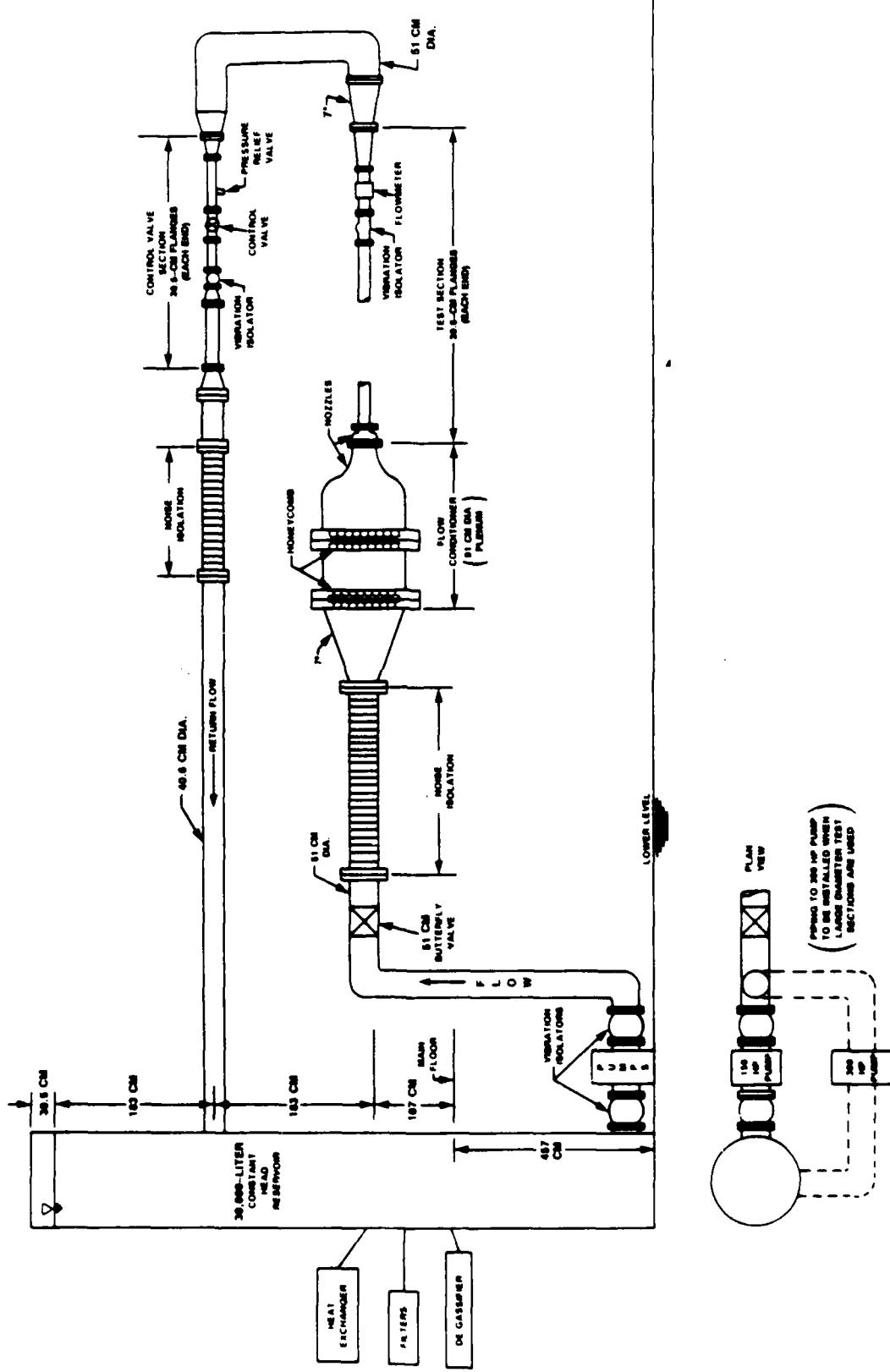
Figure II-1. Flow Loop Facility Lay-Out

atmosphere. A 150-hp, constant-speed pump provides an essentially constant discharge pressure over the range of flow rates used during the present study. Vibration isolators are located on both sides of the pump. A 51-cm diameter butterfly valve is installed after the pump and is always maintained in the fully opened position during any flow tests. This valve is followed by a 51-cm diameter by 305-cm long rubber hose leading to a 91-cm diameter plenum chamber, which immediately precedes the test section. The plenum chamber consists of two honeycomb sections and a specially designed nozzle leading to the entrance of the test section. The rubber hose provides acoustic noise and structural vibration isolation, while the plenum chamber provides a test section entrance flow that is uniform to within 1 percent and has a steady-state turbulence intensity between 0.8 and 1.3 percent, depending on the pipe Reynolds number [20].

The test section, shown in figure II-2, is a multisection, 5-cm diameter, circular pipe with a total length of 606 pipe diameters. The first six sections of the test section are identical. They are made from stainless steel with a honed internal surface having a ±0.0025-cm tolerance on the 5-cm diameter and a surface roughness of 0.5 microns. Each section is 100 pipe diameters (5 m) long. The seventh and last section is made from clear-cast acrylic to provide a means by which LDV measurements could be made. The dimension and tolerance of the inside diameter is the same as the stainless steel sections; however, the surface roughness is as cast and its length is 6 pipe diameters (30 cm). Each of these sections is joined by a flanged connection,

19

SENSOR STATIONS: #1

PLENUM CHAMBER NOZZLE

FLOW →

7.6 CM TYP.

5 METERS TYP.

#2 #3 #4 #5 #6 #7 #8 #9

CLEAR ACRYLIC SECTION

30 CM

DIFFUSER FROM 5 TO 30.5 CM DIA.

VIBRATION ISOLATOR

TRANSIENT FLOWMETER

(AT VERTICAL RETURN LINE)

STATION	INSTRUMENTATION
1-6	PRESSURE TAP/FLUSH PRESSURE SENSOR/SURFACE SHEAR STRESS SENSOR
7	LASER DOPPLER VELOCIMETER
8	TRANSIENT FLOWMETER
9	TEMPERATURE PROBE

PHYSICAL SPECIFICATIONS
1. INSIDE DIAMETER = 5 ± .0025 CM
2. INSIDE SURFACE FINISH = 0.5 MICRONS
3. MATING AT FLANGES WITHIN 0.0025 CM
4. O-RING FACE SEAL AT FLANGES (NO HORIZONTAL GAP AT FLANGES)

Figure II-2. 5-cm Diameter Test Section

20

which has a face o-ring seal. To accurately align adjacent sections, a close tolerance plug is inserted into adjacent ends of mating sections. Theflanges are bolted together and two dowel holes subsequently drilled through the mating flanges. The plug is then removed and dowel pins inserted into the flanges upon reassembly. This procedure assures that adjacent sections can be reassembled so that a maximum step of 0.0025 cm in height with a negligible axial gap is provided at the interface.

Mounts are provided for a flush-mounted, hot-film, wall shear stress sensor and a flush-mounted, pressure transducer at a location of 7.6 cm from the downstream end of each of the stainless steel sections. The mounts are 180° apart. A pressure tap is also machined into the wall at a 90° angle to the two sensor mounts. The tap is 0.1 cm in diameter through to the inside wall with a 0.15-cm counterbore. A short length of stainless steel tubing is glued into the counterbore. The pressure taps are used to establish the steady-state wall shear stress versus pipe Reynolds number characteristic of the test section as described later in this report. The sensor stations were numbered 1 through 6 as shown in figure II-2.

A transient flowmeter is placed at the end of the test section. This flowmeter, designed and built as part of the NUSC facility, monitors cross-sectional averaged velocity in the test section versus time. This flowmeter is discussed further in the next section.

The control valve, which is inserted in the return line, is part of the feedback control system that provided the accelerating flow

21

capability. The control system is comprised of the control valve, a
position indicator on the valve stem, an Apple 2e computer, a Moog
servo-amplifier, and a Moog servo-valve. A closed-loop, proportional
control was utilized. The Apple computer was used to generate the
command signal, which was the desired valve position versus time for
100 points during each second of the acceleration. The required valve
position is based on the integrated, user-defined acceleration (mean
velocity versus time) and a steady-state calibration of control valve
position versus mean velocity in the test section.

A menu-driven, interactive software package was written for the
Apple computer to facilitate creation of the command signal data
file. This data file was based on the equation

$$U_m = \bar{U}_{m0} + At + Bt^2 \tag{II-1}$$

where U_m is the desired time dependent cross-sectional averaged
velocity, $\bar{U}_{m0}$ is the initial steady-state, cross-sectional averaged
velocity before acceleration, and A and B are constants that define
the acceleration (i.e., setting the constant B equal to 0.0 and the
constant A to some finite value would result in constant acceleration,
whereas setting A to 0.0 and B to some finite value would result in
constant time rate of change of acceleration). Final cross-sectional
averaged velocity was also an input variable to the program.
Provision was included for steady-state operation of the facility.

During a transient run, the command signal was converted from
digital to analog and continuously compared to the analog feedback
signal from the control valve position indicator. This comparison was

22

made in the Moog servo-amplifier which, in turn, generated an error signal when a difference between the command and feedback signals was detected. This error signal was subsequently sent to the Moog servo-valve, which adjusted the control valve position via a hydralic cylinder connected to the control valve stem. Validation of the control system operation proved that the system could provide constant accelerations ranging from 1.8 to 11.8 m/s/s up to cross-sectional averaged velocities of 11.3 m/s. Extensive details of the control system are provided in LaPointe and Lefebvre [21].

A 40.6-cm diameter by 2-m-long rubber hose section, which was used for acoustic noise isolation and structural vibration damping, followed the control valve. The return line then entered the reservoir tank below the tank's water level to reduce the possibility of introducing acoustic flow noise and any air entrapment into the fluid.

Conditioning of the water was provided by a heat exchanger, filters, and a degassifier. The heat exchanger maintained water temperature within 20°C to 23°C. The filters provided filtering capabilities between 0.5 and 25 microns. The degassifier removed dissolved air and gasses in the water down to a vacuum of 73 cm of mercury.

CROSS-SECTIONAL AVERAGED VELOCITY MEASUREMENTS

To satisfy a preliminary requirement of the present study, a flowmeter that could measure both steady-state and transient, cross-sectional averaged velocity in the test section was successfully developed. Up to that time, all known commercially available flowmeters were restricted to the measurement of steady-state flows and had no transient flow measurement capabilities. This additional measurement capability was another distinct advantage of the present study over previous ones. The capability allowed direct measurement of instantaneous, cross-sectional averaged velocity and also, by differentiating the velocity versus time curve, the instantaneous cross-sectional averaged acceleration was easily obtained.

Details of the flowmeter design and calibration are documented by Lefebvre and Durgin [22]. Some of the major points contained in that reference are presented here.

Electromagnetic technology was chosen as the basis for the transient flowmeter because of inherent, fast response to transients and the insensitivity of steady-state, electromagnetic flowmeters, in general, to changes in velocity profile. The electromagnetic flowmeter is based on Faraday's law of induction.

The approach taken in the development of the flowmeter was to utilize as much of a commercially available, electromagnetic flowmeter as was feasible. The final version of the transient flowmeter, therefore, consisted of the flow tube (or body) portion of a Foxboro

24
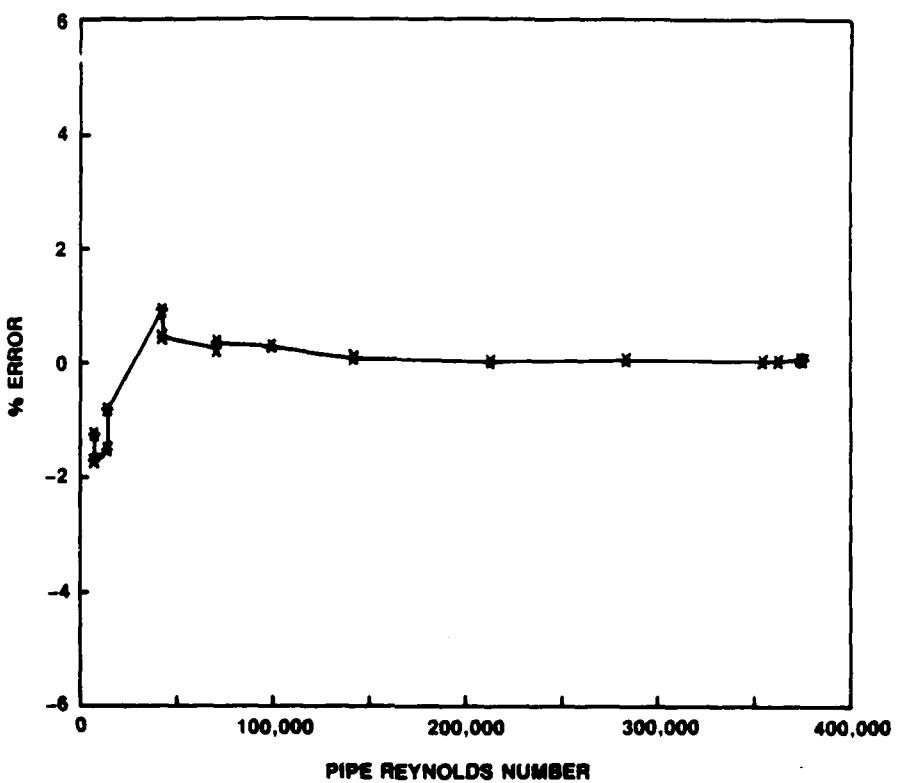
Figure II-3. Transient Flowmeter Steady-State
Calibration Curve

Co., ac-powered, electromagnetic flowmeter and a specially designed

electronics transmitter developed for the present study. The new

electronics provided the capability of measuring cross-sectional

averaged velocity with a data rate of 60 Hz under both steady-state

and transient flow conditions.

A steady-state calibration of the flowmeter was conducted at the

Alden Research Laboratory Flowmeter Calibration Facility, Holden, MA.

This calibration was performed by using the gravimetric method, which

is considered accurate to ±0.25 percent. The results of the

calibration, presented in figure II-3, show that the flowmeter

accuracy was ±1.7 percent over the complete range tested and ±0.5

percent over the 40,000 to 40,0000 pipe Reynolds number range, a

25

substantial portion of the total range.

A transient flow calibration facility consisting of a free-falling water column was also designed and built for this study. Optical sensors, which were placed every 5 cm along the 5-cm diameter, vertical water column, monitored the change in elevation of the free-falling water surface and, hence, the flow versus time.

Results of one typical transient calibration run are shown in the flow rate versus time curve of figure II-4, which compares the measured values from the facility and the flowmeter. The run lasted approximately 1 second. From 0.0 to approximately 0.4 second, the flow experienced an almost constant acceleration of 9.8 m/s/s, reaching a velocity of 5 m/s. Beyond 0.4 second, the free surface of the water column experienced considerable instability precluding any accurate measurements. Results for 12 such runs were analyzed, and it was concluded that the flowmeter could measure transient flows with an estimated accuracy of ±1.0 percent of reading.

WALL PRESSURE MEASUREMENTS

As discussed in the "Flow Loop Facility" section of this report, six static pressure taps were distributed along the test section at sensor stations 1 through 6, each 5 m or 100 pipe diameters apart. These pressure taps were used to define the steady-state pressure gradient along the test section as a function of pipe Reynolds number. Wall shear stress and friction factor were subsequently
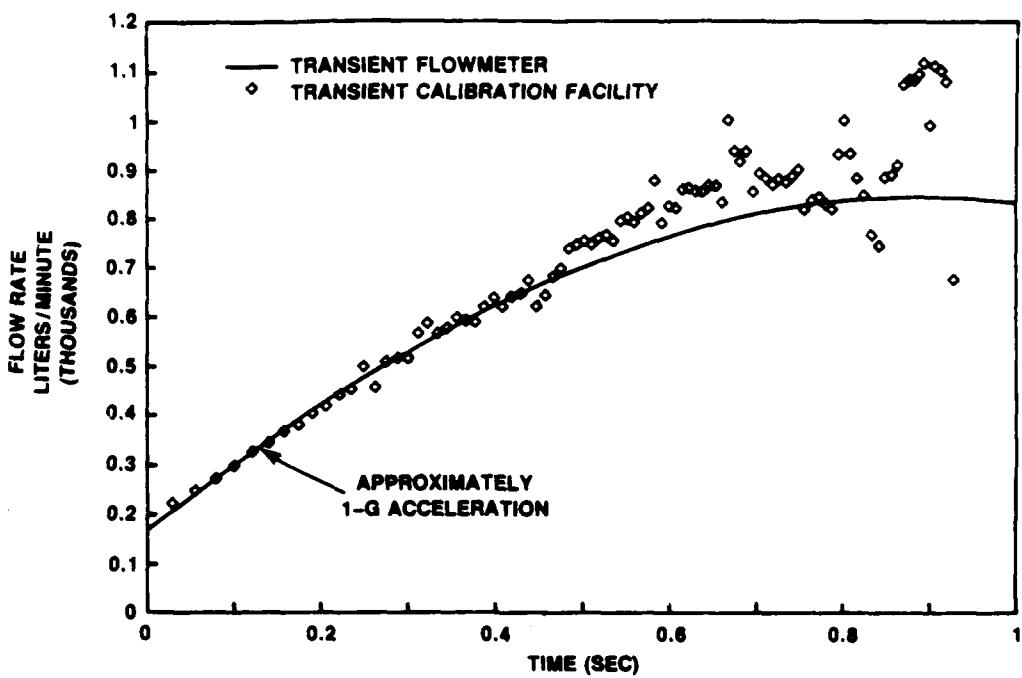
Figure II-4. Transient Flowmeter Typical Transient
Calibration Curve

calculated from the pressure gradient data as discussed in the "Wall
Shear Stress Measurements" section of this report.

A Validyne model DP15 TL, multiple-range, differential pressure
transducer was used to measure the differential pressure between any
two pressure taps. This transducer had provision for changing the
sensing diaphragm to vary the upper range value of the transducer to
various values from 5.6 cm of water to 22 million pascals. The
diaphragm used had an upper range value of 88 cm. The Validyne
transducer was calibrated with a water manometer to an estimated
accuracy of ±0.25 percent of span. The connection between the
Validyne transducer and the stainless steel tubing that extended from
the pressure tap was made via Tygon plastic tubing.

27

For test section velocities above 4 m/s, steady-state wall pressure was measured with Kulite XTM-190-100, miniature, flush-mounted gage pressure transducers. These transducers were also used during the transient tests for measurement of instantaneous wall pressure. Six of these transducers were distributed along the test section at sensor stations 1 through 6. The process-wetted surface was a 0.373-cm diameter stainless steel diaphragm and the sensing element was a piezoresistive, active half bridge. The transducers had a span of 700,000 pascals and a natural frequency of approximately 80,000 Hz. The excitation voltage for the Kulite pressure transducers was provided by an Ectron model 563FL, multichannel signal conditioner. This unit also had an amplifier and low-pass filter for each channel. During all tests conducted under this study, the filters were set at 1000 Hz and the signals were amplified by a gain of 100. A dc offset adjustment in the amplifiers provided the capability of zeroing each sensor to remove the static pressure bias resulting from the constant head reservoir tank.

The calibration of each Kulite pressure transducer was initially and then periodically checked in-situ after isolating the test section by closing both the 51-cm butterfly valve and the control valve and applying various static pressures to the test section. Pressure was introduced from a regulated air supply, which was temporarily connected to the facility at the first return elbow. A Heise model 623, gage pressure transducer with a range of 0.0 to 700,000 pascals and an accuracy of ±0.1 percent of reading was connected temporarily

28

to one of the pressure taps in the test section and used as the
standard for comparison.

Table II-1 presents the results of the initial calibrations for
the six Kulite pressure transducers. Sensor sensitivity (volts output
per applied pressure) was calculated at seven static calibration
pressures from 98596 to 557789 pascals. In table II-1, the resulting
mean sensitivity and standard deviation for each sensor are presented
along with the 95-percent confidence level accuracy obtained by using
student's "t" distribution. The accuracies ranged from ±0.252 to
±0.648 percent. The accuracy of all the sensors are conservatively
considered in this study to be ±0.7 percent of reading.

Table II-1. Kulite Pressure Transducer Calibrations

| Test Section Pressure (Pa) | Sensitivity (volts/Pa x 10^8) | | | | | |
| | Station No. | | | | | |
	1	2	3	4	5	6
98,706	9.887	10.25	9.685	9.157	9.553	10.15
218,880	9.864	10.24	9.662	9.133	9.516	10.14
281,690	9.858	10.23	9.659	9.130	9.517	10.16
359,950	9.857	10.23	9.662	9.123	9.513	10.15
402,210	9.862	10.22	9.668	9.127	9.520	10.21
479,780	9.865	10.23	9.685	9.133	9.523	10.17
558,040	9.868	10.23	9.683	9.117	9.504	10.13
Average	9.865	10.23	9.672	9.130	9.520	10.16
Std. Deviation (%)	0.103	0.100	0.122	0.145	0.164	0.265
Accuracy (±% of Reading) (95% Level)	0.252	0.245	0.298	0.355	0.401	0.648

TEMPERATURE MEASUREMENTS

Temperature of the flowing fluid was measured with a Cole-Palmer model R8502-50 thermister thermometer and a model R8415-24 thermister probe placed in the first elbow downstream of the test section. The temperature, which was displayed on a digital read-out device, was accurate to ±0.05°C.

WALL SHEAR STRESS MEASUREMENTS

Instantaneous wall shear stress was measured with a multichannel, Thermal Systems Inc. (TSI) IFA 100, hot-wire anemometer and six TSI model 1237-W, flush-mounted, hot-film, wall shear stress sensors. The six sensors were placed along the test section at sensor stations 1 through 6 (see figure II-2 for actual locations). Figure II-5 shows details of the sensor. During the operation, each sensor was maintained at a constant temperature of 66.7°C, resulting in an overheat ratio of approximately 1.1. A low-pass filter, integral to the anemometer, was also set at a frequency of 500 Hz.

The basic theory for this type of sensor was developed by Bellhouse and Schultz [23] in 1966 and Brown [24] in 1967. They showed that the operation of these sensors was based on Reynolds analogy between momentum and heat transfer. The relationship or transfer function between wall shear stress and voltage output from the anemometer was shown to be

30

$$\tau_w = A E^2 + B , \qquad \qquad (II-2)$$

where τ_w is the instantaneous wall shear stress, E is the

instantaneous, hot-film anemometer output, and A and B are constants

determined from calibration. This equation assumes that the wall

shear stress is a function of the near-wall, linear velocity profile

and that pressure gradient effects are second order and negligible if

the wall shear stress is larger than the pressure gradient, i.e., away

from stagnation points or points of separation. Equation (II-2) is

valid for laminar flows and also for turbulent flows when the thermal

boundary layer is smaller than the viscous sublayer (the linear

portion of the velocity profile).
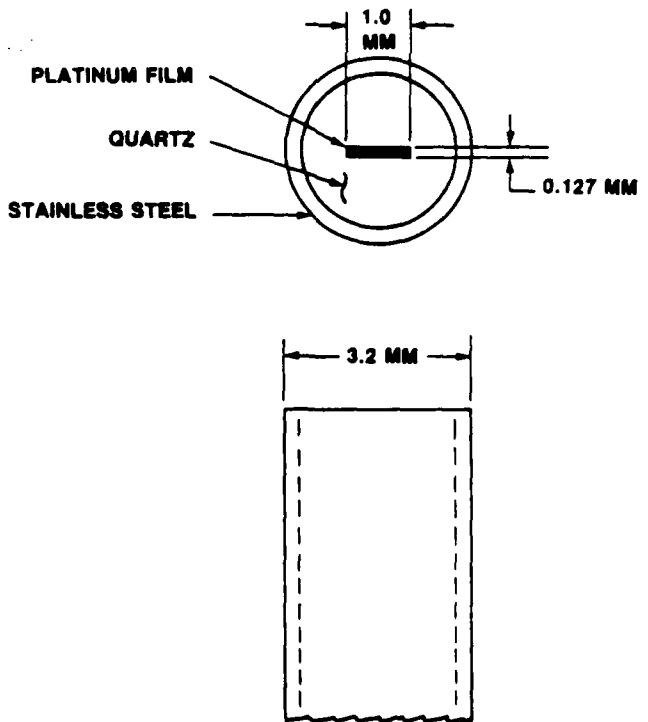
Figure II-5. Hot-Film Wall Shear Stress Sensors

Geremia [25] showed that flush-mounted, hot-film, wall shear stress sensors could be conveniently calibrated in steady-state, turbulent pipe flow. The basis for this method was the transfer function between the time-mean wall shear stress $\overline{\tau_w}$ and time-mean voltage output from the anemometer $\overline{E}$. The transfer function was taken to be of the form

$$\overline{\tau_w} = A \, \overline{E}^2 + B \, , \qquad (II-3)$$

which was similar to the instantaneous transfer function from equation (II-2). The constants in equation (II-3) were assumed equal to those in equation (II-2).

With this method, mean wall shear stress is obtained experimentally from differential pressure measurements and the relation

$$\overline{\tau_w} = \frac{R}{2} \frac{\Delta p}{L} \qquad (II-4)$$

where Δp is the differential pressure, L is the distance between pressure sensors, and R is the pipe radius. During calibration, the flow is set to a steady-state value, and the pressure measurement is taken in the fully developed, turbulent flow region of the pipe. The time-mean voltage output from the anemometer is simultaneously monitored. These measurements are repeated at several pipe Reynolds numbers. Equation (II-4) is applied to all data points, and the constants in equation (II-3) are then determined by using a least-squares-curve fit.

Sandborn [26], the first to point out that nonlinear averaging errors would be substantial when large fluctuations in wall shear stress were present in the calibration facility, showed how to correct for this

32

effect. Nonlinear averaging errors occur because of the nonlinear transfer function between wall shear stress and output voltage as evidenced in equation (II-2). For example, positive and negative fluctuations of the same magnitude about the mean wall shear stress may affect the sensor mean voltage output by different amounts. Therefore, the mean voltage obtained from time averaging is not the correct value associated with the experimentally determined value of mean wall shear stress and must be corrected. Once corrected, the constants in the instantaneous and mean transfer functions, given in equations (II-2) and (II-3), respectively, are equal. It should be noted that Sandborn's approach to correct for nonlinear averaging was very time-consuming. A more straightforward approach was presented by Ramaprian [27].

Sandborn also showed that the wall shear stress fluctuations in pipe flow were not large enough to give rise to nonlinear averaging errors and that the calibration method given by Geremia was accurate for determining the instantaneous and mean transfer functions. However, calibrating wall shear stress sensors in flat plate flows could result in large nonlinear errors.

The wall shear stress sensors in the present study were calibrated in-situ essentially by Geremia's method. However, to facilitate initial calibration and subsequent calibration checks that were conducted throughout testing, the test section friction factor (or nondimensional shear stress) versus pipe Reynolds number characteristic was first established. Friction factor was defined as

$$\bar{f} = 8\overline{\tau_w}/\rho \ \bar{U}_m^2 \ , \tag{II-5}$$

33

and pipe Reynolds number as

$$\overline{Re}_D = \overline{U}_m D/\nu , \qquad (II-6)$$

where U_m is the cross-sectional averaged pipe velocity, ρ is the mass density, D is the test section diameter, and ν is the kinematic viscosity which, in the present study, was calculated to an accuracy of a fraction of a percent using Bingham's equation [28]

$$\nu = \frac{1}{\{21.482 (T-8.435) + [(T-8.435)^2 + 8078.4]^{1/2} - 1200\} \rho} \qquad (II-7)$$

where T is the fluid temperature in °C, and ρ and ν are in units of kg/m^3 and m^2/sec, respectively.

The friction factor was obtained by using equations (II-4) and (II-5) and the differential pressure measurement from either the pressure taps/Validyne transducer combination or the flush-mounted pressure transducers, depending on the flow rate and resulting differential pressure. For any particular calibration pipe Reynolds number, the combination of pressure sensor and distance between sensors was chosen to give the greatest accuracy by considering the most accurate range of each sensor. In general, the measurements from the flush-mounted pressure sensors were used for the high pipe Reynolds number range where large differential pressures were observed. Previous tests documented by Lefebvre [20] proved that the test section did exhibit a constant pressure gradient from the first sensor station to the last.

Table II-2 presents the data obtained from the friction factor versus pipe Reynolds number calibration and lists the various pressure sensor/pressure station combinations used. A least-squares-curve fit

34

was generated from the data, which resulted in the following equation:

$$\overline{f} = 0.1936 \; \overline{Re}_D - 0.2034 \; . \tag{II-8}$$

The test data fit equation (II-8) with a mean error of ±0.009 percent and a standard deviation of ±1.39 percent.

An error analysis was conducted according to the method of Kline and McClintock [29] and included the use of student's "t" distribution to account for the small data sample. Propagation of the errors in the measuring instruments and the error of the mean in the curve fit resulted in a friction factor accuracy of ±4.0 percent (95 percent confidence level) when using equation (II-8). Figure II-6 is a graph of the friction factor versus pipe Reynolds number data along with the curves calculated from equation (II-8) and from Prandtl's well known formula for smooth pipes [28], which is shown in equation (II-9), such that

$$\frac{1}{\sqrt{f}} = 2.0 \; \log \; [Re_D \sqrt{f}] \; -0.8 \; . \tag{II-9}$$

The two curves agree to within 3 percent.

With the friction factor available, wall shear stress sensor calibration consisted of setting the flow to a steady-state value and then simultaneously sampling the velocity signal from the transient flowmeter and the voltage from each of the six wall shear stress sensors. A Masscomp data acquisition system, described later in this report, was used to sample the signals at a rate of 20 Hz for 2.5 minutes, which resulted in a total of 3000 samples. Mean voltage for each sensor and mean velocity were then calculated. The mean velocity was subsequently used to calculate mean wall shear stress using

35

Table II-2. Friction Factor Data

$\overline{Re}_D$ x 105	Pressure Transducer	Sensor Locations	L (m)	ΔP (Pa)	$\overline{f}$ Measured	Eq.II-8	% Error
0.3943	Validyne	1,5	20	1879	0.02212	0.02250	-1.67
0.2207	Validyne	1,5	20	6833	0.02608	0.02531	3.02
0.2956	Validyne	1,5	20	1129	0.02424	0.02385	1.62
0.4615	Validyne	1,5	20	2456	0.02213	0.02179	1.57
0.5580	Validyne	1,5	20	3396	0.02102	0.02096	0.27
0.6829	Validyne	1,5	20	4783	0.02018	0.02012	0.31
0.7624	Validyne	1,5	20	5765	0.01952	0.01967	-0.77
0.9276	Validyne	1,5	20	7922	0.01837	0.01890	-2.82
0.7831	Validyne	3,5	10	3145	0.01951	0.01957	-0.28
0.9253	Validyne	3,5	10	4231	0.01876	0.01891	-0.81
1.172	Validyne	3,5	10	6412	0.01770	0.01802	-1.80
1.310	Validyne	3,5	10	7819	0.01729	0.01762	-1.88
1.731	Validyne	4,5	5	7039	0.01659	0.01665	-0.36
1.937	Validyne	4,5	5	8522	0.01601	0.01627	-1.62
3.003	Kulite	1,6	25	107,972	0.01503	0.01488	0.97
3.696	Kulite	1,6	25	156,994	0.01436	0.01427	0.64
4.010	Kulite	1,6	25	183,126	0.01412	0.01403	0.61
4.283	Kulite	1,6	25	208,016	0.01395	0.01385	0.73
4.621	Kulite	1,6	25	238,767	0.01376	0.01364	0.91
4.923	Kulite	1,6	25	270,897	0.01353	0.01346	0.51
5.627	Kulite	1,6	25	342,258	0.01308	0.01310	-0.15
6.212	Kulite	1,6	25	361,081	0.01299	0.01284	1.18

Mean Error = 0.0093%
Standard Deviation = 1.39%

36
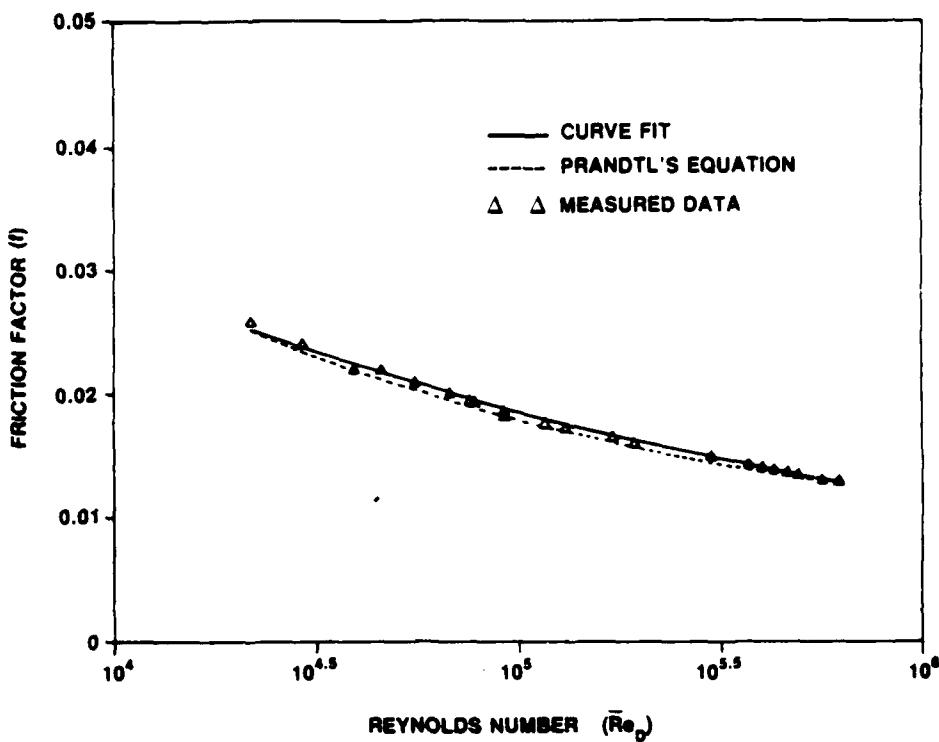
Figure II-6. Test Section Friction Factor vs Reynolds Number

equations (II-8) and (II-5). This procedure was repeated for 11 calibration points.

A fourth-order, least-squares-curve fit was then calculated for each sensor. The general form of the curve was

$$\tau_w = A + B\left(\frac{\overline{E}^2}{\Delta T}\right) + C\left(\frac{\overline{E}^2}{\Delta T}\right)^2 + D\left(\frac{\overline{E}^2}{\Delta T}\right)^3 + F\left(\frac{\overline{E}^2}{\Delta T}\right)^4, \qquad (II-10)$$

where ΔT is the temperature difference between the wall shear stress sensor and the flowing fluid, and A, B, C, D, and F are constants determined from the curve fit. A fourth-order curve was shown to fit the data better than the second order fit of equation (II-3) and wall shear stress was taken to be a function of $E^2/\Delta T$ rather than E to account for temperature variations in the fluid. $E^2/\Delta T$ is actually proportional to the heat transfer coefficient for the

37

hot-film sensor. These calibration curves were then taken to be valid
representations of both the instantaneous and mean transfer functions.

A typical calibration curve, sensor 2, is shown in figure II-7.
Propagation of the errors, in a manner analogous to that used
previously, resulted in a wall shear stress accuracy of ±14.0
percent (95-percent confidence level) when using these calibration
curves. Unfortunately, the calibration curves for sensors 4 and 5
continuously drifted throughout the test program and were considered
unuseable for absolute level of wall shear stress. Therefore, these
curves were used only to monitor transition from laminar to turbulent
flow during the transient tests.
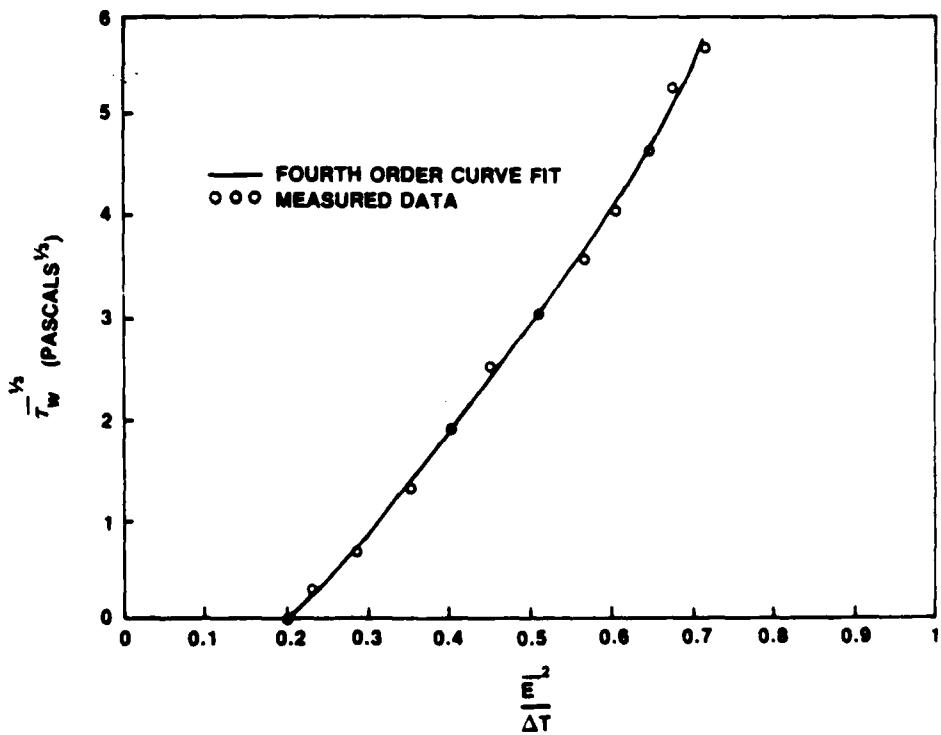
Figure II-7. Calibration Curve for Wall Shear
Stress Sensor No. 2

Prior to conducting the previously mentioned calibrations, two preliminary studies were conducted. The first was a calibration of one of the wall shear stress sensors using Ramaprian's approach [27] for incorporating effects of nonlinear averaging. The study proved that nonlinear averaging errors were indeed negligible and the calibrations as conducted for this study were accurate. The second preliminary study was an investigation of the effect of mounting position on the wall shear stress sensors. The results, documented by Lefebvre and LaPointe [30], show that the sensors should be positioned so that the spanwise center of the sensor is flush with the inside wall of the test section. Figure II-8 illustrates this position. Accurate positioning of the sensor was easily verified since each sensor was only 7.6 cm from a flanged joint.
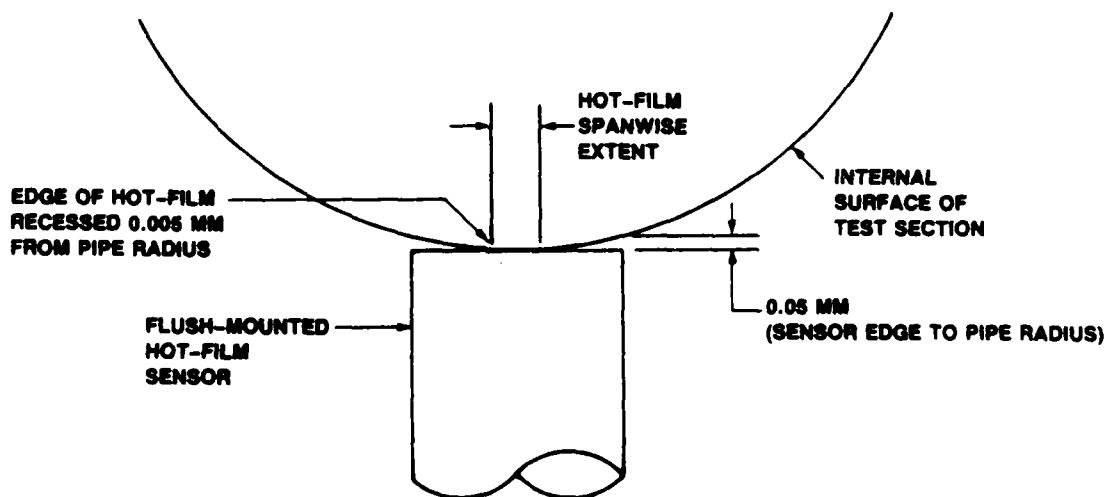
NOTE: SCALE OF TEST SECTION
AND SENSOR ARE DISTORTED

Figure II-8. Flush-Mounting Position for Hot-Film
Wall Shear Stress Sensor

39

Although wall shear stress sensors of the type used here have been used by many other investigators to measure instantaneous wall shear stress in unsteady flows, the question of whether the sensors can accurately respond to transients is still unanswered. This question has been investigated in the present study by using the transient capabilities of the Flow Loop Facility. The approach and results are presented later in this report.

LOCAL VELOCITY AND REYNOLDS STRESS MEASUREMENTS

A three-beam, two-component LDV operating in the dual-beam mode was configured for measurement of the axial and radial velocity components in the clear acrylic portion of the test section. The setup of this system differed from that normally used in a two-component system. This new setup was based on the system presented by Arnold et al. [31] with some changes to accomodate the particularities of the present test program. One of the major advantages of the present setup was that unlike most other multicomponent systems this system was operated in a forward scatter mode, which resulted in much higher data rates.

The arrangement of the LDV optics and laser are shown in figure II-9. The major components consisted of a Lexel, 2-watt, argon-ion laser, which emitted a green beam having a wave length of 514.5 nanometers, beam splitters to separate the beam from the laser into three separate beams all in the same plane, and two acousto-optic

40
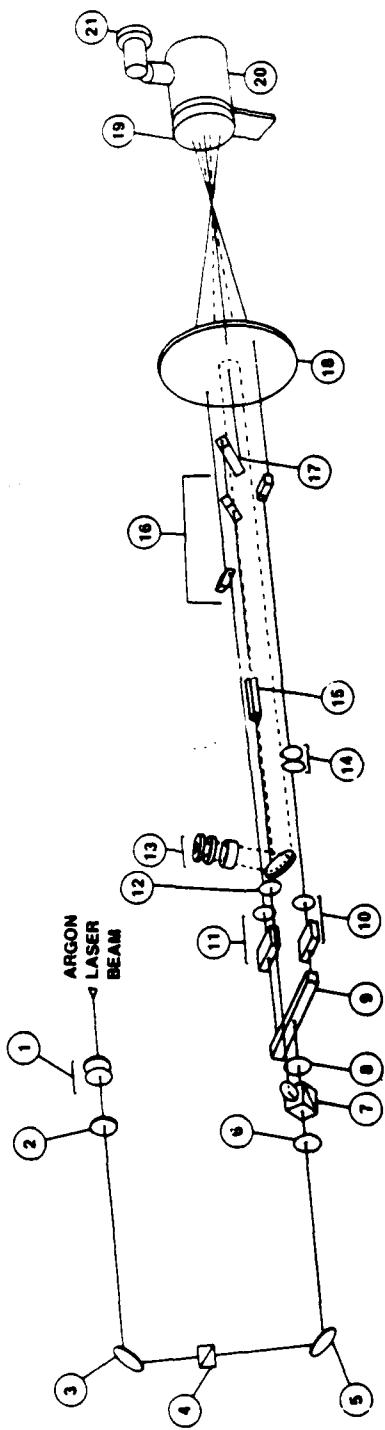
ITEM	TSI MODEL	DESCRIPTION
1	9166	COLLIMATOR
2	9101	POLARIZATION ROTATOR
3	9107	MIRROR
4	9136	ATTENUATOR
5	9107	MIRROR
6	9102-12	POLARIZATION ROTATOR
7	9216-1	BEAM SPLITTER
8	9102-12	POLARIZATION ROTATOR
9	9115-1	BEAM SPLITTER
10	9282-12	80 MHz BRAGG CELL
11	9182-12	40 MHz BRAGG CELL

ITEM	TSI MODEL	DESCRIPTION
12	9103-12	POLARIZATION ROTATOR
13	9140,9162	RECEIVING OPTICS
14	9175	BEAM STEERER
15	9220	BEAM ANGLE ADJUSTER
16	9207	BEAM SHIFTER
17	9205	BEAM SHIFTER
18	9169-250	FOCUSING LENS
19	9118-250	RECEIVING LENS
20	9140	RECEIVING OPTICS
21	9162	PHOTO MULTIPLIER

ARGON LASER BEAM

Figure II-9. Laser Doppler Velocimeter Schematic

Bragg cells for frequency shifting the two outer beams. In addition, it had a 10-cm diameter focusing lens, a 5-cm diameter receiving lens, two photo-multipliers, and the electronics, which included two TSI model 1980, counter-type signal processors. The laser and optics were mounted on a one-axis traversing mechanism, which had a readability of 0.001 cm.

The theory of operation of the LDV system is explained in reference to figure II-10. Detail is given to the extent necessary to describe the basic features of this new configuration. Extensive detail on the conventional aspects of the system operation are provided in reference [32].
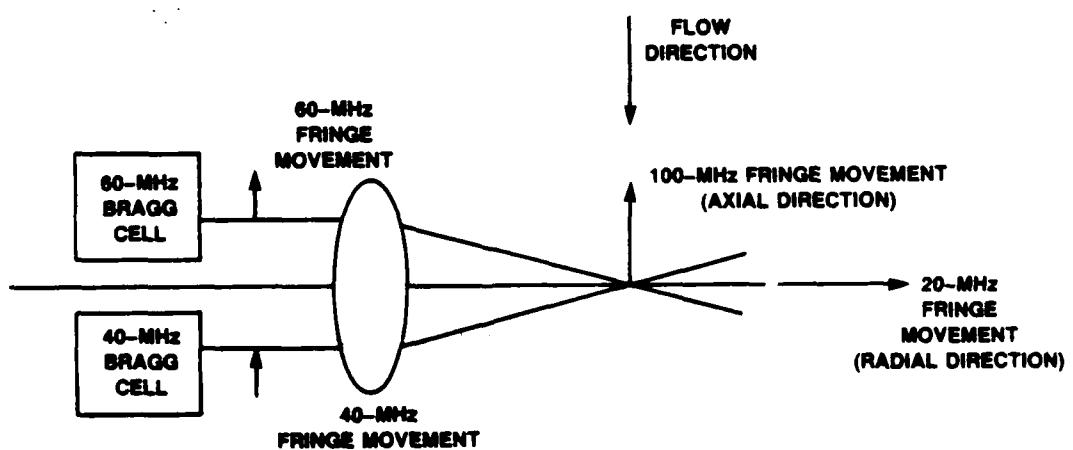
Figure II-10. Laser Doppler Velocimeter Frequency Shifting

The two outer beams are frequency shifted by the acousto-optic Bragg cells. The top beam is shifted by 60 MHz and the bottom beam is

42

shifted by 40 MHz in the directions shown in figure II-10. At the

measuring volume (the focal point of the three beams), the two outer

beams combine to set up the fringe pattern (light wave interference

pattern) normally present in LDV systems operating in the dual beam

mode. These fringes are parallel to the bisector of the two outer

beams and in planes perpendicular to that of the three beams. Since

the two outer beams are frequency shifted, the fringe pattern is not

stationary but moves at a rate of 100 MHz (the addition of the two

shift frequencies) and in a direction opposite that of the axial

flow. The distance between fringes is based on the half angle between

the two outer beams κ and the wave length of laser light λ, both

accurately known. The distance between fringes, d_f, is then

accurately calculated from the following equation:

$$d_f = \frac{\lambda}{2 \sin \kappa} \cdot$$ (II-11)

The axial velocity component of the flow, which is perpendicular

to this fringe pattern, is obtained by measuring the frequency of

scattered light generated by particles in the flow as they move past

the fringes. Instantaneous local axial velocity U is then calculated

by the relationship

$$U = f_D \cdot d_f$$ (II-12)

where f_D is the scattering or Doppler frequency seen by the laser

counter processor minus the shift frequency (that is, the frequency

that would be generated if there was no frequency shifting and the

fringe pattern was stationary).

43

The center, unshifted beam is included for the measurement of the radial component of velocity. The three beams combine to set up a virtual fringe pattern, shown in figure II-11, perpendicular to both the center beam and the axial component fringe pattern. This provides a means of measuring the radial velocity component, which is parallel to the center beam. As shown by Arnold et al. [31], this fringe pattern has an effective shift frequency equal to the difference between the two outer beam shift frequencies, or 20 MHz in this case. The equation for the fringe spacing was also shown to be

$$d_z = \frac{\lambda}{4 \sin^2 (\kappa/2)} .$$ (II-13)

Radial velocity can then be calculated by using equations (II-13) and (II-12) with d_f replaced by d_z.
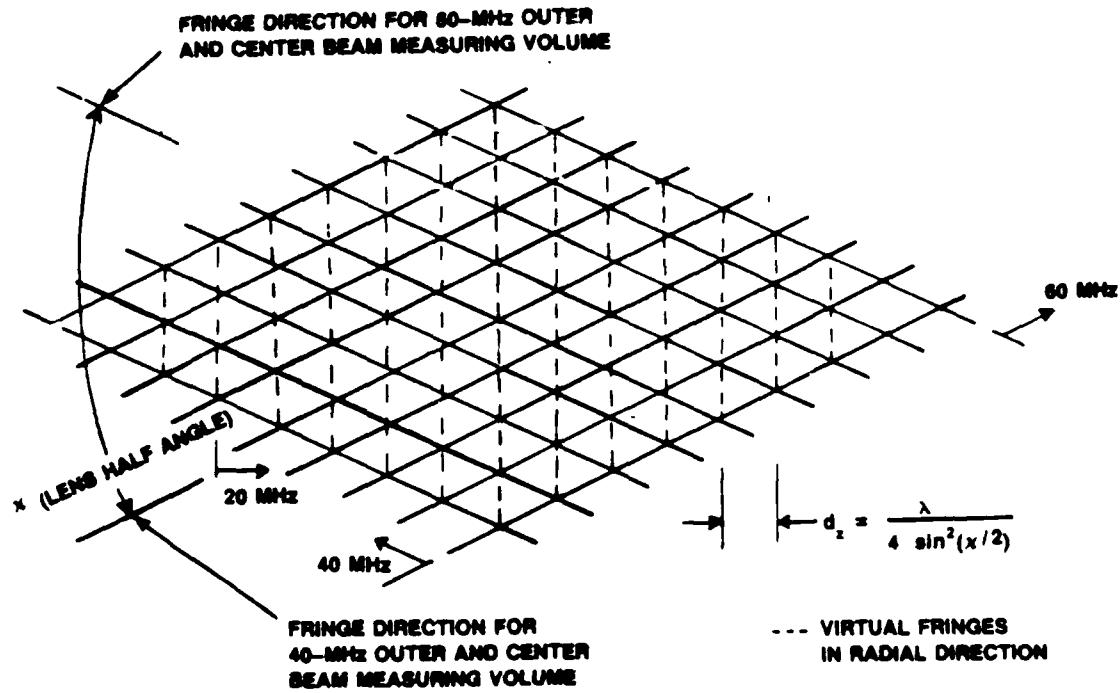
Figure II-11. Laser Doppler Velocimeter Virtual Fringe
Spacing in the Radial Direction

44

In actual operation, the scattered light was detected in a forward scatter mode by a single photo-multiplier placed after the receiving lens. The signal from the photo-multiplier was then filtered to separate the 100-MHz shifted axial velocity component signal from the 20-MHz shifted radial component signal. Both signals were then processed separately by the counter-signal processors. The processors provided a digital data-ready signal on output whenever valid data had been acquired and latched on to the processors' digital output buffers. Since data to the counter processors were only available when a particle traversed the measuring volume, and since the processors performed a statistical operation on each data point to determine whether it was valid or should be rejected, the data-ready signals from each processor occurred randomly.

A special electronics interface was developed to provide a link between the two counter-processors and the data acquisition system. This interface accepted the velocity data from each of the two counters and provided three output latch buffers or ports for three velocities.

The first output port contained the axial velocity component updated at each data-ready signal from the axial component counter-processor. The remaining two ports were for the values of axial and radial velocity only when the data-ready signal from each counter-processor was obtained within a time window that was user selectable on the interface.

45

These last two data are referred to as coincident velocity components for the remainder of this report. The data were used to calculate Reynolds stress, which is the average of the product of the fluctuations of the two velocity components. The time window was set to assure that the two velocity components were indeed coincident (occurring simulaneously), being generated from the same particle. The data on each of the three buffers were continually updated at each data-ready signal until a data-inhibit signal was generated by the data acquisition system during its data sampling phase. Following the sampling, the three buffers on the interface were reset to zero to assure that any new data were actually generated within the next sampling time window.

To assure accurate measurements of the radial velocity component, the center beam had to be accurately centered between the two outer beams. This was accomplished by using a TSI model 10925 calibrator. This unit consisted of a wheel that rotates in both directions at constant angular velocity and has a rubber scattering surface. During calibration, the focal point of the three beams was positioned on the rubber surface. The center beam was then adjusted with an optical wedge until the same velocity was measured for both rotational directions of the wheel. During this calibration, the LDV system was operated in the backscatter mode since the wheel was not transparent and the scattered light was reflected back into the focusing lens. This was the only purpose for the photo-multiplier that was located between the laser and the focusing lens.

46

The measuring volume for this LDV system was 0.93 mm long in the radial direction by 0.161 mm high. Due to the finite length of the measuring volume, there was some uncertainty as to its effective center. The zero of the traversing mechanism was initially set by visually aligning the measuring volume on the inside wall of the clear test section. The true zero was established by obtaining velocity profiles across the test section diameter at several steady-state pipe Reynolds numbers and adjusting the traversing mechanism until the profiles were symmetrical about the test section centerline.

The radial velocity component that was measured was parallel to the center beam and in the horizontal plane at the vertical centerline of the test section. For velocity profile measurements, the traversing mechanism was traversed across the pipe in the direction of the center beam and always in the horizontal plane at the test section vertical centerline. Since all three beams always entered the clear test section at its vertical centerline, problems involving pipe curvature were circumvented. This innovation plus the forward scattering operational mode, were the two major advantages of the LDV system specifically configured for this study.

To account for the change in the index of refraction between air and water, the traversing mechanism was moved 0.753 units for each unit displacement of the measuring volume in the water. The calculation procedure used to arrive at this value was straightforward and can be found in reference [32].

The overall accuracy for the LDV measurements was estimated to be

47

±1.0 percent of the reading for the axial velocity and ±3.0 percent for the radial velocity. Calculations for various measuring volume parameters with and without a 2.27X beam expander are contained in appendix B. Note that during the present study, the beam expander was not used.

DATA ACQUISITION AND POST PROCESSING HARDWARE

A Masscomp MC-500 data acquisition system was utilized to acquire and process all data. The system was a 32-bit, Unix-based, embedded processor minicomputer configured with a high-capacity hard disk (50 Mbytes); a 16-channel, analog input board; and three, bit-parallel, digital input boards.

This system had the capability of acquiring both analog and digital data simultaneously without any data loss at the sampling rates required by the present study. In the present experiments, the LDV data were in digital form, whereas all remaining instruments had analog output from 0 to 10 volts.

MEASUREMENTS ACCURACY SUMMARY

Table II-3 is a summary of those accuracy statements, presented in the previous sections, which are associated with the measurements made during the testing phase of this study. All accuracies are based on a 95-percent confidence level.

Table II-3. Summary of Measurement Accuracy

Measurement	Accuracy (of reading)
Temperature	±0.05° C
Wall pressure	±0.7 percent
Wall shear stress	±14.0 percent
Cross-sectional averaged velocity	±1.0 percent
Local axial velocity (LDV)	±1.0 percent
Local radial velocity (LDV)	±3.0 percent

III. EXPERIMENTAL PROCEDURE

The experimental phase of the present study included preliminary steady-state experiments and two series of transient tests. These tests were separated into three catagories:

1. Steady-state experiments conducted at several pipe Reynolds numbers mainly to characterize the Flow Loop Facility.

2. Individual transient tests at constant accelerations ranging from 1.8 to 12.2 m/s/s in approximately 0.6 m/s/s increments to investigate transition.

3. Repeat transient tests at two selected accelerations where velocity profiles and other flow field details were obtained.

The details of the procedures followed during these experiments are described in detail in this section of the report.

STEADY-STATE EXPERIMENTS

The steady-state experiments were conducted at several pipe Reynolds numbers. The purpose was to: (1) establish the steady-state characteristics of the test section, (2) assure that all of the instruments used were functioning properly, and (3) obtain a reference to which quasi-steady comparisons of the transient tests could be made.

As discussed in the previous section on "Wall Shear Stress Measurements," the friction factor versus pipe Reynolds number curve, shown in figure II-6 and described by equation (II-8), was obtained to facilitate wall shear stress sensor initial and periodic calibrations.

50

The approach was presented in that section since it was part of the
calibration procedure. These data were also used to satisfy the three
previously stated purposes for the steady-state tests as regards to
test section friction factor, wall shear stress, and pressure gradient
versus pipe Reynolds number.

The next set of steady-state tests were velocity profile
measurements at three different pipe Reynolds numbers using the LDV.
The pipe Reynolds numbers--65,000, 275,000, and 450,000--covered the
approximate range over which the transient tests were conducted.

The velocity profiles were obtained as follows. The flow was set
to a steady-state value of pipe Reynolds number using the control
system to hold the control valve at a constant position. Time-mean,
cross-sectional averaged velocity (U_m) in the test section was
measured by the transient flowmeter, while fluid temperature (to
subsequently obtain fluid properties) was measured by the temperature
probe. The measuring volume for the LDV was positioned near one of
the inside walls at the closest point of measurement. The LDV data at
the three output ports of the LDV interface were then sampled at a
rate of 20 Hz for a total time of 2.5 minutes or 3000 sampling
intervals. As previously stated, the LDV data included the axial
velocity component of the flow along with the coincident axial and
radial flow components. Since the LDV interface automatically zeroed
the output buffers following sampling by the Masscomp, only the
non-zeroed data (valid data since the previous sample) were included
in the calculation of time-mean axial velocity $(\bar{U})$ at a point and the

51

root-mean-square (RMS) of its fluctuations $\sqrt{u'^2}$ by using the following equations:

$$\bar{U} = \frac{1}{N} \sum_{i=1}^{N} U_i , \qquad (III-1)$$

$$\sqrt{u'^2} = \left[\frac{1}{N} \sum_{i=1}^{N} U_i^2 - \bar{U}^2 \right]^{1/2} , \qquad (III-2)$$

where U is the instantaneous measurement of axial velocity and N is the total number of valid non-zero data points obtained during the sampling time.

Similarly, the calculation of Reynolds stress $\overline{\rho u'v'}$ was obtained using the following:

$$\overline{\rho u'v'} = \frac{\rho}{N} \sum_{i=1}^{N} u_i' v_i' , \qquad (III-3)$$

where u_i' and v_i' are the coincident, instantaneous fluctuations of the axial and radial velocity components, respectively.

Since the mean radial velocity was zero, v_i' was used as measured. However, since the axial velocity fluctuations u_i' were superimposed on the mean axial velocity, u_i' was calculated as

$$u_i' = \bar{U} - U_i . \qquad (III-4)$$

Pipe Reynolds number was then calculated from equation (II-6) and used in equation (II-8) to calculate friction factor. Equation (II-5) was subsequently used to calculate wall shear stress. The computed local mean velocity and Reynolds stress values were then nondimensionalized with friction velocity u*, where

$$u^* = \sqrt{\frac{\tau_w}{\rho}} . \qquad (III-5)$$

52

The above procedure was repeated for about 25 points across the diameter of the clear test section. The complete sequence was then repeated for the remaining two pipe Reynolds numbers at which steady-state tests were conducted.

TRANSIENT EXPERIMENTS

The first set of transient experiments were conducted to investigate the effect of acceleration on laminar to turbulent transition and also on wall shear stress and pressure gradient along the test section in both the laminar and turbulent regimes. This series of transient tests was divided into four basic groups with accelerations ranging from 1.8 to 11.8 m/s/s. The groups were:

1. Constant acceleration from rest to a final mean velocity of 8.8 m/s in 0.6 m/s/s-acceleration increments.

2. Same as group 1 but to a final mean velocity of 11.3 m/s.

3. Constant acceleration from an initially turbulent flow at approximately 1 m/s mean velocity to a final mean velocity of 8.8 m/s in 1.2 m/s/s-acceleration increments.

4. Same as group 3 but to a final mean velocity of 11.3 m/s.

The measurements made during each of the experiments in the above groups were identical and consisted of the following. The LDV was utilized for the measurement of instantaneous axial velocity at the test section centerline. The radial flow component was not measured during these tests since only one run at each acceleration was conducted and, therefore, an ensemble-averaged Reynolds stress at any time t

53

as calculated for the second series of transient tests was not possible.

Instantaneous, cross-sectional averaged velocity was acquired from the transient flowmeter. Instantaneous wall pressure and wall shear stress at each of the six sensor stations were measured via the flush-mounted pressure transducers and the flush-mounted, hot-film, wall shear stress sensors, respectively.

These data were sampled continuously throughout the transient run by the Masscomp data acquisition system at a rate of 480 Hz for a total of 6 seconds. At the start of each run, the Masscomp prompted the user for the fluid temperature, which was input via the terminal. Temperature was subsequently used in applying the wall shear stress sensor calibrations to the raw data and to calculate fluid properties.

The procedure to initiate a test run within each of these groups was also essentially identical. The control system command signal data file was generated for the particular test conditions of the run. Various information pertaining to the run such as run number, along with fluid temperature, were input into the Masscomp. The 150-hp pump was started and allowed to reach a steady-state speed (approximately 30 seconds). The control system software on the Apple computer was then run to initiate the test. If the test started from rest, the Apple computer would send a signal to the Masscomp to trigger the start of data acquisition. After approximately a 1-second delay following the start of data acquisition, the flow acceleration was initiated. If an initial velocity other than 0.0 was called for,

54

the control system would achieve that flow in the test section and wait for a prompt to continue. The signal to continue with the acceleration phase was then given to the Apple computer after approximately 30 seconds to allow the flow to stabilize. The process continued in the same manner as for the 0.0 initial velocity tests.

Post-processing software was developed to apply the calibrations of each of the instruments to the raw data. Data were then output in graph form for every fourth data point (120/second) and in tabular form for every eighth data point (60/second). Since the transient flowmeter only updated tne cross-sectional averaged velocity measurement at a rate of 60 Hz, every eighth data point, which corresponded to a recent update, was valid. The intermediate points were then calculated by using a linear interpolation between the two valid update points.

The second series of transient tests were similar to the previous set of tests except that many repeat tests were conducted at two selected constant accelerations. These tests were conducted to obtain velocity profile and Reynolds stress measurements in addition to the data of the previous tests. The two accelerations were 2.4 and 6.1 m/s/s. At each acceleration, two sets of tests were conducted: one starting from rest and the other from an initially turbulent state with an initial velocity of approximately 1 m/s. Tests with an acceleration of 2.4 m/s/s had a final velocity of 8.8 m/s, while those at an acceleration of 6.1 m/s/s had a final velocity of 11.3 m/s.

The measurements and procedures during each of these tests were

55

similar to the first set of transient tests except for the additional measurements of the coincident axial and radial velocity components. For each acceleration and initial velocity combination, 20 repeat tests were conducted at each of 12 LDV measuring volume positions across the radius of the clear test section ($0.05 < Y/R < 1.0$).

Following the 20 repeat tests at any one LDV measuring volume position, all data were converted to physical units via the calibrations for each of the instruments and ensemble averages were subsequently calculated for each data channel. Ensemble averages were calculated for every eighth data point (60/second of data). Ensemble averaging was equivalent to averaging over the measurements obtained at identical times during the test runs. Thus, the ensemble average for an instantaneous quantity $I(t)$ at time t was

$$\langle I(t) \rangle = \frac{1}{M} \sum_{i=1}^{M} I(t)_i \, , \qquad (III-6)$$

where $\langle \rangle$ denotes the ensemble averaged quantity and M is the total number of repeat tests. Again, for the LDV data, only those repeat tests where valid data were obtained at the particular time t were included in the calculations.

In addition to the ensemble average, the RMS fluctuations about that average was also calculated according to

$$\langle I(t)_{RMS} \rangle = \frac{1}{M} \left[\sum_{i=1}^{M} I(t)_i^2 - \langle I(t) \rangle^2 \right]^{1/2} \qquad (III-7)$$

The RMS calculations were used to analyze the repeatability between tests and to determine the time dependent turbulent fluctuations in the axial direction.

56

IV. RESULTS

In this section of the thesis, results are presented first for
the steady-state tests and then for the two series of transient
tests. For the steady-state tests, results are compared to similar
data obtained by others. The various transient data are compared to
the quasi-steady values obtained from the steady-state measurements on
the Flow Loop Facility and to exact solutions where applicable for
times when the flow is laminar. A quasi-steady value is the
corresponding steady-state value for a particular instantaneous
cross-sectional averaged velocity.

STEADY-STATE EXPERIMENTS

In figure II-6, the steady-state friction factor versus pipe
Reynolds number characteristic of the test section was presented as
part of the calibration data for the hot-film wall shear stress
sensors. The data were shown to agree with the curve fit given by
equation (II-8), which resulted in a mean error of +0.009 percent and
a standard deviation of ±1.39 percent. This curve was also shown to
agree within 3 percent to the well-known formula for smooth pipe
friction factor given by Prandtl as equation (II-9).

As mentioned in section III of this thesis, the remaining
steady-state experiments were conducted at pipe Reynolds numbers of
65,000, 275,000, and 450,000 covering the approximate range over which
the transient tests were conducted. These steady-state tests are

described next and include data on velocity profile, turbulence intensity and Reynolds stress.

Mean Velocity Profiles

Figures IV-1 through IV-3 show the mean velocity profiles at pipe Reynolds numbers of 65,000, 275,000, and 450,000, respectively, taken with the LDV. The data are presented in the usual wall layer coordinates U^+ versus Y^+ where

$$U^+ = U/u* \qquad (IV-1)$$

and

$$Y^+ = Yu*/\nu \ . \qquad (IV-2)$$

Data were collected across the test section diameter at Y/R values of 0.05 and 0.1 from each wall and at subsequent increments of Y/R = 0.1 to the centerline. Results are distinguished as to the side
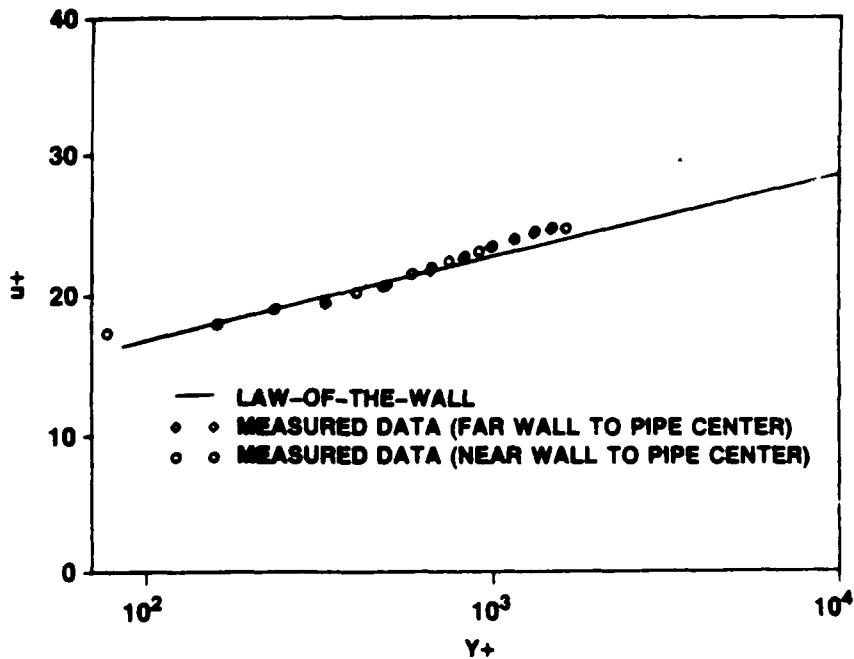
Figure IV-1. Steady-State Velocity Profile at $\overline{Re}_D$ = 65,000

58
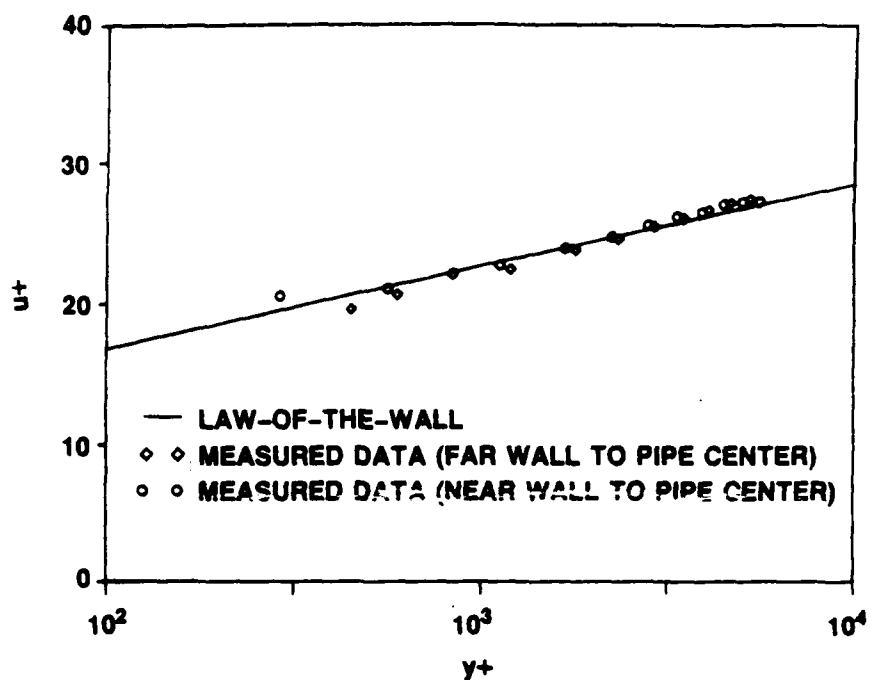
Figure IV-2. Steady-State Velocity Profile at $\overline{\text{Re}}_D = 275,000$
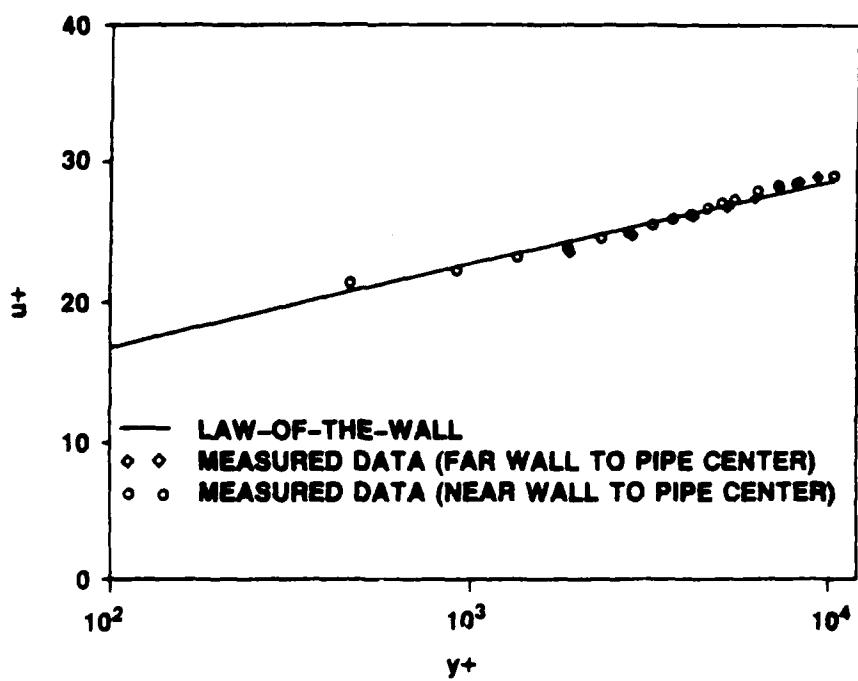
Figure IV-3. Steady-State Velocity Profile at $\overline{\text{Re}}_D = 450,000$

59

of the test section at which the data were taken (the near and far walls being relative to the LDV focusing lens). It should be noted that the rate at which valid LDV data were obtained for the axial velocity component was as high as 50,000 Hz. This is a considerable improvement over previous LDV techniques that utilized back-scattering, which resulted in data rates of about 500 Hz.

Figures IV-1 through IV-3 show very good agreement with the theoretical values of the universal log law as calculated using Spalding's law-of-the-wall

$$Y^+ = U^+ + e^{\kappa' B}[e^{\kappa' U^+} - 1 - \kappa' U^+ - \frac{(\kappa' U^+)^2}{2} - \frac{(\kappa' U^+)^3}{6}] \qquad (IV-3)$$

shown as the solid line in the figures. κ' and B in this equation are constants taken as 0.4 and 5.5, respectively. Some deviation, however, can be noticed at the upper values of Y^+ due to a slight wake effect not accounted for in equation (IV-3). Additionally, the data show that the velocity profiles are indeed axisymmetric with values of U^+ from each side of the pipe at the same Y^+ values essentially overlapping each other. Figure IV-4 is a composite of the near wall to centerline data of the three previous figures.

Based on these data, all subsequent LDV measurements were taken only on the one side of the pipe from the near wall to the pipe centerline. Also, for the transient tests, actual data of instantaneous values of velocity were compared to quasi-steady values calculated using Spalding's law-of-the-wall (equation (IV-3)).
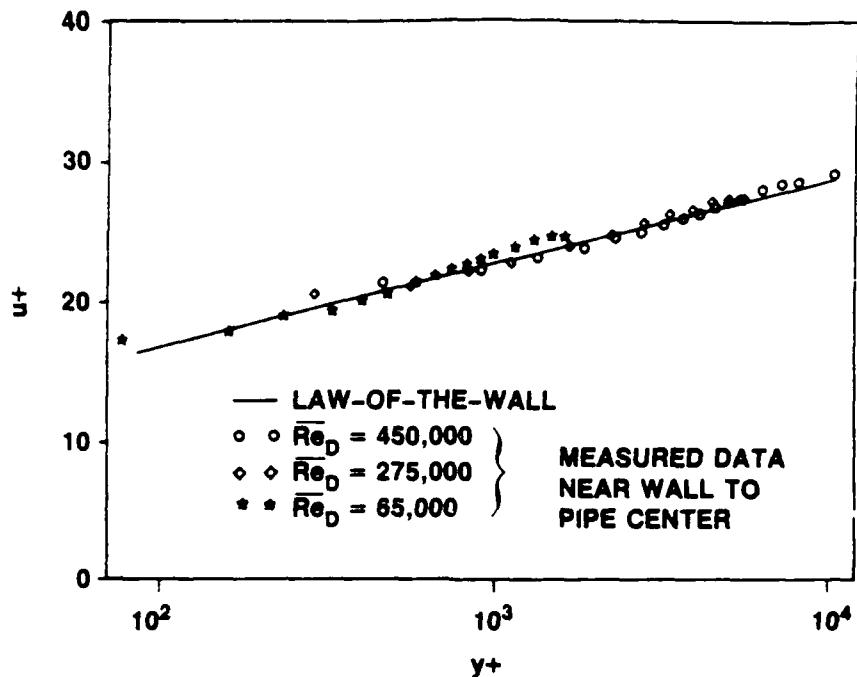
Figure IV-4. Combined Steady-State Velocity Profiles

Mean Turbulence Distributions

The distribution of turbulence intensity, $\sqrt{\overline{u'^2}}/u^*$, across the pipe radius for the three test Reynolds numbers are plotted in figures IV-5 through IV-7. Similar data by Laufer [33] at Reynolds numbers, based on centerline velocity, $\overline{Re}_{cl} = D\overline{U}_{cl}/\nu$, of 50,000 and 500,000, which are generally accepted as the baseline for comparison in smooth pipe flow, are also plotted on each figure. Since $\overline{U}_{cl}$ is approximately 20 percent higher than $\overline{U}_m$ for the $\overline{Re}$ tested, the corresponding $\overline{Re}_D$ for Laufer's data are approximately 42,000 and 420,000. The data of Laufer was shown to be virtually independent of $\overline{Re}_{cl}$.

Considering the low absolute values for the turbulence intensity (from 1 to 2.7 percent) across the pipe at any of the stated Reynolds
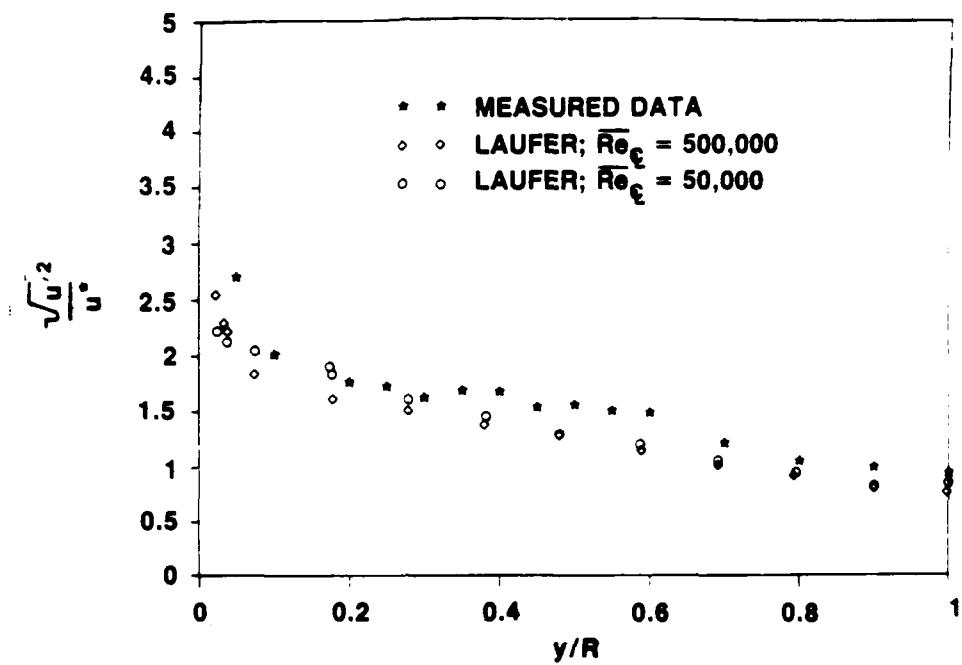
Figure IV-5. Steady-State Turbulence Intensity at $\overline{Re}_D = 65,000$
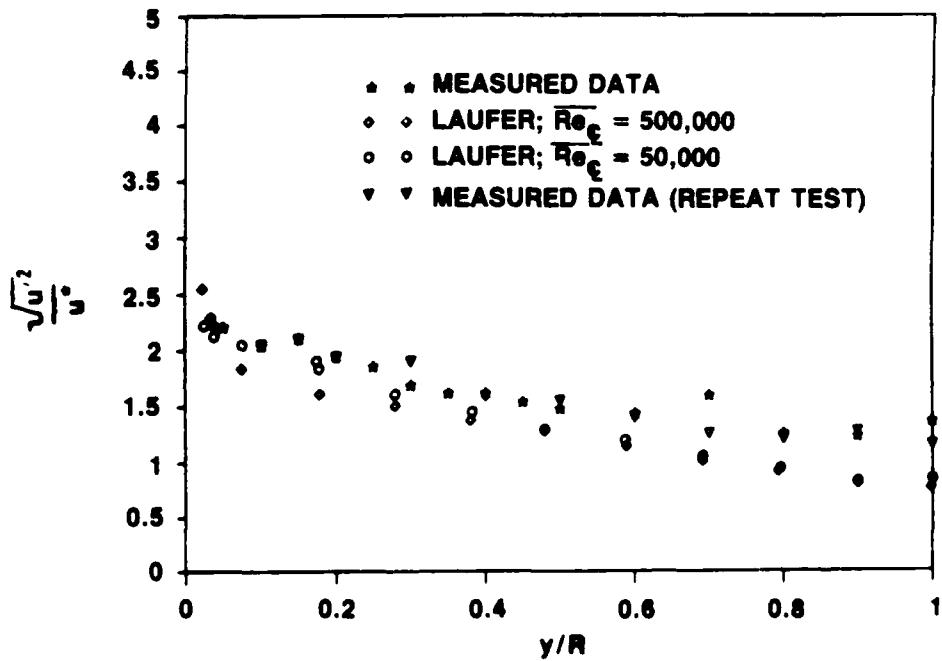
Figure IV-6. Steady-State Turbulence Intensity at $\overline{Re}_D = 275,000$

62
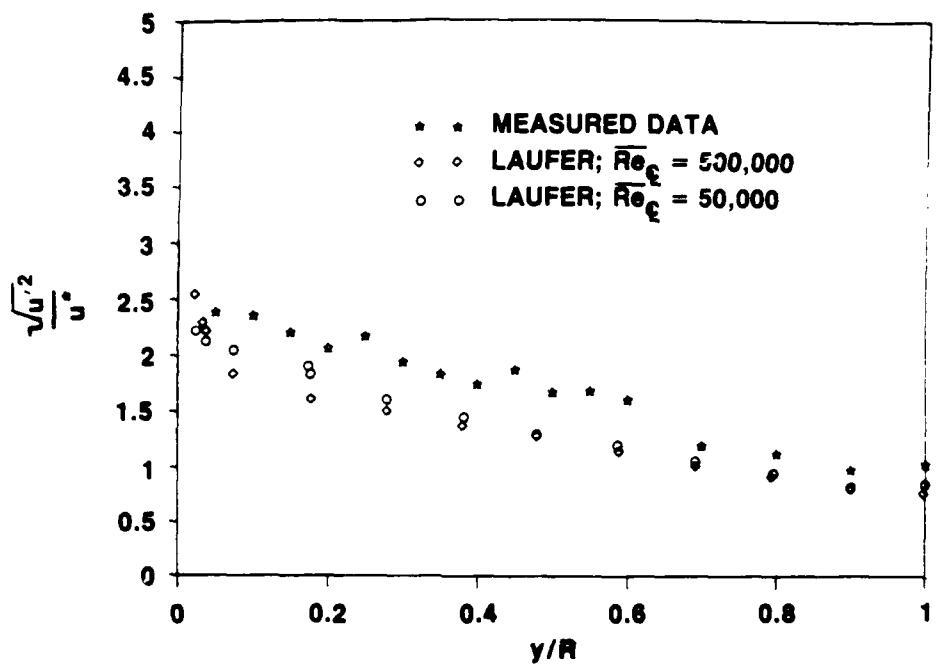
Figure IV-7. Steady-State Turbulence Intensity at $\overline{Re}_D = 450,000$

numbers, the difference between the measured values for the test

section and those of Laufer can be considered negligible. The largest

differences observed, however, were at a pipe Reynolds number of

450,000 and were approximately 0.5 percent.

Repeatability of the turbulence intensity measurements was

verified by repeating measurements at a pipe Reynolds number of

275,000 for several locations across the pipe radius. The measured

values at each repeat point, included in figure IV-6, were all

essentially at the same value of turbulence intensity as the initial

set of data, thus indicating very good repeatability.

Data for Reynolds stress distribution, in the form $-\overline{uv}/u^*$, are

given in figure IV-8 for the three test pipe Reynolds numbers. Also

63
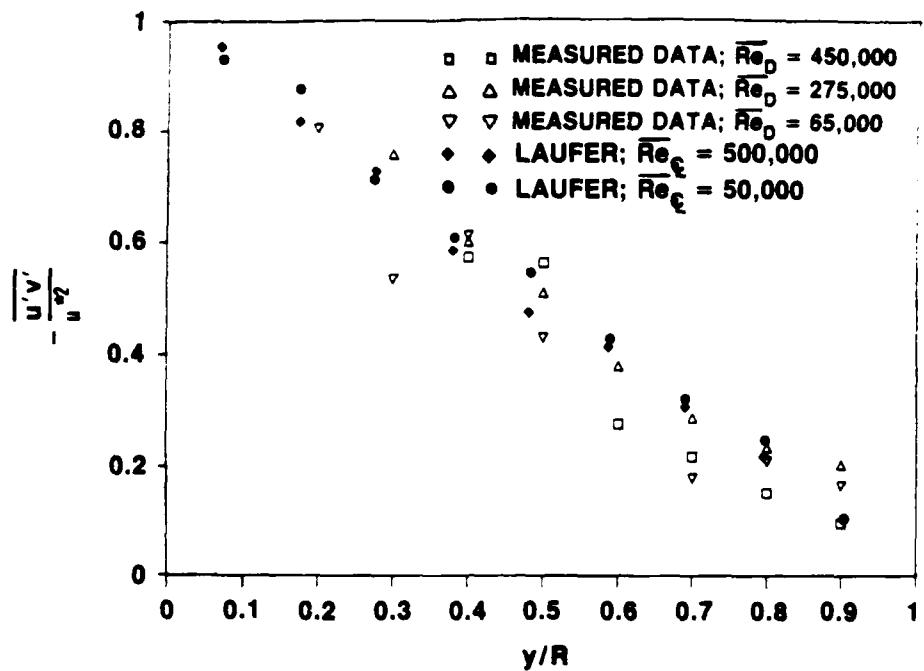
Figure IV-8. Steady-State Reynolds Stress

plotted are the data of Laufer [33] at $\overline{Re}_{cl}$ of 50,000 and 500,000.
Only data from Y/R locations between 0.2 and 0.9 are given for the
present study. This is due to the difficulty in obtaining Reynolds
stress measurements near the wall due to scattering of the laser beam
by the wall and the difficulty in obtaining values near the centerline
because of the low absolute values of $\overline{u'v'}$.

For the range given, however, very good agreement is displayed
between all the data. As expected, since the Y/R locations of the
data points are all at Y^+ values beyond 300, the data follow a
straight line between $-\overline{u'v'}/u^*$ of 1.0 at the wall to a value of 0.0 at
Y/R equal to 1.0 (pipe centerline).

Since the mean or steady-state values of the turbulence
quantities discussed here are in close agreement with the widely

accepted smooth pipe values from Laufer's data, Laufer's data will be
used for the quasi-steady values for comparison with the transient
results obtained from this study.

TRANSIENT EXPERIMENTS

Transition to Turbulence

The first set of transient data to be presented consists of the
37 tests conducted with constant acceleration from rest to a final
mean velocity of either 8.8 or 11.3 m/s, depending on the acceler-
ation. The range of the actual accelerations was from 1.8 to 11.8
m/s^2.

Figures IV-9 through IV-28 show time histories of various
measurements made during five different runs covering the acceleration
range tested. These figures are presented to indicate the type and
quality of the instantaneous transient measurements made. Measurements
shown are of the cross-sectional velocity (U_m) from the transient
flowmeter, centerline velocity (U_{cl}) from the LDV, uncalibrated
output of the six hot-film wall shear stress sensors, and pressure at
each of the six sensor stations. Note that in some figures, pressure
sensor 3 was malfunctioning. The actual accelerations represented by
these figures are 1.77 m/s^2 for figures IV-9 through IV-12, 4.36
m/s^2 for figures IV-13 through IV-16, 6.73 m/s^2 for figures IV-17
through IV-20, 6.53 m/s^2 for figures IV-21 through IV-24, and 11.79
m/s^2 for figures IV-25 through IV-28.

65
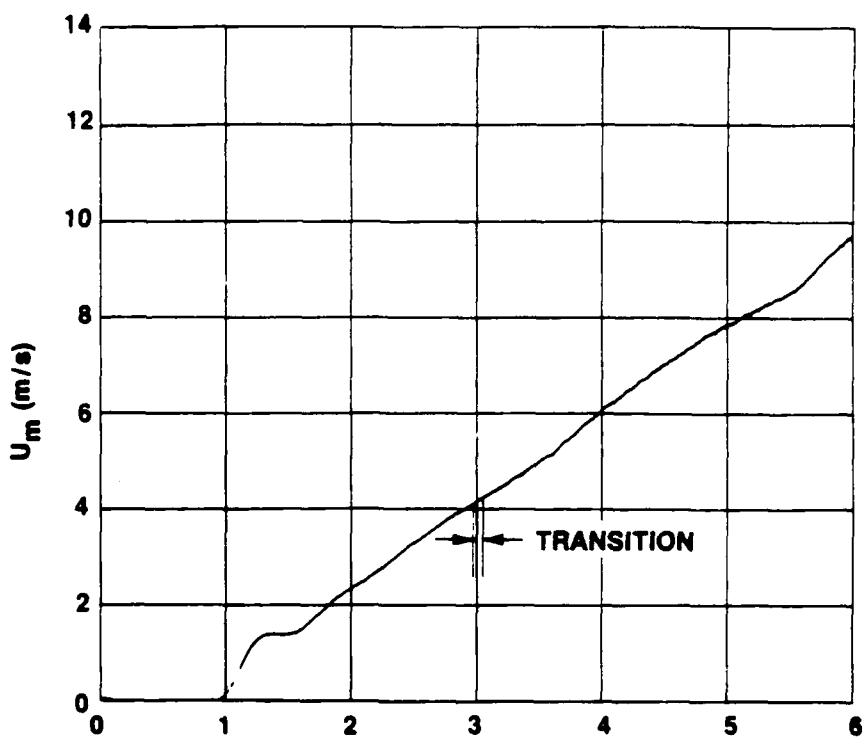
Figure IV-9. U_m vs t for $\ddot{X} = 1.77$ m/s^2 and $\bar{U}_{m0} \approx 0$ (Run No. 1)
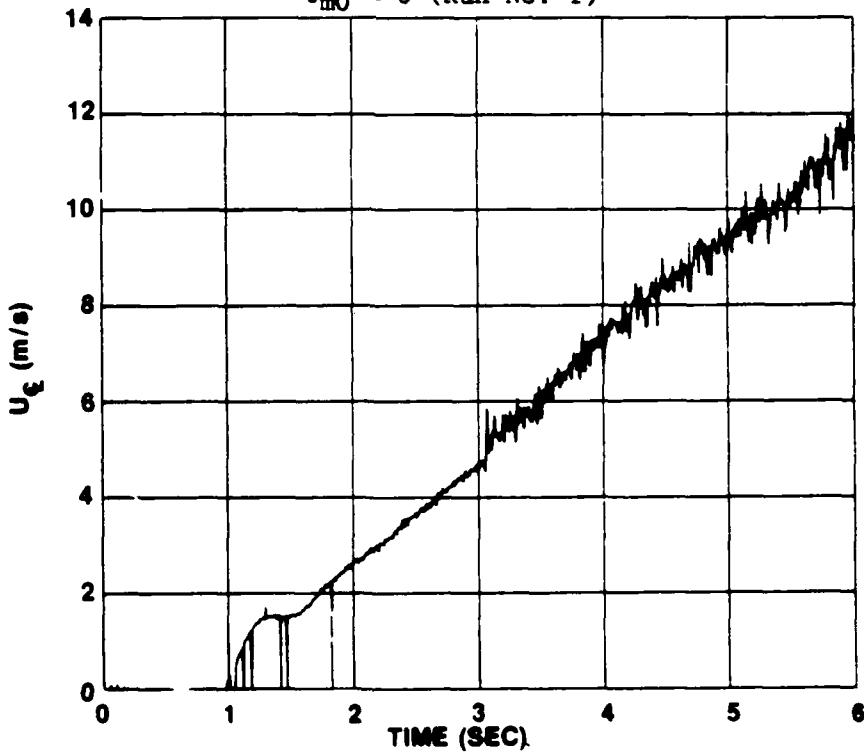
Figure IV-10. U_{c1} vs t for $\ddot{X} = 1.77$ m/s^2 and $\bar{U}_{m0} = 0$ (Run No. 1)
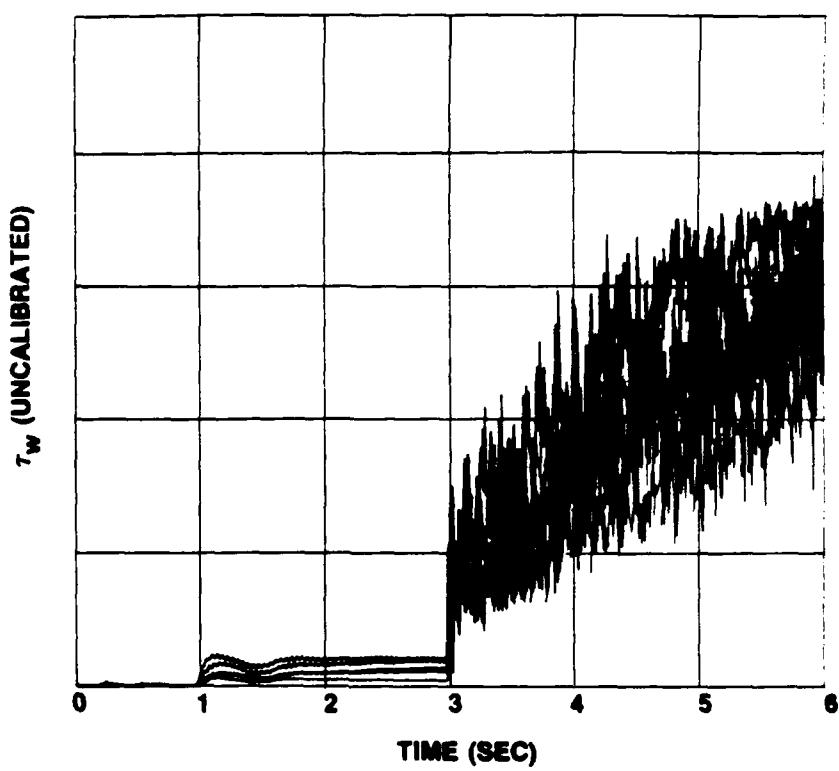
Figure IV-11. τ_w vs t for $\ddot{X} = 1.77$ m/s^2 and $\bar{U}_{m0} = 0$ (Run No. 1)
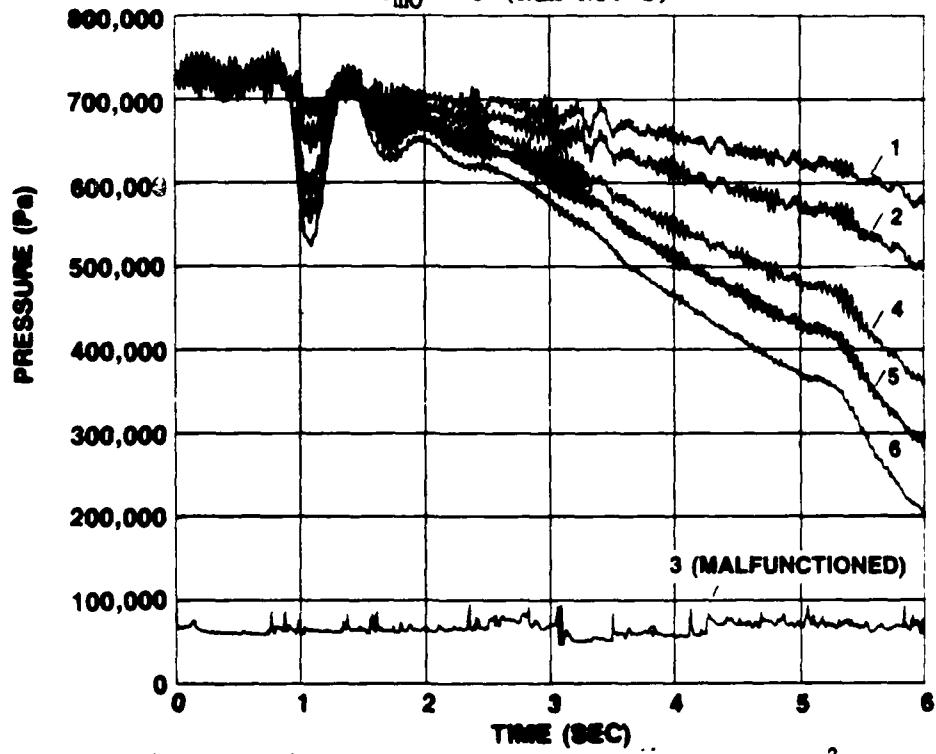
Figure IV-12. Pressure vs t for $\ddot{X} = 1.77$ m/s^2 and $\bar{U}_{m0} = 0$ (Run No. 1)

67
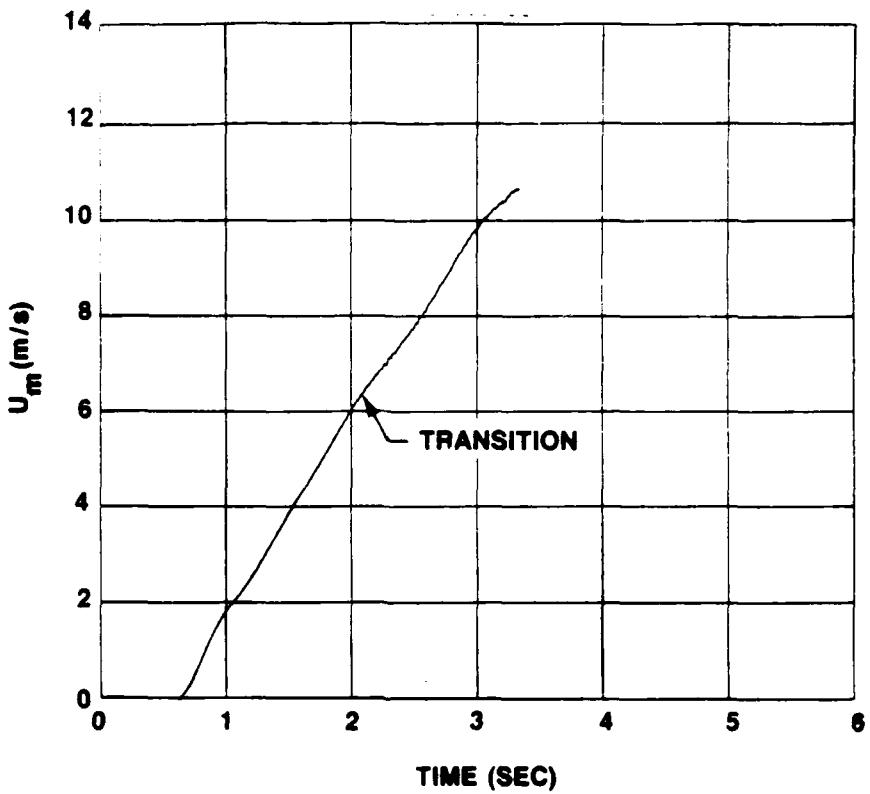
Figure IV-13. U_m vs t for $\ddot{X} = 4.36$ m/s^2 and $\bar{U}_{m0} = 0$ (Run No. 16)
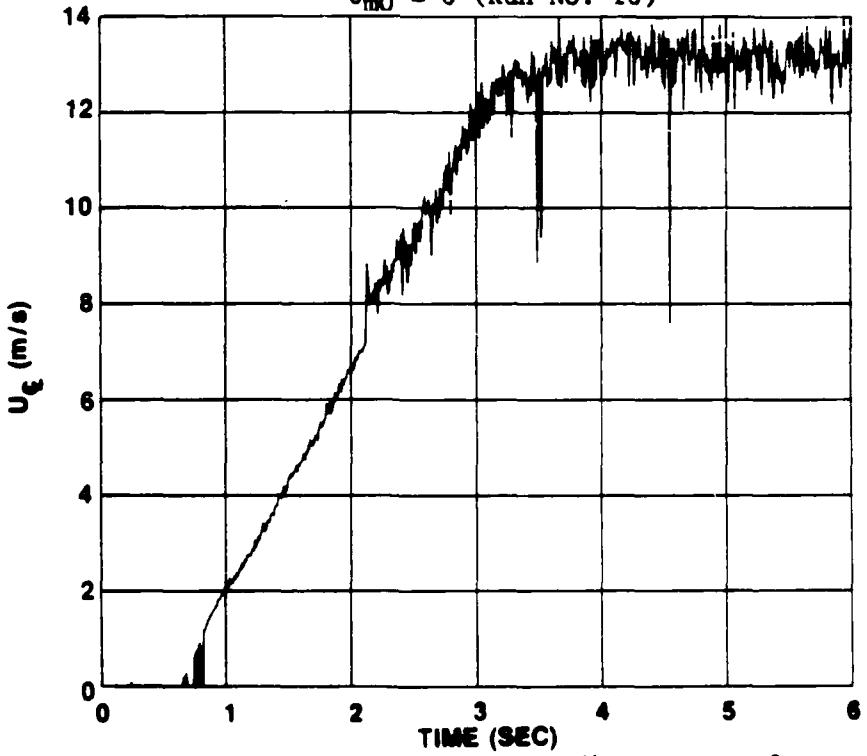
Figure IV-14. U_{c1} vs t for $\ddot{X} = 4.36$ m/s^2 and $\bar{U}_{m0} = 0$ (Run No. 16)
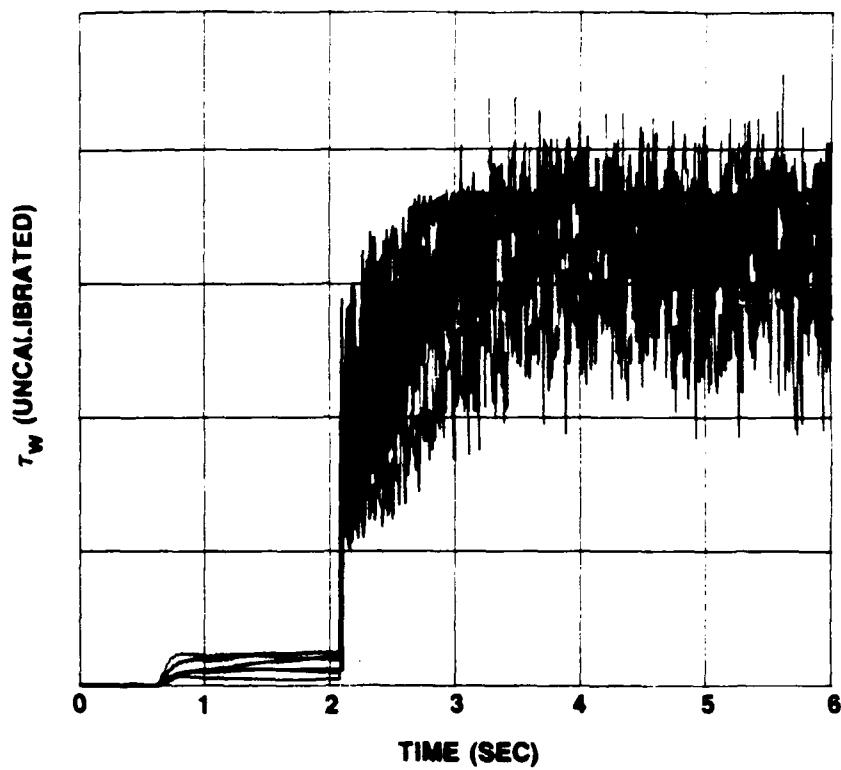
Figure IV-15. τ_w vs t for $\ddot{X} = 4.36$ m/s^2 and $\bar{U}_{m0} = 0$ (Run No. 16)
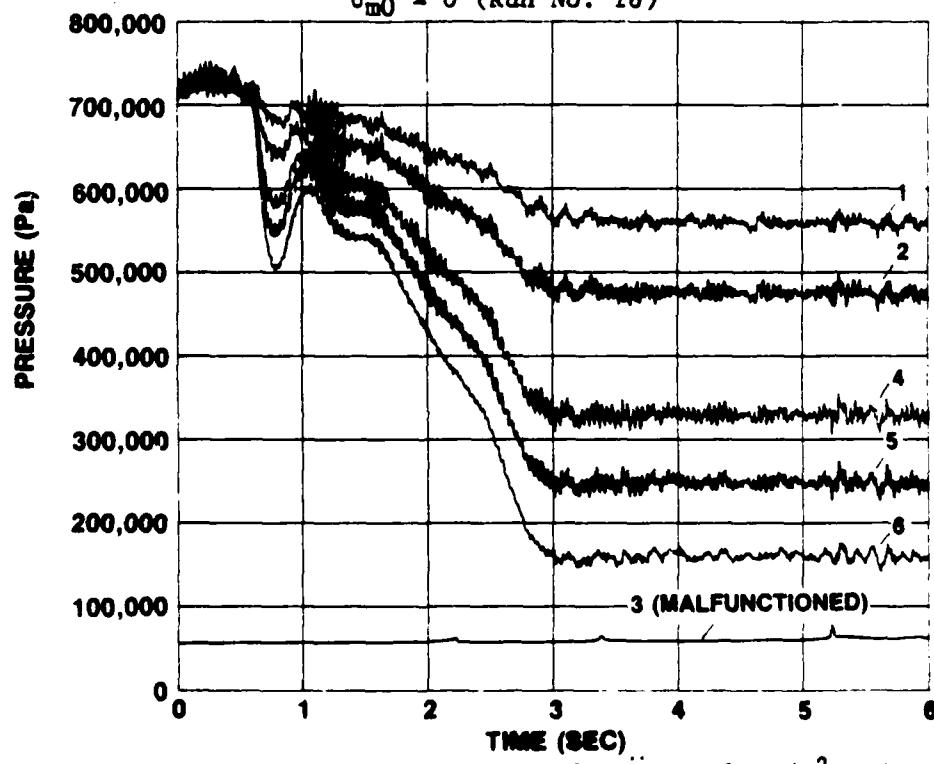
Figure IV-16. Pressure vs t for $\ddot{X} = 4.36$ m/s^2 and $\bar{U}_{m0} = 0$ (Run No. 16)
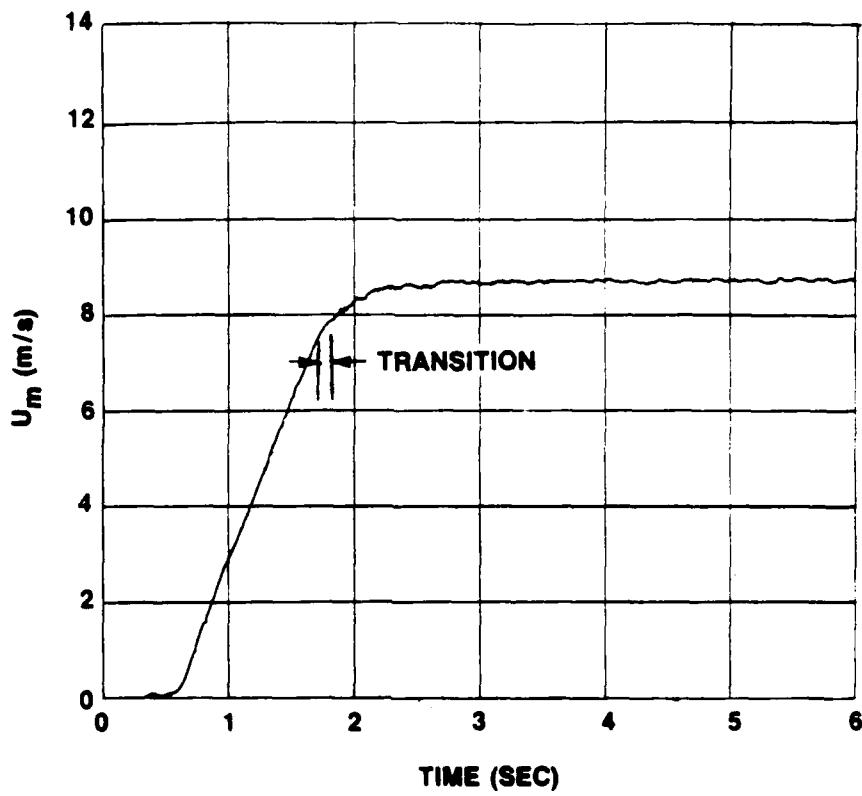
Figure IV-17. U_m vs t for $\ddot{X} = 6.73$ m/s² and $\bar{U}_{m0} = 0$ (Run No. 26)
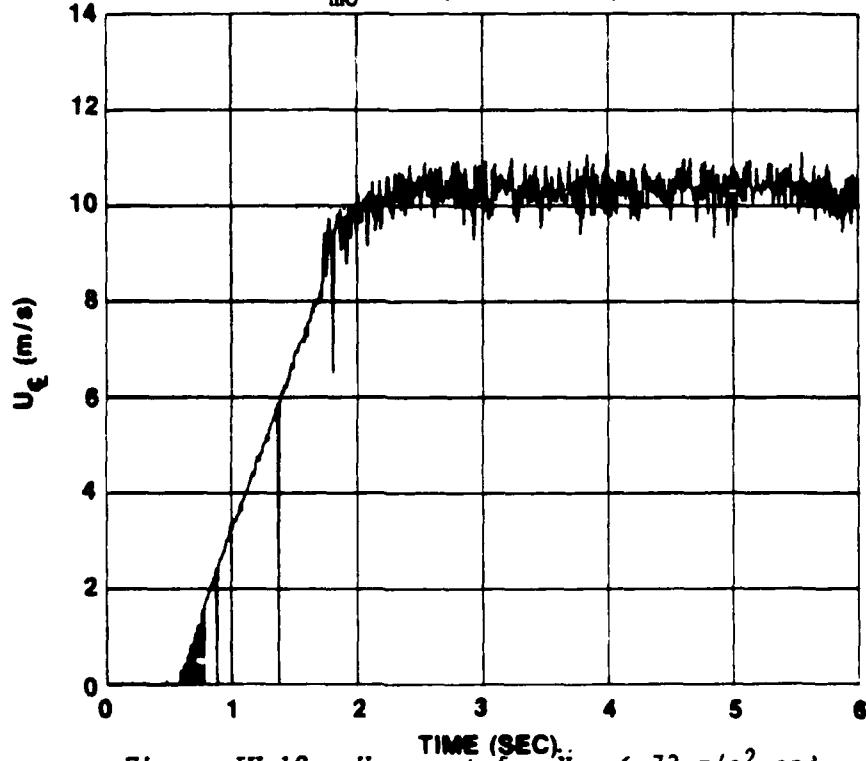
Figure IV-18. U_{c1} vs t for $\ddot{X} = 6.73$ m/s² and $\bar{U}_{m0} = 0$ (Run No. 26)
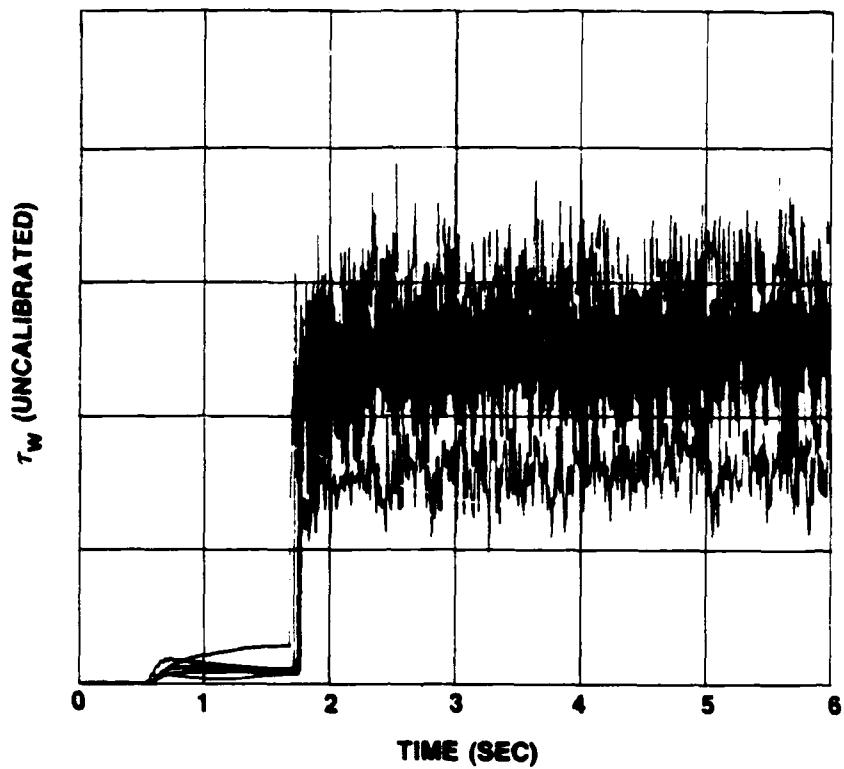
Figure IV-19. τ_w vs t for $\ddot{X}$ = 6.73 m/s^2 and $\bar{U}_{m0}$ = 0 (Run No. 26)
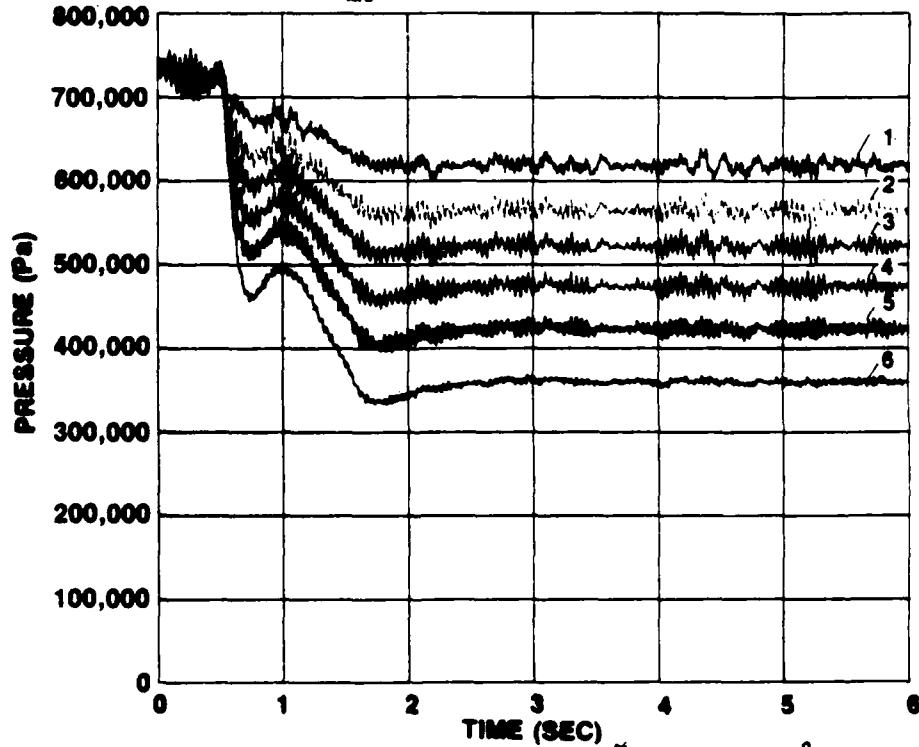
Figure IV-20. Pressure vs t for $\ddot{X}$ = 6.73 m/s^2 and $\bar{U}_{m0}$ = 0 (Run No. 26)
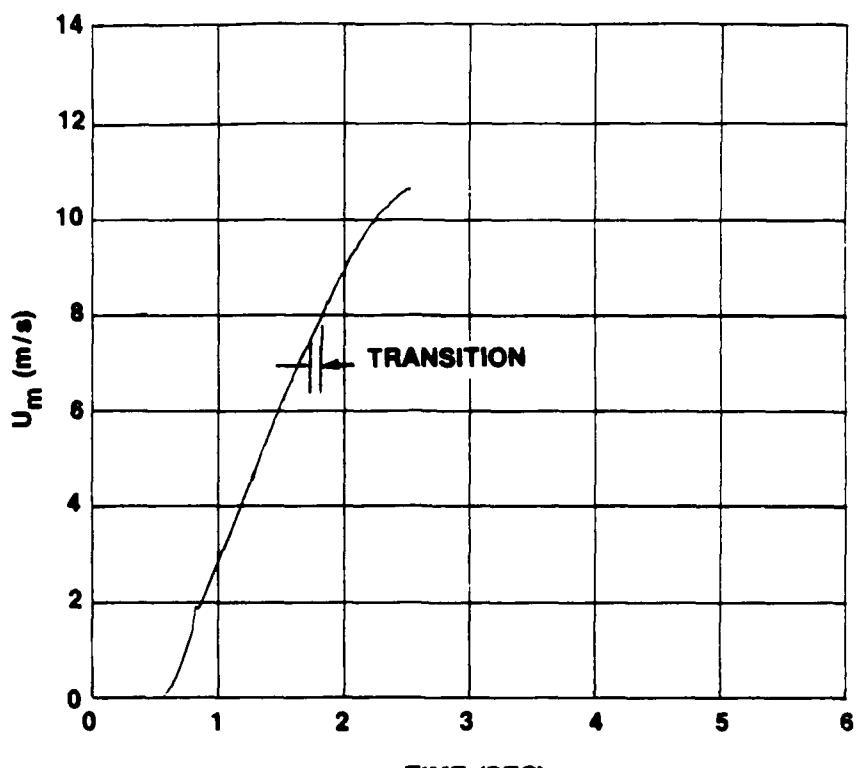
Figure IV-21. U_m vs t for $\ddot{X} = 6.53$ m/s^2 and $\bar{U}_{m0} = 0$ (Run No. 25)

Figure IV-22. U_{cl} vs t for $\ddot{X} = 6.53$ m/s^2 and $\bar{U}_{m0} = 0$ (Run No. 25)

72

Figure IV-23. τ_w vs t for $\ddot{X} = 6.53$ m/s^2 and $\bar{U}_{m0} = 0$ (Run No. 25)

Figure IV-24. Pressure vs t for $\ddot{X} = 6.53$ m/s^2 and $\bar{U}_{m0} = 0$ (Run No. 25)

73

Figure IV-25. U_m vs t for $\ddot{X} = 11.79$ m/s^2 and $\bar{U}_{m0} = 0$ (Run No. 37)
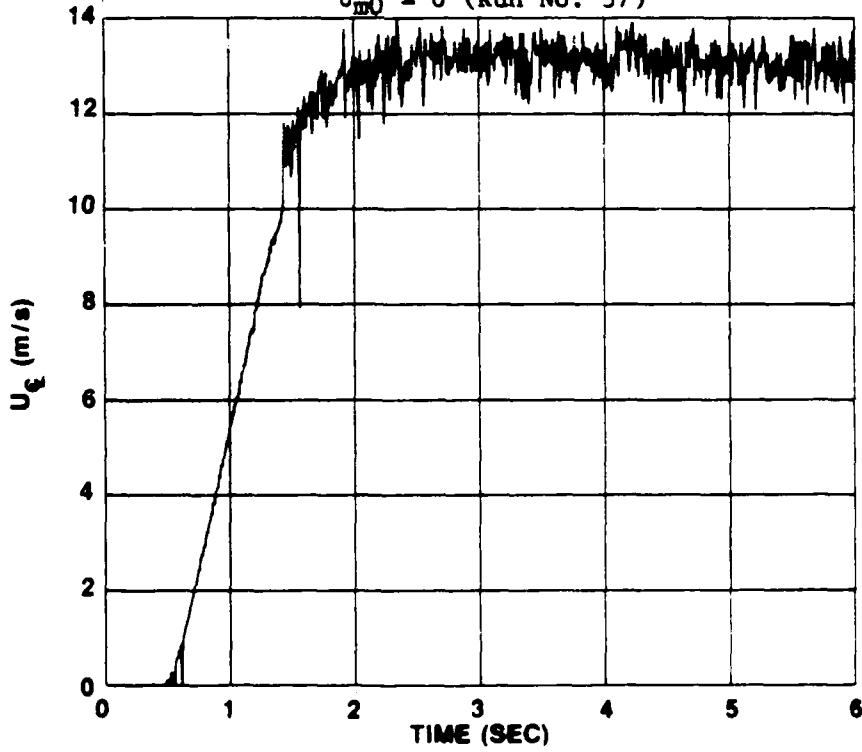
Figure IV-26. U_{c1} vs t for $\ddot{X} = 11.79$ m/s^2 and $\bar{U}_{m0} = 0$ (Run No. 37)
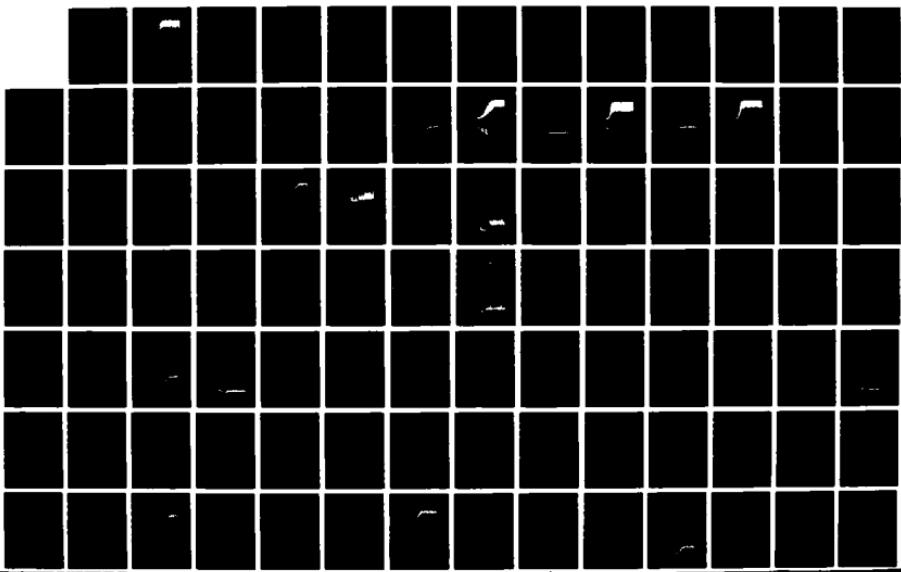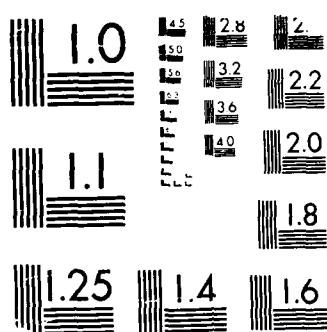
MICROCOPY RESOLUTION TEST CHART

Figure IV-27. τ_w vs t for $\ddot{X} = 11.79$ m/s^2 and $\bar{U}_{m0} = 0$ (Run No. 37)

Figure IV-28. Pressure vs t for $\ddot{X} = 11.79$ m/s^2 and $\bar{U}_{m0} = 0$ (Run No. 37)

75

Figure IV-9, presenting U_m versus time for an acceleration of 1.77 m/s^2, shows that the actual acceleration started at approximately 0.95 second. This reflects the time delay between initiation of data acquisition and triggering of the control system to start the acceleration. The observed range for the start of all the acceleration test runs conducted under this project was 0.5 to 0.95 seconds from time t = 0.0.

Over the range of accelerations tested, each individual test run exhibited essentially constant acceleration over the complete transient. This is documented in figures IV-9, IV-13, IV-17, IV-21, and IV-25 by the linear U_m versus time curve. However, at very low accelerations, an instability in the control valve at low velocities was manifested as a short duration nonlinearity in the U_m versus time curve, which occurred immediately after the start of the run. Selection of a valve without a similar instability was difficult due to the extensive range of flow rates that the control valve had to operate over. As indicated in figure IV-13, this nonlinearity was virtually negligible for accelerations above 4.0 m/s^2. For low accelerations, this instability had no effect on transition to turbulence since transition always occurred well into the linear portion of the velocity versus time curve, as will be shown later.

The data acquisition system recorded values of U_m from the transient flowmeter up to 10.3 m/s and registered zero velocity for any actual flows above 10.3 m/s. Therefore, as shown in figure IV-13, the value for velocity goes abruptly to zero once 10.3 m/s is reached,

meaning only that velocity is not being recorded automatically from that time on. Final velocity was subsequently recorded manually from the flowmeter electronics digital display.

The test run conducted at the acceleration of 6.73 m/s^2 and presented in figures IV-17 through IV-20 was for a final velocity of 8.8 m/s. For the remaining cases presented in figures IV-9 through IV-28, the final velocity was 11.3 m/s.

At the outset of the program, it was felt that a final velocity of 8.8 m/s would adequately encompass all velocities of interest. It was observed early in the program, however, that as the acceleration was being sequentially increased, transition occurred at remarkably high values of pipe Reynolds number with the transition cross-sectional averaged velocity approaching the final velocity. The final velocity was then increased to 11.3 m/s so as not to affect transition.

Out of the 37 test runs investigating transition, 17 were with a final velocity of 8.8 m/s. The maximum acceleration at which this final velocity was considered satisfactory was 8.0 m/s^2. By comparing figures IV-17 through IV-20 for an acceleration of 6.73 m/s^2 and a final velocity of 8.8 m/s with figures IV-21 through IV-24 for an acceleration of 6.53 m/s^2 and a final velocity of 11.3 m/s, it is obvious that transition was not affected by the value of final velocity. A similar observation was made at an acceleration of 8.0 m/s^2.

Table IV-1 list the times at which transition occurred for each

77

of the 37 transition-related test runs. For each run, times are given

at which transition was observed at each of the six wall shear stress

sensors and at the pipe centerline as monitored via the LDV. Times

were obtained by noting the large and abrupt change in value of the

measurement from data that were tabulated at each 1/60th of a second

and taken from time $t = 0.0$. Previous figures showing the centerline

velocity and wall shear stress time histories also indicate the large

changes seen at transition. The maximum spread in transition time

between the measurement locations is also given as actual maximum

spread in seconds and in percent based on the time from the actual

start of the acceleration (not time $t = 0.0$) to the transition time

observed by the LDV. For convenience, the run numbers were assigned

in order of increasing acceleration, not the order in which the runs

were conducted.

The data from table IV-1 were used in each of the previous

figures of U_m versus time to indicate the range in time over which

transition was observed at the six wall shear stress sensors and at

the LDV (positioned at the pipe centerline).

For each run, the spread in the transition time over the various

locations indicate that virtually global transition along and within

the test section occurred. For accelerations up to 6.0 m/s^2,

transition between locations occurred within 0.087 second or within

6.8 percent when based on the time of LDV transition since the start

of the actual acceleration.

For accelerations above 6.0 m/s^2, the maximum spread in

78

Table IV-1. Time of Transition as Indicated by the LDV
and Wall Shear Stress Sensors

Run No.	X (m/s²)	LDV	t_{tr} (from time t = 0.0)						Maximum Δt_{tr}		Maximum Δt_{tr} Ex judg τ_{w3}	
			τ_{w1}	τ_{w2}	τ_{w3}	τ_{w4}	τ_{w5}	τ_{w6}	(sec)	(%)	(sec)*	(%)
1	1.77	3.050	2.983	3.016	3.000	2.966	2.966	2.966	0.084	3.5	0.084	3.5
2	1.85	3.020	2.950	2.983	2.950	2.933	2.933	2.966	0.087	3.8	0.087	3.8
3	1.86	3.020	2.950	2.983	2.950	2.950	2.933	2.950	0.087	3.8	0.087	3.8
4	2.33	2.670	2.600	2.617	2.600	2.600	2.600	2.583	0.087	4.2	0.087	4.2
5	2.39	2.688	2.633	2.650	2.633	2.617	2.617	2.617	0.071	3.5	0.071	3.5
6	2.43	2.633	2.583	2.616	2.600	2.583	2.583	2.583	0.050	2.5	0.050	2.5
7	2.61	2.650	2.600	2.633	2.600	2.600	2.600	2.583	0.067	3.6	0.067	3.6
8	3.01	2.400	2.366	2.400	2.366	2.350	2.367	2.350	0.050	2.8	0.050	2.8
9	3.07	2.400	2.366	2.383	2.383	2.383	2.366	2.366	0.034	1.9	0.034	1.9
10	3.09	2.433	2.383	2.416	2.383	2.366	2.366	2.383	0.067	3.8	0.067	3.8
11	3.46	2.230	2.200	2.217	2.217	2.200	2.200	2.183	0.047	2.9	0.047	2.9
12	3.49	2.250	2.183	2.216	2.183	2.183	2.183	2.200	0.067	3.8	0.067	3.8
13	3.61	2.250	2.216	2.233	2.216	2.200	2.200	2.200	0.050	3.0	0.050	3.0
14	3.67	2.250	2.216	2.230	2.216	2.200	2.216	2.200	0.050	3.0	0.050	3.0
15	3.70	2.233	2.200	2.216	2.200	2.183	2.200	2.183	0.050	3.1	0.050	3.1
16	4.36	2.116	2.083	2.100	2.083	2.067	2.067	2.067	0.049	3.3	0.049	3.3
17	4.37	2.100	2.066	2.083	2.083	2.066	2.066	2.066	0.034	2.3	0.034	2.3
18	4.91	2.030	1.966	1.983	1.966	1.950	1.950	1.950	0.080	5.6	0.080	5.6
19	4.92	2.000	1.966	2.000	1.983	1.966	1.966	1.966	0.034	2.5	0.034	2.5
20	5.39	1.880	1.883	1.900	1.883	1.883	1.866	1.833	0.067	5.1	0.067	5.1
21	5.48	1.866	1.883	1.916	1.883	1.883	1.883	1.866	0.050	3.9	0.050	3.9
22	5.99	1.780	1.800	1.833	1.816	1.800	1.800	1.750	0.083	6.8	0.083	6.8
23	6.01	1.816	1.800	1.833	1.883	1.816	1.816	1.766	0.117	9.6	0.067	5.5
24	6.04	1.783	1.783	1.833	1.816	1.816	2.000	1.750	0.250	20.7	0.250	20.7
25	6.53	1.716	1.716	1.783	1.766	1.750	1.750	1.683	0.100	8.8	0.100	8.8
26	6.73	1.710	1.716	1.766	1.750	1.750	1.750	1.700	0.066	5.9	0.066	5.9
27	7.01	1.650	1.650	1.716	1.716	1.700	1.700	1.633	0.083	7.6	0.083	7.6
28	7.22	1.666	1.666	1.733	1.716	1.716	1.700	1.616	0.117	11.1	0.117	11.1
29	7.60	1.483	1.616	1.683	1.616	1.667	1.667	1.450	0.233	22.5	0.233	22.5
30	8.05	1.630	1.616	1.683	1.600	1.666	1.666	1.566	0.117	12.1	0.117	12.1
31	8.59	1.583	1.583	1.650	1.600	1.633	1.633	1.550	0.100	10.5	0.100	10.5
32	8.80	1.550	1.550	1.616	1.450	1.600	1.600	1.516	0.166	17.4	0.100	10.4
33	9.25	1.533	1.516	1.583	1.433	1.566	1.566	1.483	0.150	16.0	0.100	10.7
34	9.87	1.500	1.483	1.550	1.380	1.533	1.533	1.450	0.170	19.0	0.100	11.2
35	10.60	1.466	1.466	1.533	1.316	1.516	1.516	1.433	0.217	25.9	0.100	11.9
36	10.61	1.450	1.433	1.516	1.300	1.500	1.500	1.416	0.216	25.5	0.100	11.8
37	11.79	1.433	1.416	1.500	1.250	1.483	1.483	1.400	0.250	32.4	0.100	13.0

*Percent (%) values based on time from beginning of transient.

transition time essentially increased with acceleration up to a value

of 0.25 second or 32.4 percent from the start of the acceleration.

However, at these relatively high values, the order in which

transition occurred at the various locations generally repeated in the

same sequence. Specifically, the order was: sensor stations 3,6,1;

the LDV location; sensor stations 4,5; and then 2. It is obvious that

transition is not manifested here as a phenomenon that propagates down the length of the test section. It appears that something locally is tripping the flow at different times at the various locations (probably some surface irregularity or more likely a sensor itself due to a slight protrusion into the flow or recess into the wall).

At these higher accelerations, transition at sensor station 3, which is located at the axial center of the test section, generally occurs considerably earlier than that at the other locations. In fact, if station 3 is omitted, the spread in transition time at the various locations for run 37 is reduced from 0.25 second to 0.1 second or from 32.4 percent to 13.0 percent. The last two columns in table IV-1 reflect the spread in transition time when sensor station 3 is ignored for all the runs. This results in considerable reduction in the spread of transition times (to within approximately 13 percent).

For the remainder of this report, transition time is taken as the value seen at the LDV. This is for the following reasons: (1) the LDV measuring volume was positioned at the pipe centerline and without any sensors or other surface irregularities in the vicinity that may trip transition; (2) for most of the runs, transition at the LDV occurred in the middle of the spread of transition times; and (3) when station 3 was ignored, the maximum spread was generally less than 13 percent, or relatively small anyway, leading to reasonable accuracy no matter which location was chosen for transition time.

Table IV-2 lists the values of the various transition parameters to be presented in the following paragraphs and figures in an attempt

80

Table IV-2. Transition Parameters

Run No.	$\ddot{X}$ (m/s^2)	T (°C)	ν (m^2/s ×10^{-7})	$\overline{U_{mf}}$ (m/s)	$U_{m,tr}$ (m/s)	t (sec)	r^*_{tr}	δ_{tr}/R	$K_{a,tr}$ (×10^{-8})	$Re_{\delta,tr}$	$Re_{D,tr}$
1	1.77	25.78	8.82	11.30	4.23	2.390	0.00327	0.172	2.06	20952	244000
2	1.85	25.22	8.93	8.84	4.25	2.297	0.00318	0.170	2.15	20550	242000
3	1.86	24.72	9.03	8.84	4.26	2.290	0.00320	0.171	2.17	20490	240000
4	2.33	24.72	9.03	8.84	4.88	2.094	0.00293	0.164	1.81	22511	274000
5	2.39	25.72	8.83	11.30	4.85	2.029	0.00278	0.160	1.85	22321	279000
6	2.43	26.39	8.70	10.40	4.79	1.971	0.00266	0.157	1.92	21955	280000
7	2.61	25.33	8.91	8.84	4.84	1.854	0.00256	0.153	2.05	21109	276000
8	3.01	25.33	8.91	8.84	5.43	1.804	0.00249	0.152	1.67	23528	310000
9	3.07	24.84	9.01	8.84	5.44	1.772	0.00247	0.152	1.72	23310	307000
10	3.09	25.72	8.83	11.30	5.44	1.760	0.00241	0.152	1.69	23785	313000
11	3.46	25.33	8.91	8.84	6.01	1.637	0.00226	0.148	1.42	25356	343000
12	3.49	25.00	8.98	8.84	6.01	1.772	0.00247	0.152	1.44	25838	340000
13	3.61	25.67	8.84	11.30	5.97	1.654	0.00227	0.148	1.50	25387	343000
14	3.67	25.24	8.93	8.84	6.01	1.637	0.00226	0.148	1.51	25299	342000
15	3.70	25.33	8.91	8.84	6.00	1.622	0.00224	0.148	1.53	25314	342000
16	4.36	25.67	8.84	11.30	6.47	1.484	0.00203	0.139	1.42	25840	372000
17	4.37	25.28	8.92	8.84	6.47	1.480	0.00205	0.140	1.44	25792	369000
18	4.91	25.33	8.91	8.84	6.99	1.423	0.00196	0.136	1.28	27099	399000
19	4.92	25.67	8.84	11.30	6.83	1.388	0.00190	0.133	1.36	26100	393000
20	5.39	25.39	8.90	8.84	7.16	1.328	0.00183	0.131	1.31	26768	409000
21	5.48	25.67	8.84	11.30	6.95	1.268	0.00174	0.126	1.44	25161	399000
22	5.99	25.44	8.89	8.84	7.30	1.219	0.00168	0.123	1.37	25653	417000
23	6.01	25.67	8.84	11.30	7.33	1.220	0.00167	0.123	1.35	25905	421000
24	6.04	25.22	8.93	10.40	7.30	1.209	0.00167	0.123	1.43	25539	411000
25	6.53	25.72	8.83	11.30	7.40	1.133	0.00155	0.117	1.42	24904	426000
26	6.73	25.44	8.89	8.84	7.51	1.116	0.00154	0.116	1.41	24889	429000
27	7.01	25.39	8.90	8.84	7.66	1.093	0.00151	0.115	1.39	25139	437000
28	7.22	25.72	8.83	11.30	7.61	1.054	0.00144	0.111	1.41	24298	441000
29	7.60	25.72	8.83	11.30	7.86	1.034	0.00141	0.109	1.38	24644	452000
30	8.05	25.39	8.90	8.84	7.80	0.969	0.00134	0.105	1.51	23373	445000
31	8.59	25.72	8.83	11.30	8.17	0.951	0.00130	0.103	1.39	24206	470000
32	8.80	25.72	8.83	11.30	8.42	0.957	0.00131	0.103	1.30	24946	484000
33	9.25	25.83	8.81	11.30	8.68	0.938	0.00128	0.101	1.25	25275	501000
34	9.87	25.72	8.83	11.30	8.82	0.894	0.00122	0.098	1.27	24863	507000
35	10.60	25.72	8.83	11.30	8.87	0.837	0.00114	0.093	1.34	23728	510000
36	10.61	25.72	8.83	11.30	8.98	0.846	0.00116	0.095	1.29	24539	517000
37	11.79	25.78	8.82	11.30	9.09	0.771	0.00105	0.088	1.38	23035	524000

to further define when transition occurs. For each of the 37 test runs, values are also given for acceleration, temperature of the water during the run, kinematic viscosity, final mean cross-sectional averaged velocity, cross-sectional averaged velocity at transition, and the time of transition since the start of the acceleration. This time of transition was obtained by assuming exact constant acceleration over the run and back calculating time by dividing the cross-sectional averaged velocity at transition by the acceleration. It was felt that since the acceleration was essentially constant during any one run, especially is the vicinity of transition, using the value of average acceleration as given in table IV-2 and back calculating the virtual start time was more representative than trying to determine the actual start time from the data themselves.

Figure IV-29 shows the relationship between pipe Reynolds number at transition and acceleration. The transition Reynolds number grows larger with increasing acceleration and ranges between a Reynolds number of 240,000 at the lower accelerations to 524,000 at the higher accelerations so that no unique or "critical" value can be cited. These values are extremely high when compared to the usual transition Reynolds number range of approximately 2000 to 4000 for steady-state flows. The steady-state transition Reynolds number for the Flow Loop Facility was found to be approximately 8000.

Nondimensional time at transition, t^*_{tr}, is plotted against pipe Reynolds number at transition, $Re_{D,tr}$ in figure IV-30. It can be seen that neither transition time nor pipe Reynolds number is
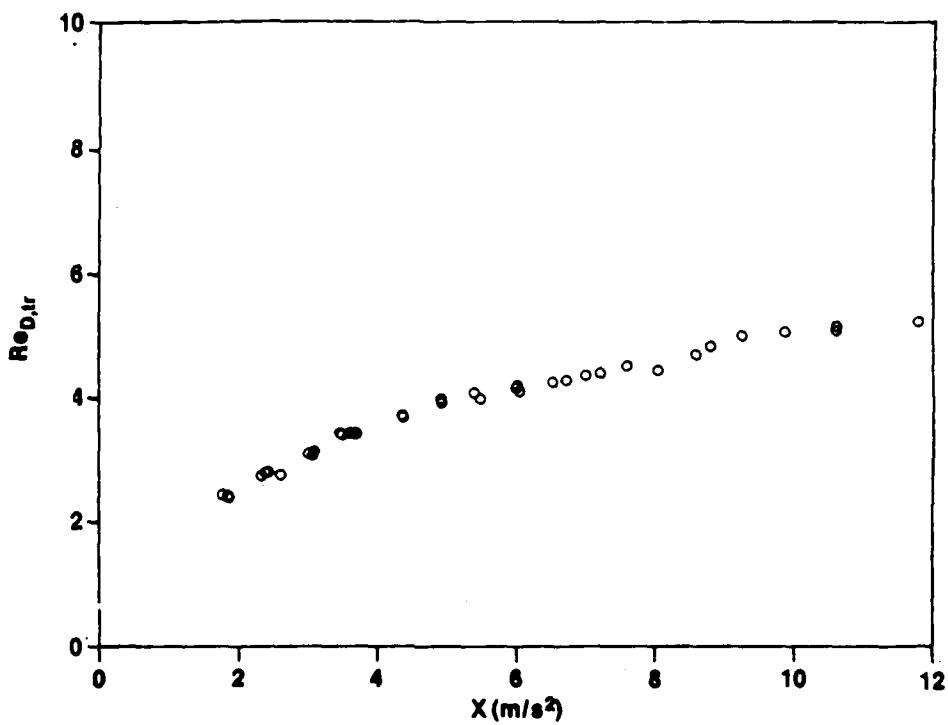
Figure IV-29.   Pipe Reynolds Number vs Acceleration at Transition
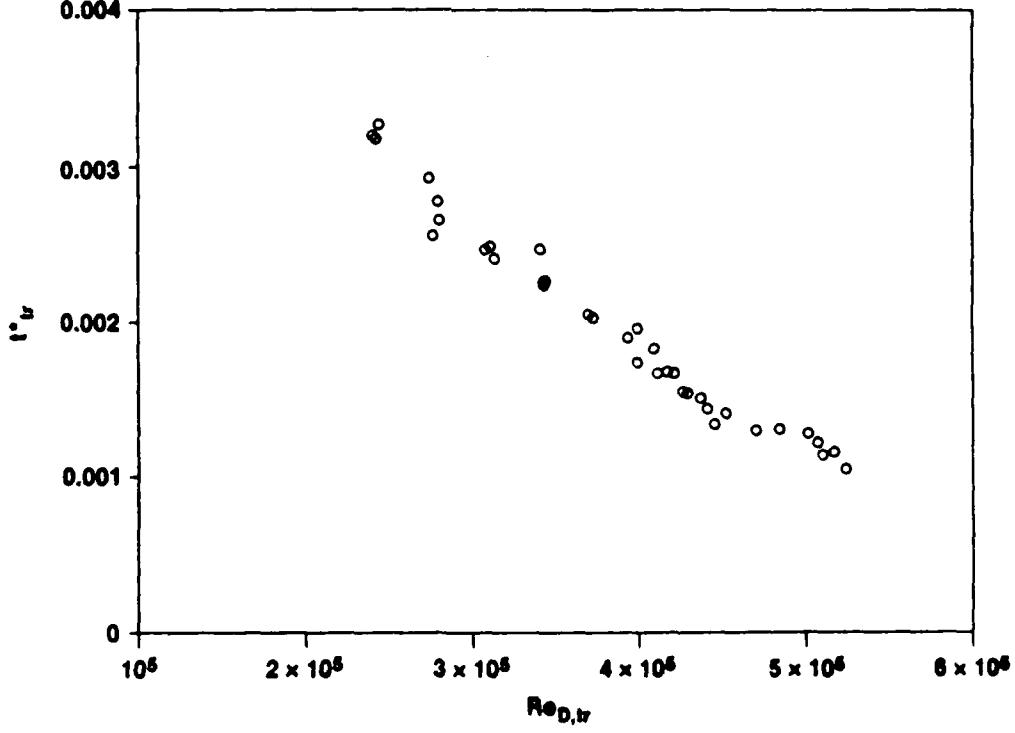
Figure IV-30.   Nondimensional Time vs Pipe Reynolds Number
at Transition

83

constant at the transition point of an accelerating flow. However, these two parameters do seem to correlate with each other. Neither, however, includes the acceleration as a parameter.

A second attempt at correlation would be to nondimensionalize the acceleration $\ddot{X}$. The best parameter found was

$$K_a = (\nu/U_m^3)\ddot{X} . \tag{IV-4}$$

This is the "local acceleration" analog of the "convective acceleration" parameter K often used to define relaminarization in convectively accelerating flows and defined as

$$K = (\nu/U_m^2)(dU_m/dx) \tag{IV-5}$$

where dU_m/dx is the local value of convective acceleration. As discussed by Jones and Launder [34], K is a reasonable but not definitive criterion for relaminarization since it does not account for size effects. They concluded that a value of $K = 3.0 \times 10^{-6}$ is usually sufficient to suppress turbulence in a boundary layer. This result is confirmed by Patel and Head [35], but Narasimha and Sreenivasan [36] show that other details, such as the surface shear stress variation, can also influence relaminarization.

Figure IV-31 shows that the transition value of K_a is approximately constant over the entire range of the experiments. The mean value is

$$K_a = 1.53 \times 10^{-8} \tag{IV-6}$$

with a standard deviation of 0.26×10^{-8} or 17 percent. The data, however, did follow a trend about which data scatter was considerably lower than that indicated by the above value of standard deviation.

84
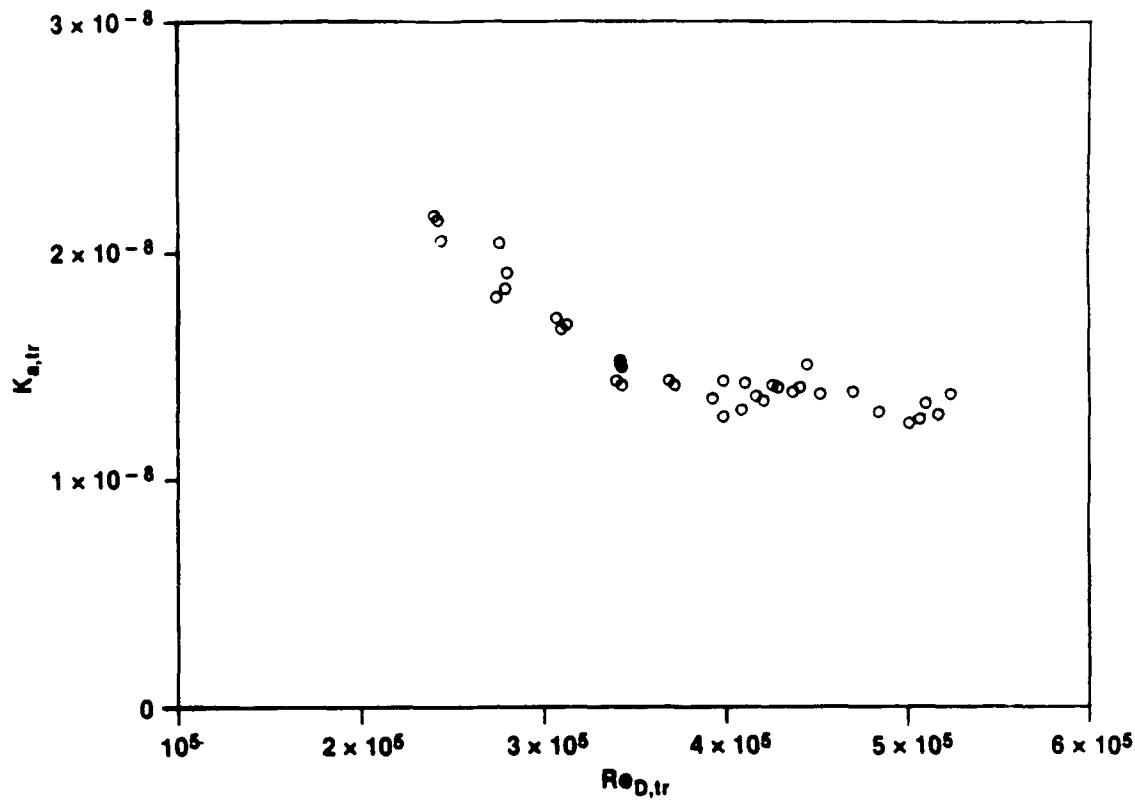
Figure IV-31. Transition Parameter vs Pipe Reynolds Number
at Transition

There is a tendency for $K_{a,tr}$ to increase with decreasing

Reynolds number, a relationship that is substantiated by the single

experiment of van de Sande et al. [19]. From their figure 8, one can

estimate the very low acceleration at the transition point was about

0.1 m/s^2, and the cross-sectional averaged velocity was 1.1 m/s.

Then, for their low $Re_{D,tr}$ of 57,500, the estimated value of $K_{a,tr}$

would be about 8×10^{-8}, which is five times higher than that found

in this study. Clearly, more experiments are needed at low acceler-

ations.

A second correlation is suggested by the failure of figure IV-30,

which indicates that t^{*}_{tr} increases with decreasing Reynolds

85

number. The probable reason is the thickening of the laminar shear

layer at larger times and the subsequent increase in scale of the

instabilities. This hypothesis can be tested by basing the transition

Reynolds number on the shear layer thickness at that time.

To establish a length scale for the shear region, the 99-percent

boundary layer thickness δ_{99} is defined. This parameter was

calculated using the classic analytic solution for startup of laminar

pipe flow, caused by a suddenly applied constant pressure gradient as

given by Szymanski [1]. His solution for the unsteady velocity

profile was given by equation (I-1). The core velocity used in the

calculation of δ_{99} was the calculated value of velocity at the

pipe centerline.

For small $t^* < 0.05$, figure I-2 showed that the instantaneous

cross-sectional average velocity is linear with time, simulating a

constant acceleration startup. For the 37 experiments of the present

study, the values of t^* at transition varied from 0.00105 to 0.0032.

These values are small enough for Szymanski's solution to be a valid

approximation of a constant acceleration.

The computer on which the calculations were performed was a

Digital Equipment Corporation VAX 11-780. Thirty terms in the

summation of equation (I-1) were found to provide solutions accurate

to the computers epsilon, which was 1.3×10^{-7}.

Results from the δ_{99} calculations were used to compute the

estimated value of boundary layer thickness Reynolds number Re_{δ} at

transition where

86

$$Re_\delta = U_m \delta/\nu . \tag{IV-7}$$

The data are plotted in figure IV-32 as $Re_{\delta,tr}$ versus $\ddot{X}$. It is seen that this type of transition Reynolds number is nearly constant over the entire range of experiments. The mean value is

$$Re_{\delta,tr} = 24,300 \tag{IV-8}$$

with a standard deviation of 1700 or 7.0 percent. This can be compared to the usual value of $Re_{\delta,tr} = 5000$ for steady-state boundary layers with a zero pressure gradient. The spread in the data are less than that found in figure IV-31, so that equation (IV-8) seems to be a reliable transition estimate for an accelerating flow.
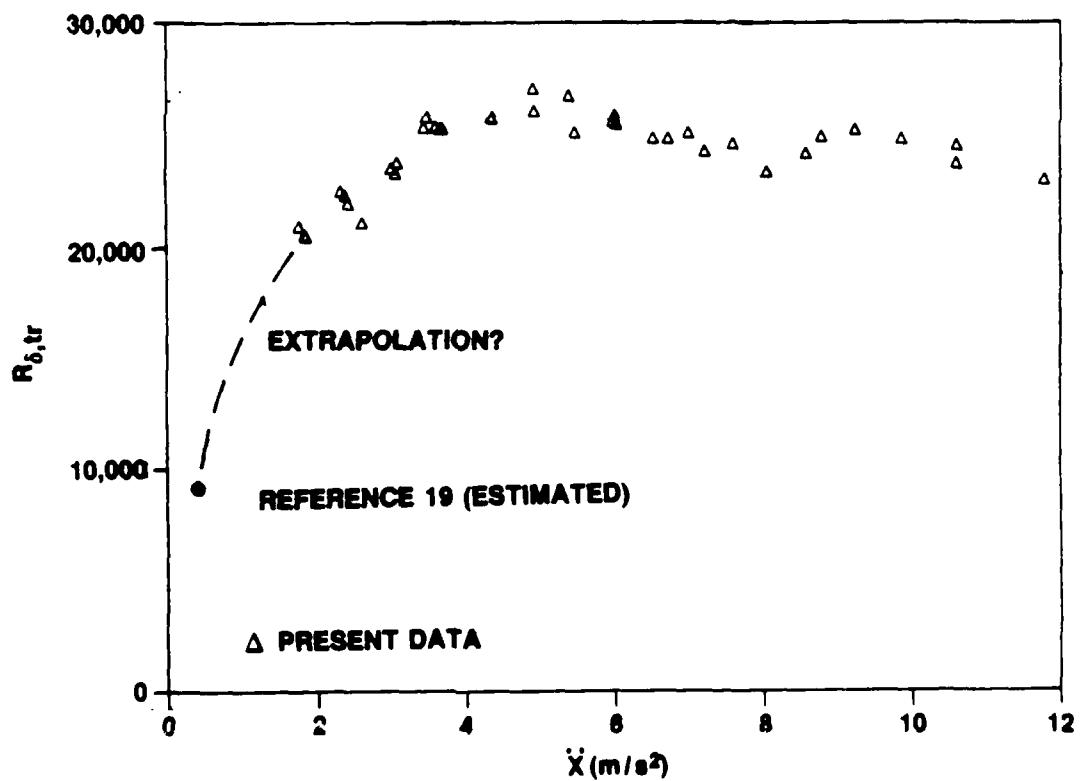

Figure IV-32. Boundary Layer Thickness Reynolds Number
vs Acceleration at Transition

There is a tendency in figure IV-32 for $Re_{\delta,tr}$ to decrease with the rate of acceleration. The single (estimated) data point of van de Sande et al. [19], which gives $Re_{\delta,tr} = 8600$ at $\ddot{X} = 0.1$ m/s^2, substantiates this tendency. One would also expect the transition pipe Reynolds number at zero acceleration to revert to the usual steady-state estimate of 2000. This downward trend is hypothesized by the dashed line in figure IV-32. Again, there is a clear need for more transition data at low accelerations.

Transition Wall Shear Stress

Values of the average measured wall shear stress at transition for each of the 37 transition related test runs are given in table IV-3 and illustrated in figure IV-33. Calculated wall shear stress at transition based on Szymanski's exact solution is also given. Calculated values were computed by differentiating equation (I-1) to obtain

$$\tau_w = \mu \frac{\partial U}{\partial r}\Big|_{r\,=\,R} \tag{IV-9}$$

$$\tau_w = \frac{2\mu U_{max}}{R}\left[1 - 4\sum_{n=1}^{\infty} \frac{e^{(-\lambda_n^2 t^*)}}{\lambda_n^2}\right] \tag{IV-10}$$

where U_{max} was found by first calculating U_{cl}/U_{max} from equation (I-1) at t^*_{tr}. Then, since $U_{cl,tr}$ was known from the LDV measurements, U_{max} was easily obtained.

88

Table IV-3. Wall Shear Stress at Transition

| Run No.	t^*	$\ddot{X}$ (m/s^2)	$\tau_{w,tr}$ Measured (Pa)	Calculated (Pa)
1	0.00327	1.77	5.480	2.812
2	0.00318	1.85	5.340	2.902
3	0.00320	1.86	5.040	2.932
4	0.00293	2.33	5.210	3.514
5	0.00278	2.39	5.760	3.508
6	0.00266	2.43	4.720	3.492
7	0.00256	2.61	5.400	3.685
8	0.00249	3.01	5.260	4.193
9	0.00247	3.07	5.730	4.266
10	0.00241	3.09	5.710	4.233
11	0.00226	3.46	5.670	4.877
12	0.00247	3.49	5.690	4.697
13	0.00227	3.61	6.040	4.795
14	0.00226	3.67	5.500	4.888
15	0.00224	3.70	6.010	4.891
16	0.00203	4.36	5.890	5.502
17	0.00205	4.37	5.620	5.524
18	0.00196	4.91	5.560	6.100
19	0.00190	4.92	5.660	6.008
20	0.00183	5.39	5.720	6.464
21	0.00174	5.48	5.560	6.394
22	0.00168	5.99	5.360	6.876
23	0.00167	6.01	5.380	6.886
24	0.00167	6.04	————	6.928
25	0.00155	6.53	5.030	7.213
26	0.00154	6.73	5.140	7.394
27	0.00151	7.01	4.920	7.626
28	0.00144	7.22	4.730	7.701
29	0.00141	7.60	4.860	8.039
30	0.00134	8.05	5.090	8.252
31	0.00130	8.59	4.650	8.709
32	0.00131	8.80	4.690	8.940
33	0.00128	9.25	4.740	9.304
34	0.00122	9.87	4.610	9.710
35	0.00114	10.60	4.650	10.107
36	0.00116	10.61	4.650	10.143
37	0.00105	11.79	4.740	10.787
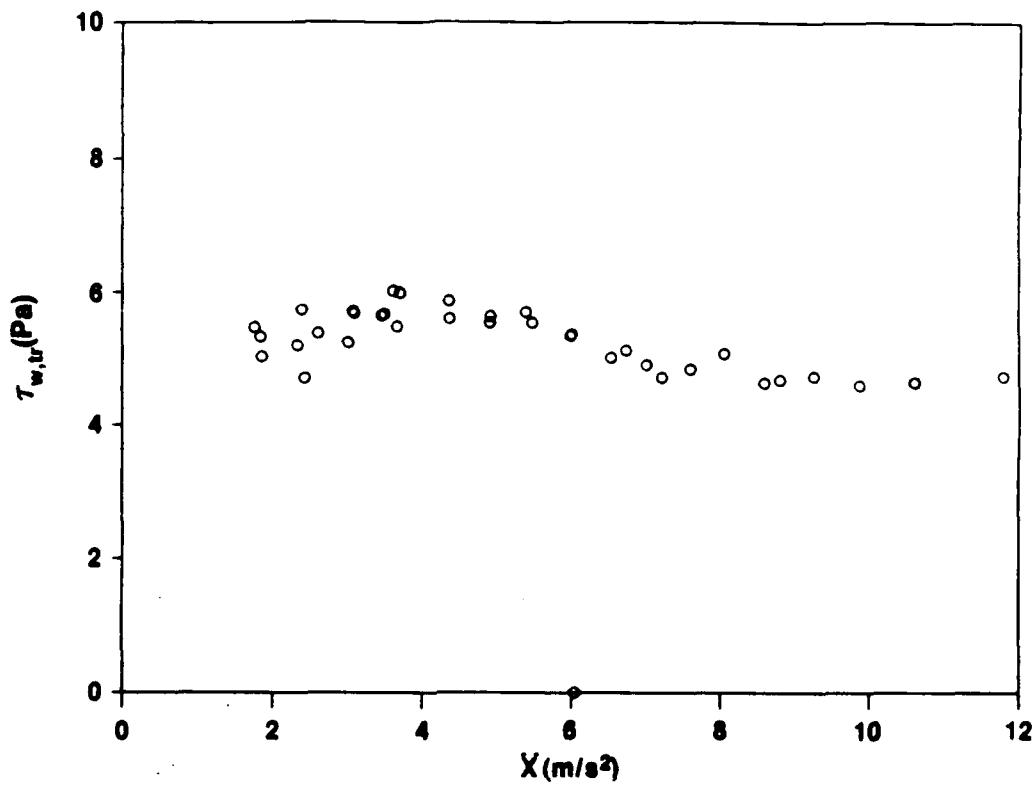
Figure IV-33. Wall Shear Stress vs Acceleration at Transition

Figure IV-34 is a graph of the wall shear stress measured data
and calculations contained in table IV-3. The shear stress
measurements show a nearly constant value essentially independent of
acceleration with a mean value of 5.3 pascals and a standard deviation
of 8.3 percent. This is in contradiction to the calculated values,
which show a linearly increasing value with increasing acceleration
and ranging from 2.8 to 10.8 pascals. Both the measured and
calculated values are, however, within the same range. This apparent
discrepancy will be discussed further during the presentation of the
ensemble-averaged transient tests where wall shear stress will again
be presented but in more detail over the complete transient.

90
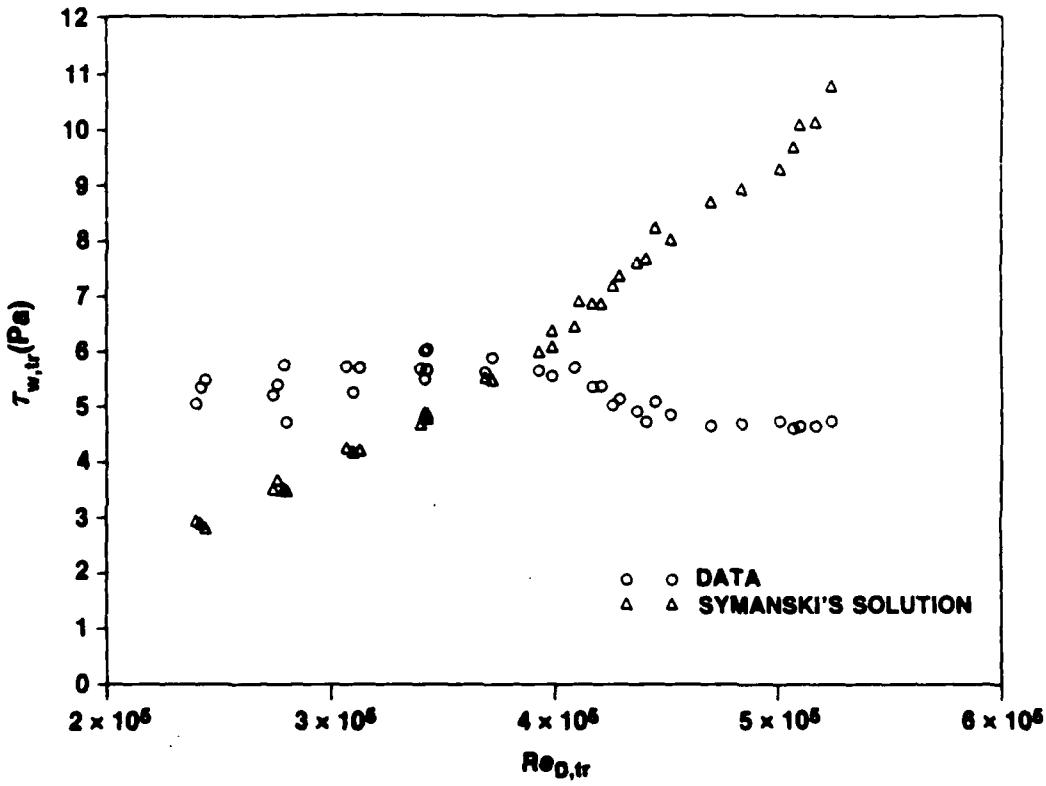
Figure IV-34. Wall Shear Stress vs Pipe Reynolds Number
at Transition

Relaminarization

In an effort to determine if relaminarization was possible over
the acceleration range of the previous transient tests, 19 tests were
conducted with an initial mean cross-sectional averaged velocity of
approximately 1 m/s, which was in the turbulent regime. As with the
previous tests, final mean cross-sectional averaged velocity was
either 8.8 or 11.3 m/s. Accelerations ranged from 1.80 to 9.64
m/s^2, the maximum acceleration achievable from an initially
turbulent flow.

91

Figures IV-35 through IV-46 are similar to figures IV-9 through IV-28, which show time histories of cross-sectional averaged velocity, centerline velocity, and uncalibrated output of the wall shear stress sensors and pressures. Here, data are shown for three representative accelerations covering the range of test values. Specifically, the three are at accelerations of 3.00, 9.43, and 9.64 m/s^2. The run at 9.43 m/s^2 was to a final velocity of 8.8 m/s, while the run at an acceleration of 9.64 m/s^2 was to a final velocity of 11.3 m/s.

Table IV-4 lists the accelerations of each of the 19 test runs that were assigned numbers 38 through 56, again in the order of increasing acceleration. For each of these runs, the cross-sectional averaged velocity was essentially linear with time indicating constant acceleration as desired. Relaminarization was not observed at any time during any of the runs. No anomalies in any of the measured parameters were present at any time and a smooth transition from the initial to the final state appeared to have taken place.

Maximum values of the acceleration parameter K_a, as calculated using equation (IV-6) for each of the 19 relaminarization runs, are also given in table IV-4. Since acceleration was constant during each transient, maximum K_a occurred at the minimum velocity, that at the beginning of the transient or 1 m/s.

As shown, values ranged from 1.57×10^{-6} to 8.52×10^{-6}. These values can be compared to the related convective acceleration parameter, K, where relaminarization typically occurs at a value of approximately 3.0×10^{-6}. Based on this value, relaminarization

92
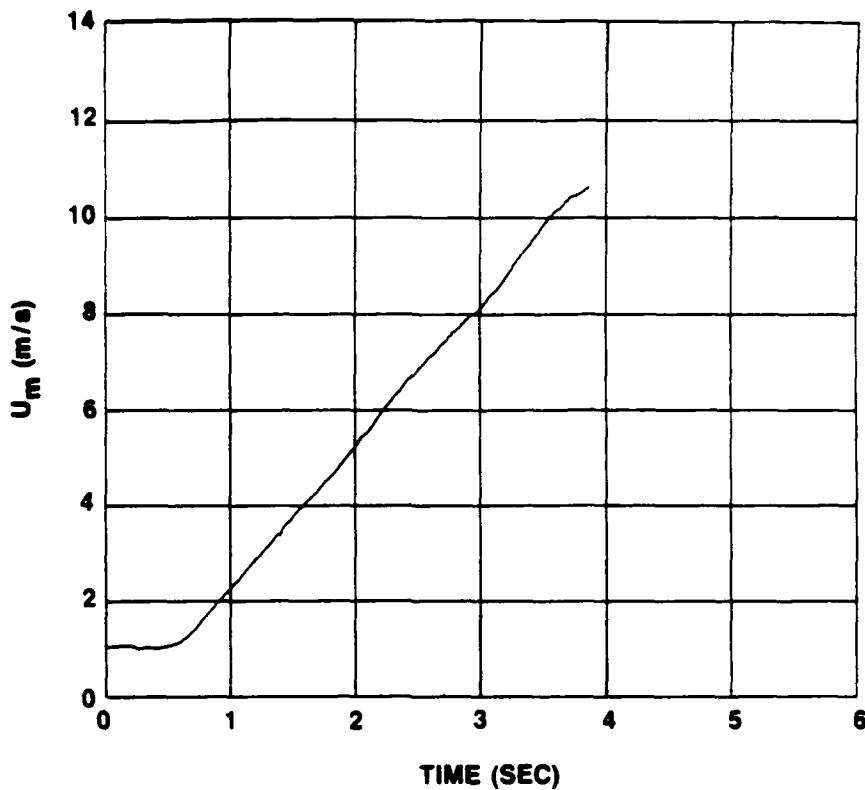
Figure IV-35. U_m vs t for $\ddot{X} = 3.00$ m/s^2 and $\bar{U}_{m0} = 1$ m/s (Run No. 41)

Figure IV-36. U_{c1} vs t for $\ddot{X} = 3.00$ m/s^2 and $\bar{U}_{m0} = 1$ m/s (Run No. 41)

93
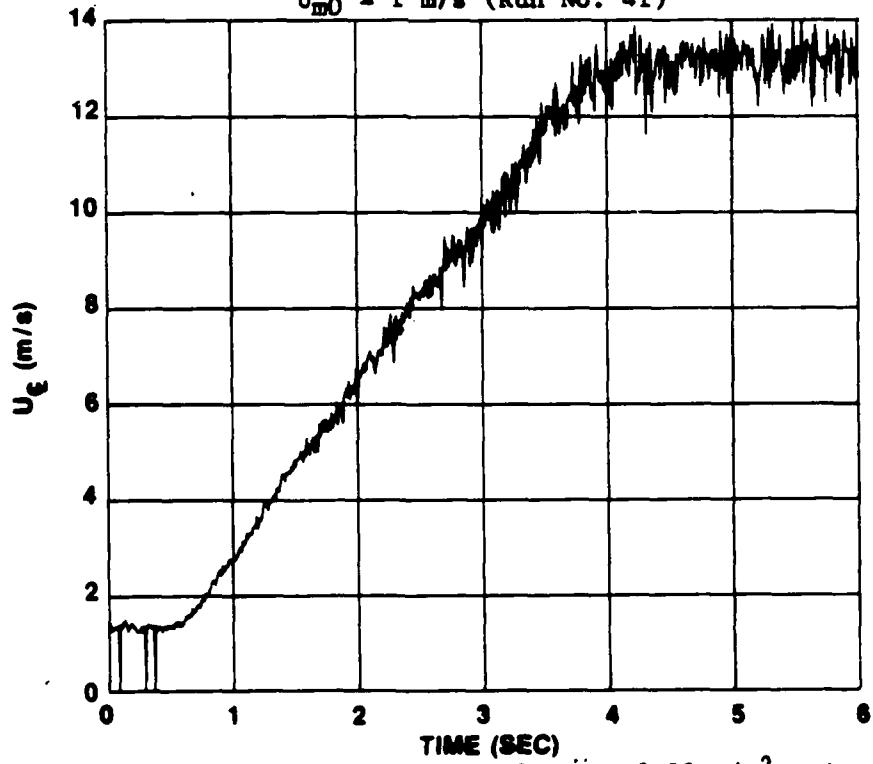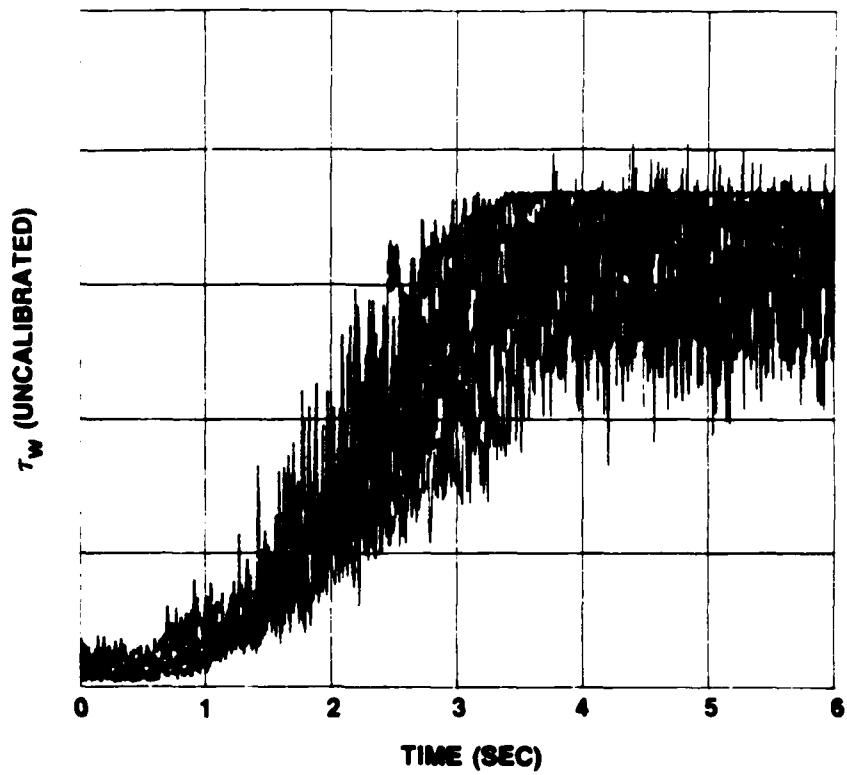
Figure IV-37. τ_w vs t for $\ddot{X}$ = 3.00 m/s² and $\bar{U}_{m0}$ = 1 m/s (Run No. 41)
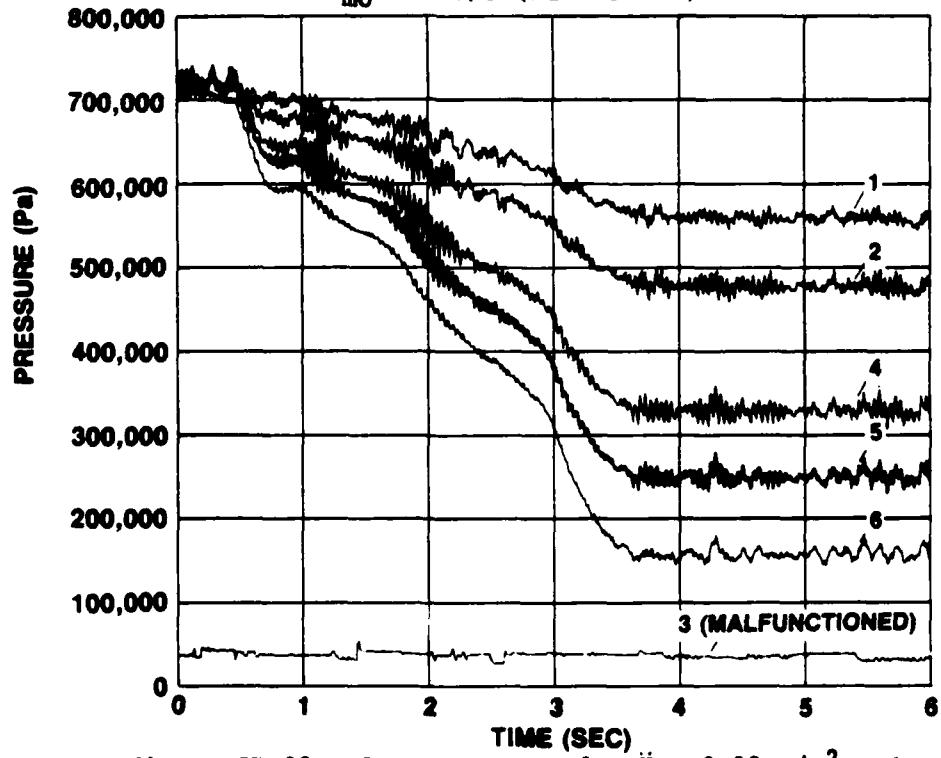
Figure IV-38. Pressure vs t for $\ddot{X}$ = 3.00 m/s² and $\bar{U}_{m0}$ = 1 m/s (Run No. 41)
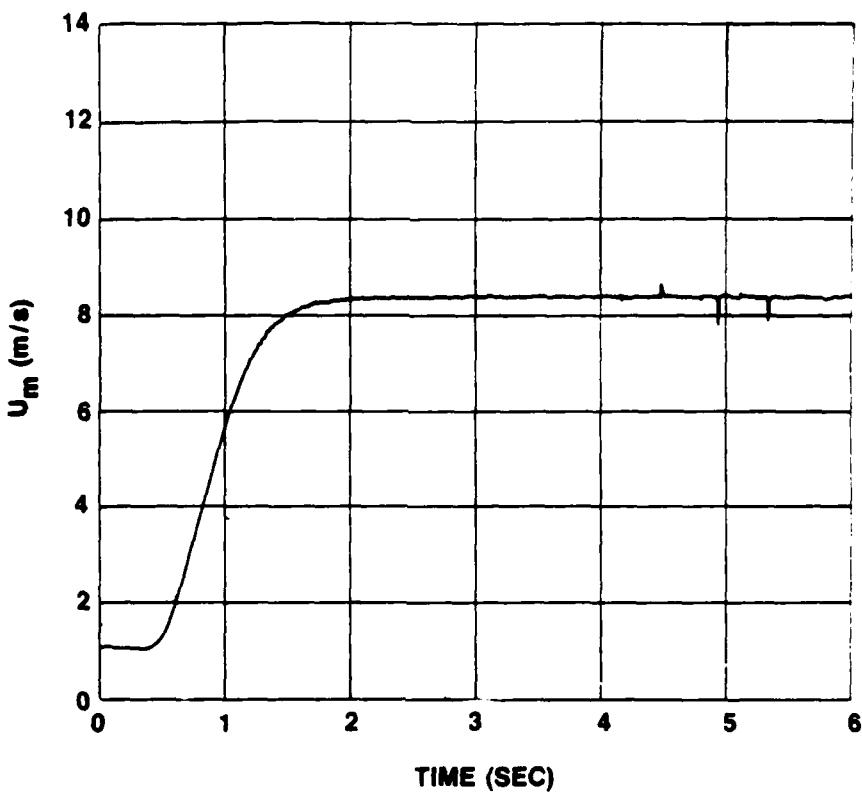
Figure IV-39. U_m vs t for $\ddot{X} = 9.43$ m/s^2 and
$\bar{U}_{m0} = 1$ m/s (Run No. 54)
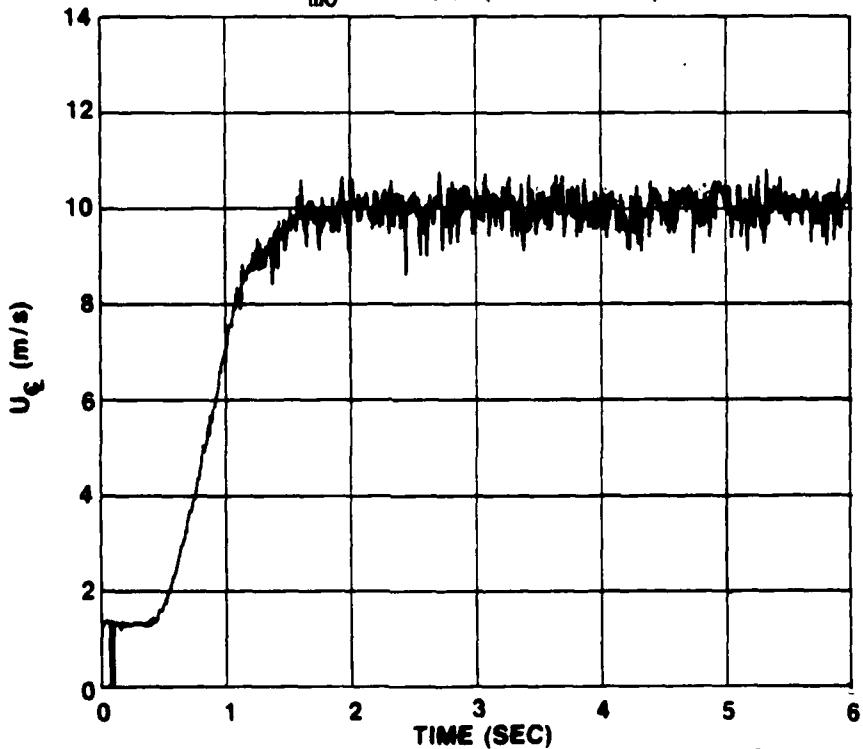
Figure IV-40. U_{c1} vs t for $\ddot{X} = 9.43$ m/s^2 and
$\bar{U}_{m0} = 1$ m/s (Run No. 54)

95
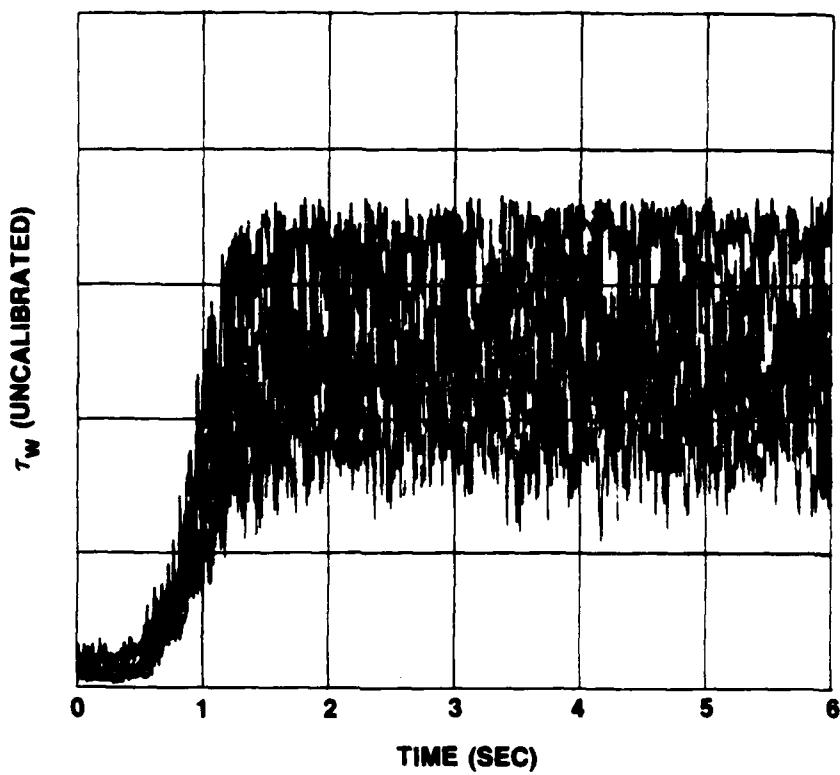
Figure IV-41. τ_w vs t for $\ddot{X} = 9.43$ m/s^2 and $\bar{U}_{m0} = 1$ m/s (Run No. 54)
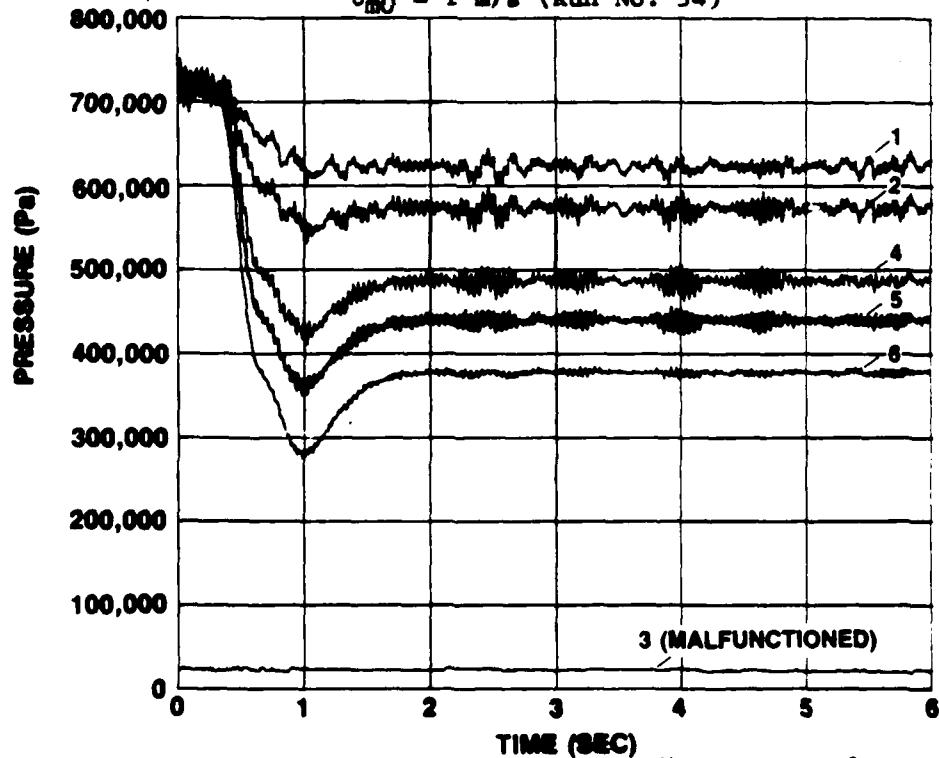
Figure IV-42. Pressure vs t for $\ddot{X} = 9.43$ m/s^2 and $\bar{U}_{m0} = 1$ m/s (Run No. 54)

96
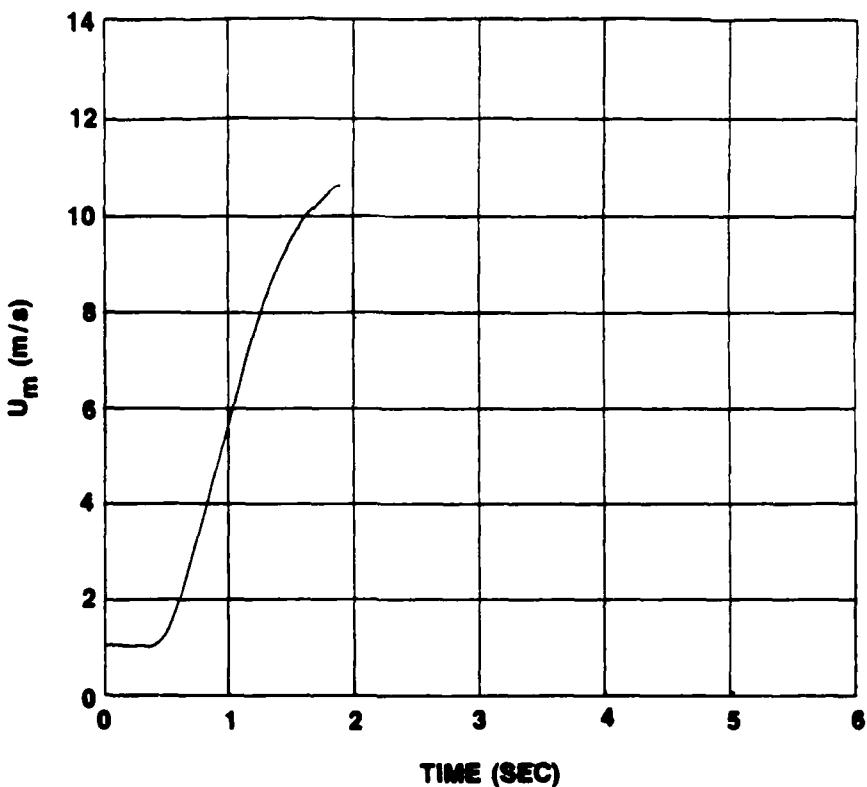
Figure IV-43. U_m vs t for $\ddot{X}$ = 9.64 m/s^2 and
$\bar{U}_{m0}$ = 1 m/s (Run No. 56)
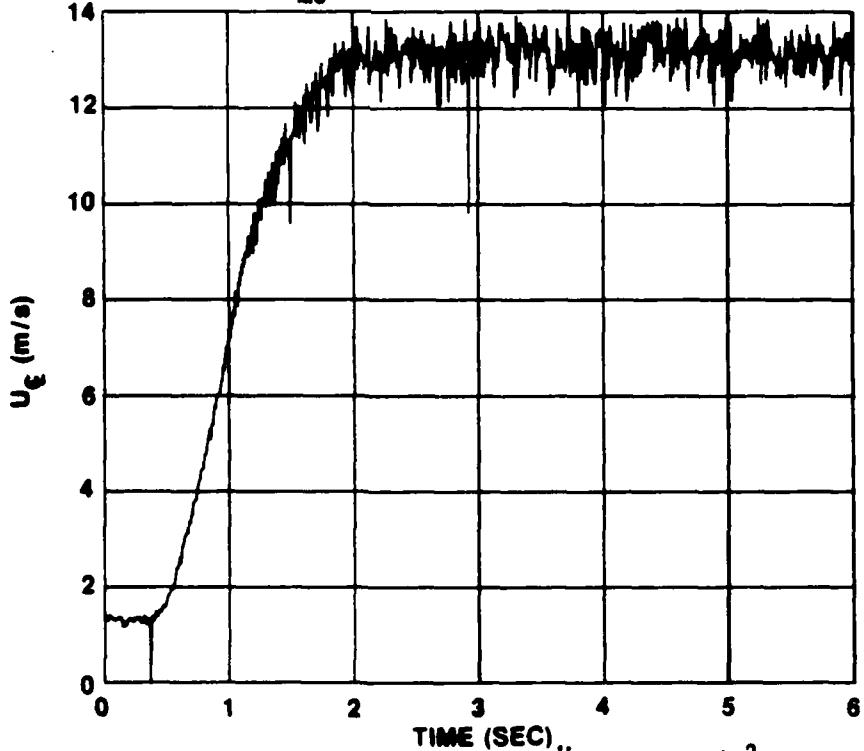

Figure IV-44. U_{c1} vs t for $\ddot{X}$ = 9.64 m/s^2 and
$\bar{U}_{m0}$ = 1 m/s (Run No. 56)

97
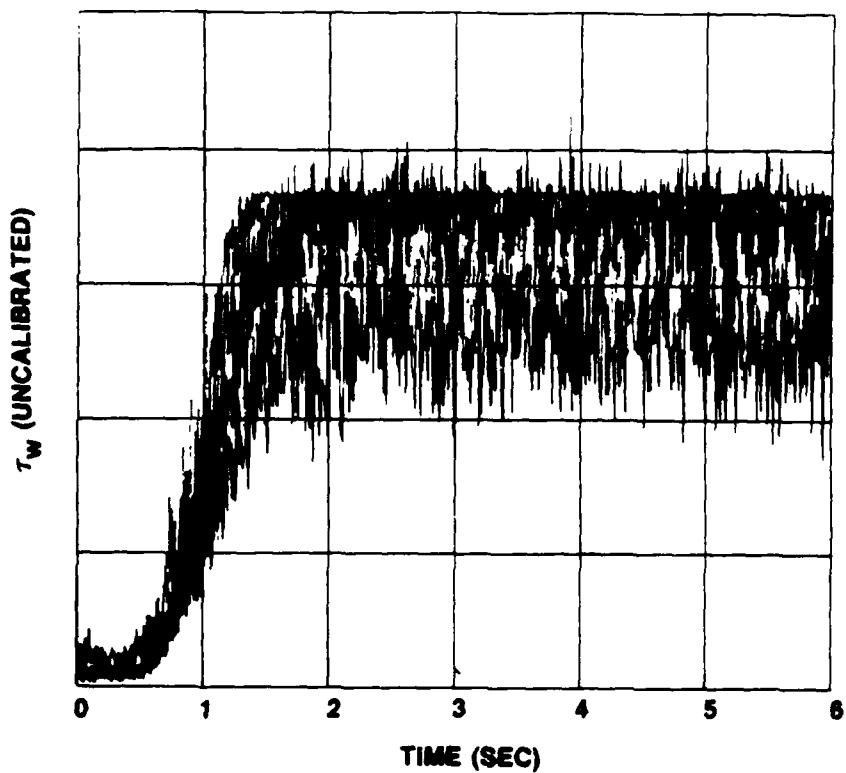
Figure IV-45. τ_w vs t for $\ddot{X} = 9.64$ m/s^2 and $\bar{U}_{m0} = 1$ m/s (Run No. 56)
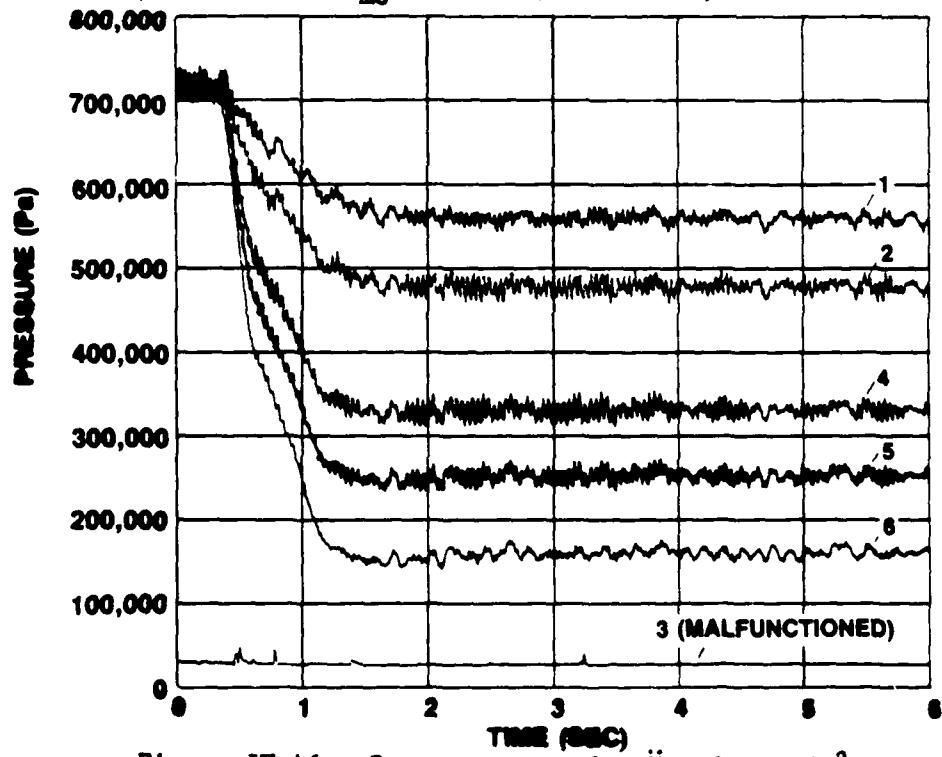
Figure IV-46. Pressure vs t for $\ddot{X} = 9.64$ m/s^2 and $\bar{U}_{m0} = 1$ m/s (Run No. 56)

98

Table IV-4. Local Acceleration Parameter, K_a, for Test Runs
With an Initial Velocity of 1 m/s

Run No.	$\ddot{X}$ (m/s^2)	Temperature $(°C)$	$\bar{U}_{mf}$ (m/s)	ν $(m^2/s \times 10^{-7})$	K_a $(\bar{U}_{mo} = 1\ m/s)$ $(\times 10^{-6})$
38	1.80	26.17	8.84	8.74	1.57
39	1.82	26.06	11.30	8.76	1.60
40	2.99	26.06	8.84	8.76	2.62
41	3.00	26.06	11.30	8.76	2.63
42	4.11	26.06	11.30	8.76	3.60
43	4.12	26.06	8.84	8.76	3.61
44	5.59	26.28	11.30	8.72	4.88
45	5.64	26.06	8.84	8.76	4.94
46	6.50	26.67	11.30	8.65	5.62
47	7.30	26.06	8.84	8.76	6.40
48	7.69	26.06	8.84	8.76	6.74
49	7.82	26.94	11.30	8.59	6.72
50	7.95	25.33	8.84	8.91	7.08
51	8.85	26.06	8.84	8.76	7.76
52	8.86	26.83	11.30	8.61	7.63
53	9.32	25.33	8.84	8.91	8.30
54	9.43	26.06	8.84	8.76	8.26
55	9.62	25.61	11.30	8.85	8.52
56	9.64	26.83	11.30	8.61	8.30

would have been expected for runs 42 through 56. Probable reasons for not seeing relaminarization are: (1) the values of K_a listed were only valid at the initiation of the transient and decreased at a very fast rate proportional to U_m^3, leaving little time for relaminarization to occur, or (2) a direct correlation between K and K_a is not valid. More experiments at higher accelerations are required to answer these unknowns.

As an alternate for comparison, the mean transition values of $K_a = 1.53 \times 10^{-8}$ from this study can be used. Assuming that the value of K_a, which was sufficient to delay transition to turbulence, was also sufficient to cause relaminarization of an initially turbulent flow, then relaminarization would be expected for each of the 19 runs. Obviously, this is not true since relaminarization did not occur even though values of K_a during these 19 runs were greater than the values found at transition for most of the transient. This could be because more energy is required to suppress existing turbulence than to delay transition to turbulence from an initially laminar flow.

To continue an investigation of potential relaminarization due to local acceleration of the flow, more experiments are required. To conduct these tests on the present facility, increased pumping power is required to increase the upper range of the accelerations and hence, K_a.

Ensemble-Averaged Runs

The remainder of this report discusses results of the test runs that were repeated 20 times at each LDV measurement location across the pipe radius to allow for suitable ensemble averaging. These tests are referred to in section III as the second series of transient tests. There were four cases as follows:

- Case 1: An acceleration of 2.4 m/s^2 starting from rest.

- Case 2: An acceleration of 6.1 m/s^2 starting from rest.

- Case 3: An acceleration of 2.4 m/s^2 from an initially turbulent flow at 1 m/s.

- Case 4: An acceleration of 6.1 m/s^2 from an initially turbulent flow at 1 m/s.

Results of detailed transient velocity profile measurements are presented first for each of the four cases conducted under this series of tests. For the initially turbulent cases, time dependent turbulent intensity data, as derived from the ensemble-averaged standard deviation (RMS), are also presented. Wall shear stress time histories are then presented, which are followed in turn by the pressure data. All values of RMS that are to be presented were calculated using equation (III-7) and, subsequently, nondimensionalized by the corresponding instantaneous ensemble-averaged value.

Transient Velocity Profiles

Before detailed velocity profile measurements are presented for each case, a comparison between time histories for several parameters of an individual run and the corresponding ensemble average of 20 runs is made.

Results for case 1 are presented first. The time history of cross-sectional averaged velocity, U_m, as obtained from the transient flowmeter for an individual run, is given is figure IV-47. The corresponding ensemble-averaged data are shown in figure IV-48. As stated in section III, all of the time histories in the figures show data at each 1/120th of a second.

Both curves indicate the resulting constant acceleration over most of the transient. Visually, the two curves are indistinguishable except for some very small fluctuations at the upper end of the curve for the individual run that were smoothed by averaging in figure IV-48. The comparison is quantified in figure IV-49, which presents the RMS of the ensemble-averaged data as calculated using equation (III-7) and nondimensionalized with the ensemble-averaged value at each instant of time. From figure IV-49, the RMS values are seen to be less than 0.25 percent of $\langle U_m \rangle$ for most of the transient portion of the run. From this result, the ability of the system to repeat a given transient is estimated, at the 95-percent confidence level, to be within 0.5 percent of the desired value at each time increment.
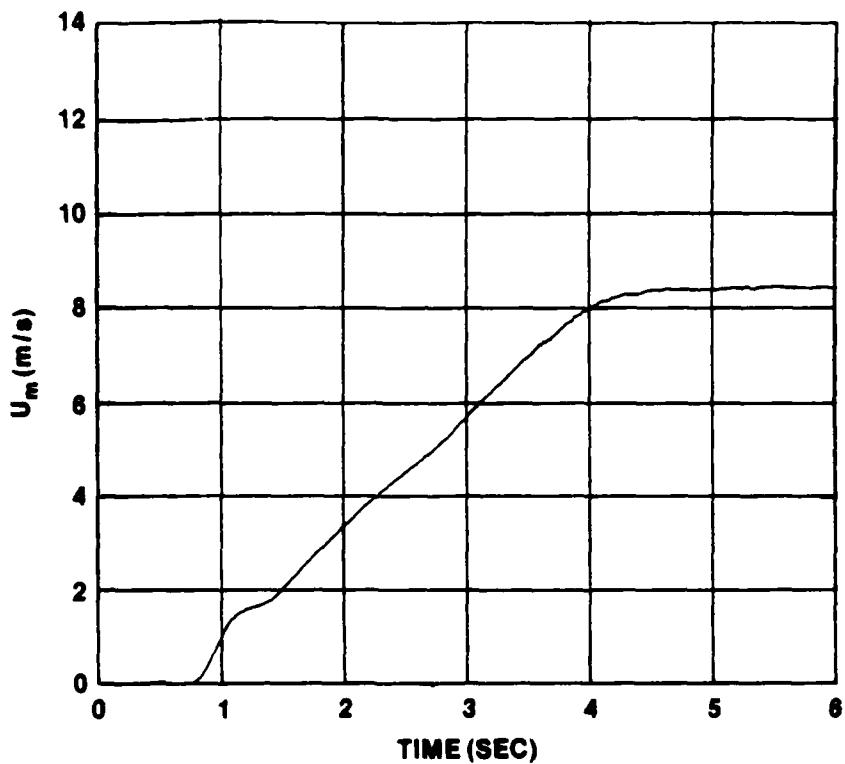
Figure IV-47. U_m vs t for One Typical Run at
$\ddot{X} = 2.4$ m/s^2 and $\bar{U}_{m0} = 0$
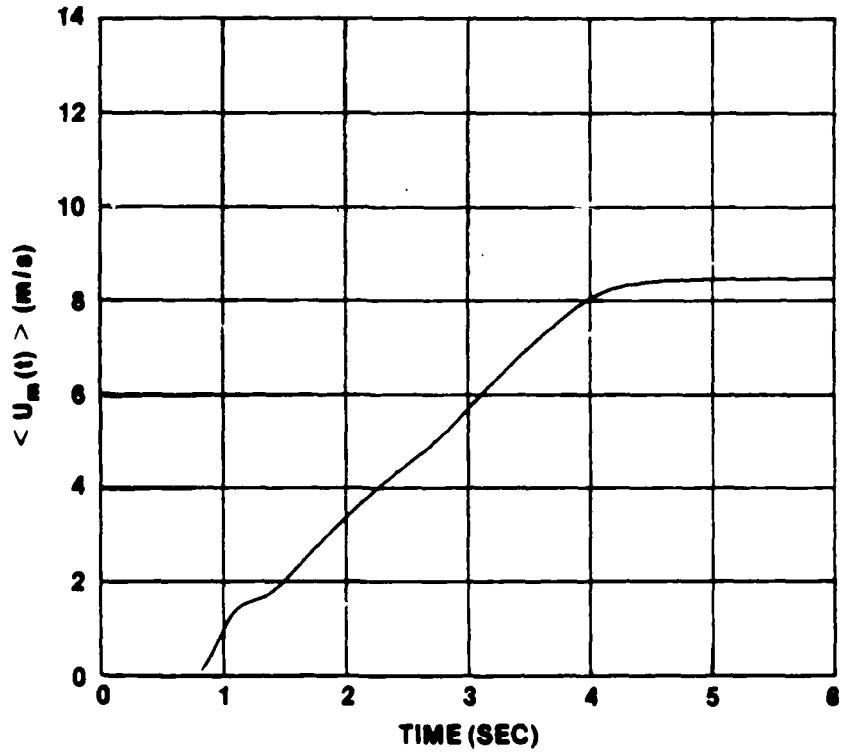
Figure IV-48. $\langle U_m(t) \rangle$ vs t for Ensemble Average of 20 Runs at
$\ddot{X} = 2.4$ m/s^2 and $\bar{U}_{m0} = 0$

103
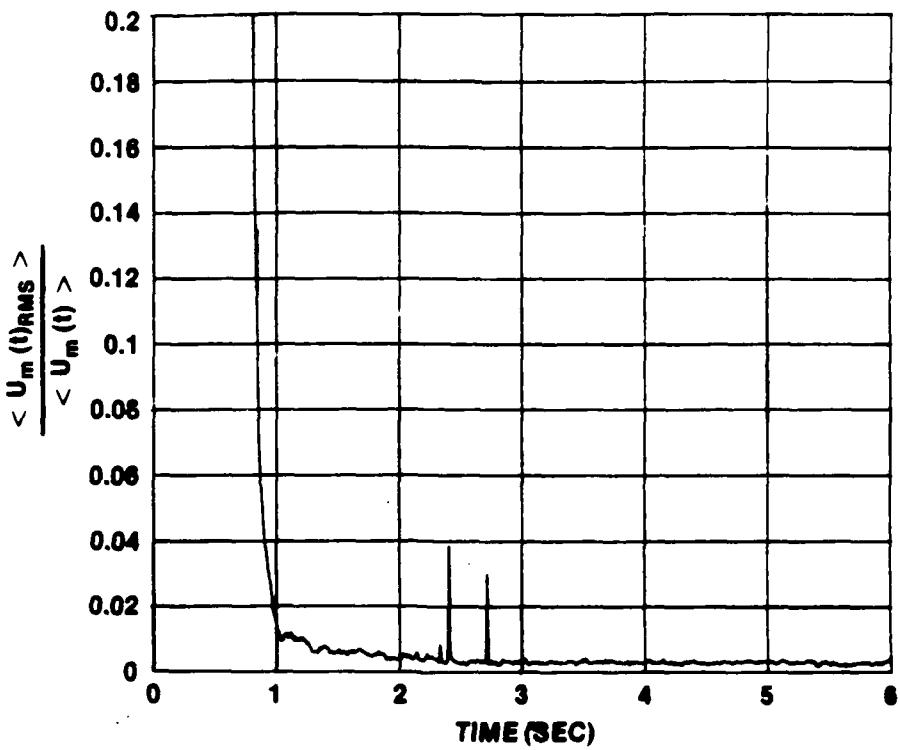
Figure IV-49. RMS of $\langle U_m(t) \rangle$ vs t for 20 Runs at $\ddot{X} = 2.4$ m/s^2
and $\bar{U}_{m0} = 0$

Figure IV-50 shows the output from the LDV with the measuring

volume positioned at the pipe centerline. The ensemble-averaged time

history is given in figure IV-51 and the nondimensionalized RMS history

in figure IV-52. As expected, the ensemble-averaged curve is much

smoother than the individual run. Transition is evidenced by the abrupt

change in output and is shown to have occurred at the same time for each

run. The RMS value prior to transition was approximately 1.8 percent of

the ensemble-averaged value, while after transition the RMS increased to

approximately a mean value of 3.5 percent due to the turbulent

fluctuations.

104
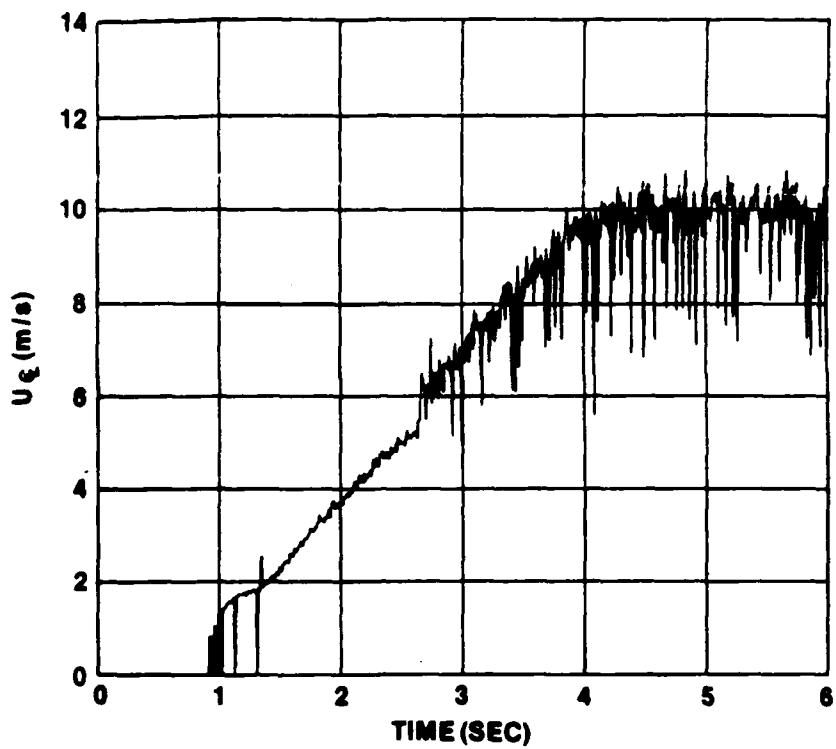
Figure IV-50. U_{cl} vs t for One Typical Run at
$\ddot{X} = 2.4$ m/s^2 and $\bar{U}_{m0} = 0$
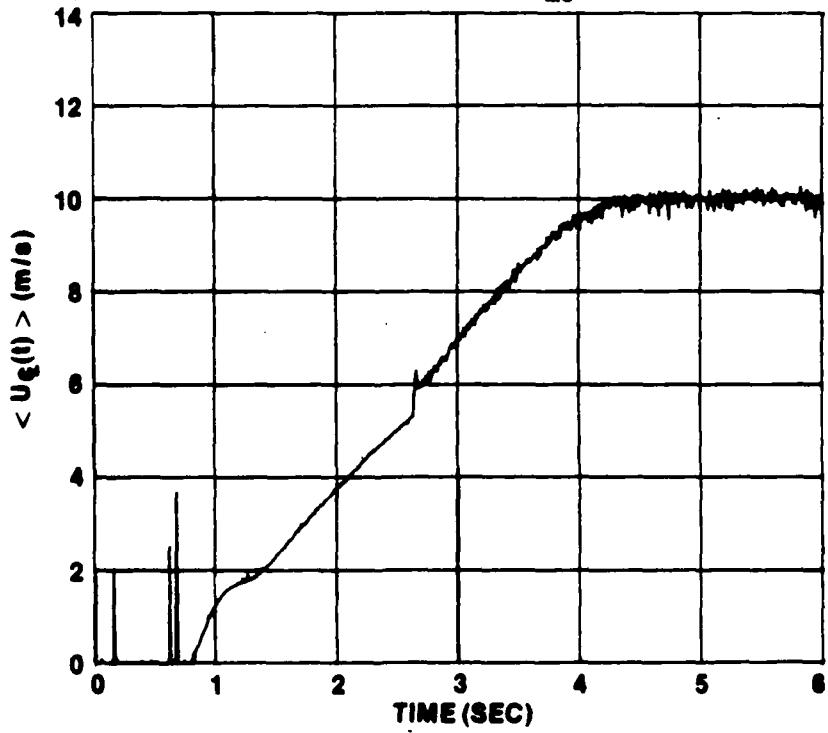
Figure IV-51. $\langle U_{cl}(t) \rangle$ vs t for Ensemble Average of 20 Runs at
$\ddot{X} = 2.4$ m/s^2 and $\bar{U}_{m0} = 0$

105
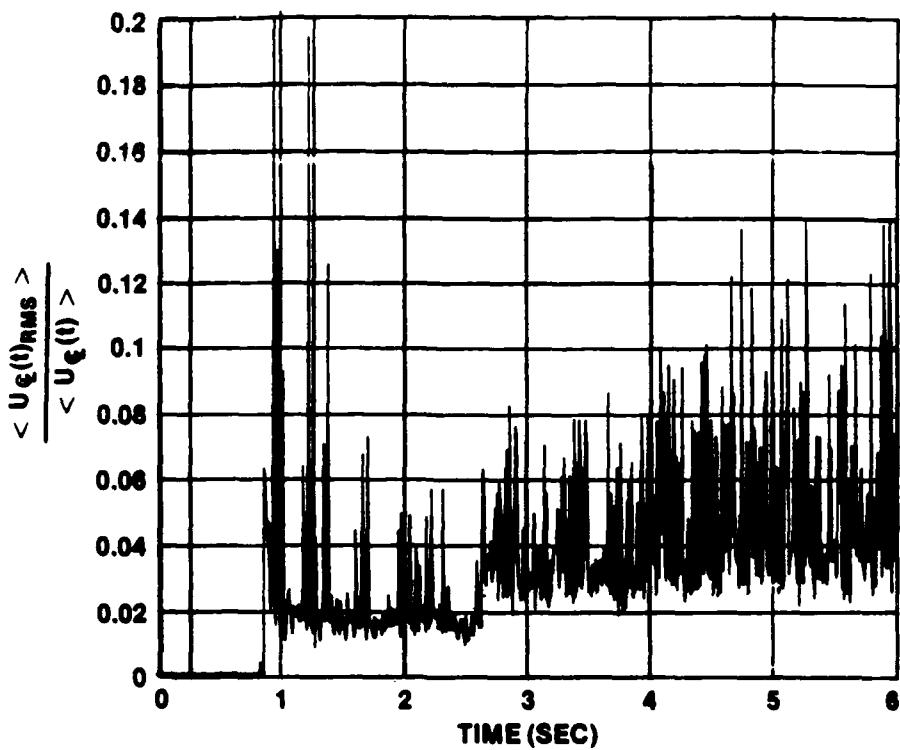
Figure IV-52. RMS of $\langle U_{c_1}(t) \rangle$ vs t for 20 Runs at $\ddot{X} = 2.4 \text{ m/s}^2$ and $\bar{U}_{m0} = 0$

In both figures IV-50 and IV-52, there are relatively large fluctuations about the mean curve. They are due to inaccurate measurements from the LDV due to excessive scattered light during the transient, which resulted in additional noise and a low data rate output from the LDV. During subsequent runs, this problem was eliminated by eliminating the center beam of the laser to reduce the amount of scattered light and resulting noise. Much improved signals of the axial component of the flow were then obtained as will be shown later. However, measurement of the radial component, hence, Reynolds stress were no longer possible. The decision to eliminate the measurement of Reynolds stress from the transient test runs was also

106

based on the observation from some of these early tests that averaging only 20 runs to calculate Reynolds stress was not enough for any reasonable accuracy. Many additional runs would have been required, which was not justifiable, as shown later.

Figure IV-53 is the time history of the ensemble-averaged LDV measurements taken at $r/R = 0.80$. Figure IV-54 shows the RMS values associated with figure IV-53. For these runs, the center beam of the LDV was eliminated, thus resulting in a greatly improved signal and accuracy at each time increment during the run.

Unfortunately, it is not possible to estimate the data rate at which valid LDV data were obtained during the transient for use as a guide to future experimenters. However, whenever the LDV measuring volume was repositioned, the LDV was adjusted and optimized at several steady-state velocities that covered the range of transient velocities tested. The data rate at these steady-state velocities can be stated as a guideline. At each velocity when the center beam was present, the data rate was approximately 10,000 per second, while for the cases without the center beam (as in figure IV-53) the data rate was approximately 50,000.

For the case at $r/R = 0.80$, the RMS value prior to transition was approximately 1.0 percent, while after transition it was closer to 7.0 percent. Clearly, for times prior to transition when the flow was laminar, the RMS values are only an indication of the repeatability of conditions from one run to the next and the LDV accuracy. For the turbulent portion of the curve, the RMS values can indicate the

107
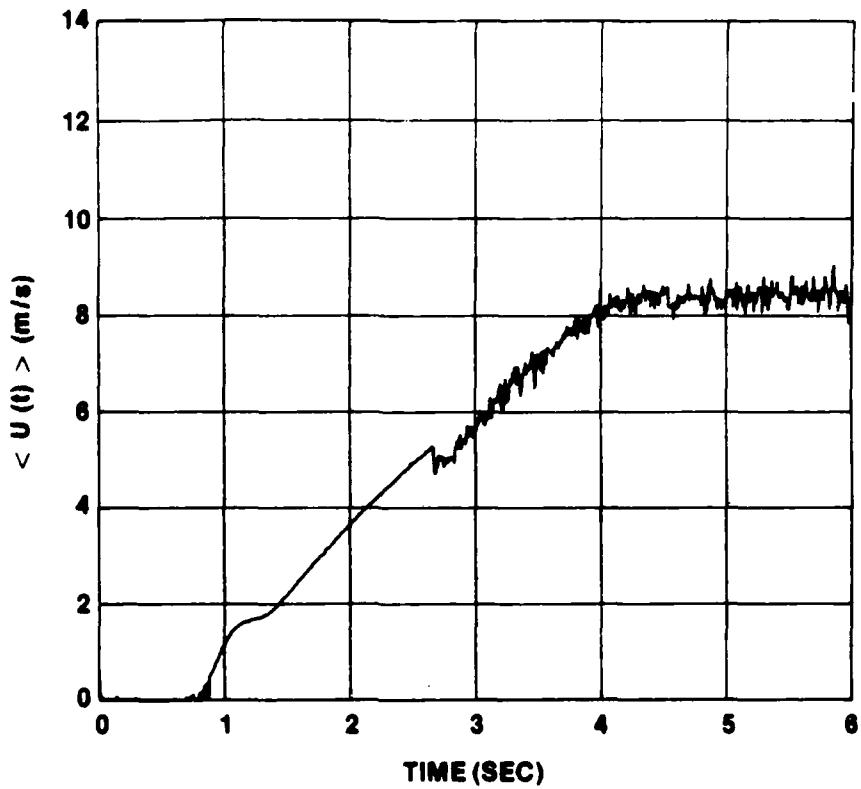
Figure IV-53. $\langle U(t)\rangle$ at $r/R = 0.80$ vs t for Ensemble Average
of 20 Runs at $\ddot{X} = 2.4$ m/s^2 and $\bar{U}_{m0} = 0$
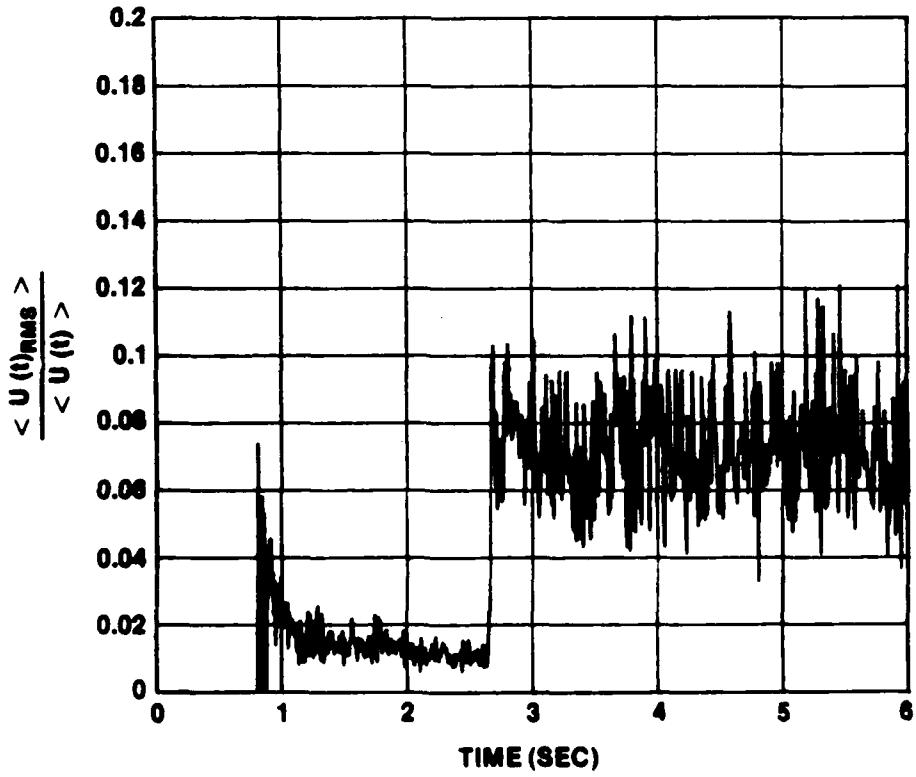

Figure IV-53.   RMS of $\langle U(t)\rangle$ at $r/R = 0.80$ vs t for Ensemble Average
of 20 Runs at $\ddot{X} = 2.4$ m/s^2 and $\bar{U}_{m0} = 0$

108

turbulence intensity if one assumes a direct correlation between ensembling averaging in transient flows and time averaging in steady flows. The accuracy of this assumption cannot be proven. However, as a minimum, these RMS values can at least be used as an order of magnitude comparison to steady-state values. A precedence was established for the use of ensembling averaging in the transient case presented by Ramaprian and Tu [13]. A presentation of time-dependent turbulence intensity for the initially turbulent runs is made later in this section.

Also indicated in figure IV-53 is the abrupt change in local velocity at transition. Inspection of the data for each of the 240 runs of the case shows that transition always occurred at the same time across the pipe diameter and between runs. As shown later in the detailed velocity profile measurements for these runs, the velocity at near wall points such as at $r/R = 0.80$ decreases after transition to account for the redistribution of momentum. This decrease in velocity is balanced by the increase observed nearer the centerline.

Figures IV-55a through IV-55p are a sequence of the time-dependent velocity profiles throughout the transient. The actual time, from time $t = 0.0$, is given along with t^*. Here, t^* is calculated in the same manner as was done for the transition tests. The profiles are presented as distance from the wall, Y/R ($Y/R = 0.05, 0.1$, then in 0.1 increments to pipe centerline), versus instantaneous local axial velocity nondimensionalized with the corresponding instantaneous centerline velocity, U/U_{cl}. For each profile, data are shown for 12

109
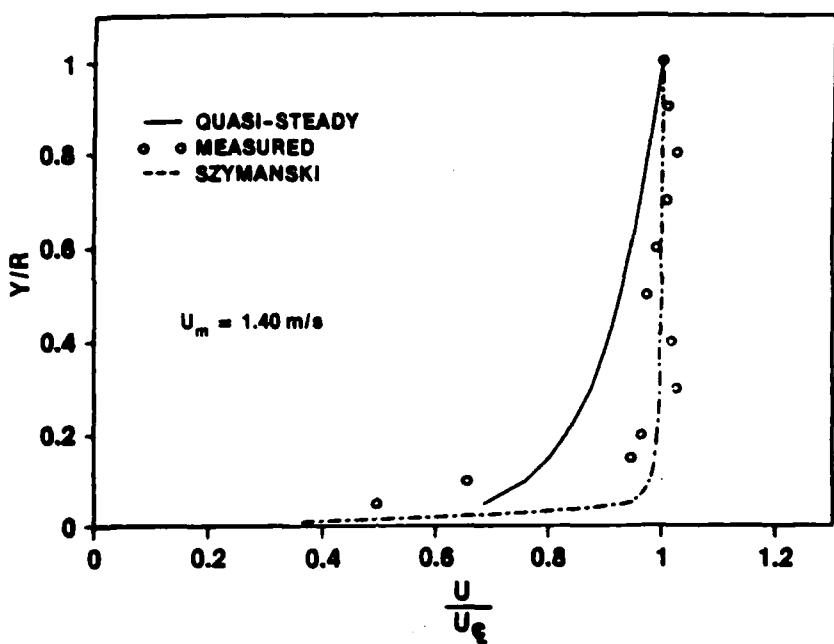
Figure IV-55a.   Velocity Profile at t = 1.100 s (t* = 0.000792)
for $\ddot{X}$ = 2.4 m/s^2 and $\bar{U}_{m0}$ = 0
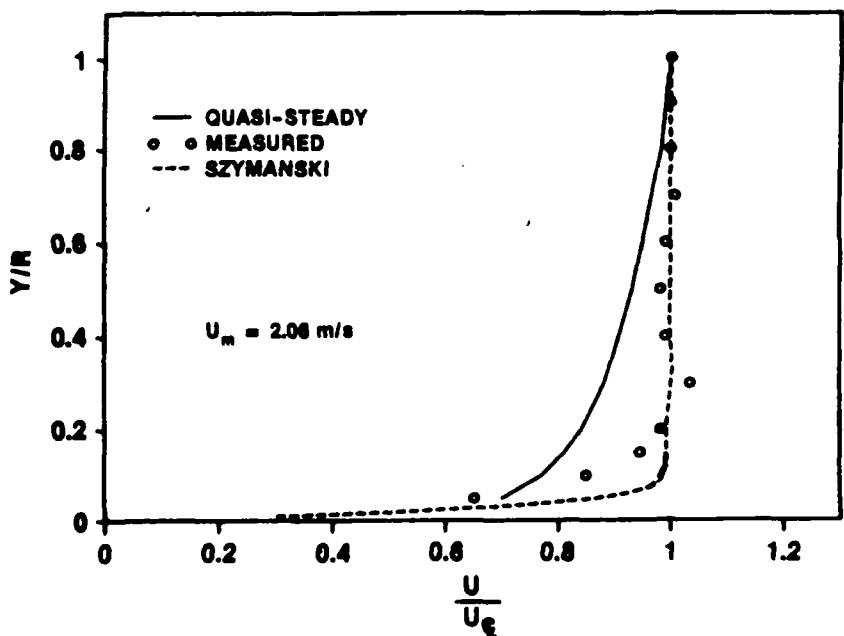
Figure 55b.   Velocity Profile at t = 1.500 s (t* = 0.00116)
for $\ddot{X}$ = 2.4 m/s^2 and $\bar{U}_{m0}$ = 0

110
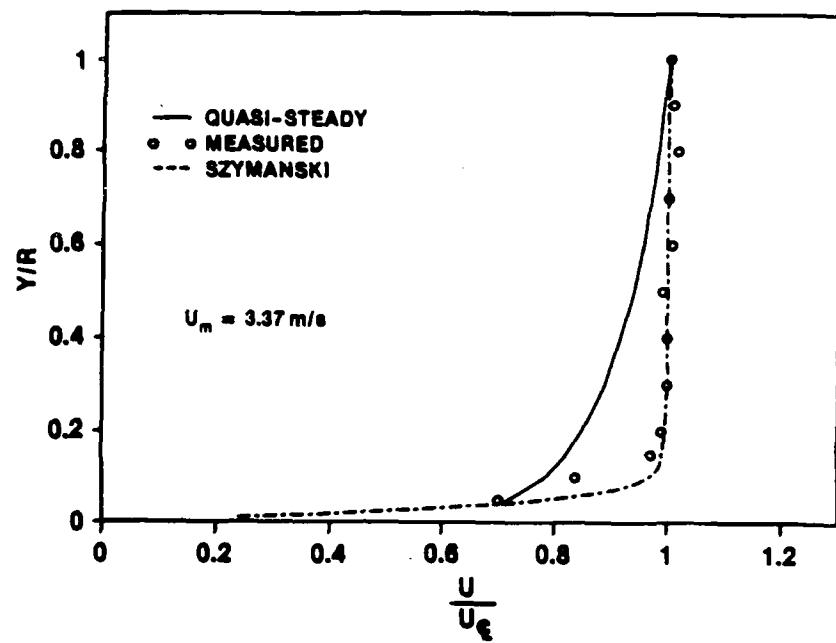
Figure 55c. Velocity Profile at t = 2.000 s (t* = 0.00190)
for $\ddot{X}$ = 2.4 m/s^2 and $\bar{U}_{m0}$ = 0
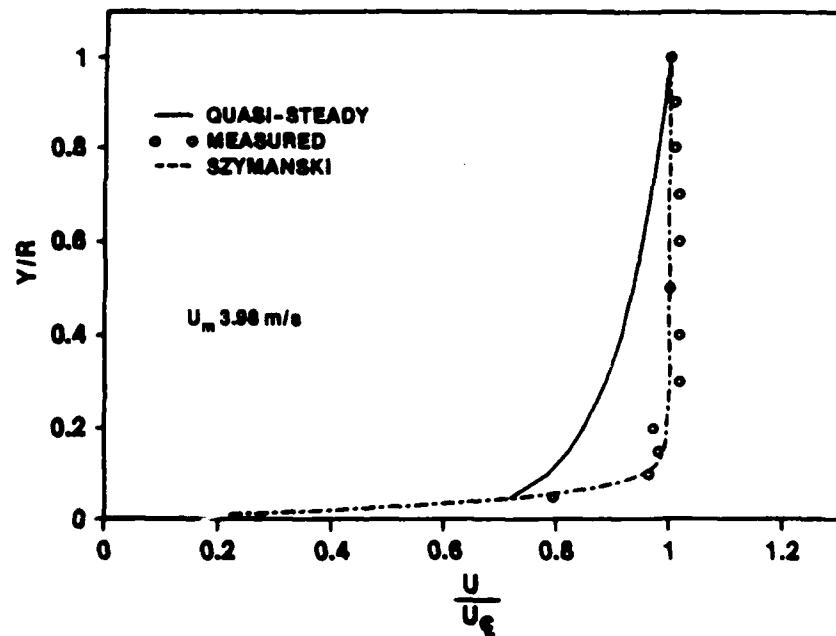
Figure 55d. Velocity Profile at t = 2.250 s (t* = 0.00224)
for $\ddot{X}$ = 2.4 m/s^2 and $\bar{U}_{m0}$ = 0

111
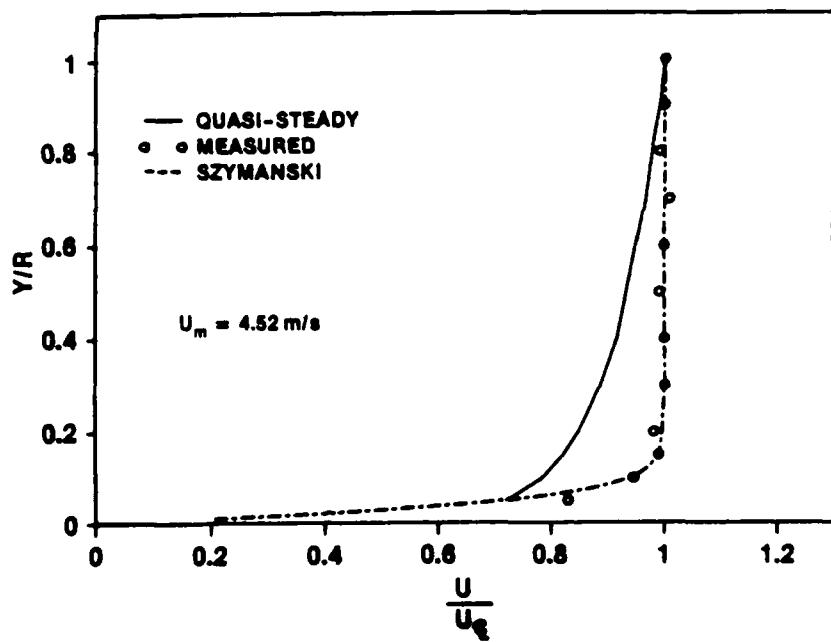
Figure IV-55e. Velocity Profile at t = 2.500 s (t* = 0.00255)
for $\ddot{X}$ = 2.4 m/s^2 and $\bar{U}_{m0}$ = 0
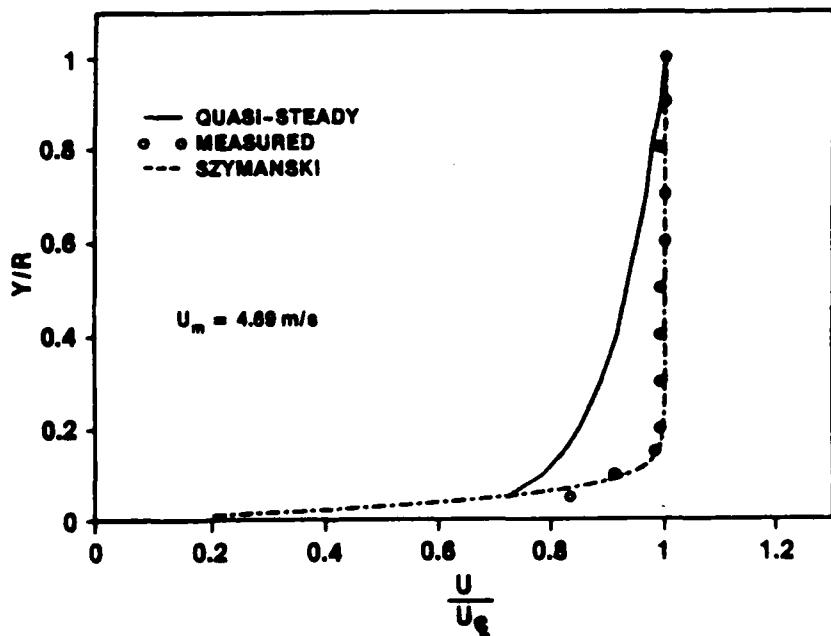
Figure 55f. Velocity Profile at t = 2.583 s (t* = 0.00265)
for $\ddot{X}$ = 2.4 m/s^2 and $\bar{U}_{m0}$ = 0

112
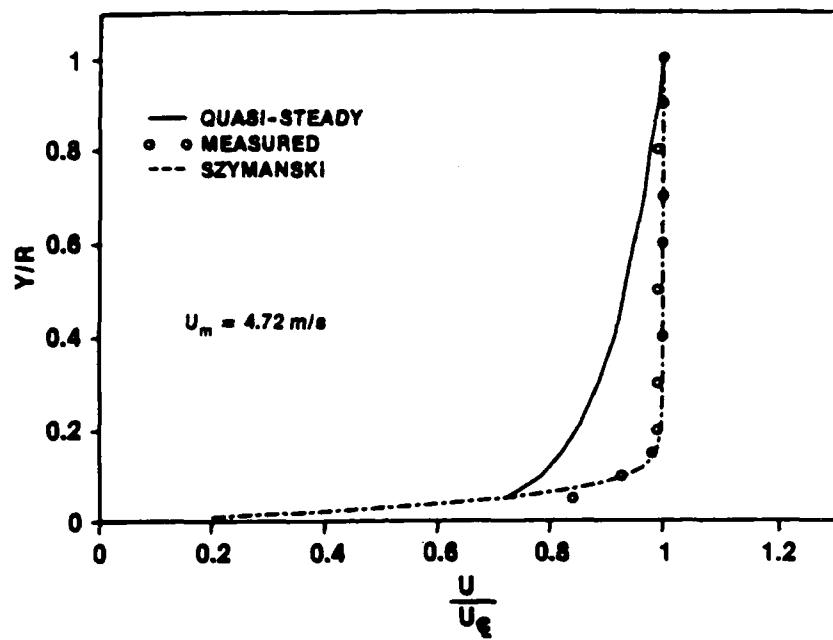
Figure 55g.   Velocity Profile at t = 2.600 s (t* = 0.00267)
for $\dot{X}$ = 2.4 m/s^2 and $\bar{U}_{m0}$ = 0
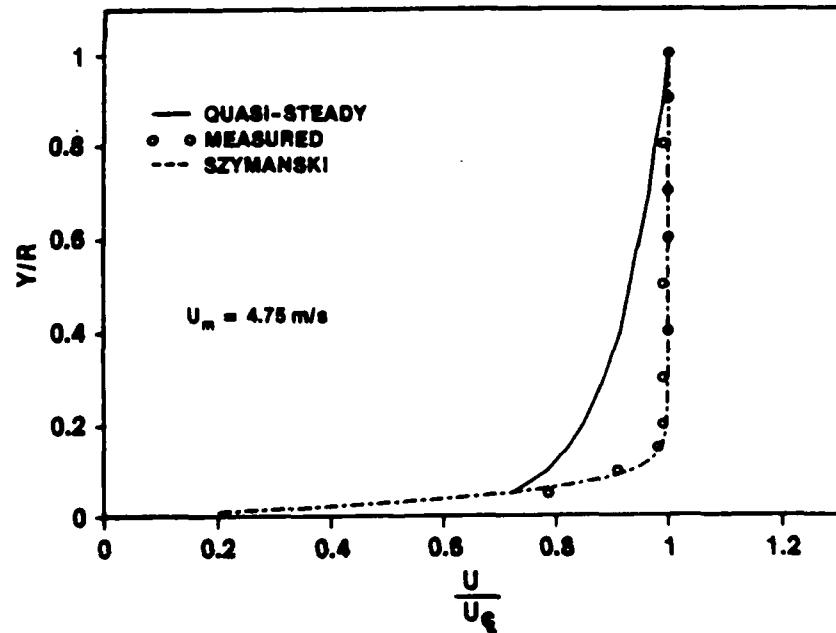
Figure 55h.   Velocity Profile at t = 2.617 s (t* = 0.00268)
for $\dot{X}$ = 2.4 m/s^2 and $\bar{U}_{m0}$ = 0

113
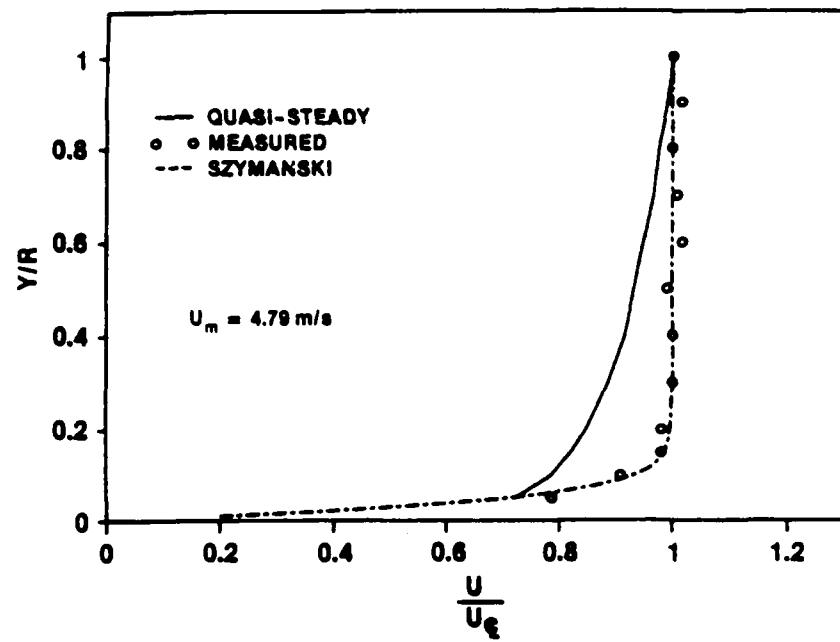
Figure IV-55i.   Velocity Profile at t = 2.633 s (t* = 0.00270)
for $\ddot{X}$ = 2.4 m/s^2 and $\bar{\bar{U}}_{m0}$ = 0
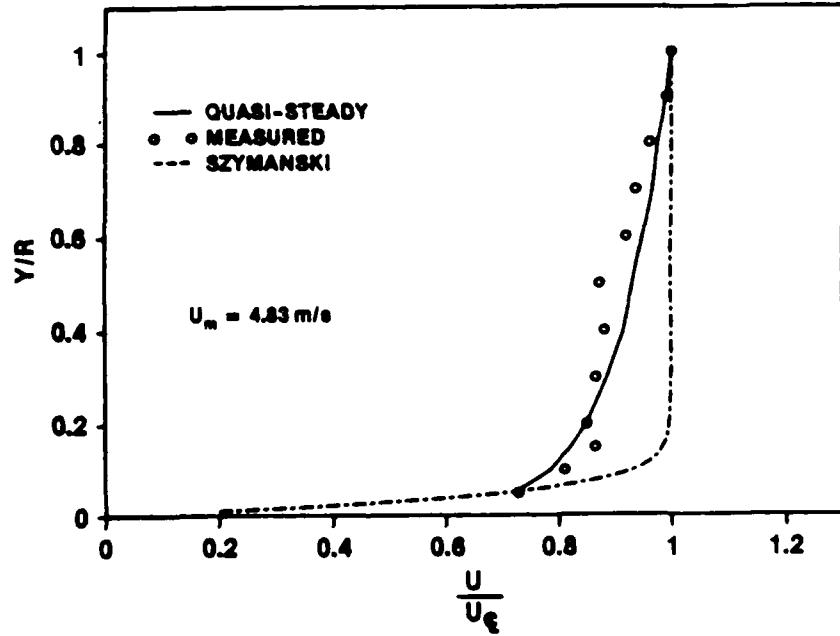
Figure 55j.   Velocity Profile at t = 2.650 s (t* = 0.00272)
for $\ddot{X}$ = 2.4 m/s^2 and $\bar{\bar{U}}_{m0}$ = 0

114
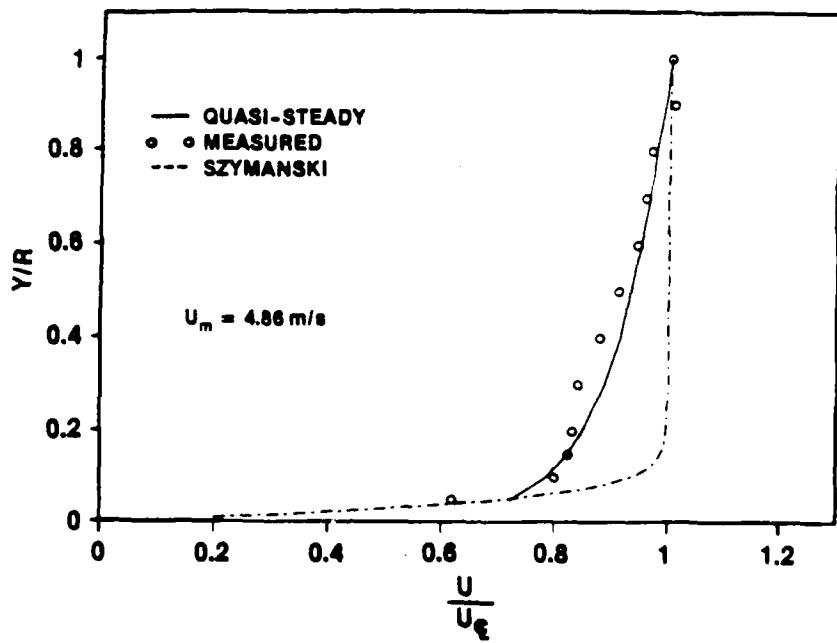
Figure 55k.   Velocity Profile at t = 2.667 s (t* = 0.00274)
for $\ddot{X}$ = 2.4 m/s^2 and $\bar{U}_{m0}$ = 0
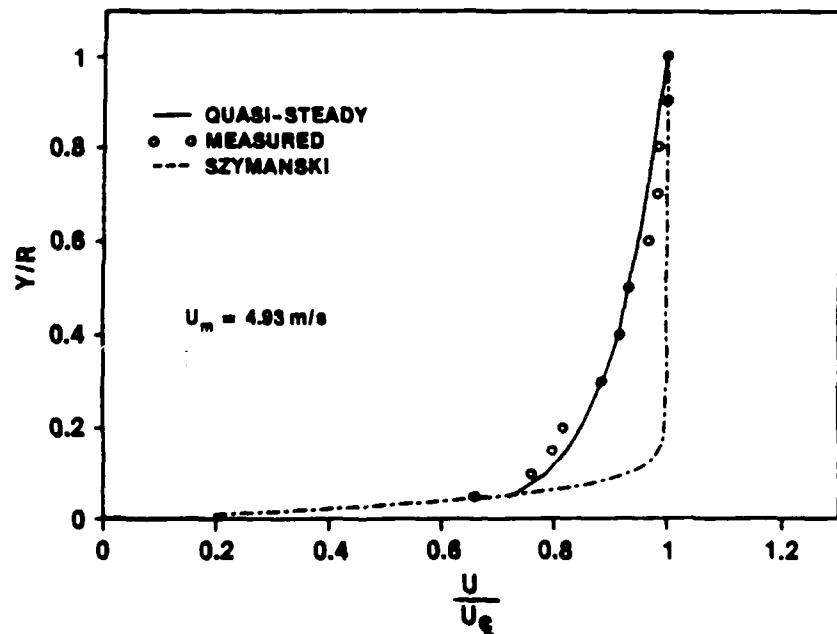
Figure 55l.   Velocity Profile at t = 2.700 s (t* = 0.00278)
for $\ddot{X}$ = 2.4 m/s^2 and $\bar{U}_{m0}$ = 0

115
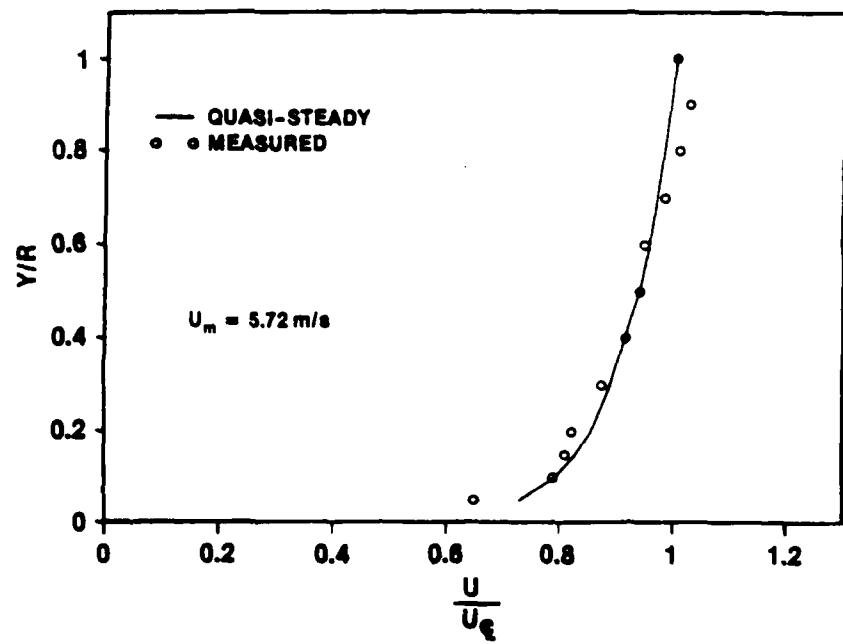
Figure IV-55m. Velocity Profile at t = 3.000 s (t* = 0.00323)
for $\ddot{X}$ = 2.4 m/s^2 and $\bar{U}_{m0}$ = 0
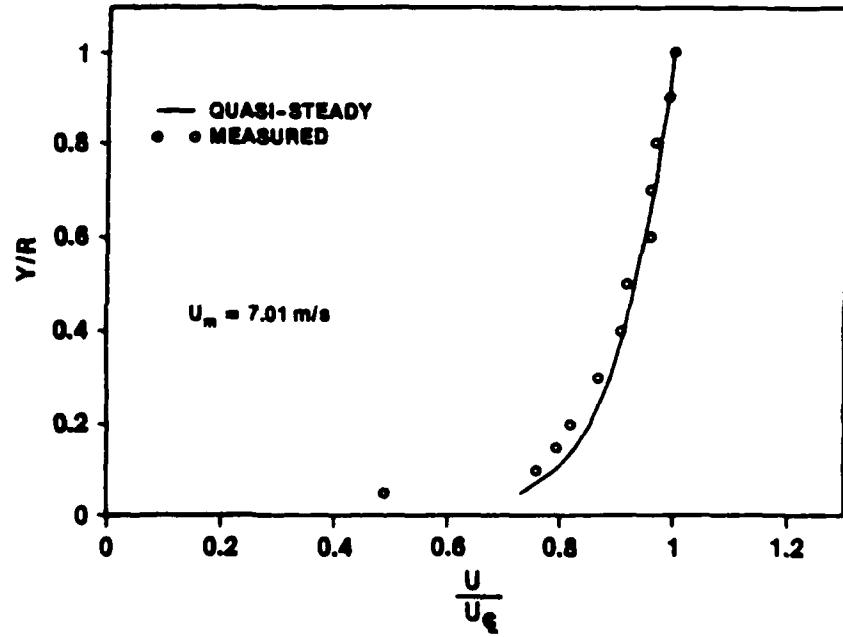
Figure 55n. Velocity Profile at t = 3.500 s (t* = 0.00396)
for $\ddot{X}$ = 2.4 m/s^2 and $\bar{U}_{m0}$ = 0

116
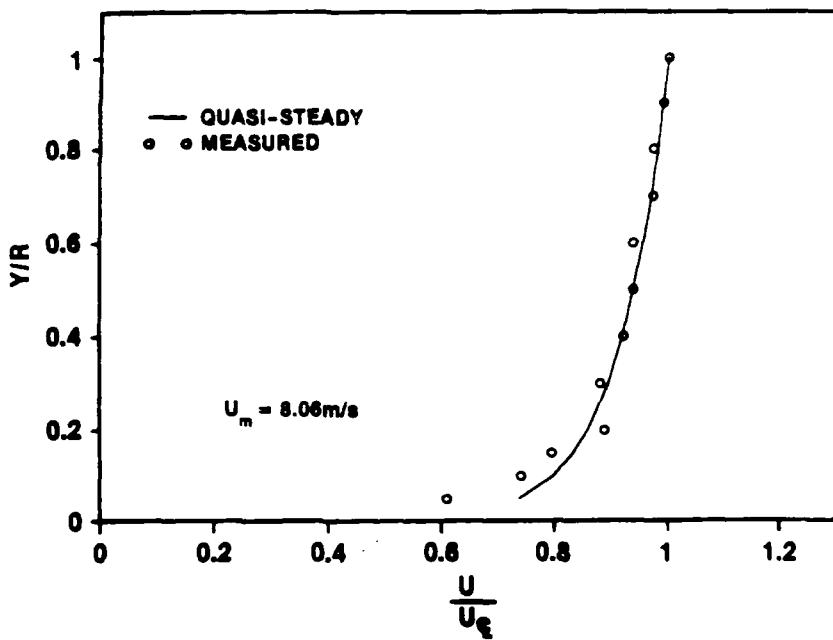
Figure 55o.   Velocity Profile at t = 4.000 s (t* = 0.00455)
for $\ddot{X}$ = 2.4 m/s^2 and $\bar{U}_{m0}$ = 0
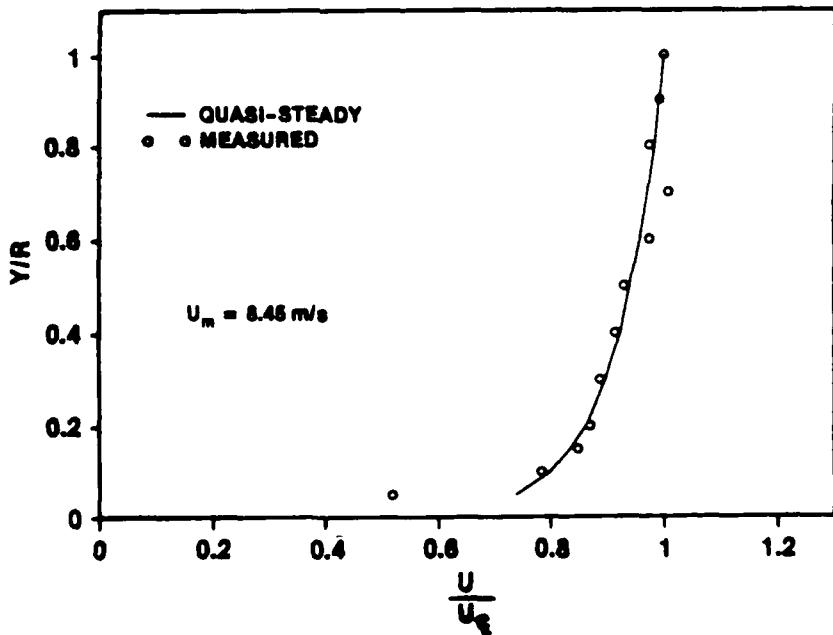
Figure 55p.   Velocity Profile at t = 5.000 s for $\ddot{X}$ = 2.4 m/s^2
and $\bar{U}_{m0}$ = 0

117

locations across the pipe radius. Again, each data point is the
ensemble average of 20 separate runs. Therefore, the number of
individual runs that were conducted to generate these profiles was
240. The value of the instantaneous cross-sectional average velocity
U_m is also given at each time.

Also included on each figure is the quasi-steady turbulent
profile as calculated using Spalding's equation for the
law-of-the-wall (equation (IV-3)). At each time increment that will
be presented, the cross-sectional average velocity is large enough
that the corresponding steady-state flow would be turbulent with the
above mentioned equation being applicable. The calculated profile
based on Szymanski's exact laminar solution, equation (I-1), is also
plotted at each time where the flow is laminar and for a few of the
profiles immediately following transition.

The first profile, figure IV-55a, occurred near the start of the
acceleration at a time of 1.1 second. Subsequent profiles prior to
transition are given at times of 1.50, 2.00, 2.25, 2.43, 2.83, 2.600,
2.617, and 2.633 seconds. The first two profiles show some scatter
about the exact solution for the points near the wall. This is
probably due to inaccuracies of the laser measurements at the
extremely low values of velocity observed. The remaining profiles up
to transition are extremely close to Szymanski's solution.

Between the times of 2.633 and 2.650 seconds, transition
occurred. It can be seen that within this 0.017 second, the velocity
profile across the entire pipe cross-section changed from the almost

118

plug flow profile to virtually the quasi-steady turbulent profile.
For times of 2.650 and 2.667 seconds, the profiles (even though very
close to the quasi-steady turbulent profile) are still changing
slightly. At time 2.700 seconds, the measured profile is almost
exactly that of the quasi-steady one. For the remainder of the
transient, which lasts until approximately 4.3 seconds, and the
subsequent steady-state portion of the run, each velocity profile
falls on the quasi-steady one.

Considering the low RMS values during the laminar portion of the
transient, the velocity profiles could have been generated using only
one run without any ensemble averaging and the profiles would have
looked similar. This is unlike the work of previous investigators who
had to make many repeat measurements at each location to have any
semblance of a reasonably smooth profile. The reason for the improved
performance of the present LDV set-up was the high data rate output
resulting from the use of forward scattering.

The second case of the ensemble-averaged tests are discussed
next. This case is for an acceleration of 6.1 m/s^2 from rest. As
with the first case, the time history of the ensemble-averaged
cross-sectional average velocity is presented first in figure IV-56
with the corresponding RMS of the runs in figure IV-57. As with the
previous runs, the acceleration is essentially constant over the
transient and the RMS value is generally less than 0.25 percent of the
instantaneous velocity resulting in a 95-percent confidence level
repeatability of 0.5 percent.

119
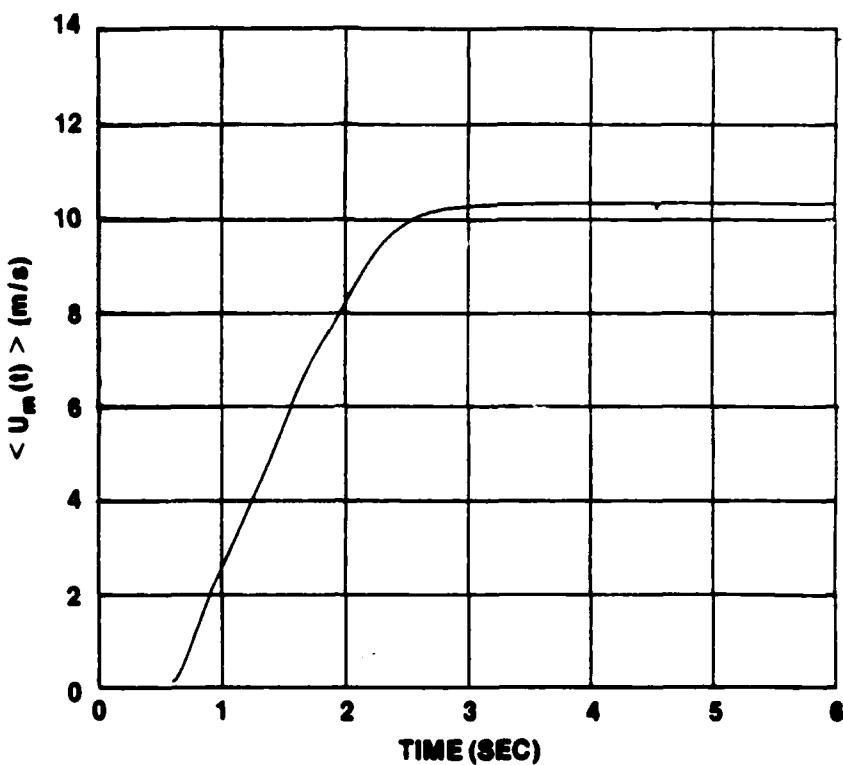
Figure IV-56. $\langle U_m(t) \rangle$ vs t for Ensemble Average of 20 Runs at $\ddot{X} = 6.1$ m/s^2 and $\bar{U}_{m0} = 0$
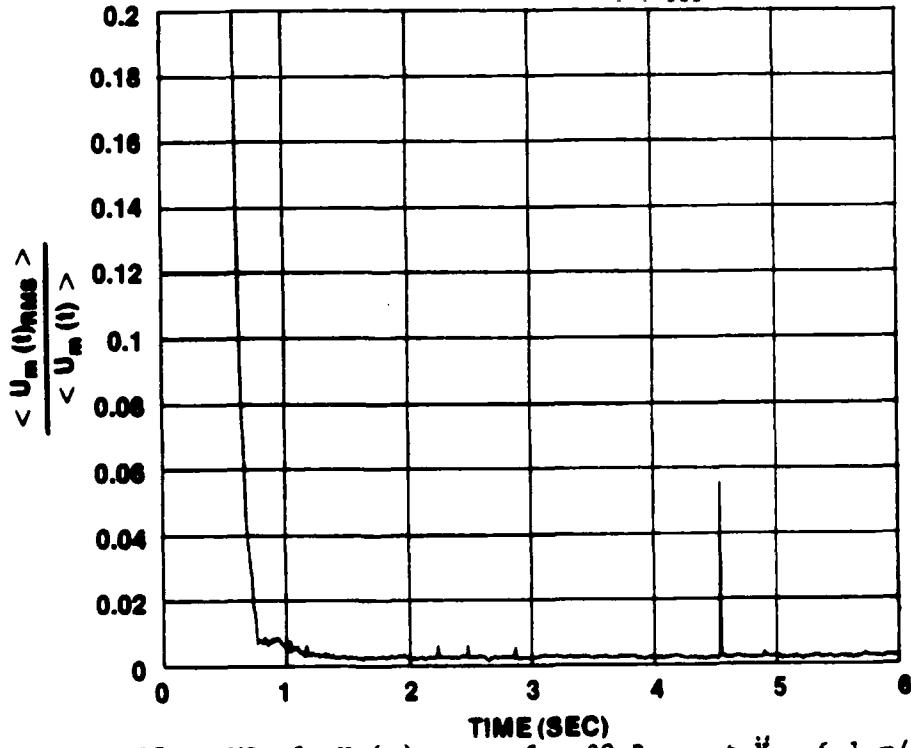

Figure IV-57. RMS of $\langle U_m(t) \rangle$ vs t for 20 Runs at $\ddot{X} = 6.1$ m/s^2 and $\bar{U}_{m0} = 0$

120

The centerline velocity is given in figure IV-58 and shows the clean output throughout the transient as a consequence of the high valid data rate obtained by eliminating the center beam of the LDV. A sharp transition to turbulence is again seen to be repeated at the same time for each of the 20 runs. As with case 1, transition occurred at the same time for each of the 240 runs of this case indicating global transition across the pipe diameter. RMS values of centerline velocity are shown in figure IV-59 to be approximately 1.6 percent prior to transition and 3.8 percent following transition.

The velocity profiles for this second case are shown in figures IV-60a through IV-601. Results are very similar to the case with an acceleration of 2.4 m/s^2. The first profile is again at the time of 1.100 seconds followed by times prior to transition of 1.300, 1.500, 1.700, and 1.783 seconds. At each of these times, the measured velocity profile follows closely the calculated profiles from Szymanski's solution.

Between times of 1.783 and 1.800 seconds, transition started. At 1.8 second, the profile is seen to be between the almost plug flow of Szymanski's solution and the quasi-steady turbulent profile. At the next time increment of 1.817 seconds, the profile has essentially changed to the quasi-steady one. Therefore, transition has taken place within 0.034 second. If the data acquisition rate was higher, the actual time could have been determined. Higher data rates were unfeasible for these initial tests conducted on the Flow Loop Facility due to the large number of channels that were being sampled. Future

121
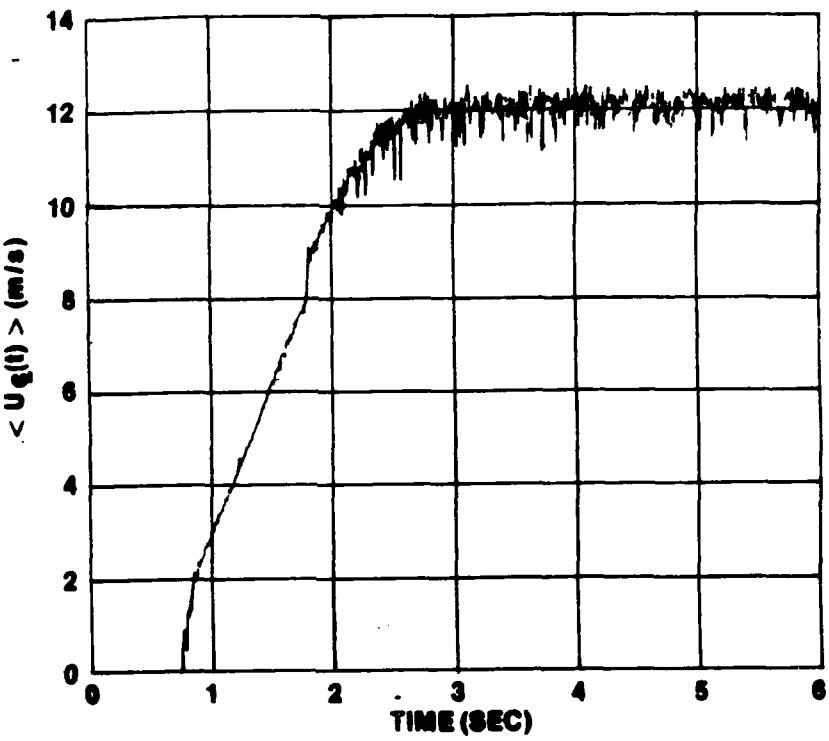
Figure IV-58. $\langle U_{c1}(t) \rangle$ vs t for Ensemble Average of 20 Runs at $\ddot{X} = 6.1$ m/s^2 and $\overline{U}_{m0} = 0$
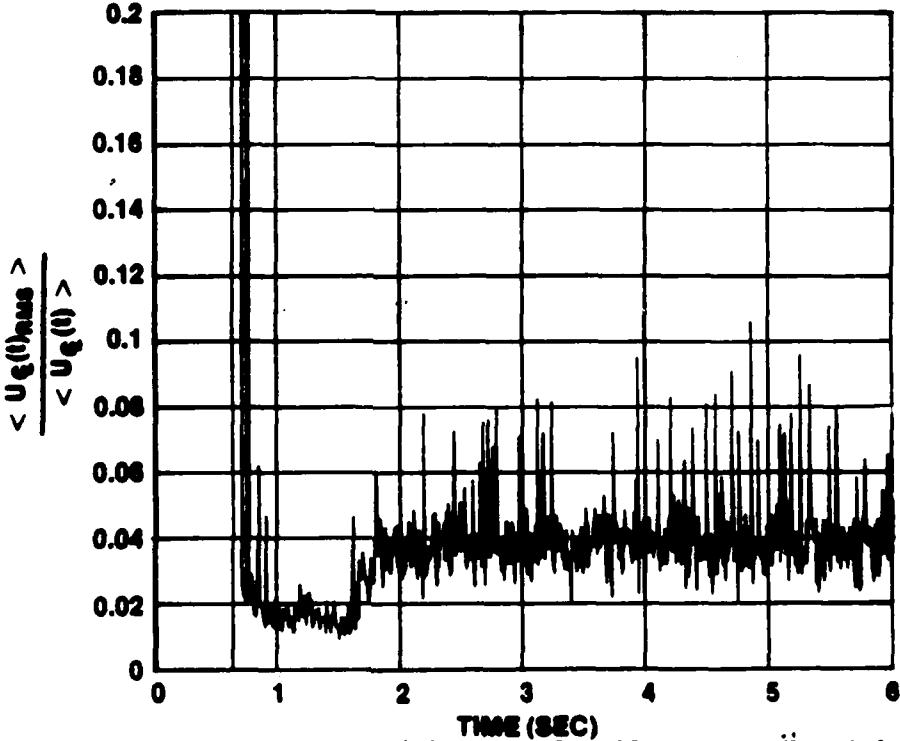
Figure IV-59. RMS of $\langle U_{c1}(t) \rangle$ vs t for 20 Runs at $\ddot{X} = 6.1$ m/s^2 and $\overline{U}_{m0} = 0$

122
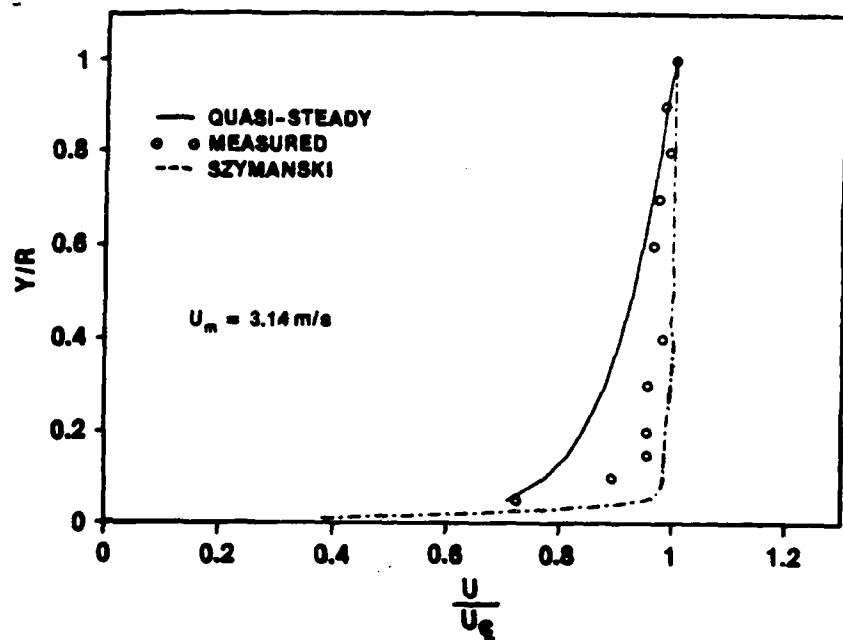
Figure IV-60a.   Velocity Profile at t = 1.100 s (t* = 0.000713)
for $\ddot{X}$ = 6.1 m/s^2 and $\bar{U}_{m0}$ = 0
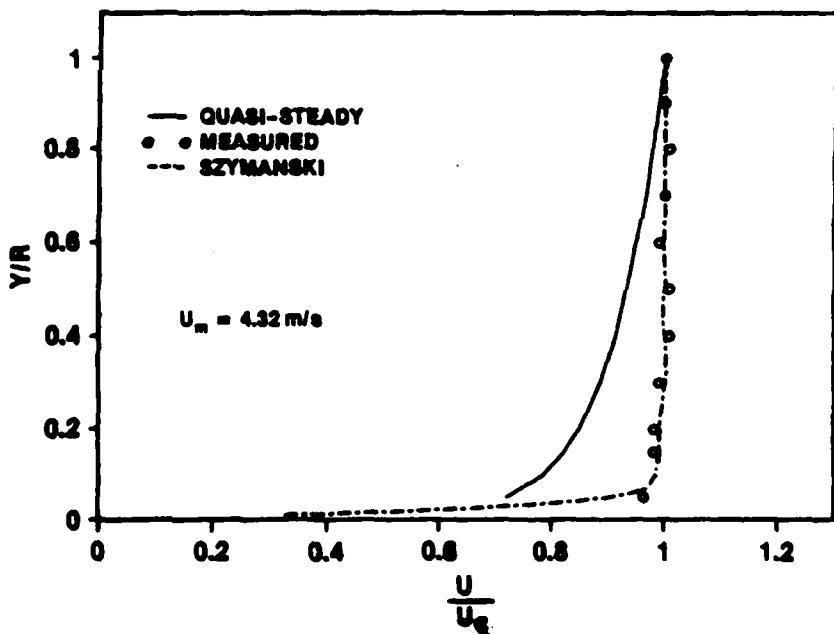
Figure IV-60b.   Velocity Profile at t = 1.300 s (t* = 0.00098)
for $\ddot{X}$ = 6.1 m/s^2 and $\bar{U}_{m0}$ = 0
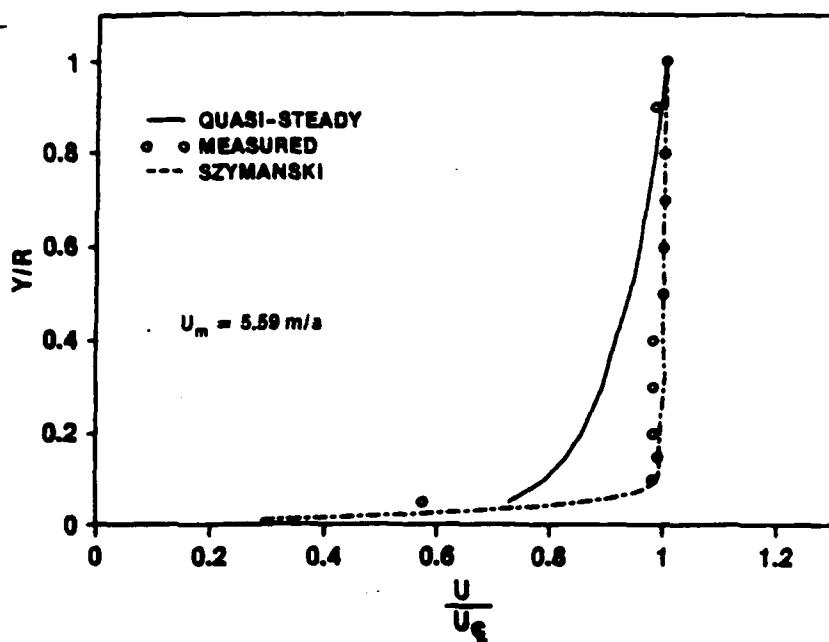
Figure IV-60c. Velocity Profile at t = 1.500 s (t* = 0.00127) for $\ddot{X}$ = 6.1 m/s^2 and $\bar{\bar{U}}_{m0}$ = 0
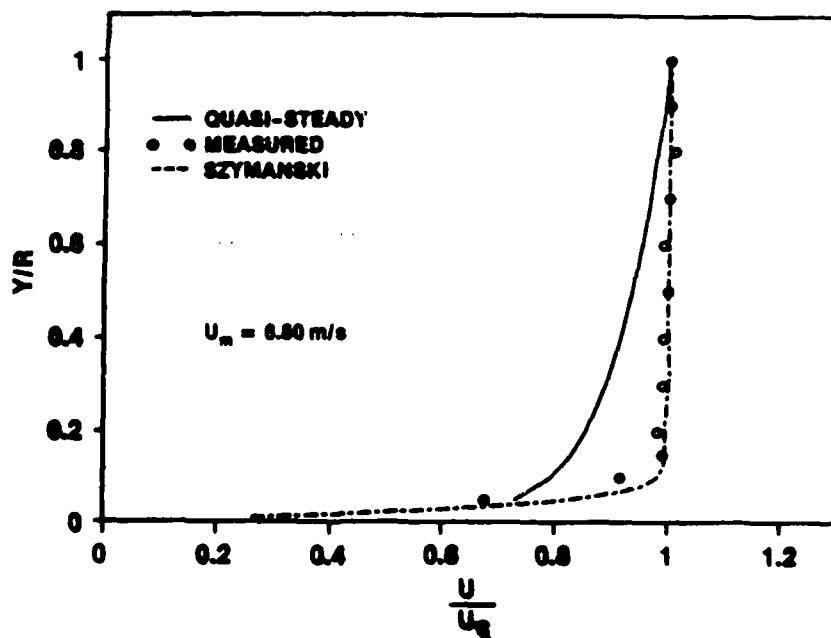
Figure IV-60d. Velocity Profile at t = 1.700 s (t* = 0.00154) for $\ddot{X}$ = 6.1 m/s^2 and $\bar{\bar{U}}_{m0}$ = 0

124
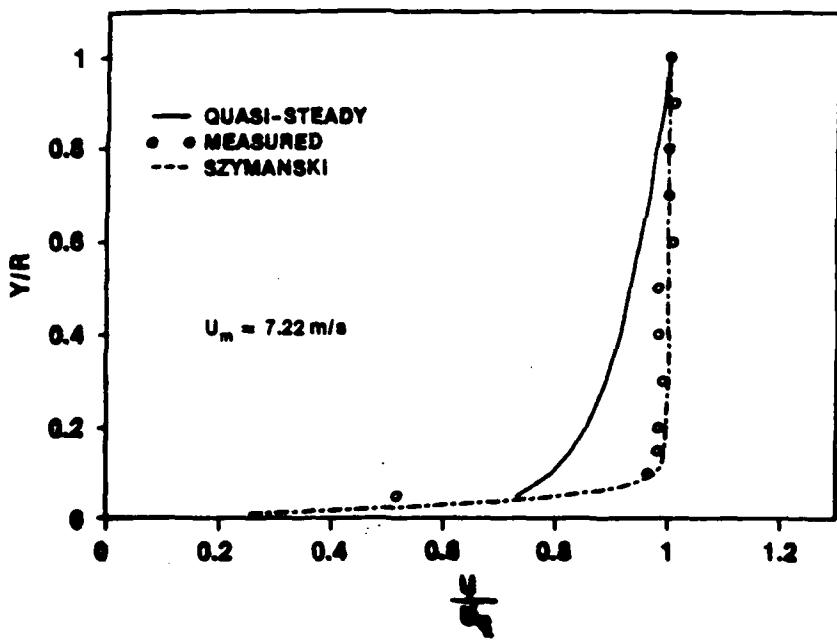
Figure IV-60e. Velocity Profile at t = 1.783 s (t* = 0.00164)
for $\ddot{X}$ = 6.1 m/s^2 and $\bar{U}_{m0}$ = 0
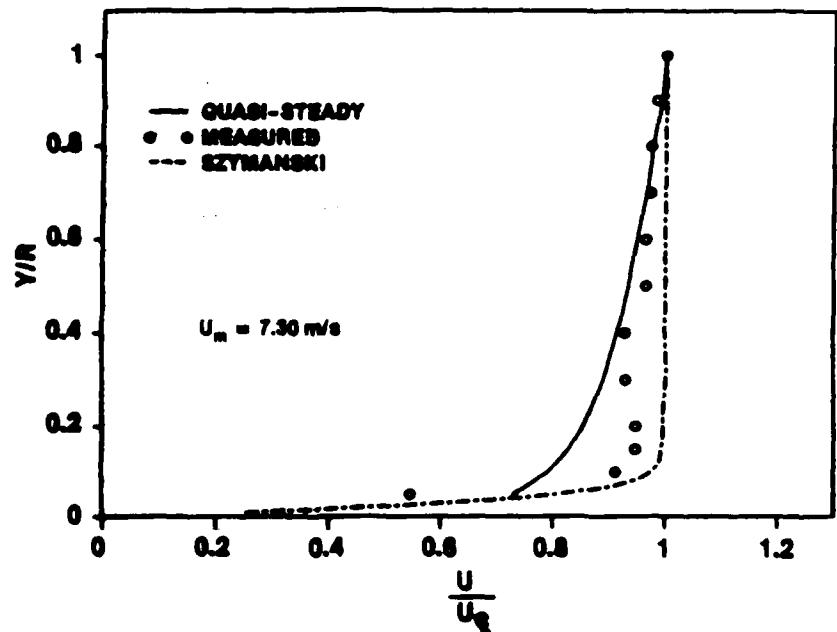
Figure IV-60f. Velocity Profile at t = 1.800 s (t* = 0.00166)
for $\ddot{X}$ = 6.1 m/s^2 and $\bar{U}_{m0}$ = 0

125
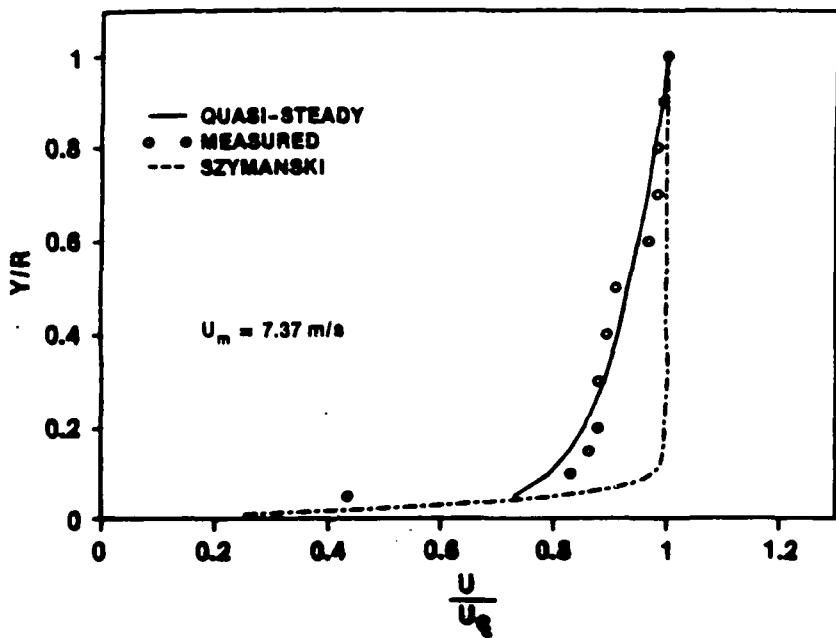
Figure IV-60g. Velocity Profile at t = 1.817 s (t* = 0.00167) for $\ddot{X}$ = 6.1 m/s^2 and $\overline{U}_{m0}$ = 0
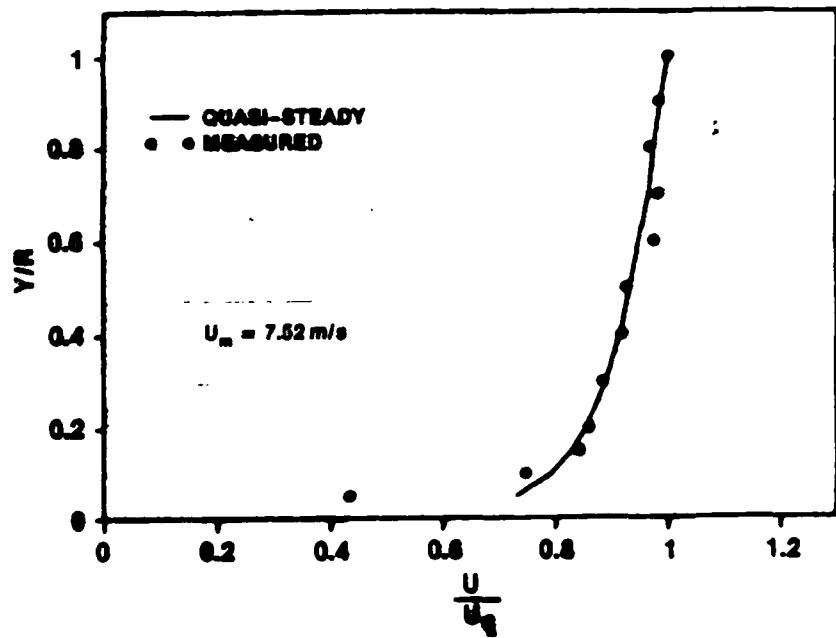
Figure IV-60h. Velocity Profile at t = 1.850 s (t* = 0.00171) for $\ddot{X}$ = 6.1 m/s^2 and $\overline{U}_{m0}$ = 0
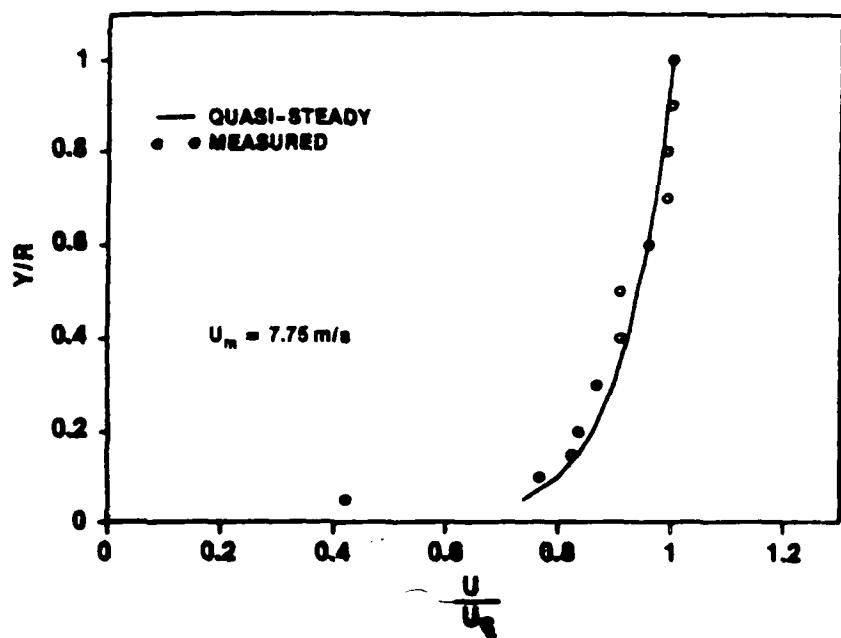
Figure IV-60i. Velocity Profile at t = 1.900 s (t* = 0.00176)
for $\ddot{X}$ = 6.1 m/s^2 and $\bar{U}_{m0}$ = 0
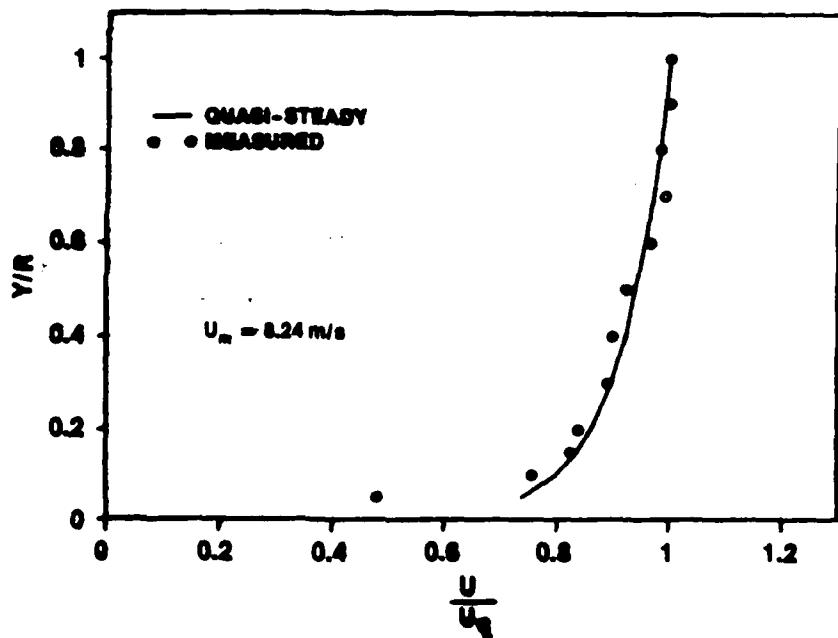
Figure IV-60j. Velocity Profile at t = 2.000 s (t* = 0.00187)
for $\ddot{X}$ = 6.1 m/s^2 and $\bar{U}_{m0}$ = 0

127
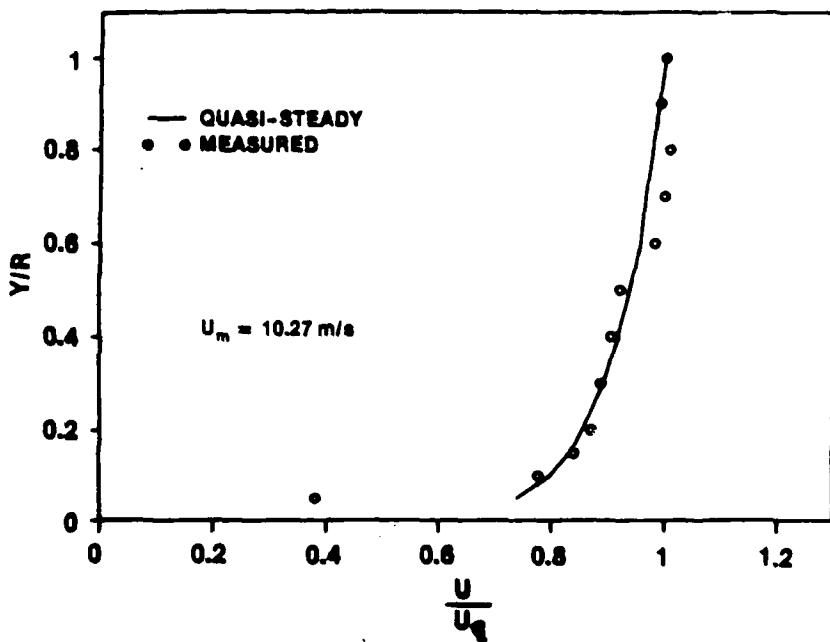
Figure IV-60k.   Velocity Profile at t = 3.000 s for $\ddot{X}$ = 6.1 m/s^2 and $\bar{U}_{m0}$ = 0
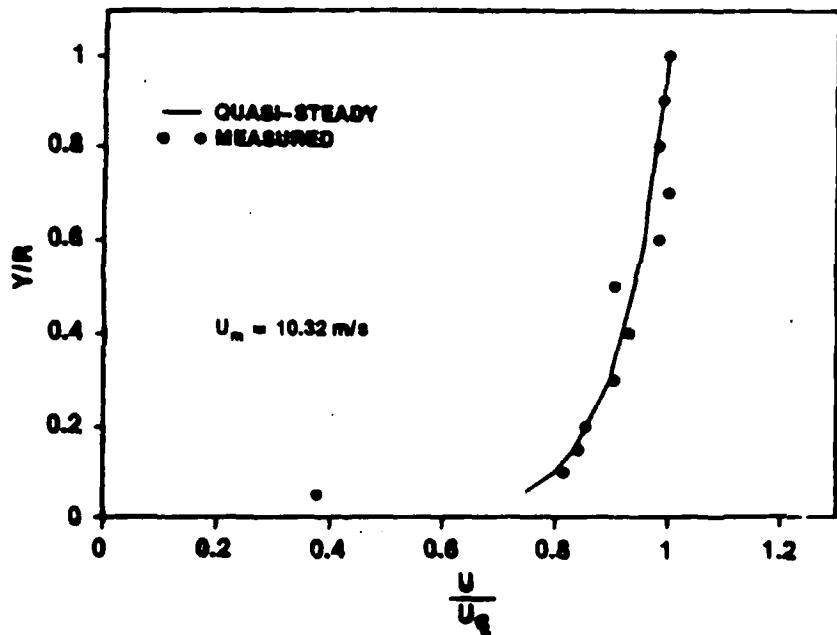
Figure IV-60l. Velocity Profile at t = 4.000 s for $\ddot{X}$ = 6.1 m/s^2 and $\bar{U}_{m0}$ = 0

tests are being planned to interrogate the details of the transition process by making measurements at one axial location alone but at high data acquisition rates.

From time 1.817 seconds to the end of the acceleration at approximately 2.5 seconds, and for the subsequent steady-state portion of the run, the velocity profiles followed the quasi-steady turbulent profile.

The third case of the ensemble-averaged tests will now be presented. This case was at an acceleration of 2.4 m/s^2 but this time with an initially turbulent flow at 1 m/s. As indicated by the curve for cross-sectional average velocity versus time for an individual run as given in figure IV-61, the acceleration was again constant over the complete transient. Excellent repeatability (within 0.5 percent) was again observed for the transient as documented in the ensemble-averaged U_m time history of figure IV-62 and the RMS of the runs in figure IV-63.

Figure IV-64 is the time history of the centerline velocity of a single run, which can be compared to the ensemble-averaged curve of figure IV-65. Both curves show an almost constant acceleration.

Around the time of 1.7 seconds, the fluctuations about the mean curve seems to increase. As shown in figure IV-66 for the RMS of the ensemble-averaged U_{cl} curve, the RMS decreases from a value of about 3.8 percent at the start of the transient at 0.75 second to an RMS of 1.6 percent at 1.3 seconds. It then increases to a value of approximately 3.0 percent at 1.7 seconds, maintains this value until
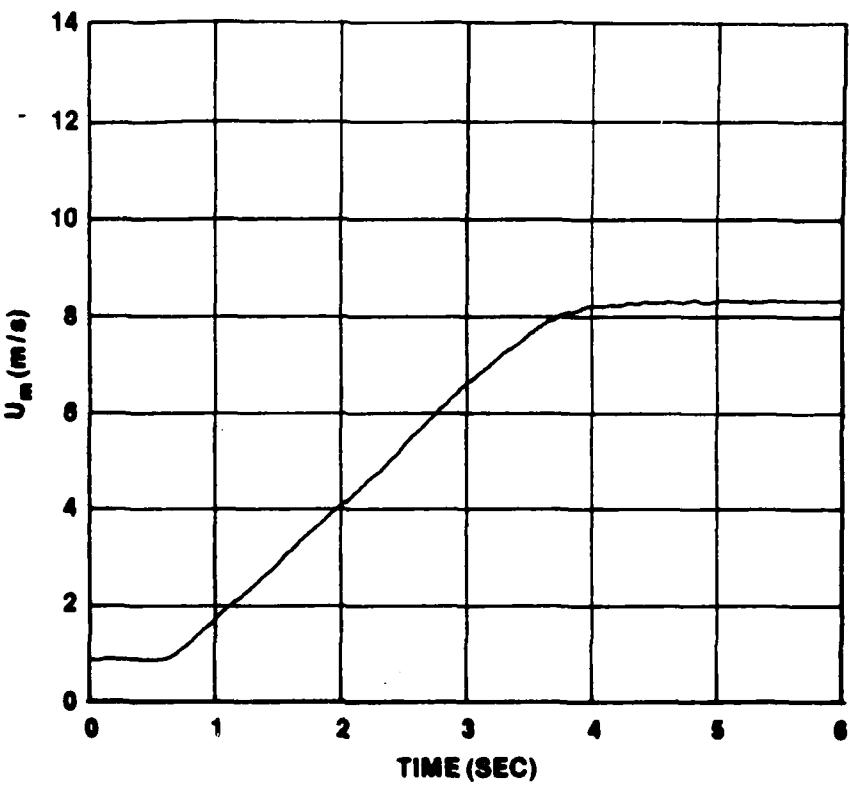
Figure IV-61. U_m vs t for One Typical Run at $\ddot{X} = 2.4$ m/s^2 and $\bar{U}_{m0} = 1$ m/s
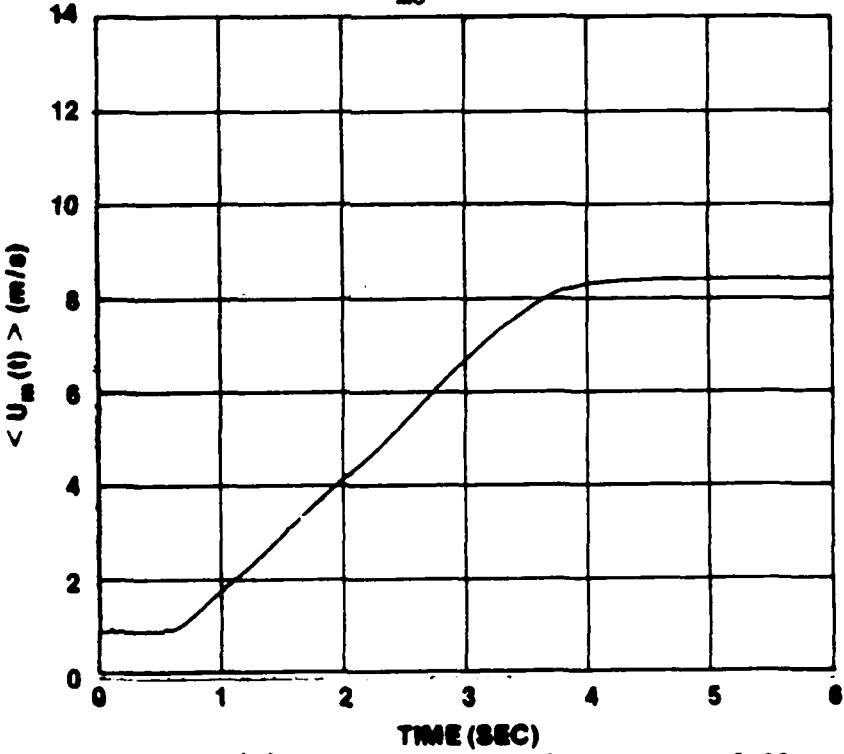
Figure IV-62. $\langle U_m(t) \rangle$ vs t for Ensemble Average of 20 Runs at $\ddot{X} = 2.4$ m/s^2 and $\bar{U}_{m0} = 1$ m/s

130
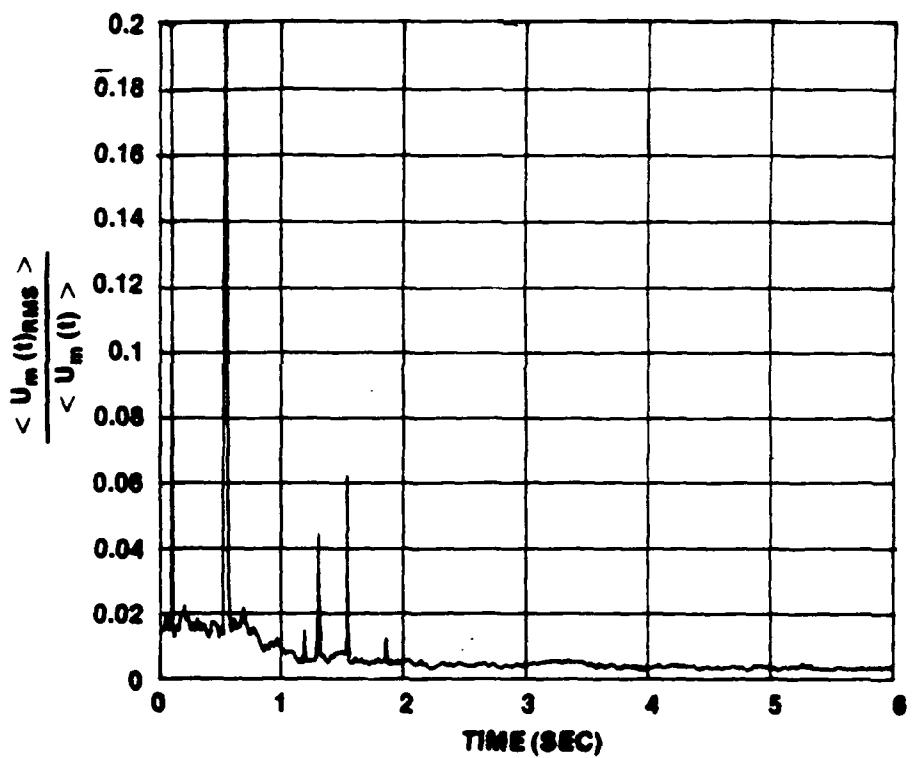
Figure IV-63.   RMS of $\langle U_m(t) \rangle$ vs t for 20 Runs at $\ddot{X} = 2.4$ m/s^2 and $\bar{U}_{m0} = 1$ m/s

Figure IV-64. U_{cl} vs t for One Typical Run at $\ddot{X} = 2.4$ m/s^2 and $\bar{U}_{m0} = 1$ m/s

131
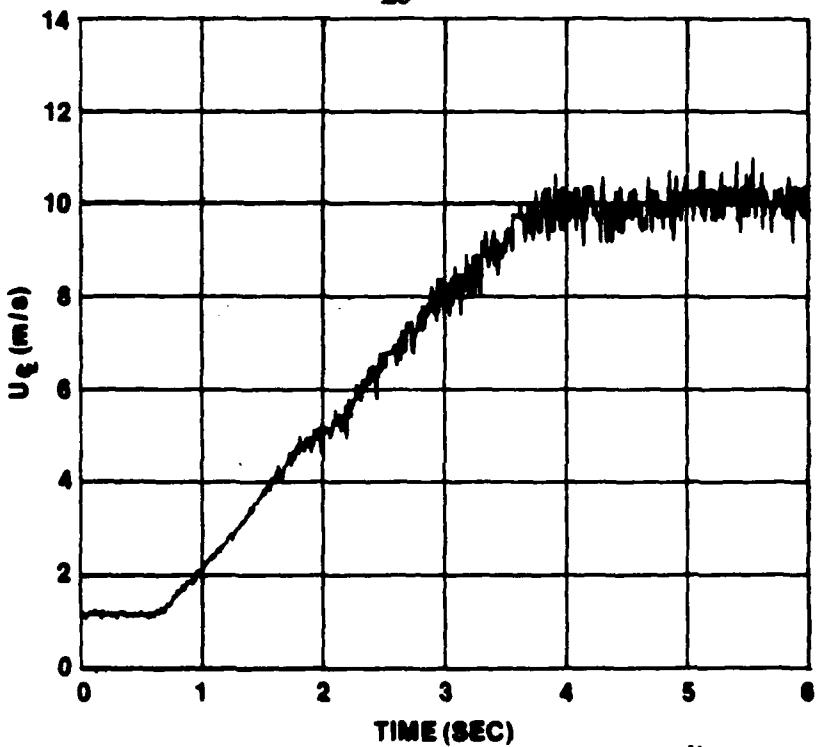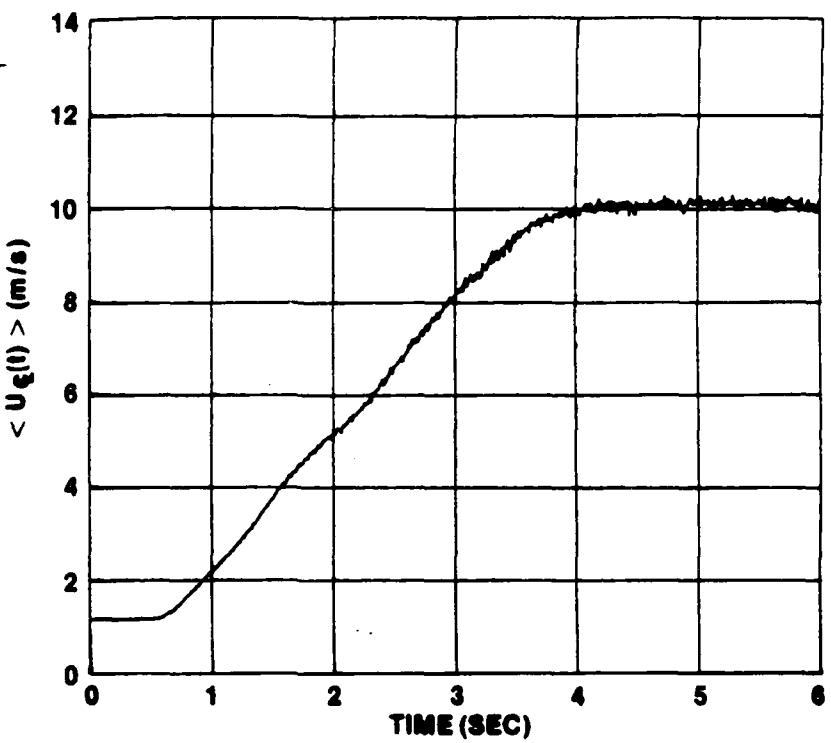
Figure IV-65. $\langle U_{c1}(t) \rangle$ vs t for Ensemble Average of 20 Runs at $\ddot{X} = 2.4$ m/s^2 and $\bar{U}_{m0} = 1$ m/s
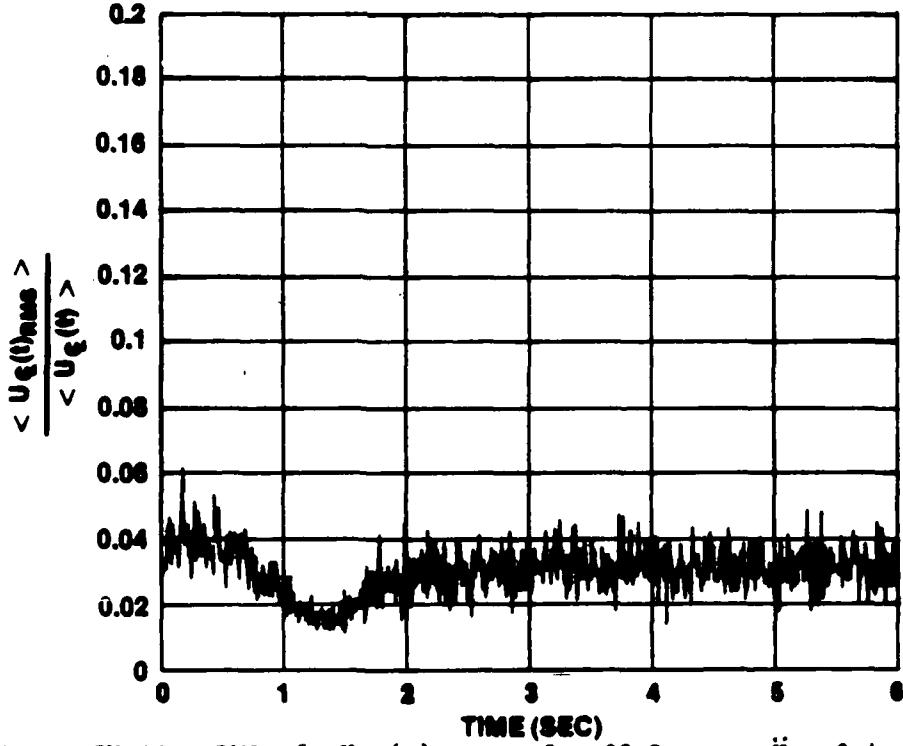
Figure IV-66. RMS of $\langle U_{c1}(t) \rangle$ vs t for 20 Runs at $\ddot{X} = 2.4$ m/s^2 and $\bar{U}_{m0} = 1$ m/s

132

the end of the acceleration at 4 seconds, and continues through the steady-state portion. This behavior was common to all Y/R locations. Unfortunately, since the flow is not constant, it is not possible to exactly identify the change in RMS values as to an indication of the change in turbulence intensity or to unrepeatable changes between runs. However, when the low value of RMS of the U_m curve (figure IV-63) is considered, it seems reasonable to associate the change in RMS with turbulent fluctuations. This phenomenon, as discussed further when the wall shear stress data are presented, appears to be associated with the acceleration tending to stabilize the flow. As mentioned in the transition-related portion of the results, relaminarization did not occur but would tend to occur at the beginning of the transient where the value of K_a was the highest.

The time-dependent velocity profiles for this case are presented in figures IV-67a through IV-671. The first profile is at 0.6 second which is the beginning of the transient. The profile is shown to follow the steady-state profile given as the solid line in the figures. Since the flow was always turbulent with no relaminarization, the curve for Szymanski's exact solution is not given in the following figures.

The next two profiles at times 0.8 and 1.0 seconds show that the measured profile follows the quasi-steady profile within 6.0 percent. The measured velocity profile from Y/R = 0.15 to the pipe centerline is greater than the quasi-steady profile. This increased velocity is compensated for by the lower than quasi-steady velocities for locations

133
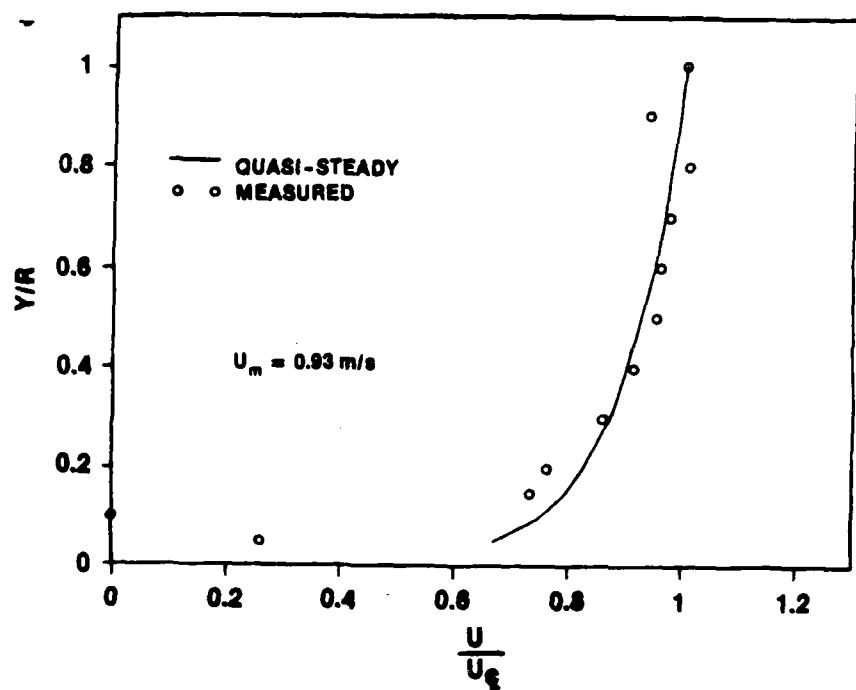
Figure 67a.   Velocity Profile at t = 0.600 s for $\ddot{X}$ = 2.4 m/s^2
and $\bar{U}_{m0}$ = 1 m/s
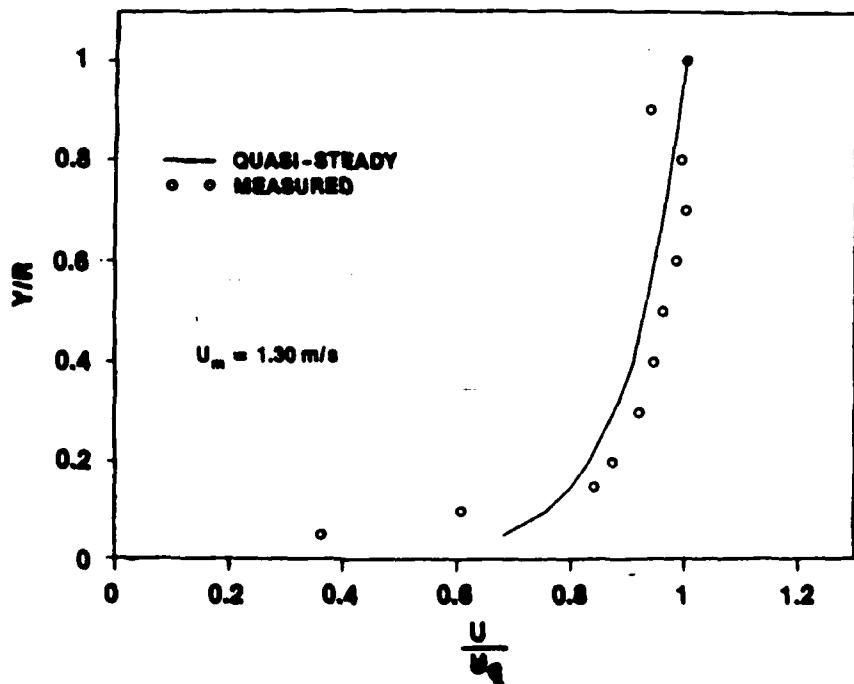
Figure 67b.   Velocity Profile at t = 0.800 s for $\ddot{X}$ = 2.4 m/s^2
and $\bar{U}_{m0}$ = 1 m/s

134
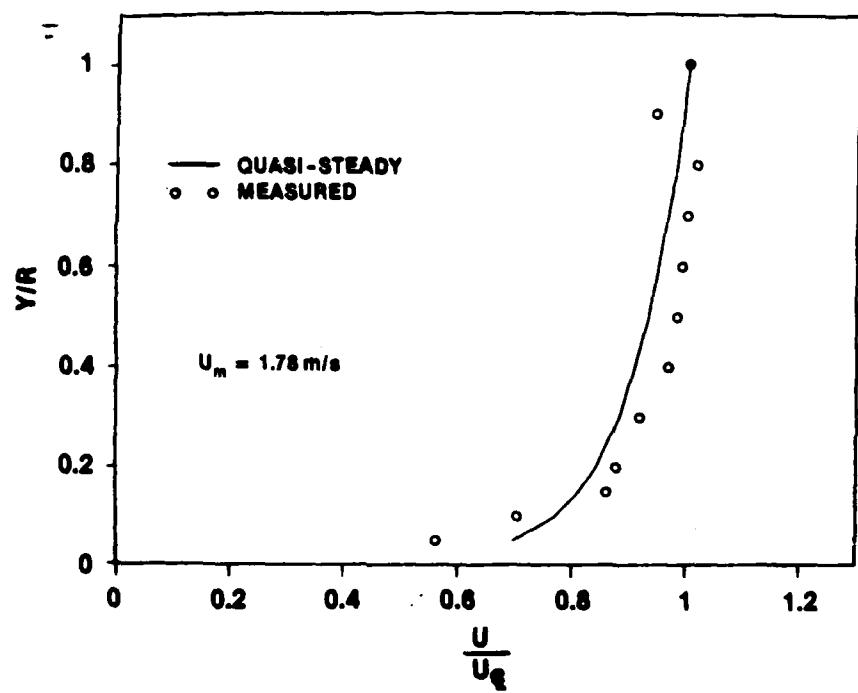
Figure 67c. Velocity Profile at t = 1.000 s for $\ddot{X}$ = 2.4 m/s^2
and $\bar{U}_{m0}$ = 1 m/s
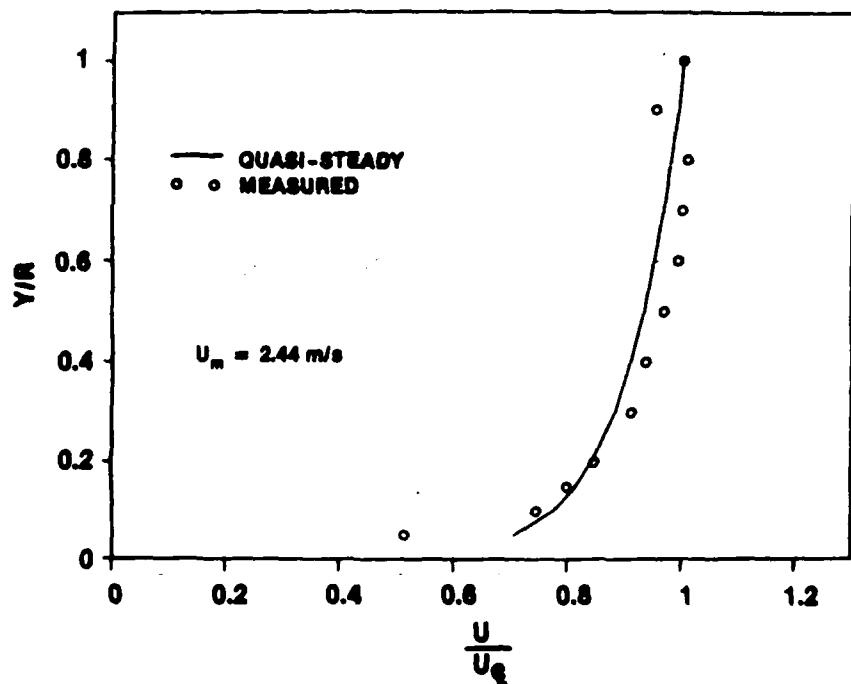
Figure 67d. Velocity Profile at t = 1.300 s for $\ddot{X}$ = 2.4 m/s^2
and $\bar{U}_{m0}$ = 1 m/s

135
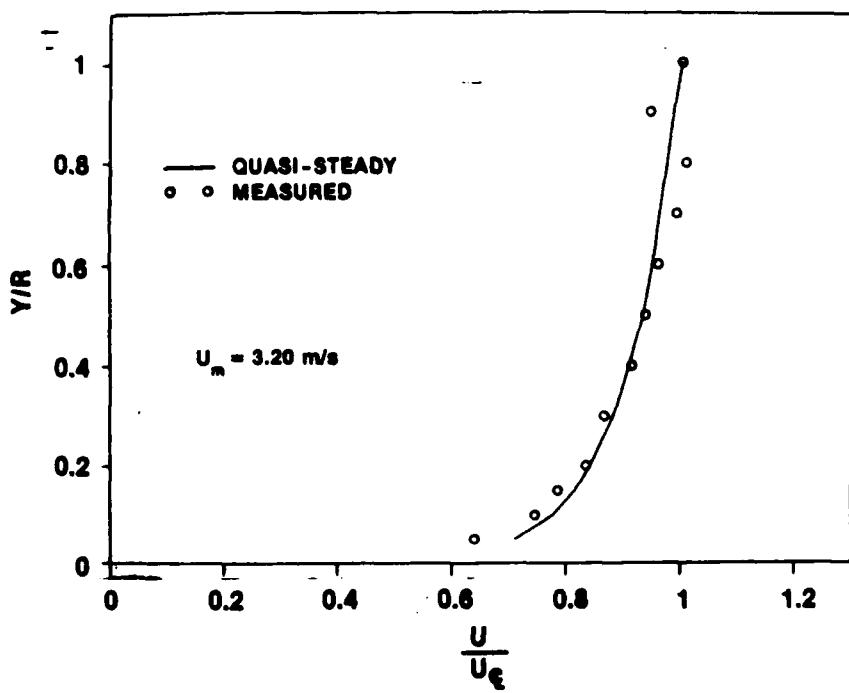
Figure 67e. Velocity Profile at t = 1.600 s for $\ddot{X}$ = 2.4 m/s^2
and $\bar{U}_{m0}$ = 1 m/s
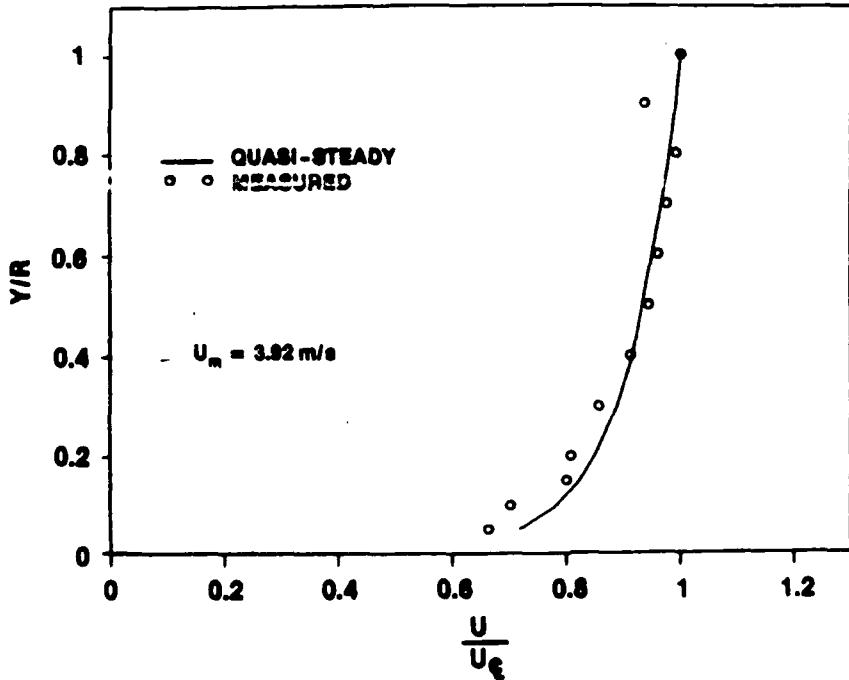
Figure 67f. Velocity Profile at t = 1.900 s for $\ddot{X}$ = 2.4 m/s^2
and $\bar{U}_{m0}$ = 1 m/s

136
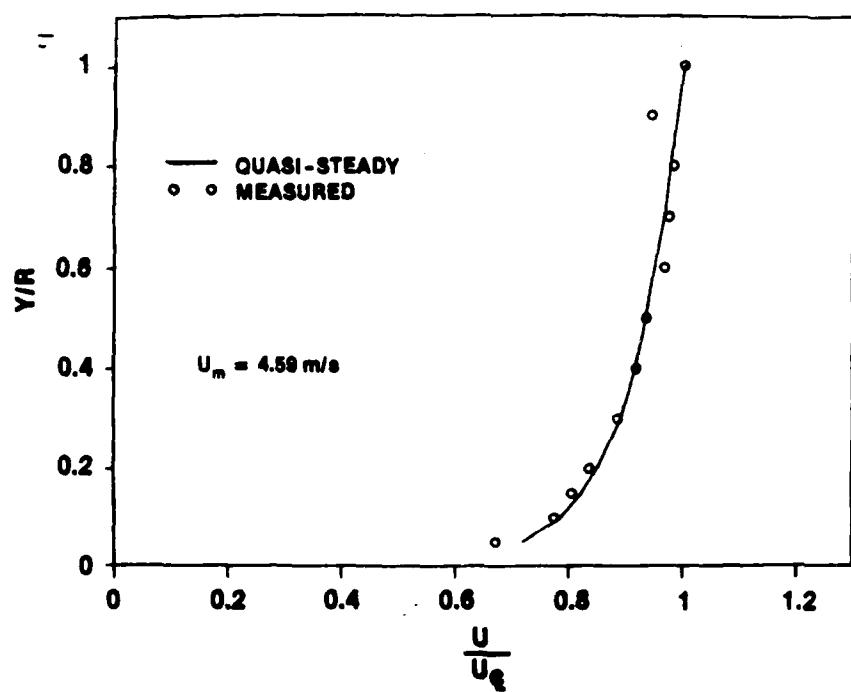
Figure 67g. Velocity Profile at t = 2.200 s for $\ddot{X} = 2.4$ m/s^2 and $\bar{U}_{m0} = 1$ m/s
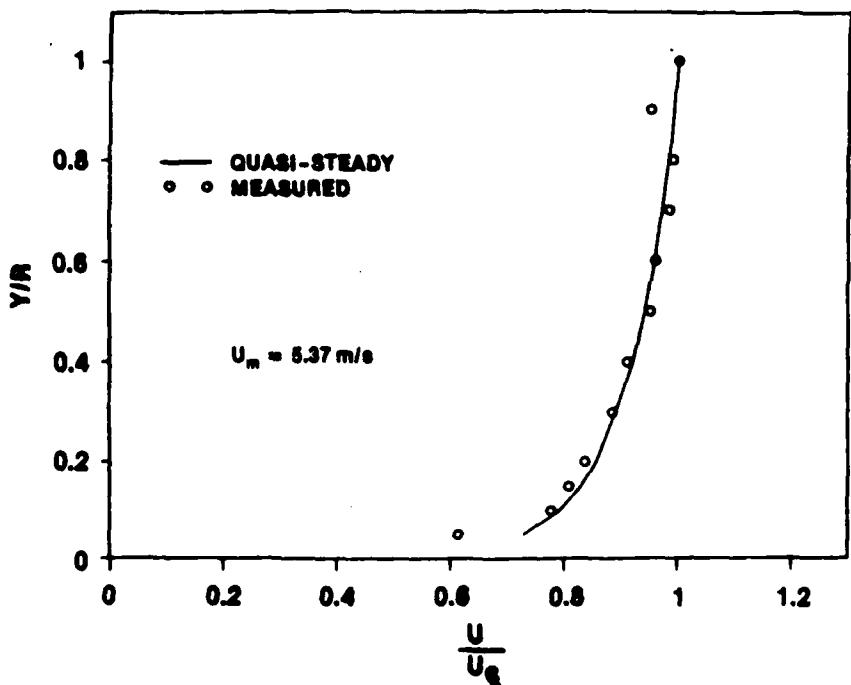
Figure 67h. Velocity Profile at t = 2.500 s for $\ddot{X} = 2.4$ m/s^2 and $\bar{U}_{m0} = 1$ m/s
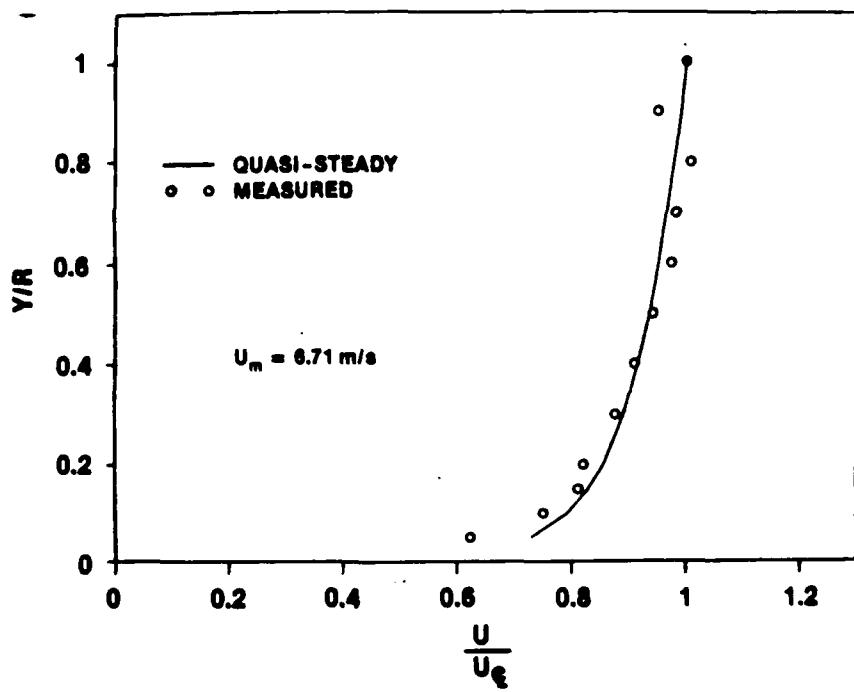
Figure 67i. Velocity Profile at t = 3.000 s for $\ddot{X}$ = 2.4 m/s^2
and $\bar{U}_{m0}$ = 1 m/s
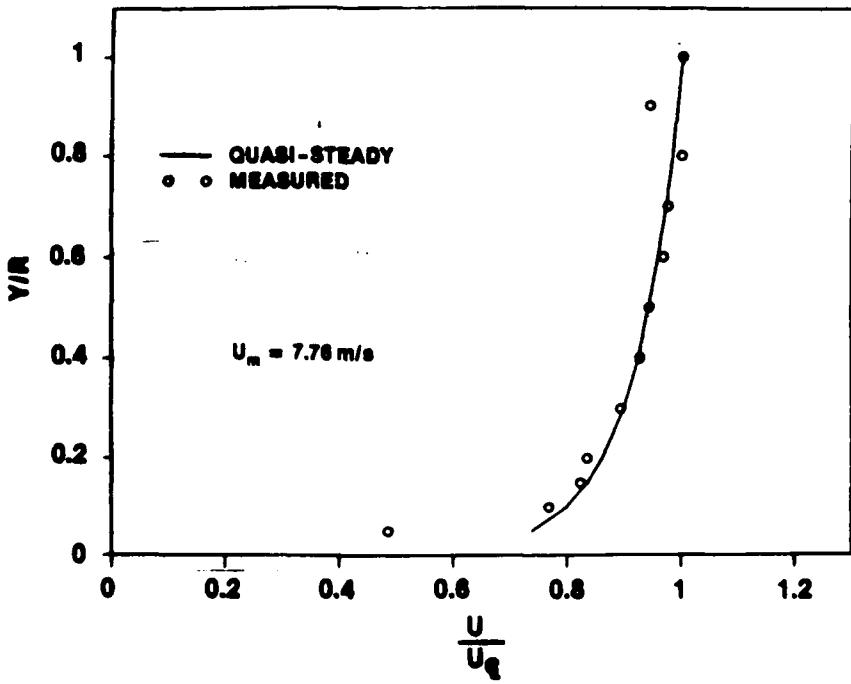
Figure 67j. Velocity Profile at t = 3.500 s for $\ddot{X}$ = 2.4 m/s^2
and $\bar{U}_{m0}$ = 1 m/s

138
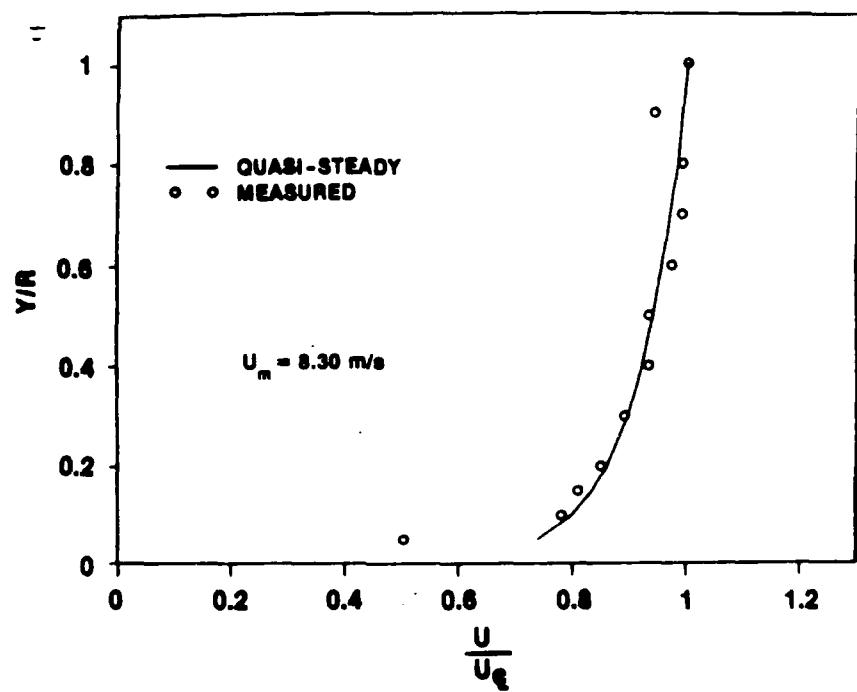
Figure 67k. Velocity Profile at $t = 4.000$ s for $\ddot{X} = 2.4$ m/s^2 and $\bar{U}_{m0} = 1$ m/s
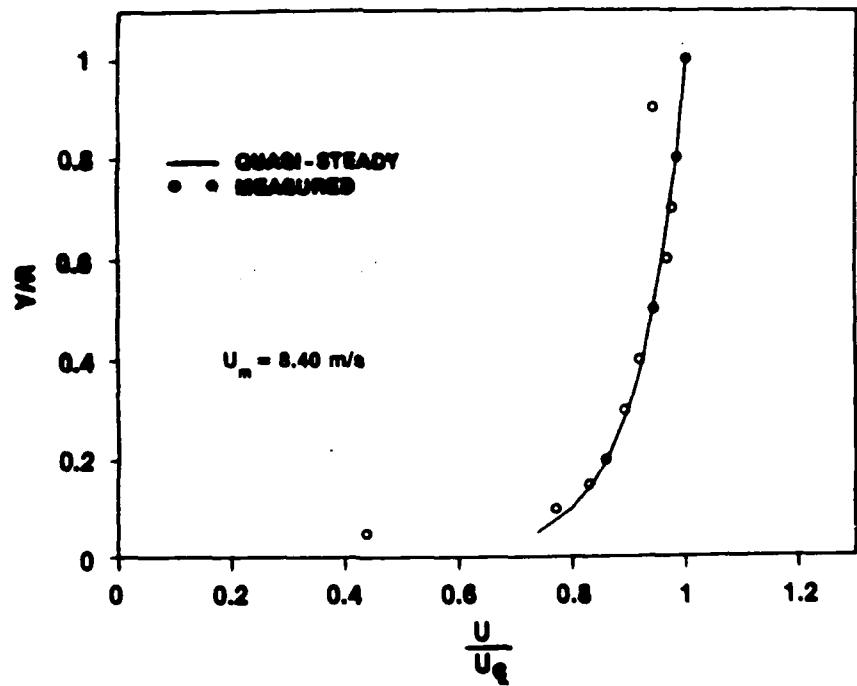
Figure 67l. Velocity Profile at $t = 5.000$ s for $\ddot{X} = 2.4$ m/s^2 and $\bar{U}_{m0} = 1$ m/s

between the wall and Y/R less than 0.15. Considering that the profiles agree within 6 percent, the two can be taken as identical for any practical purposes. For times of 1.3 seconds and beyond, the measured profiles and the quasi-steady profiles agree with one another. Note that the transient lasts until 4.0 seconds.

The fourth and final case tested was for the initially turbulent flow at 1 m/s undergoing an acceleration of 6.1 m/s^2. Figure IV-68 presents the U_m time history for the ensemble of 20 runs, while figure IV-69 gives the resulting RMS curve. Again, a highly repeatable (within 0.5 percent), constant acceleration transient was observed.

The ensemble-averaged curve for U_{cl} is given in figure IV-70 with the corresponding RMS curve in figure IV-71. For this case, U_{cl} is also very linear over the transient indicating a very constant acceleration of U_{cl}. Similar to the previous case at the acceleration of 2.4 m/s^2, the RMS value decreases from a value of about 3.8 percent at the start of the transient (t ≈ 0.5 second) to a minimum value of approximately 1.5 percent at 1.1 seconds. The value then increases to a value of about 3 percent at 1.4 seconds. These values of time and RMS are very similar to those of the previous case and are again thought attributable to the stabilizing effect of acceleration. As in case 3, this behavior was common to all Y/R locations.

Velocity profiles for this fourth case are shown in figures IV-72a through 72j. The first profile is given at 0.6 second, which

140
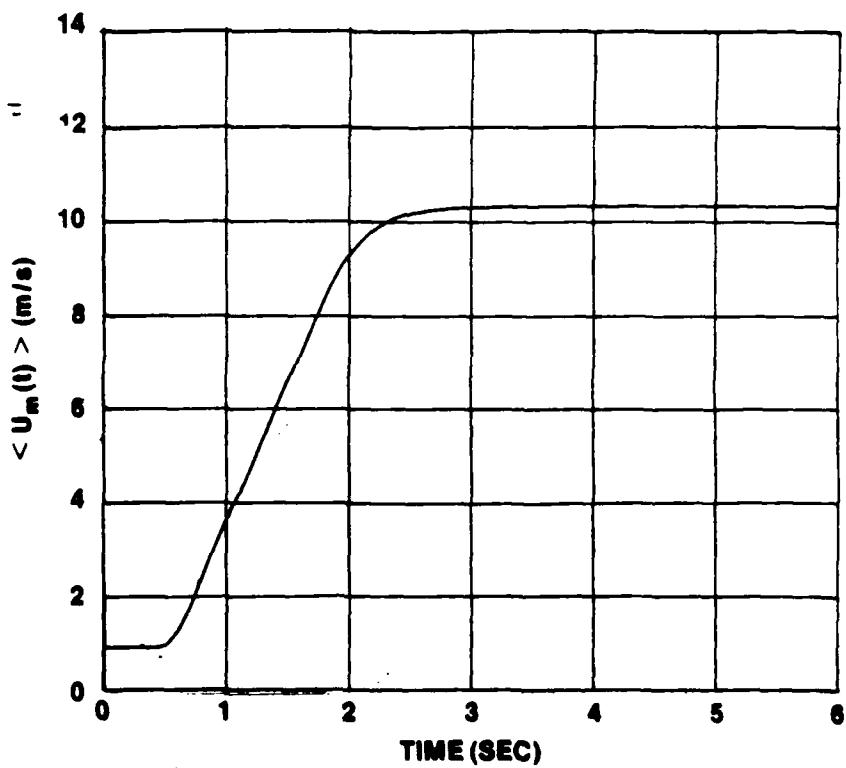
Figure IV-68. $\langle U_m(t) \rangle$ vs t for Ensemble Average of 20 Runs at
$\ddot{X} = 6.1$ m/s^2 and $\bar{U}_{m0} = 1$ m/s
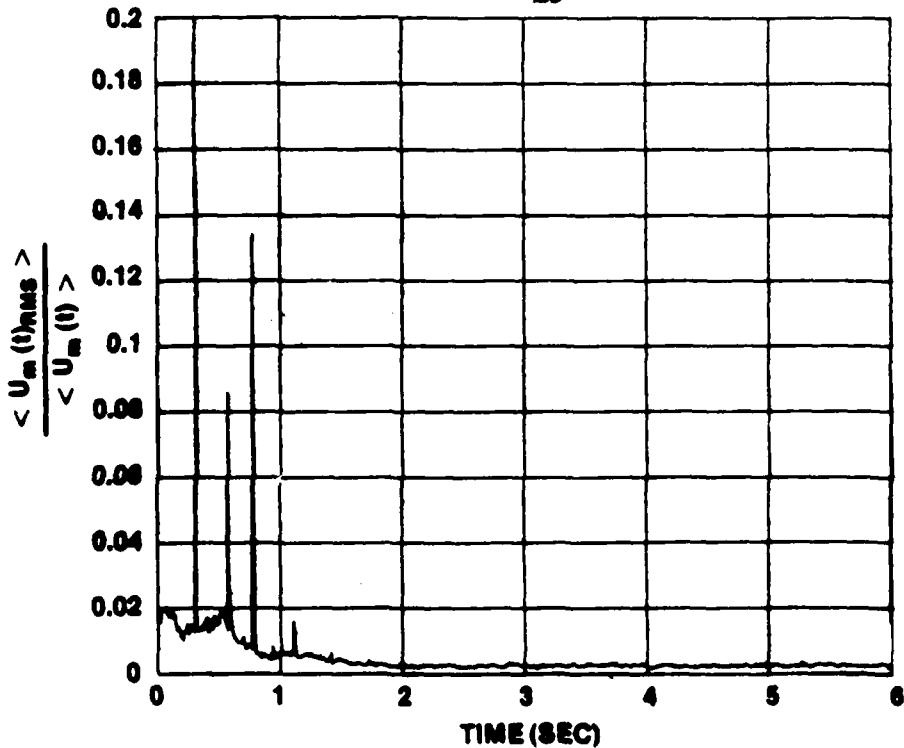
Figure IV-69. RMS of $\langle U_m(t) \rangle$ vs t for 20 Runs at
$\ddot{X} = 6.1$ m/s^2 and $\bar{U}_{m0} = 1$ m/s
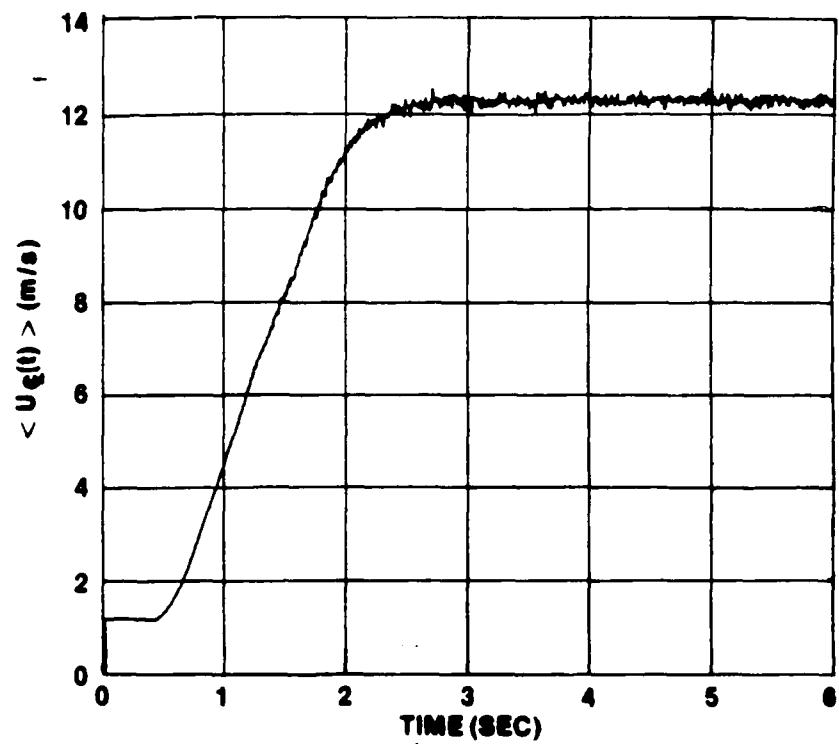
Figure IV-70. $\langle U_{c1}(t) \rangle$ vs t for Ensemble Average of 20 Runs at $\ddot{X} = 6.1$ m/s^2 and $\bar{\bar{U}}_{m0} = 1$ m/s
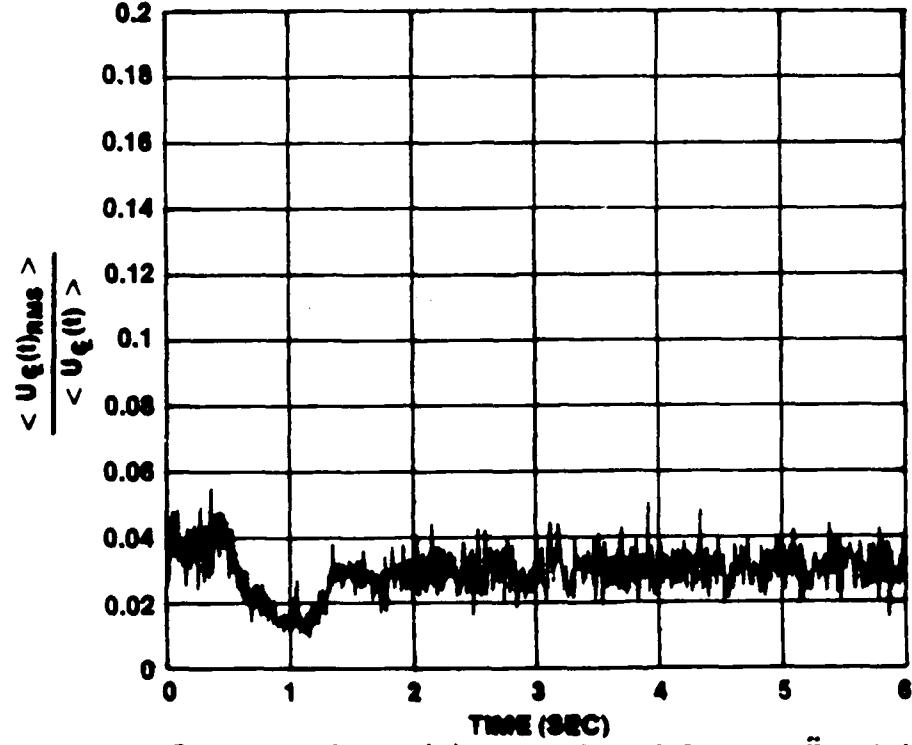
Figure IV-71. RMS of $\langle U_{c1}(t) \rangle$ vs t for 20 Runs at $\ddot{X} = 6.1$ m/s^2 and $\bar{\bar{U}}_{m0} = 1$ m/s

142
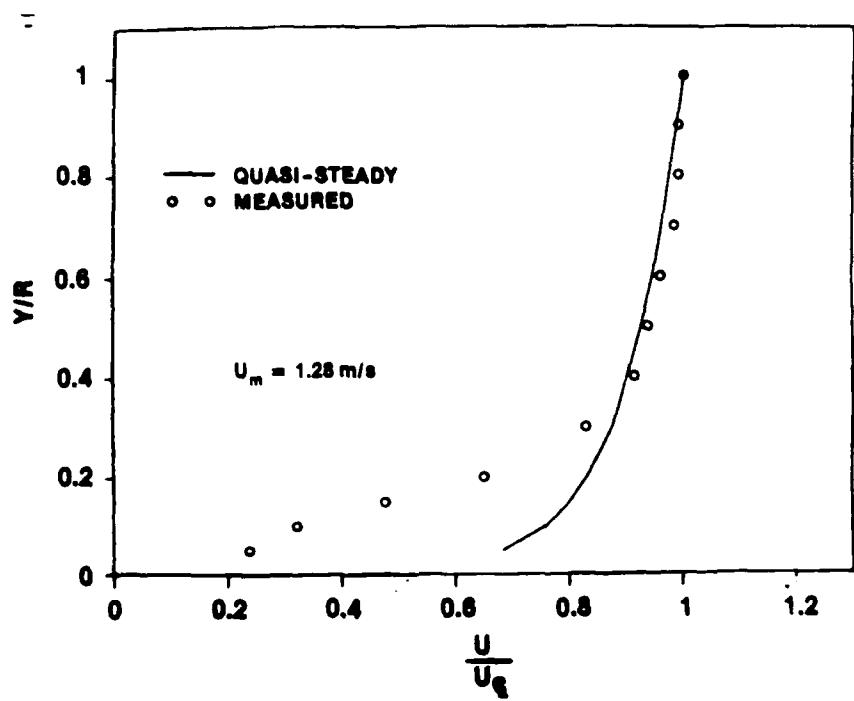
Figure IV-72a. Velocity Profile at t = 0.600 s for $\ddot{X}$ = 6.1 m/s^2
and $\bar{U}_{m0}$ = 1 m/s
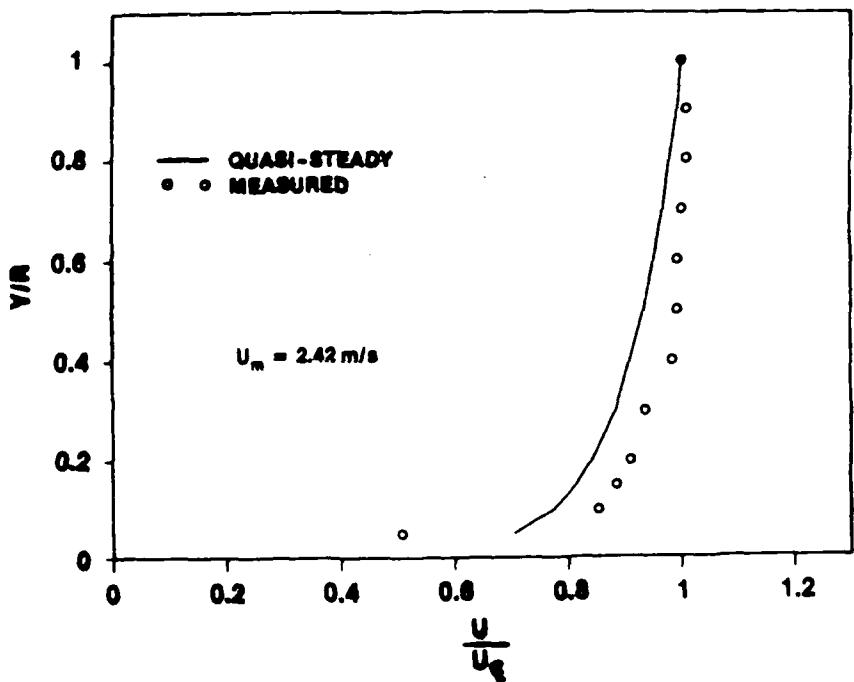
Figure IV-72b. Velocity Profile at t = 0.800 s for $\ddot{X}$ = 6.1 m/s^2
and $\bar{U}_{m0}$ = 1 m/s

143
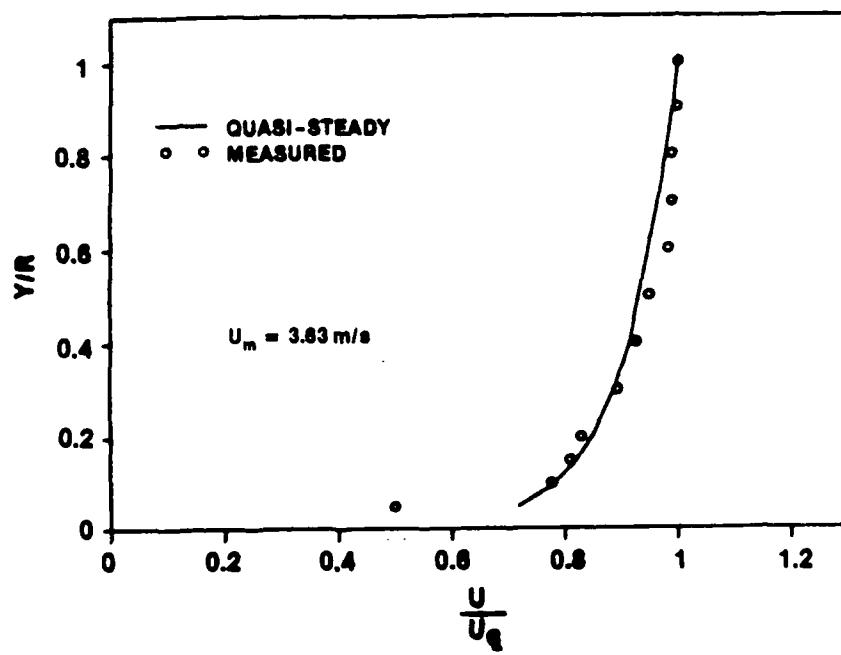
Figure IV-72c. Velocity Profile at t = 1.000 s for $\ddot{X}$ = 6.1 m/s^2
and $\bar{U}_{m0}$ = 1 m/s
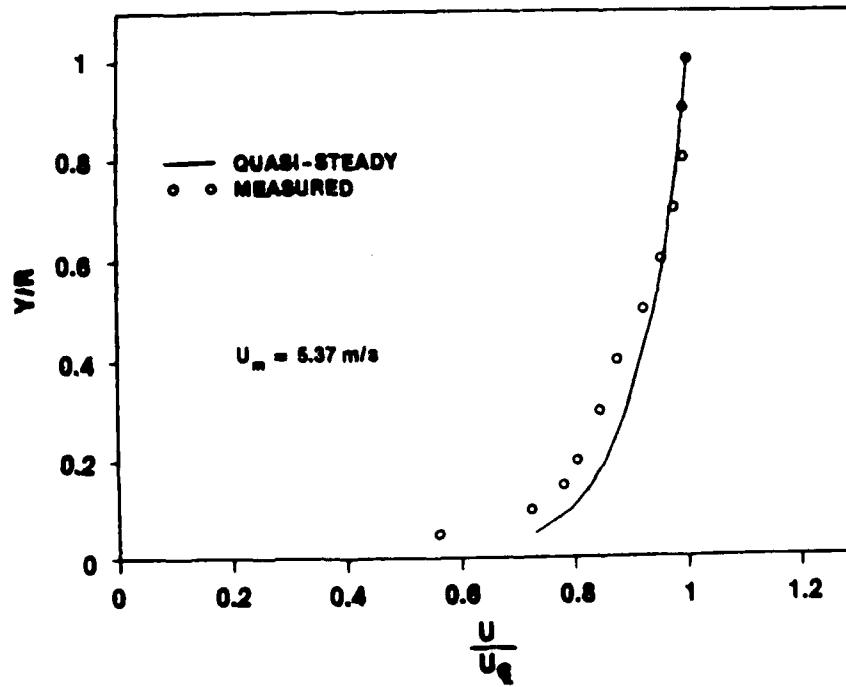
Figure IV-72d. Velocity Profile at t = 1.300 s for $\ddot{X}$ = 6.1 m/s^2
and $\bar{U}_{m0}$ = 1 m/s

144
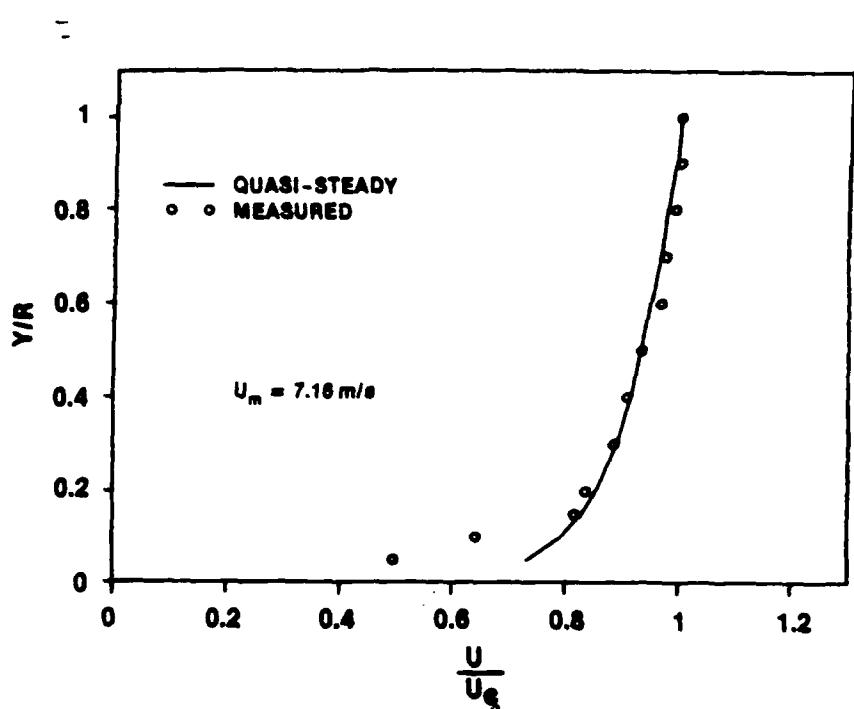
Figure IV-72e. Velocity Profile at t = 1.600 s for $\ddot{X} = 6.1$ m/s^2
and $\bar{U}_{m0} = 1$ m/s
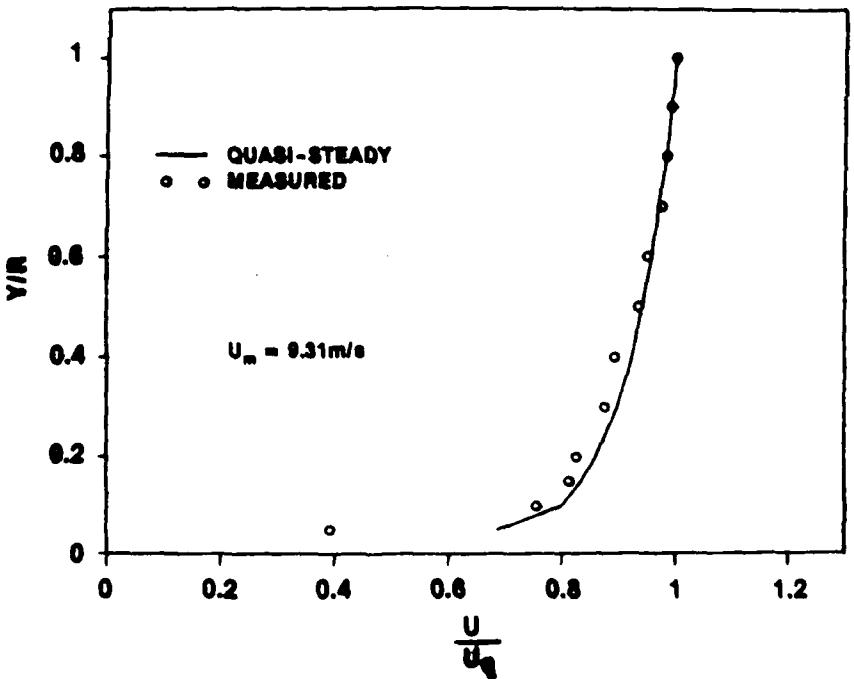
Figure IV-72f. Velocity Profile at t = 2.000 s for $\ddot{X} = 6.1$ m/s^2
and $\bar{U}_{m0} = 1$ m/s
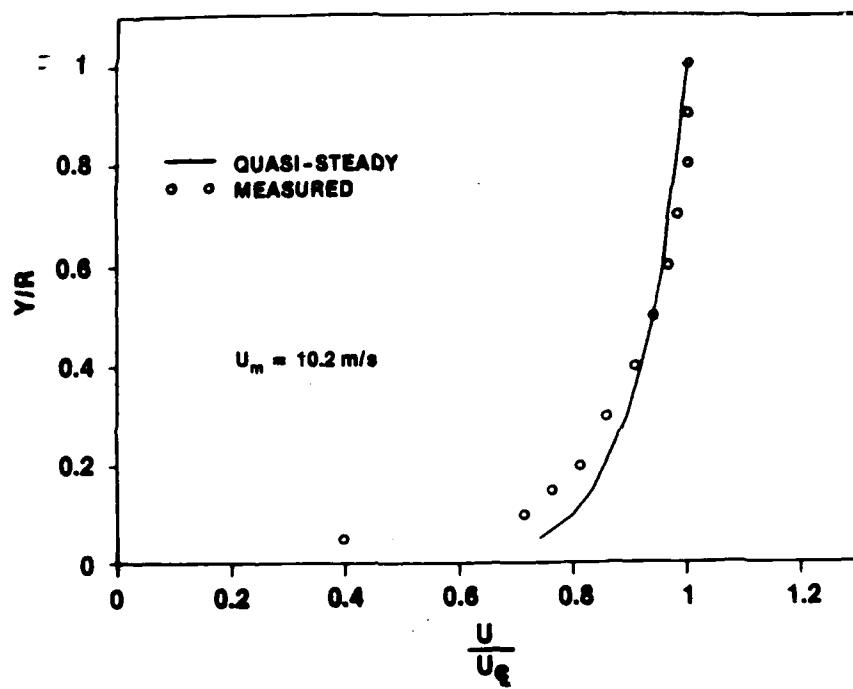
Figure IV-72g. Velocity Profile at t = 2.500 s for $\ddot{X}$ = 6.1 m/s^2
and $\bar{U}_{m0}$ = 1 m/s
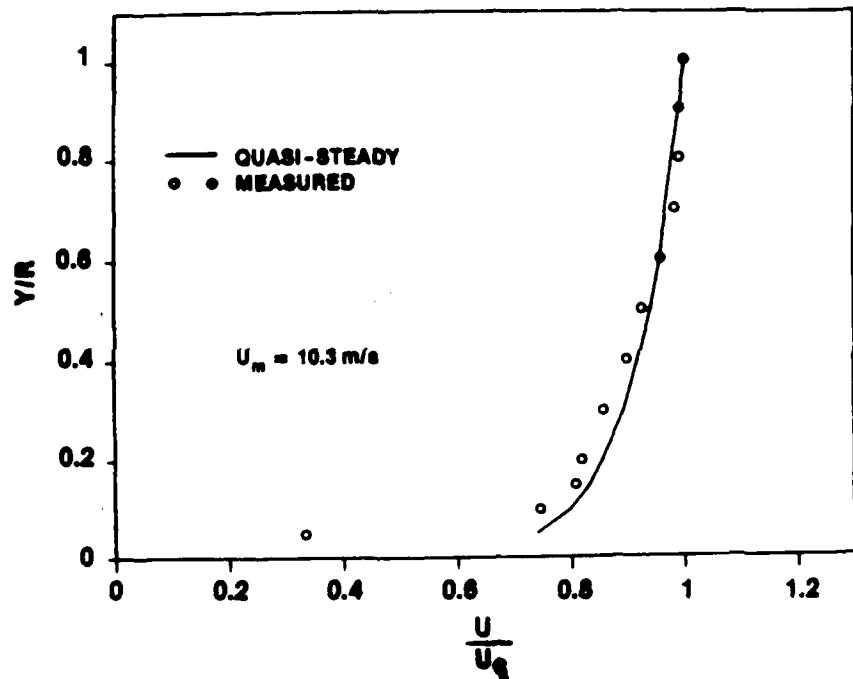
Figure IV-72h. Velocity Profile at t = 3.000 s for $\ddot{X}$ = 6.1 m/s^2
and $\bar{U}_{m0}$ = 1 m/s

146
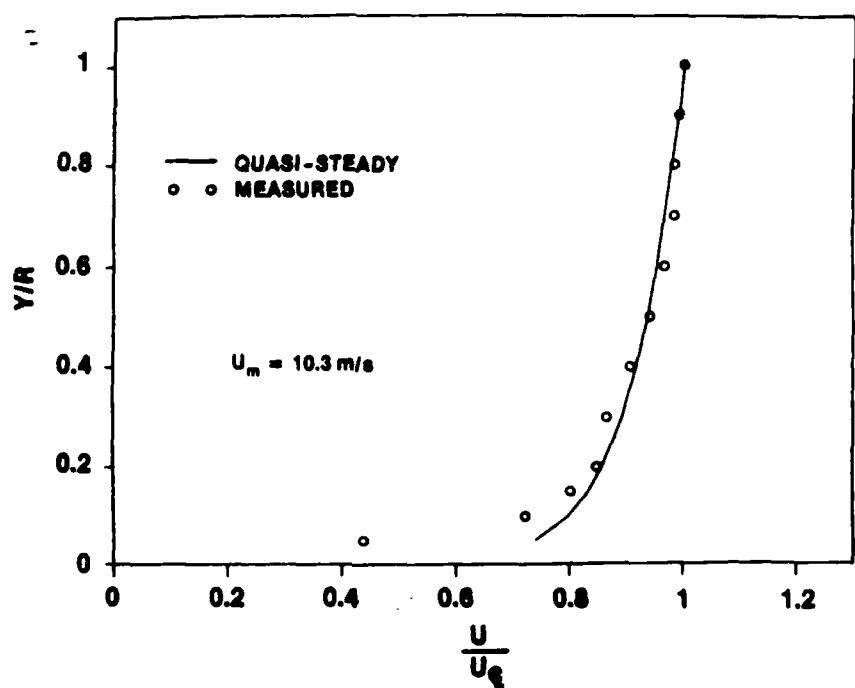
Figure IV-72i. Velocity Profile at $t = 4.000$ s for $\ddot{X} = 6.1$ m/s^2
and $\bar{U}_{m0} = 1$ m/s
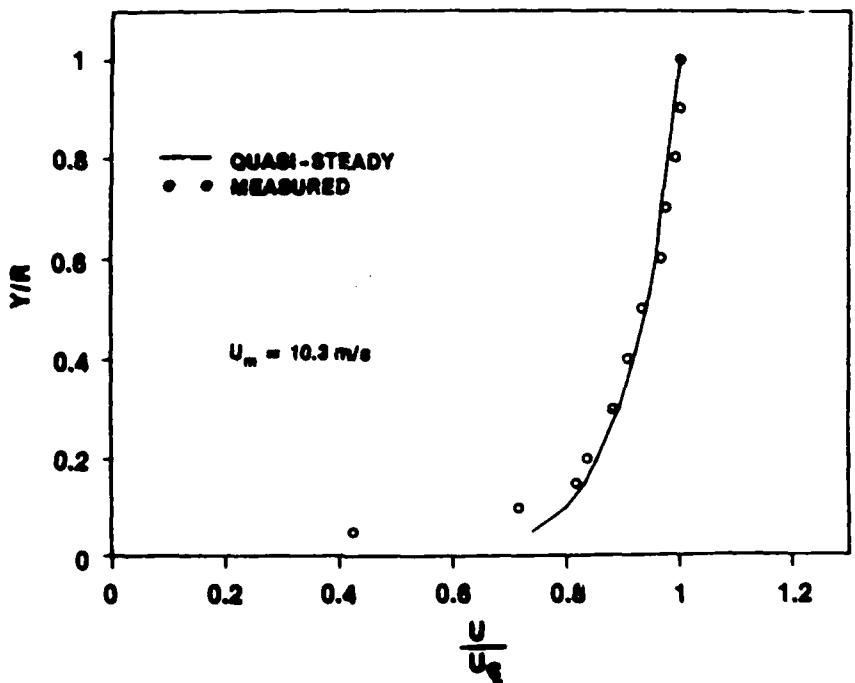
Figure IV-72j. Velocity Profile at $t = 5.000$ s for $\ddot{X} = 6.1$ m/s^2
and $\bar{U}_{m0} = 1$ m/s

147

is about 0.1 second after the start of the acceleration. The measured profile is shown to follow exactly the quasi-steady one for $Y/R = 0.4$ to 1.0. Below $Y/R = 0.4$, the measured velocities are substantially lower than the quasi-steady profile. Since continuity must be maintained, it is obvious that these measured values are in error. This inaccuracy is most probably due to the LDV not being set optimally for the very low values of velocity seen here. The next profile is at 0.8 second and shows the measured values to agree within 8.5 percent, still very close. For times of 1.0 second to the end of the transient at 2.3 seconds and for the remainder of the steady-state portion of the run, the measured and quasi-steady velocity profiles were again essentially identical.

The important conclusions resulting from the above mentioned velocity profile data are: (1) for acceleration from rest, the velocity profile prior to transition agrees with that given by Szymanski's exact laminar solution while after transition, the profile is the quasi-steady turbulent one based on the universal law-of-the-wall; (2) at transition, the velocity profile changes almost instantaneously; (3) for accelerations from an initially turbulent flow, the velocity profile follows the quasi-steady turbulent one throughout the transient; and (4) for an initially turbulent flow, the acceleration tends to stabilize the flow, as evidenced by a reduced turbulence intensity, at least during the beginning of the transient where K_a has the largest values.

148

Transient Turbulence Intensities

As discussed in the previous section, the center beam of the LDV was eliminated because including it resulted in additional scattered light and noise, which reduced the valid data rate output of the LDV system. This in turn decreased the quality of the measurement of the axial velocity component during the transient runs. The axial component was considered the most important measurement for this study. A second reason was that, based on the results from some of the initial ensemble-averaged runs for case 1, it was obvious that 20 runs was inadequate for accurate measurements of Reynolds stress as obtained from the RMS of the ensemble. More than 20 runs would have been too time-consuming for the present test plan. As discussed later, the other measurements taken lead to a conclusion concerning the Reynolds stress, which eliminates the need for direct measurement. Therefore, the only turbulence measurements made were of the time-dependent turbulence intensities.

In this section, time-dependent turbulence intensity distributions are given for the two ensemble-averaged cases that started from an initially turbulent flow, cases 3 and 4. Each of the figures have the instantaneous value of U_m included. Additionally, the turbulence intensity obtained by Laufer [37] at the steady-state center-line velocity Reynolds number of 500,000, is also given. Laufer's data were shown in the steady-state portion of the results to be representative of the turbulence intensities found in the present test section.

149

Figures IV-73a through IV-73h give the turbulence intensity

distribution for the third case of the ensemble-averaged runs. The

first distribution is near the beginning of the transient at a time of

1.0 second. Six additional distributions are given next covering the

range of the transient, which lasted until time 4.0 seconds. Finally,

one last figure is at 5.0 seconds.

Similarly for the fourth case, turbulence intensities are shown

in figures IV-74a through IV-74e. Here, the first distribution is

also near the start of the transient at 1.0 second. Two other

distributions before the end of the transient at times 1.6 and 2.0

seconds follow. The remaining two figures are at times of 2.5 and 5.0

seconds.

It is interesting to note that in figure IV-73a (case 3 at 1.0

second) the measured values, for the most part, tend to be lower than

those of Laufer. Likewise (and even more so), figure IV-74a for case

4 at 1.0 second at all locations except the closest point near the

wall have the measured data lower than Laufer's curve. No such trend

is observed at any of the other times presented. As with the RMS

curves of the local velocities for these two cases, the present

results indicate again, that, at the onset of the transient, the

acceleration tends to stabilize the flow.

At the other times for the two cases considered, the measured

turbulence intensities agree relatively closely with Laufer's data.

Virtually all of the measured points were within 50 percent of the

values given by Laufer. This is very close considering the low
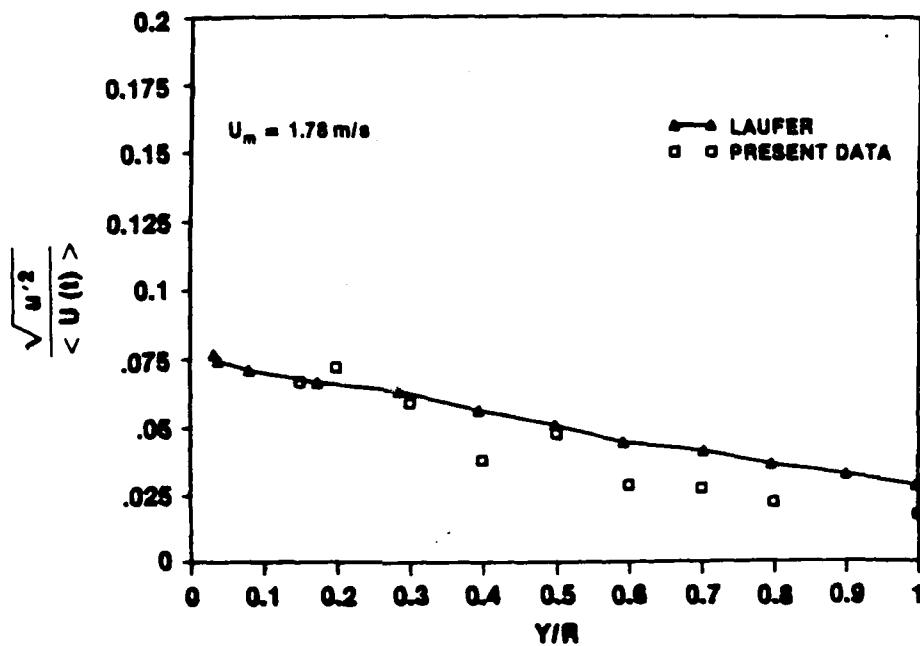
Figure IV-73a. Turbulence Intensity Profile at t = 1.000 s for $\ddot{X}$ = 2.4 m/s^2 and $\bar{U}_{m0}$ = 1 m/s
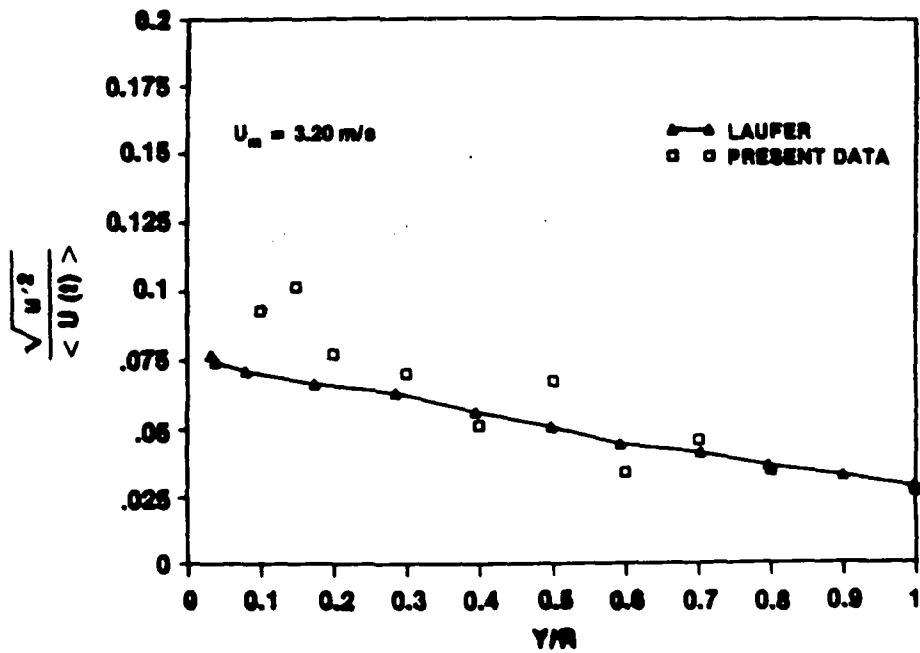
Figure IV-73b. Turbulence Intensity Profile at t = 1.600 s for $\ddot{X}$ = 2.4 m/s^2 and $\bar{U}_{m0}$ = 1 m/s

151
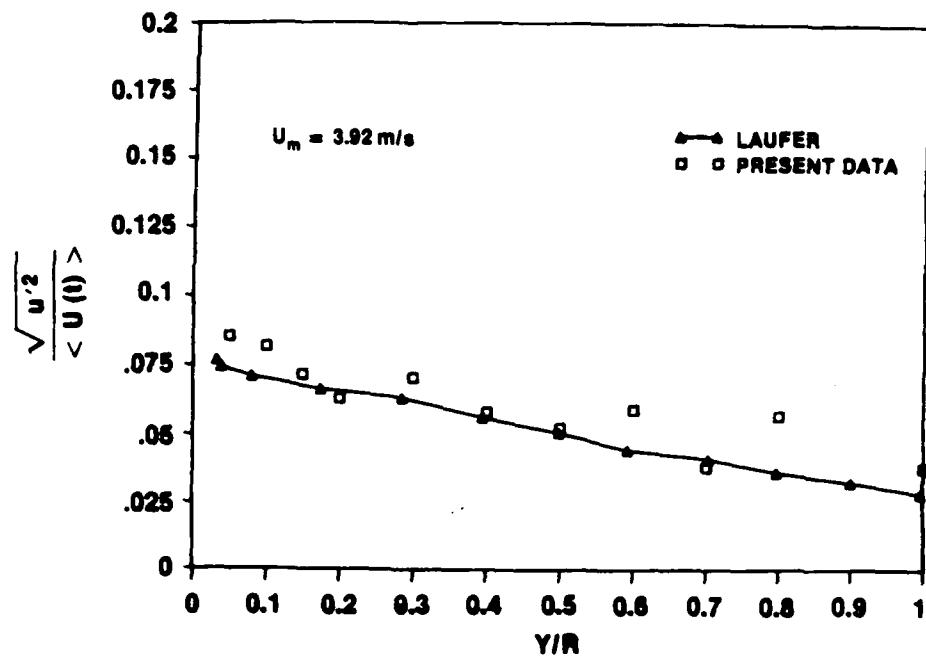
Figure IV-73c.   Turbulence Intensity Profile at t = 1.900 s for
$\ddot{X} = 6.1$ m/s^2 and $\bar{U}_{m0} = 1$ m/s
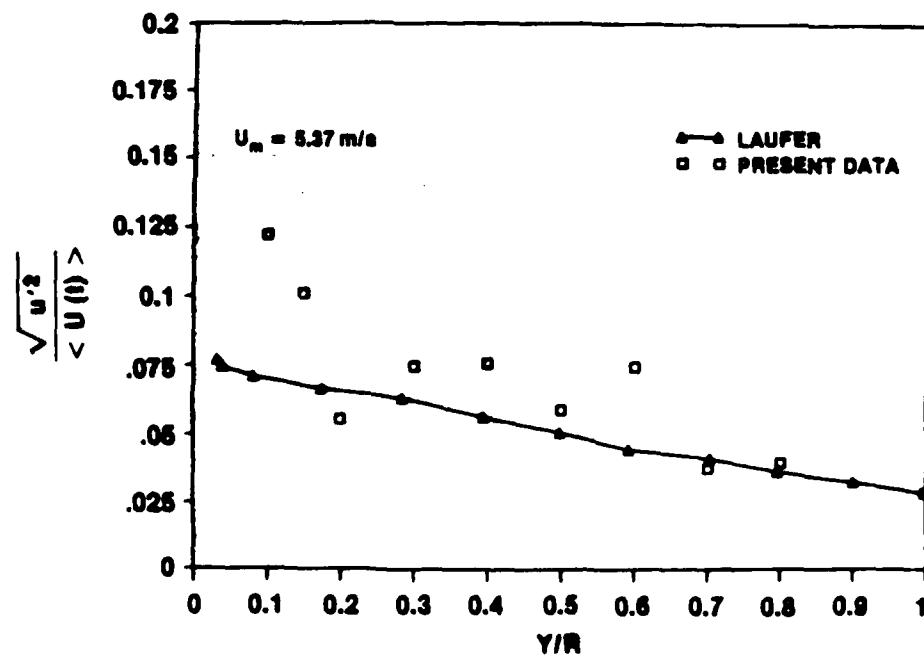
Figure IV-73d.   Turbulence Intensity Profile at t = 2.500 s for
$\ddot{X} = 2.4$ m/s^2 and $\bar{U}_{m0} = 1$ m/s

152
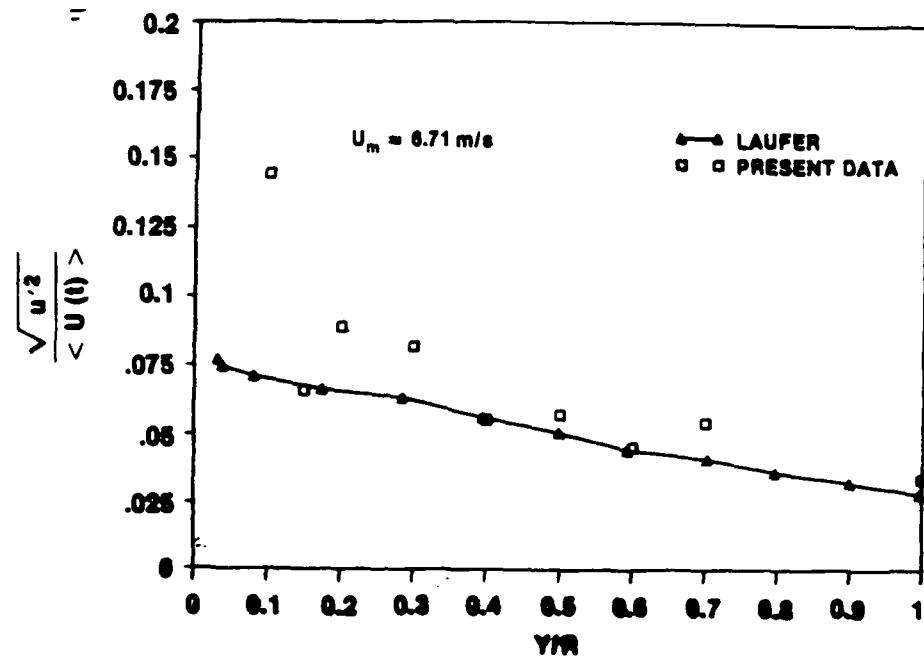
Figure IV-73e. Turbulence Intensity Profile at t = 3.000 s for
$\ddot{X}$ = 2.4 m/s^2 and $\bar{U}_{m0}$ = 1 m/s
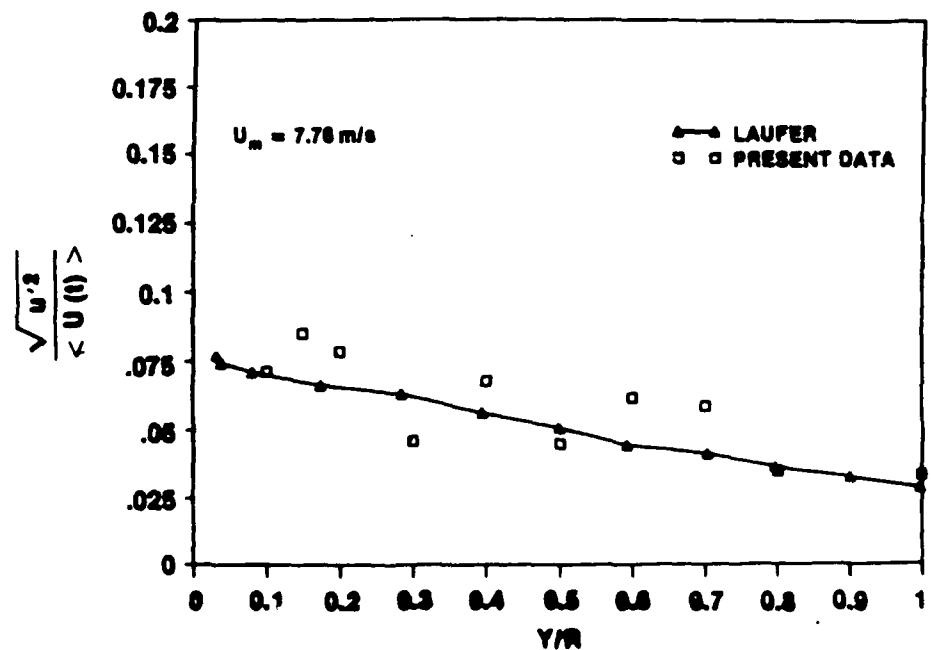
Figure IV-73f. Turbulence Intensity Profile at t = 3.500 s for
$\ddot{X}$ = 2.4 m/s^2 and $\bar{U}_{m0}$ = 1 m/s

153
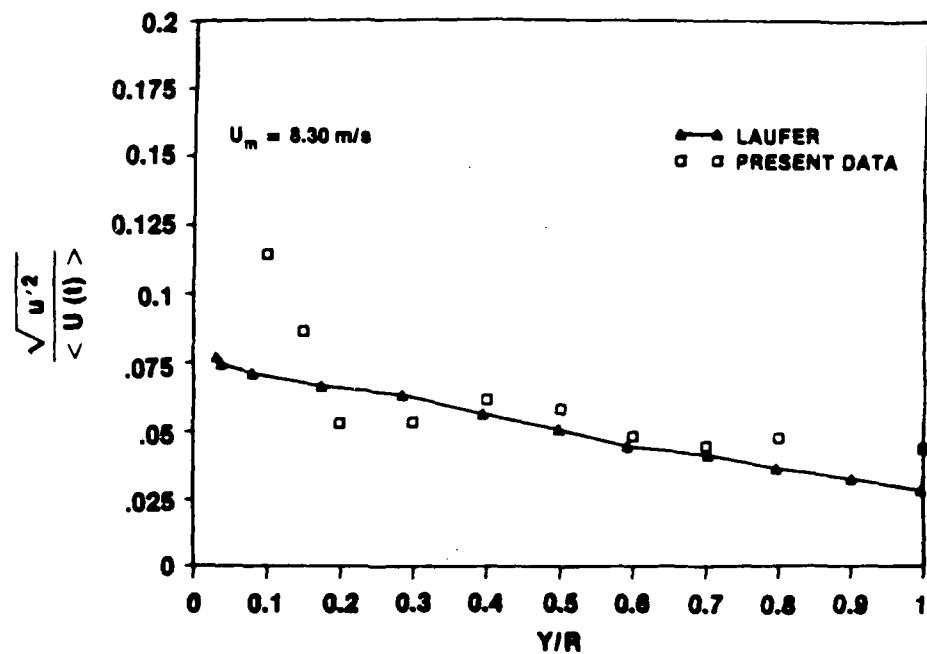
Figure 73g. Turbulence Intensity Profile at t = 4.000 s for $\ddot{X} = 2.4$ m/s^2 and $\bar{U}_{m0} = 1$ m/s
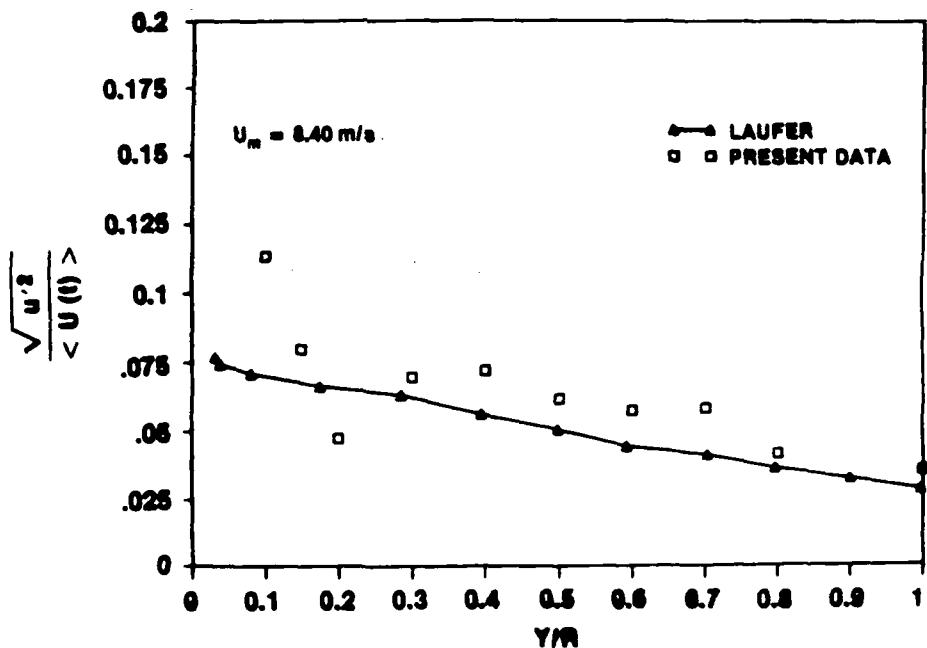
Figure IV-73h. Turbulence Intensity Profile at t = 5.000 s for $\ddot{X} = 2.4$ m/s^2 and $\bar{U}_{m0} = 1$ m/s
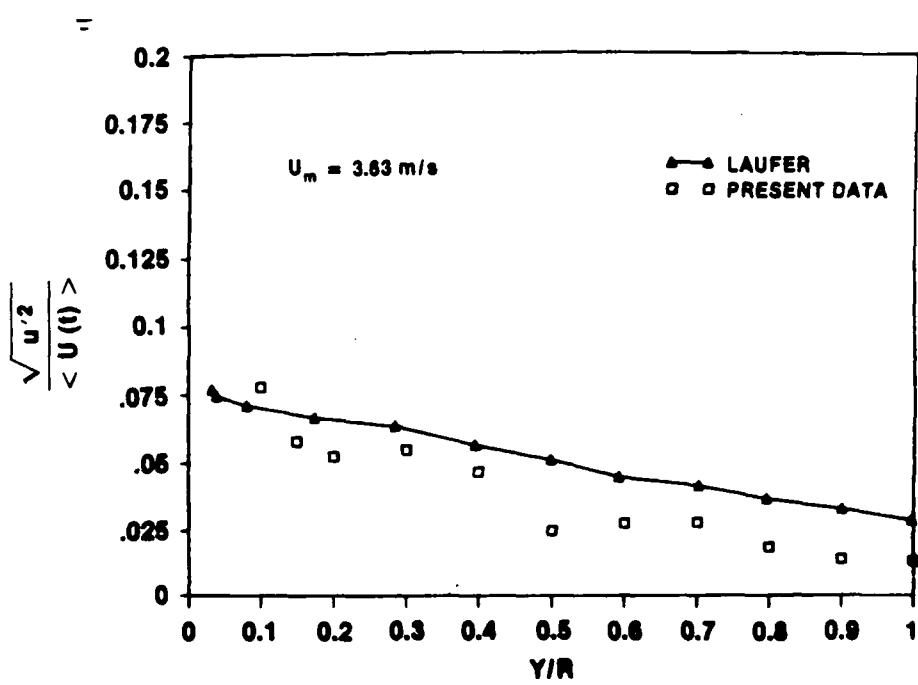
Figure IV-74a. Turbulence Intensity Profile at t = 1.000 s for
$\ddot{X}$ = 6.1 m/s^2 and $\ddot{U}_{m0}$ = 1 m/s
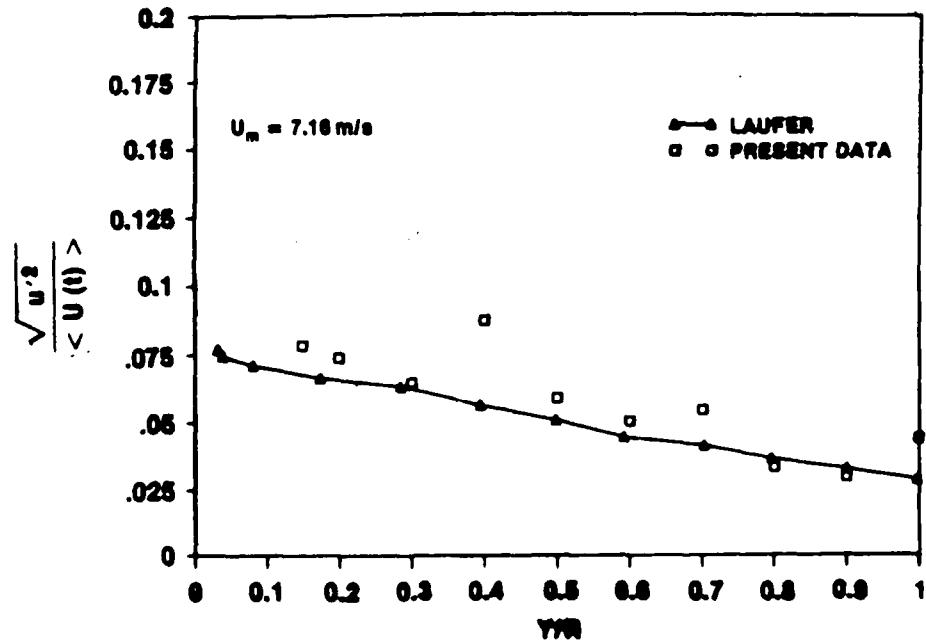
Figure IV-74b. Turbulence Intensity Profile at t = 1.600 s for
$\ddot{X}$ = 6.1 m/s^2 and $\ddot{U}_{m0}$ = 1 m/s
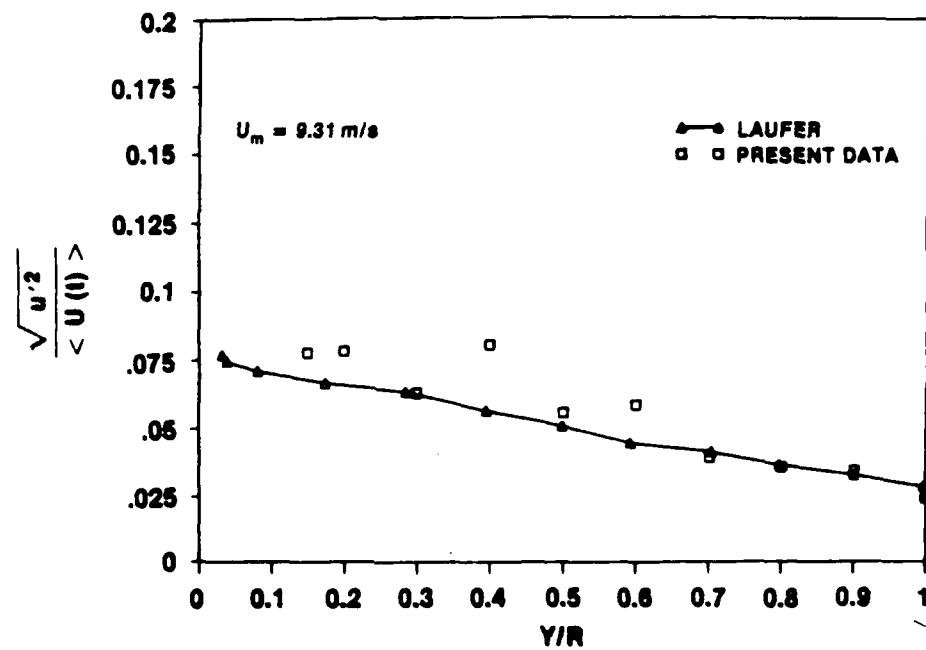
Figure IV-74c. Turbulence Intensity Profile at t = 2.000 s for
$\ddot{X} = 6.1$ m/s^2 and $\bar{\bar{U}}_{m0} = 1$ m/s
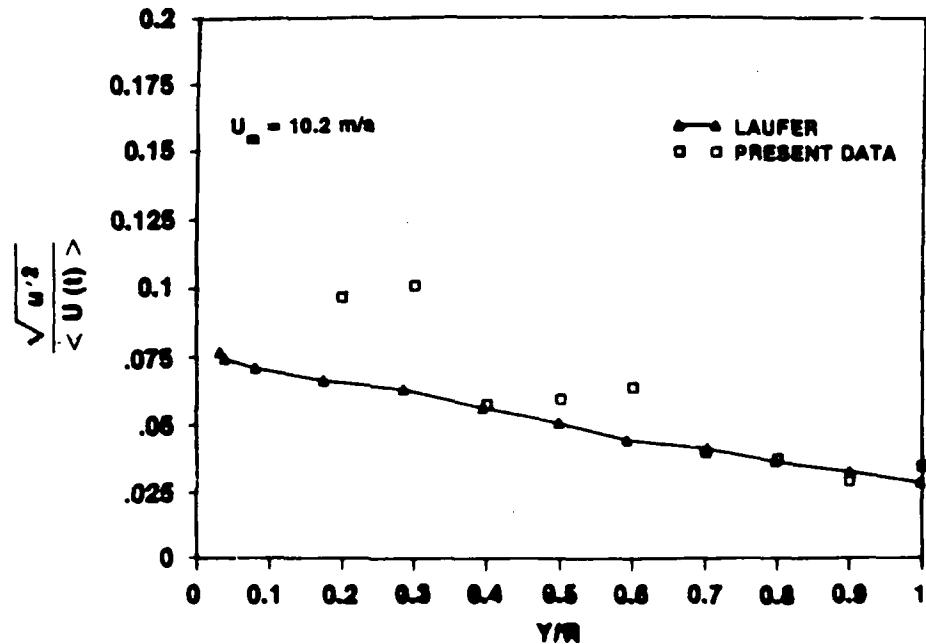
Figure IV-74d. Turbulence Intensity Profile at t = 2.500 s for
$\ddot{X} = 6.1$ m/s^2 and $\bar{\bar{U}}_{m0} = 1$ m/s
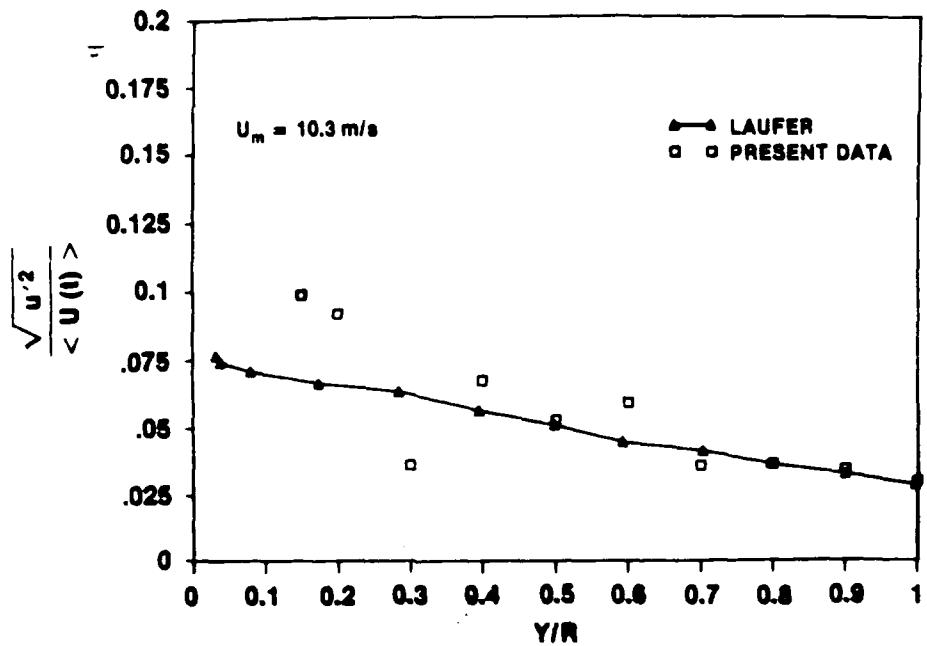
Figure IV-74e. Turbulence Intensity Profile at t = 5.900 s for $\ddot{X} = 6.1$ m/s^2 and $\bar{U}_{m0} = 1$ m/s

absolute values of the turbulence intensities, which range from a high

of 0.075 near the wall to a low of approximately 0.03 at the pipe

centerline. This agreement is also very close when one considers that

only 20 runs were included in the ensemble average.

Considering the fact that for most of the transient both the

turbulent velocity profiles and the corresponding distribution of

turbulence intensity agree with the quasi-steady values, it is

reasonable to conclude that the Reynolds stress must also follow the

quasi-steady values.

157

Transient Wall Shear Stress

This section of the results presents and discusses the time-dependent wall shear stress obtained during each of the four ensemble-averaged test cases. The output of only one sensor is considered because all of the sensors gave approximately the same results. On figures where the time over which the transient occurred is not obvious from the data itself, the range over which the transient had approximately constant acceleration is noted.

Figure IV-75 gives the time history of the wall shear stress for one sensor over one run of case 1. The graph is similar to the ones given in the transition-related portion of the results discussed previously. Figure IV-76 shows the ensemble average, which includes the run shown in figure IV-75, while the corresponding RMS curve is shown in figure IV-77.

The ensemble-averaged curve, as expected, shows greatly reduced fluctuations in the turbulent region that follows the abrupt change in τ_w at approximately 2.6 seconds, the transition point. As observed from figure IV-77, the RMS value jumps from about 5 percent of the mean value while the flow is laminar to approximately 15 percent during the turbulent portion of the run. Transition can be seen to occur at the same time for each of the runs.

Figure IV-78 shows the ratio of actual wall shear stress to the quasi-steady laminar value obtained by using the steady-state laminar value of friction coefficient, $f = 64/Re_D$. During most of the

158
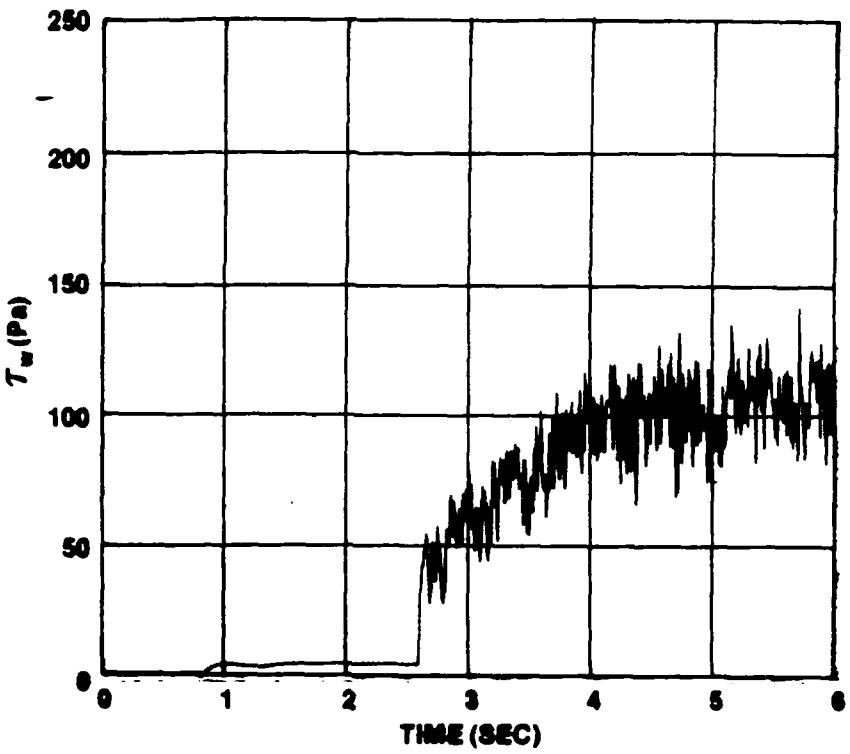
Figure IV-75. τ_w vs t for One Typical Run at $\ddot{X} = 2.4$ m/s^2 and $\bar{U}_{m0} = 0$
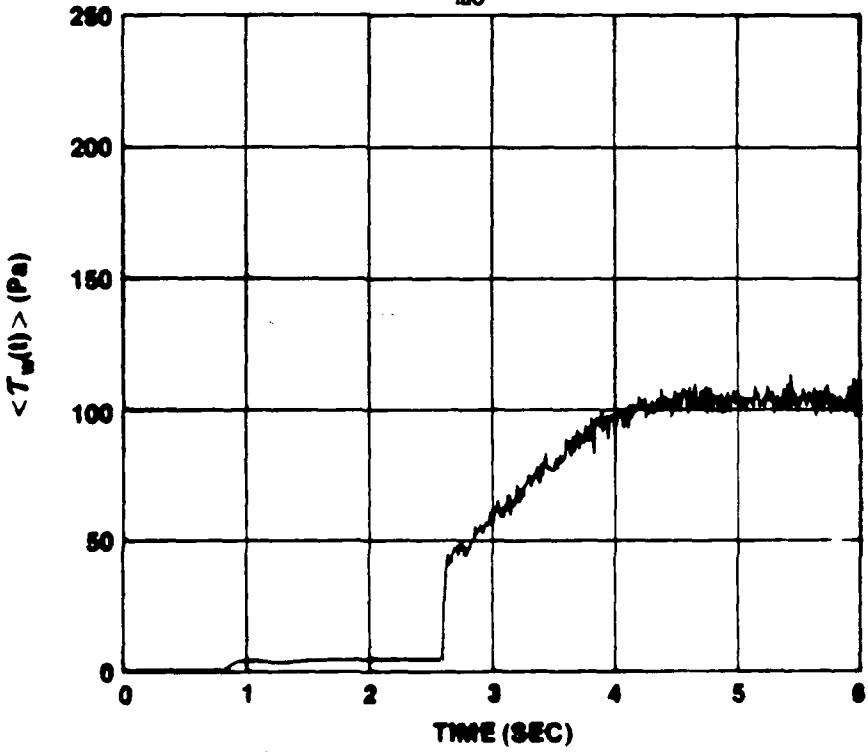
Figure IV-76. $\langle\tau_w(t)\rangle$ vs t for Ensemble Average of 20 Runs at $\ddot{X} = 2.4$ m/s^2 and $\bar{U}_{m0} = 0$

159
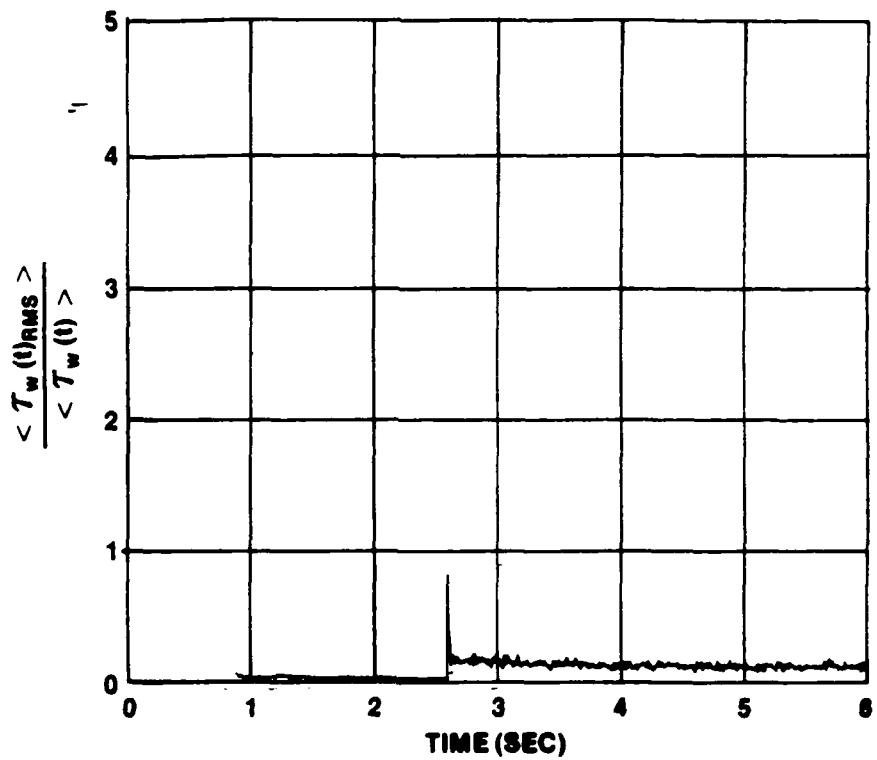
Figure IV-77. $\langle \tau_w(t)_{RMS} \rangle$ vs t at $\ddot{X} = 2.4$ m/s^2 and $\bar{U}_{m0} = 0$
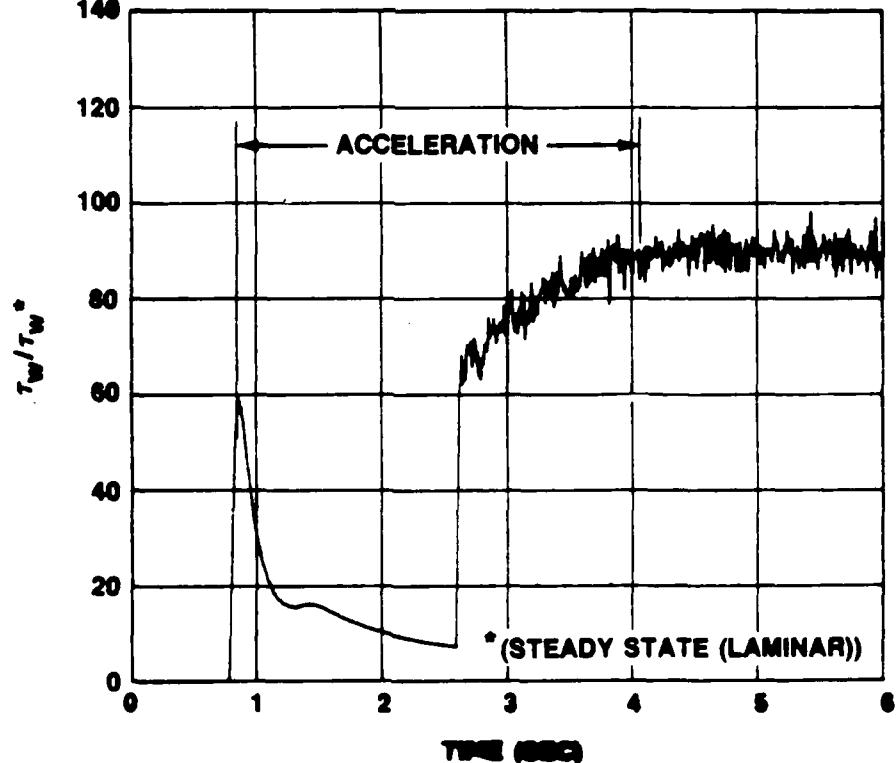
Figure IV-78. τ_w Nondimensionalized by Quasi-Steady Laminar Value
at $\ddot{X} = 2.4$ m/s^2 and $\bar{U}_{m0} = 0$

160

laminar portion of the transient, the ratio is between 10 and 20. It is obvious that this is not a reasonable estimate of τ_w for any portion of the run; the velocity profile differs substantially from the steady-state one.

Figure IV-79 shows the time history of the ratio of actual wall shear stress to the quasi-steady turbulent value. The time during which the acceleration was constant is indicated on the figure. The quasi-steady turbulent assumption is shown to be valid during the turbulent portion of the transient with the ratio being near one and within the accuracy of the measurements. As expected, the assumption does not hold during the laminar flow portion.

As a final effort to find a valid means of predicting τ_w during the laminar portion of the transient, calculations based on Szymanski's exact solution and given by equation (IV-10) were used as the comparison given in figure IV-80. Here, six times covering the laminar portion of the transient were chosen for the calculations. The figure shows that the measured data agree with the calculations within 18 percent, which is just a little greater than the accuracy of the measurements (±14 percent). Therefore, it is concluded that calculations based on the exact laminar solution can be used to predict the transient τ_w for the case of low accelerations, no greater than 2.4 m/s^2.

Wall shear stress measurements are now presented for the second case of the ensemble-averaged tests. Figure IV-81 shows the time history of one run from sensor number 2, while figure IV-82 shows the
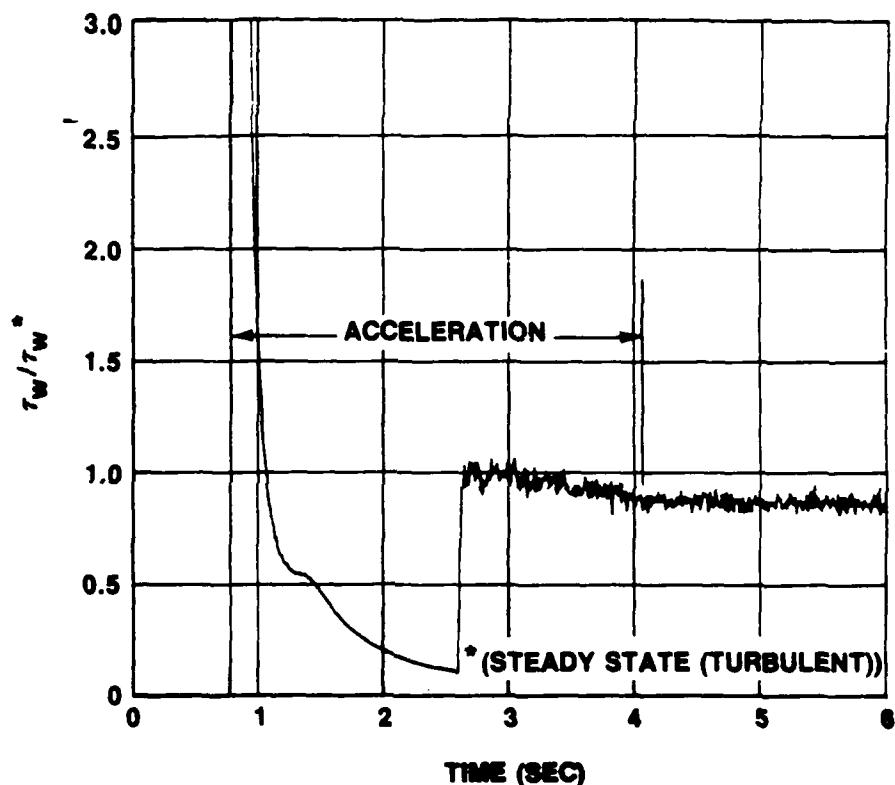
Figure IV-79. τ_w Nondimensionalized by Quasi-Steady Turbulent Value at $\ddot{X} = 2.4$ m/s^2 and $\bar{U}_{m0} = 0$
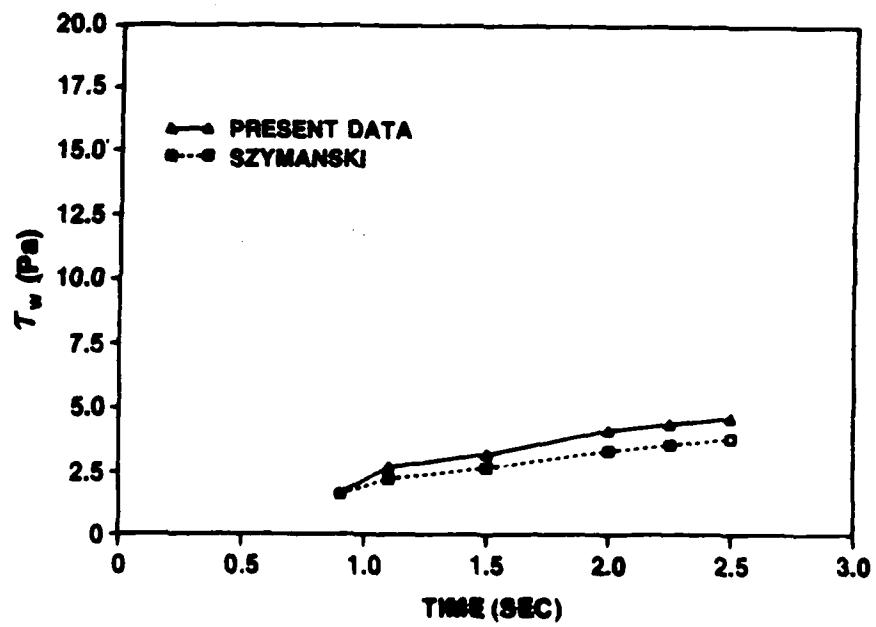
Figure IV-80. Comparison of τ_w Measured with Szymanski's Solution at $\ddot{X} = 2.4$ m/s^2 and $\bar{U}_{m0} = 0$
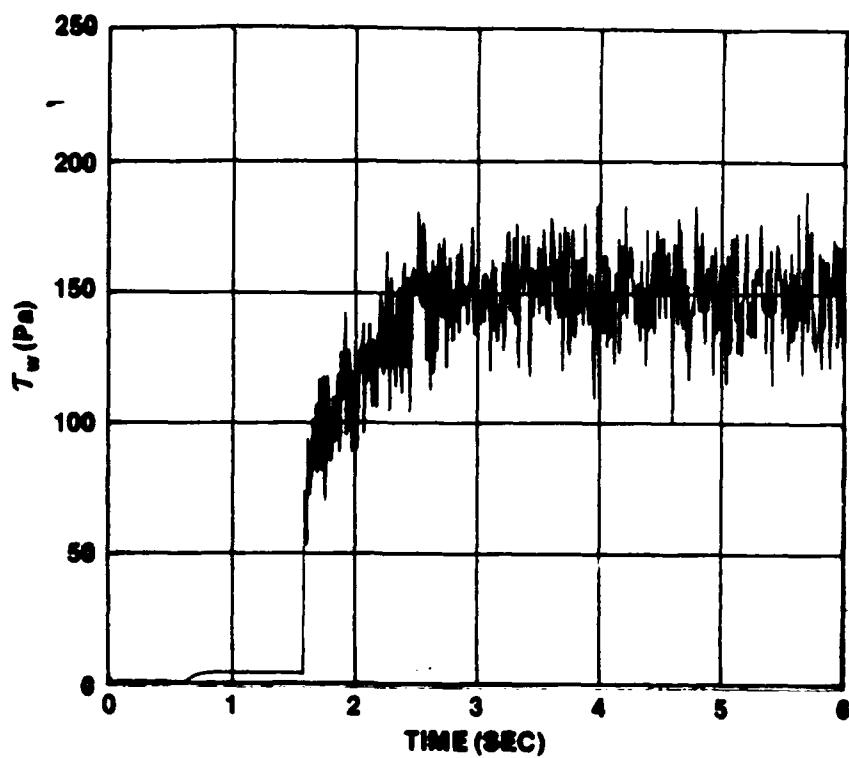
Figure IV-81. τ_w vs t for One Typical Run at $\ddot{X}$ = 6.1 m/s^2
and $\bar{U}_{m0}$ = 0
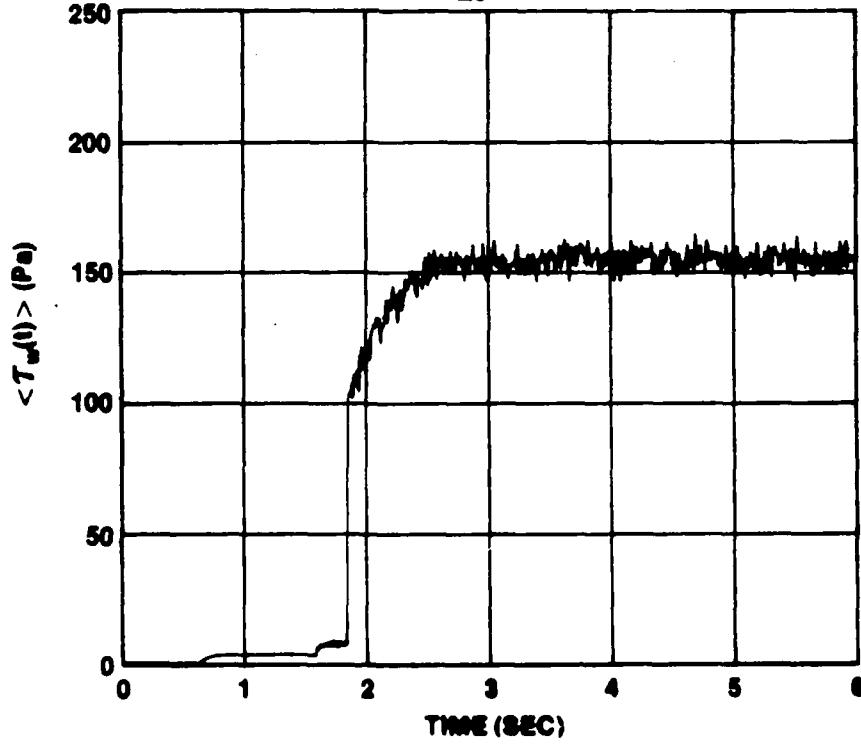
Figure IV-82. $\langle\tau_w(t)\rangle$ vs t for Ensemble Average of 20 Runs at
$\ddot{X}$ = 6.1 m/s^2 and $\bar{U}_{m0}$ = 0

163

ensemble average of 20 runs and figure IV-83 shows the RMS value. Similar remarks to those made for the corresponding figures of the first case can be made except for the repeatability of the time at which transition occurred. From both figures IV-82 and IV-83, the spread in the transition time is seen to be approximately 0.25 second. Sensor 3 exhibited a similar spread in transition time; however, transition at the remaining four sensors always occurred at the same time as at the LDV. This spread reflects the discussion given previously on the transition related tests where at the higher accelerations, the transition time observed at each of the six sensor locations differed by up to 32 percent from the start of the actual transient. As stated previously, transition at the higher accelerations appear to be not only a function of the acceleration but also highly susceptible to destabilizing local conditions such as protrusion of a sensor. Since the LDV was not positioned near either sensor 2 or 3, it is not known for sure whether transition occurred instantaneously over the whole cross section at those axial locations. However, based on the data presented so far, it appears most likely that transition was virtually instantaneous. Future experiments could look at transition across the complete pipe cross-section when a local surface perturbation is present.

The ratio of measured to quasi-steady laminar wall shear stress is given as figure IV-84. As with the first case, this is not a reasonable method to predict the time-dependent τ_w. Figure IV-85 presents the ratio of actual to quasi-steady turbulent τ_w. Even

164
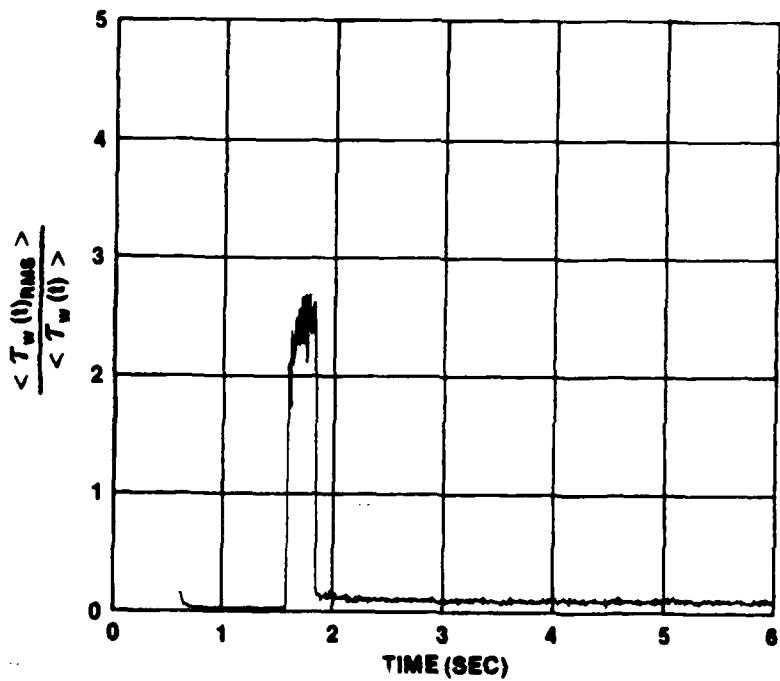
Figure IV-83. $\langle \tau_w(t)_{RMS} \rangle$ vs t at $\ddot{X} = 6.1$ m/s^2 and $\bar{U}_{m0} = 0$
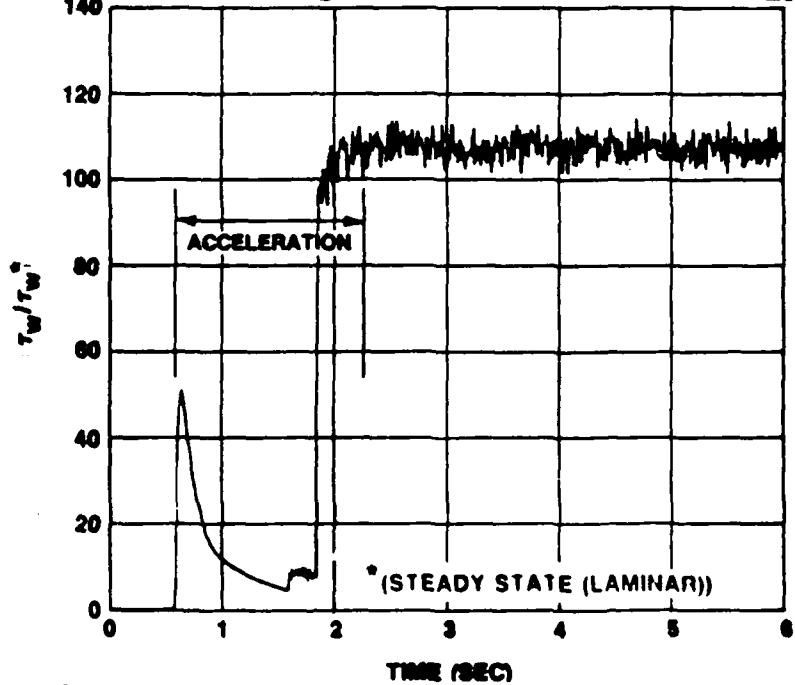
Figure IV-84. τ_w Nondimensionalized by Quasi-Steady Laminar Value at $\ddot{X} = 6.1$ m/s^2 and $\bar{U}_{m0} = 0$

165
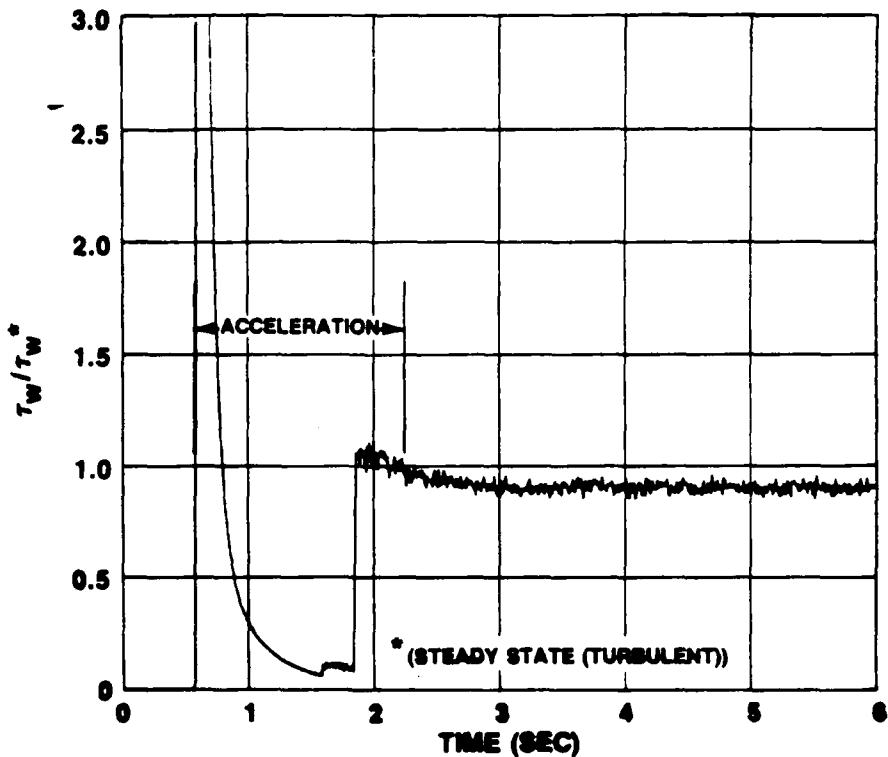
Figure IV-85. τ_w Nondimensionalized by Quasi-Steady Turbulent Value at $\ddot{X} = 6.1 \text{ m/s}^2$ and $\bar{U}_{m0} = 0$

turbulent portion of the transient only lasts for about 0.3 second, the ratio is very close to one as with the first case, proving again that the quasi-steady assumption during turbulent flow is appropriate.

Figure IV-86 compares the exact laminar solution with the measured data for eight different times over the transient. Unlike the first case, the measured data do not follow the exact solution, which increases with time. Here, the measured τ_w remains at a constant value until transition. However, like the values of τ_w at transition presented earlier, the measured τ_w data are within the same approximate range as the exact solution. Future planned experiments will investigate in more detail the reason for the constant value of τ_w as velocity increases.

Figure IV-87 is the time history of τ_w for one run of the third

166
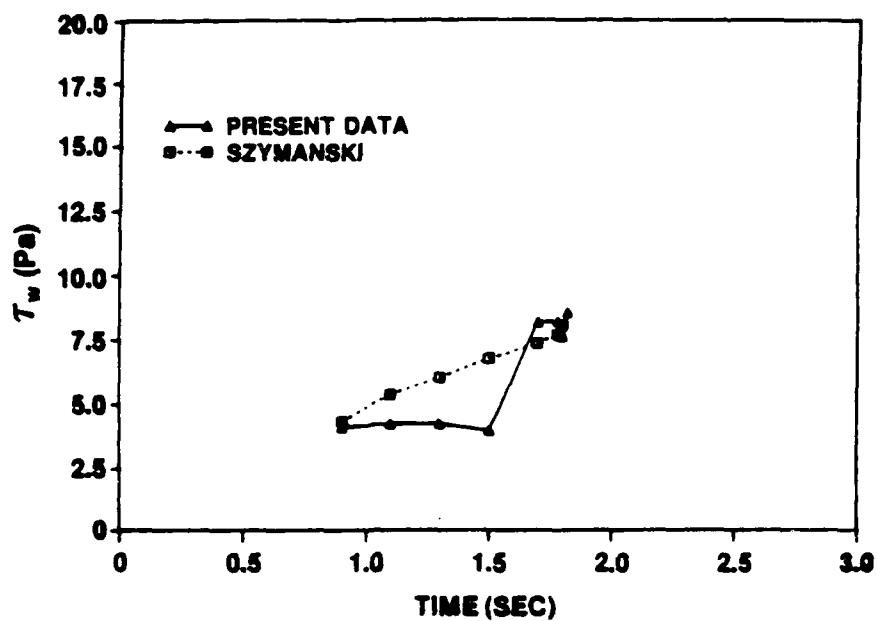
Figure IV-86. Comparison of τ_w Measured with Szymanski's Solution at $\ddot{X} = 6.1$ m/s^2 and $\bar{U}_{m0} = 0$
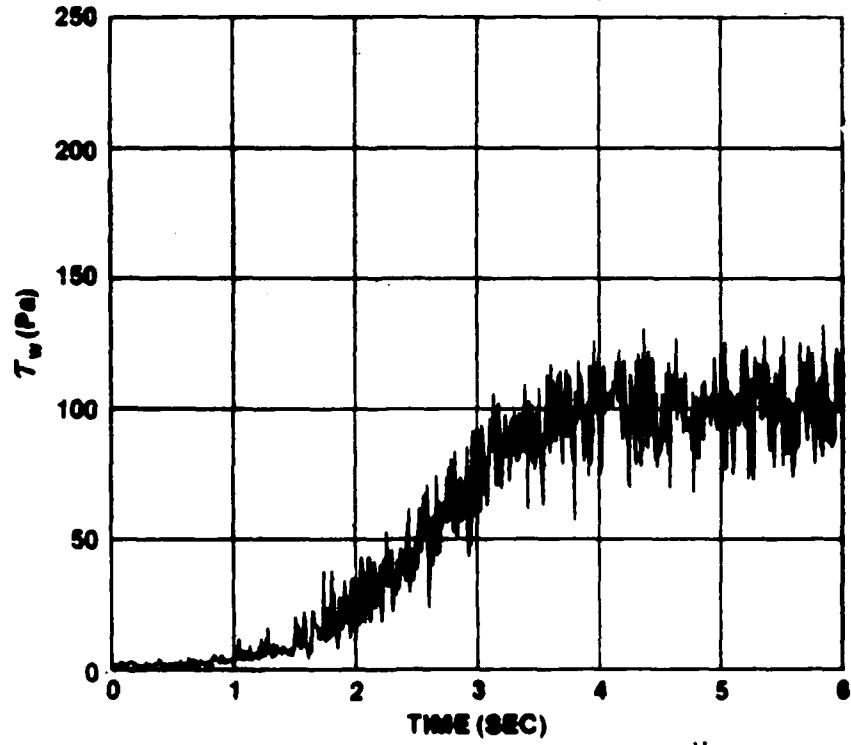
Figure IV-87. τ_w vs t for One Typical Run at $\ddot{X} = 2.4$ m/s^2 and $\bar{U}_{m0} = 1$ m/s^2

case which was an acceleration of 2.4 m/s^2 of an initially turbulent flow. This figure shows that unlike the previous case, τ_w increases continuously over the transient. The ensemble average of 20 runs is shown in figure IV-88. The reduced level of the fluctuations about the mean curve is appreciable as with all of the previous ensemble-averaged data. Figure IV-89 gives the RMS of the average. The value of RMS over the run ranges from approximately 15 to 30 percent of the instantaneous value of τ_w. This is the range of RMS values that was obtained for the time averages of the steady-state τ_w measured during sensor calibration. This is also the range normally found for RMS of the fluctuations about the mean value of τ_w in general steady-state pipe flows. This gives some credibility to the assumption that the RMS obtained from ensemble averaging the transient runs is similar to the corresponding time average RMS in steady flows.

Figure IV-90 gives the time-dependent ratio of measured τ_w to the quasi-steady turbulent value. The range over which the acceleration was constant is noted. From the start of the acceleration at approximately 0.7 second and for about a 1-second duration, the ratio deviated from 1. At first, the ratio decreased to a value of approximately 0.6 at time 1.3 seconds; it subsequently increased to a value of 1 (within the measurement accuracy of ±14 percent) at 2 seconds and until the end of the transient at 3.5 seconds.

The low values of the ratio at the start of the transient appear to be due to the stabilizing effect of the acceleration. A direct

168
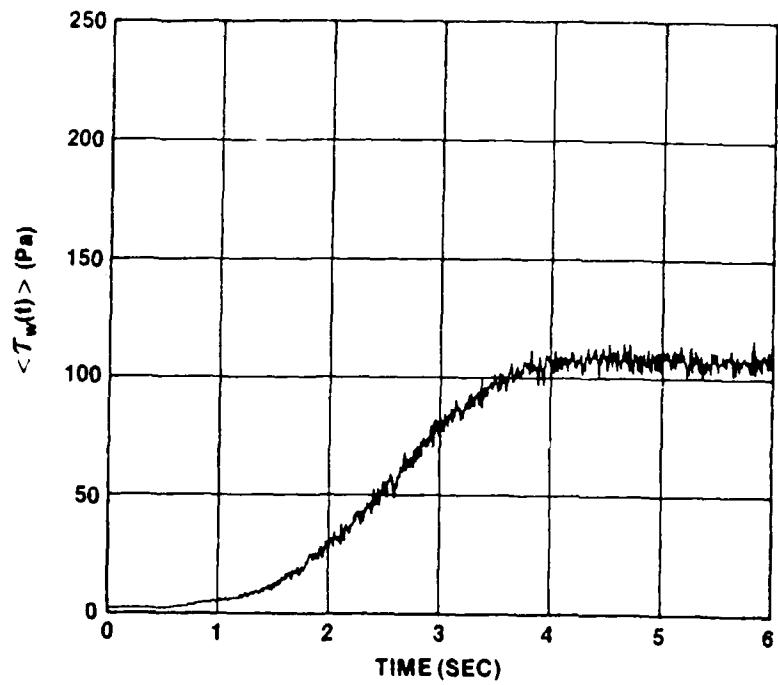
Figure IV-88.   Comparison of τ_w Measured with Szymanski's Solution
for $\ddot{X}$ = 2.4 m/s^2 and $\bar{U}_{m0}$ = 1 m/s^2
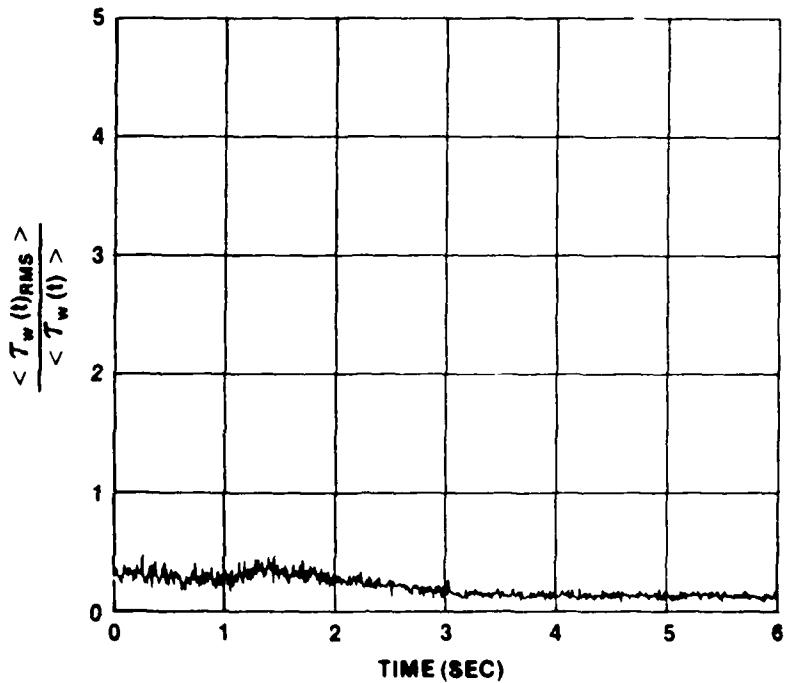
Figure IV-89.   Comparison of τ_w Measured with Szymanski's Solution
for $\ddot{X}$ = 2.4 m/s^2 and $\bar{U}_{m0}$ = 1 m/s^2

169
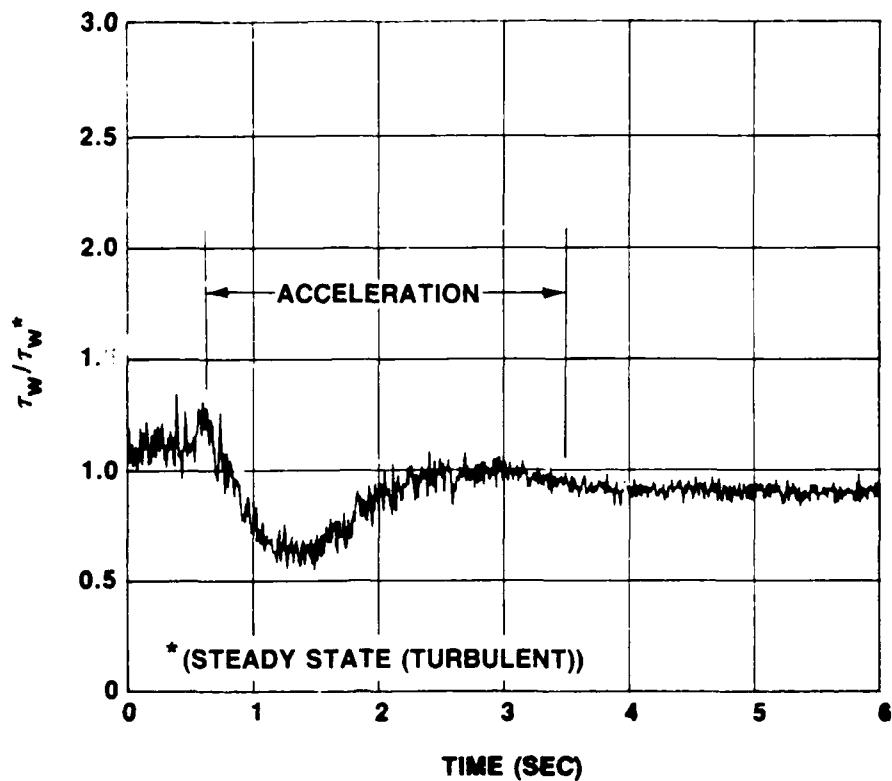
Figure IV-90.   Comparison of τ_w Measured with Szymanski's Solution for $\ddot{X} = 2.4$ m/s^2 and $\bar{U}_{m0} = 1$ m/s^2

comparison can be seen with the RMS curve of the centerline velocity for this case, figure IV-66.   The effect of acceleration on stabilizing the flow was discussed previously during the presentation of the velocity profile data and the turbulence intensity distributions, both of which indicated stabilizing effects at the start of the transient where thevalue of the acceleration parameter K_a was the largest.   The present τ_w data reinforce this argument.

The fourth and last case with an acceleration of 6.1 m/s^2 and an initially turbulent flow at 1 m/s resulted in a transient τ_w curve as shown in figure IV-91.   The ensemble-averaged curve is given in figure IV-92 and the RMS in figure IV-93.   Each curve is very similar to the corresponding curves given for case 3.

170

AD-A193 065   CHARACTERIZATION OF ACCELERATING PIPE FLOW(U) NAVAL   3/3
               UNDERWATER SYSTEMS CENTER NEWPORT RI P J LEFEBVRE
               01 MAR 88 NUSC-TD-6666

UNCLASSIFIED   F/G 20/4   NL
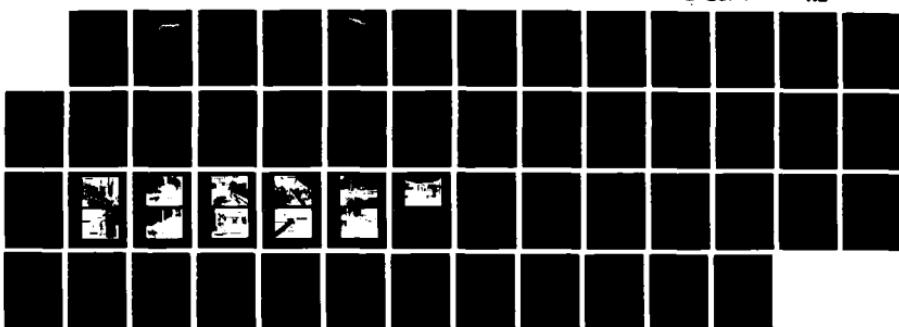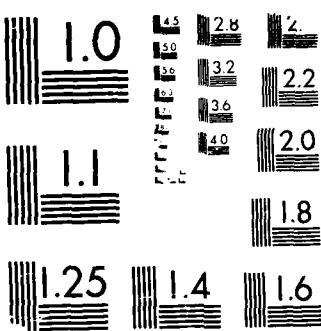
MICROCOPY RESOLUTION TEST CHART

IRFAII   TANDARDS 1963 A
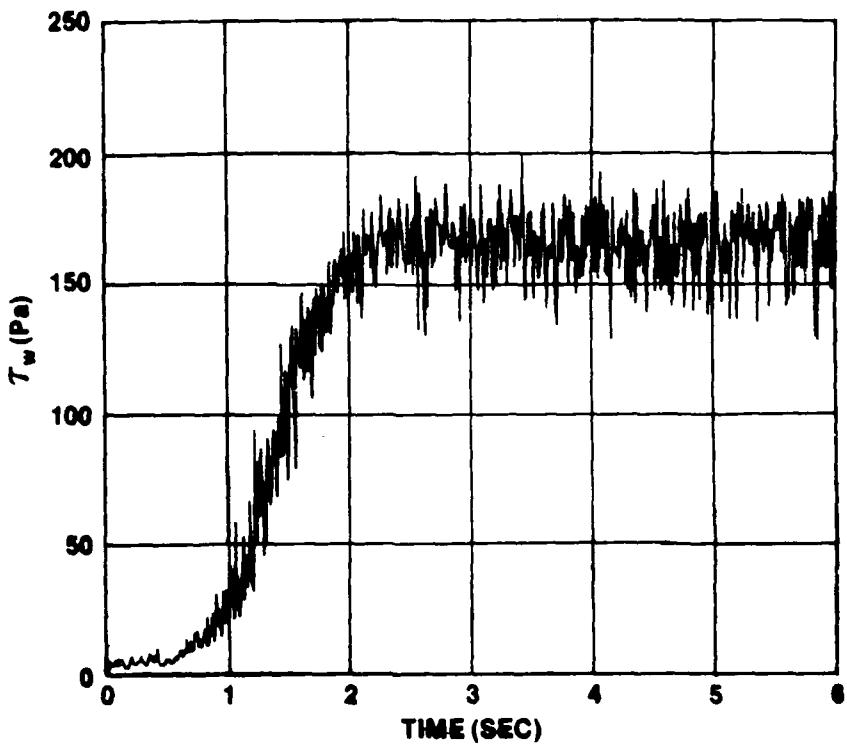
Figure IV-91. τ_w vs t for One Typical Run at $\ddot{X} = 6.1$ m/s^2 and $\bar{U}_{m0} = 1$ m/s^2
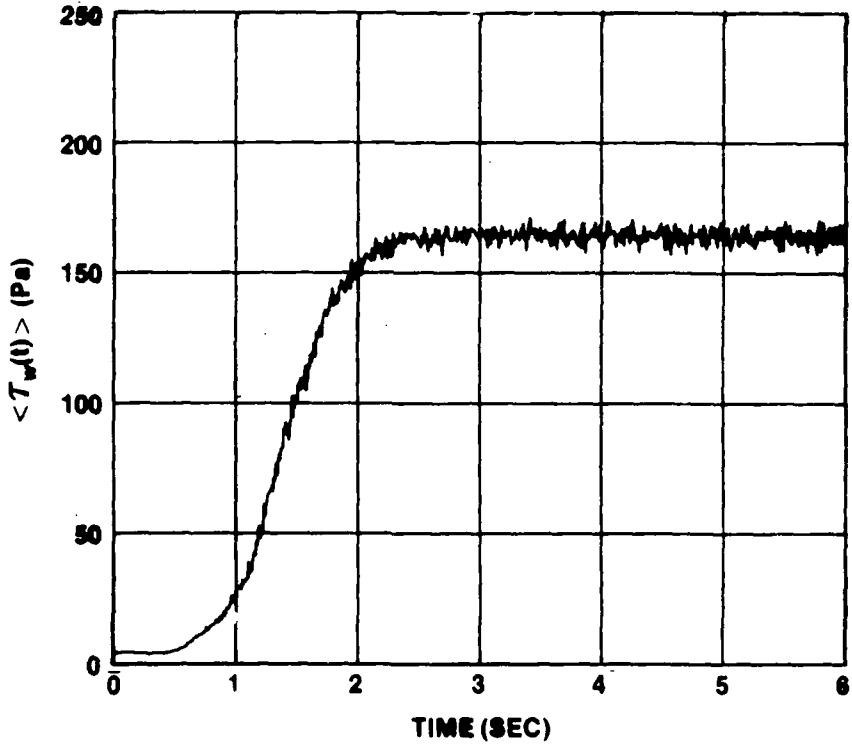
Figure IV-92. $\langle \tau_w(t) \rangle$ vs t for Ensemble Average of 20 Runs at $\ddot{X} = 2.4$ m/s^2 and $\bar{U}_{m0} = 1$ m/s^2
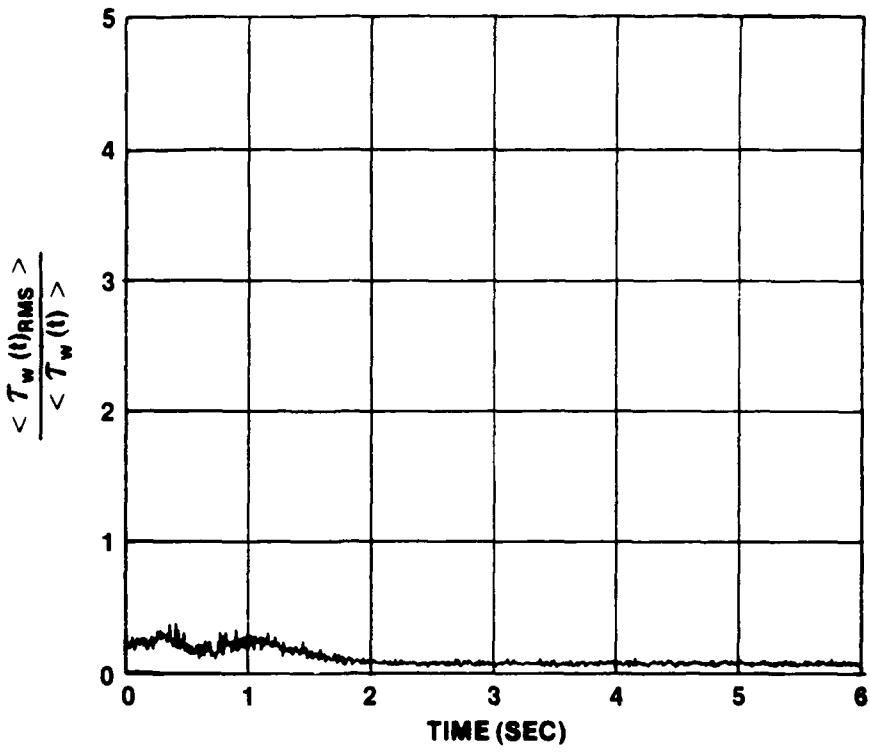
Figure IV-93. $\langle \tau_w(t)_{RMS} \rangle$ vs t at $\ddot{X} = 2.4$ m/s^2 and $\bar{U}_{m0} = 1$ m/s^2

These ensemble-averaged data are also nondimensionalized with

the corresponding quasi-steady turbulent values as shown in figure

IV-94. As with case 3, the value of the ratio decreases below 1.0 at

the outset of the transient. Again, it is interesting to observe

that the shape of this curve is almost identical to that of figure

IV-71 for the RMS of the centerline velocity. This further supports

the assumption that the acceleration stabilizes the flow.

172
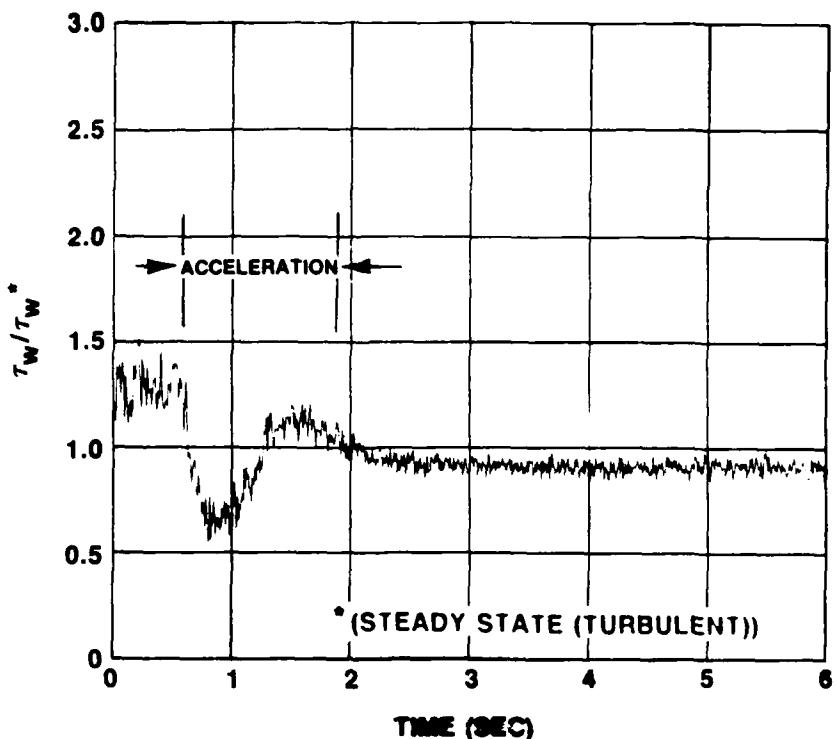
Figure IV-94. τ_w Nondimensionalized by Quasi-Steady Turbulent Value at $\ddot{X} = 2.4$ m/s^2 and $\bar{U}_{m0} = 1$ m/s^2

Transient Pressure

A typical time history of pressure for one run is given in figure IV-95. This particular run was from case 1 for an acceleration of 2.4 m/s^2 from rest. The ensemble average of 20 repeat runs is given in figure IV-96 and its RMS in figure IV-97. The ensemble-averaged curve has considerably reduced fluctuations relative to the single run curve due to the averaging. The RMS was almost constant over both the transient and steady-state portions of the run with a very small value of approximately 1.7 percent of the mean value. Similar results were observed for the other three cases and, therefore, are not presented. Instead, time histories of the pressure gradient are presented in the following paragraphs.

173
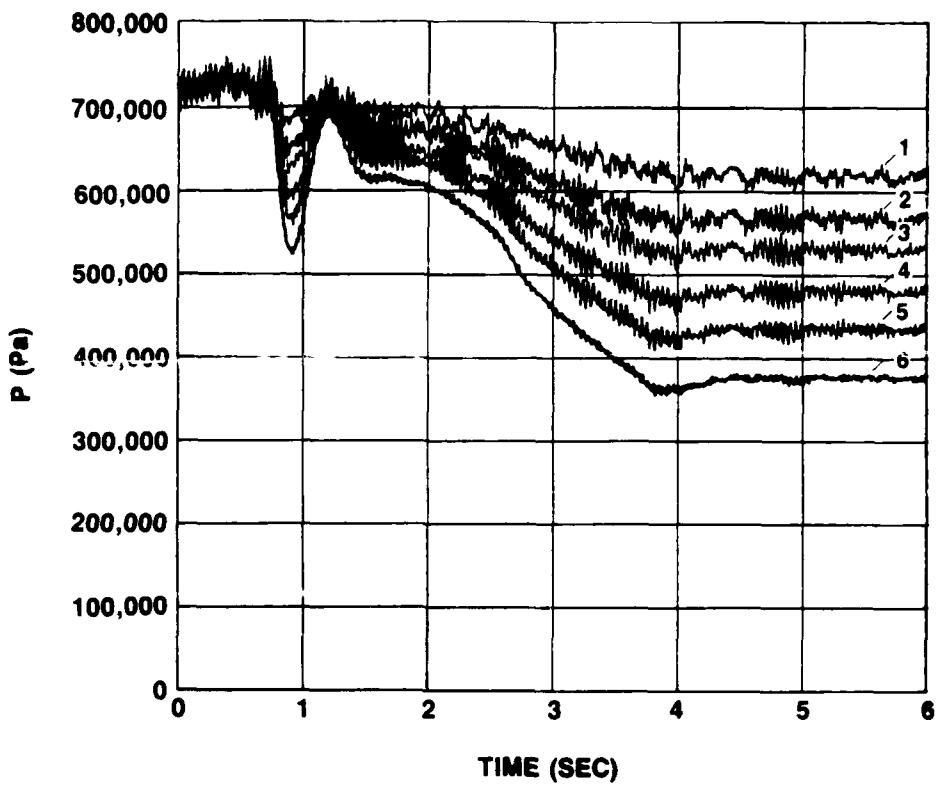
Figure IV-95. Pressure vs t for One Typical Run at $\ddot{X} = 2.4$ m/s^2 and $\bar{U}_{m0} = 0$
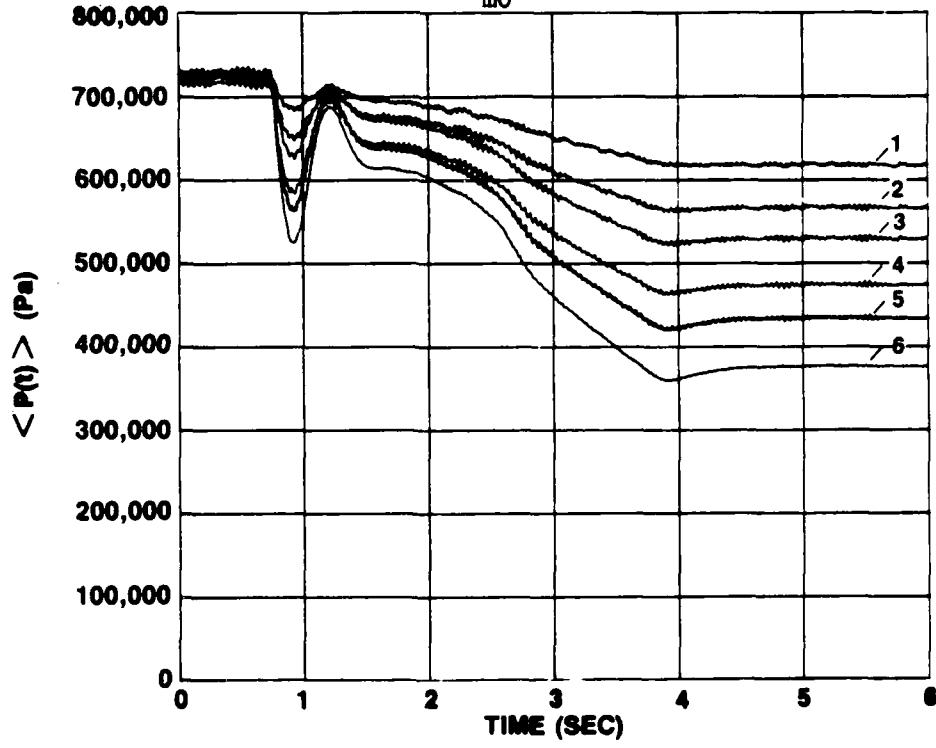
Figure IV-96. $\langle P(t) \rangle$ vs t for Ensemble Average for 20 Runs at $\ddot{X} = 2.4$ m/s^2 and $\bar{\bar{U}}_{m0} = 0$

174
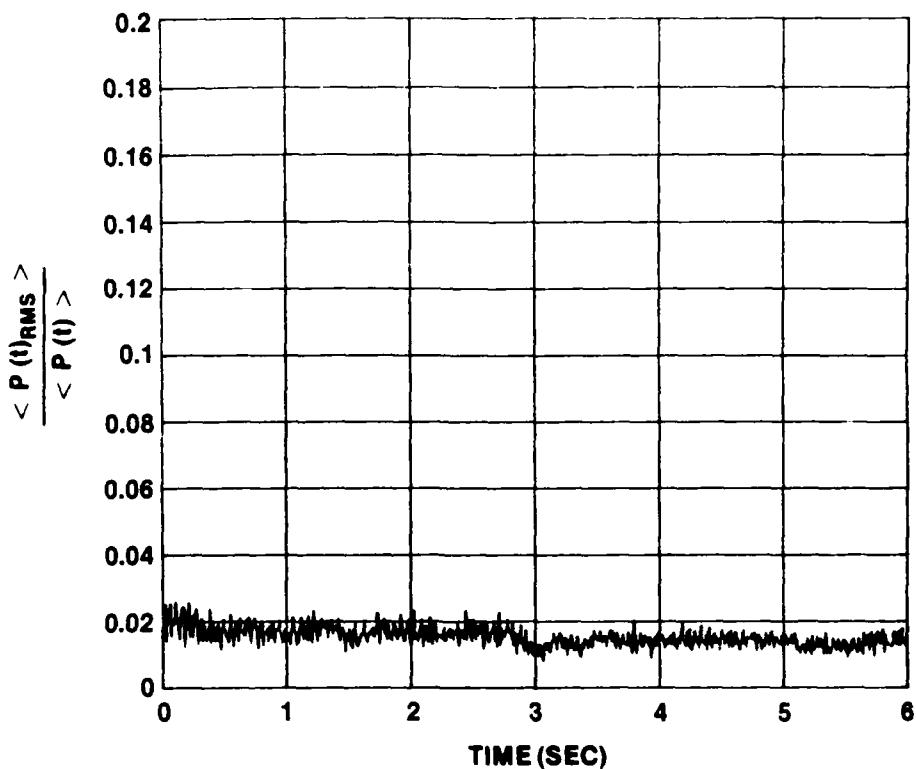
Figure IV-97. $\langle P(t)_{RMS} \rangle$ vs t for Ensemble Average of 20 Runs at $\ddot{X} = 2.4$ m/s^2 and $\bar{U}_{m0} = 0$

The pressure gradient at each instant of time was obtained by taking the difference in pressure from sensor stations 1 and 6 and dividing by the distance between the two (25 meters). Resulting curves for cases 1 through 4 are given in figures IV-98 through IV-101 respectively. Each figure gives the range in time during which the transient was observed from the U_m measurements to have approximately constant acceleration.

For the first two cases that started from rest, the pressure gradient increased sharply at the beginning of the run followed by a sharp decrease, which lasted until about 0.4 second from the start of

175
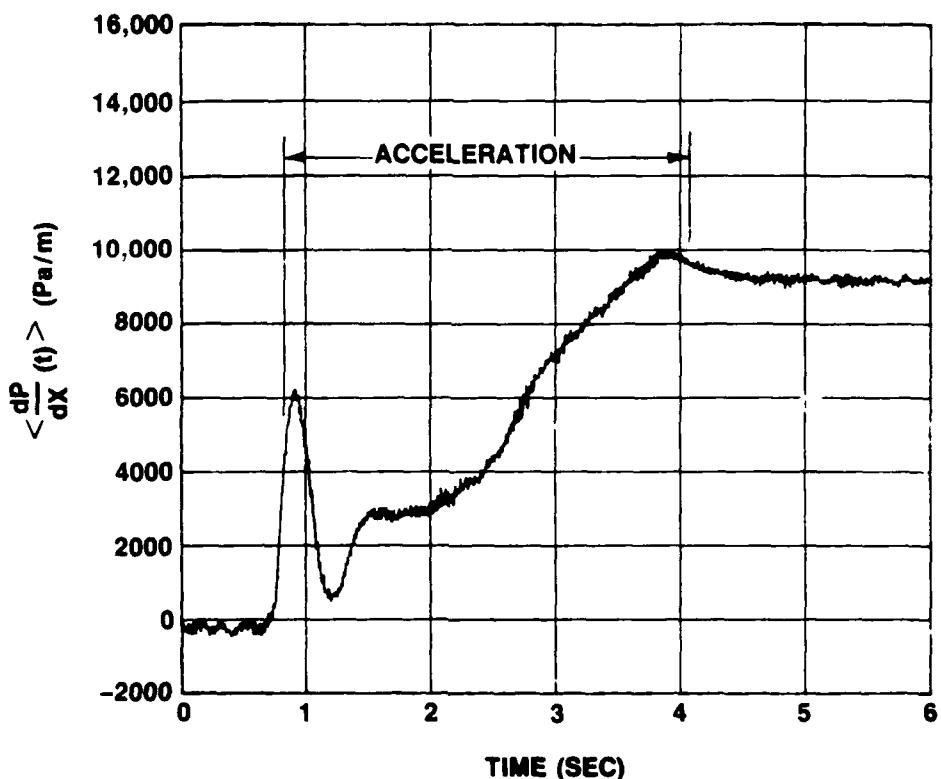
Figure IV-98. $\langle dp/dx\ (t)\rangle$ vs t for Ensemble Average of 20 runs at $\ddot{X} = 2.4\ m/s^2$ and $\bar{U}_{m0} = 0$
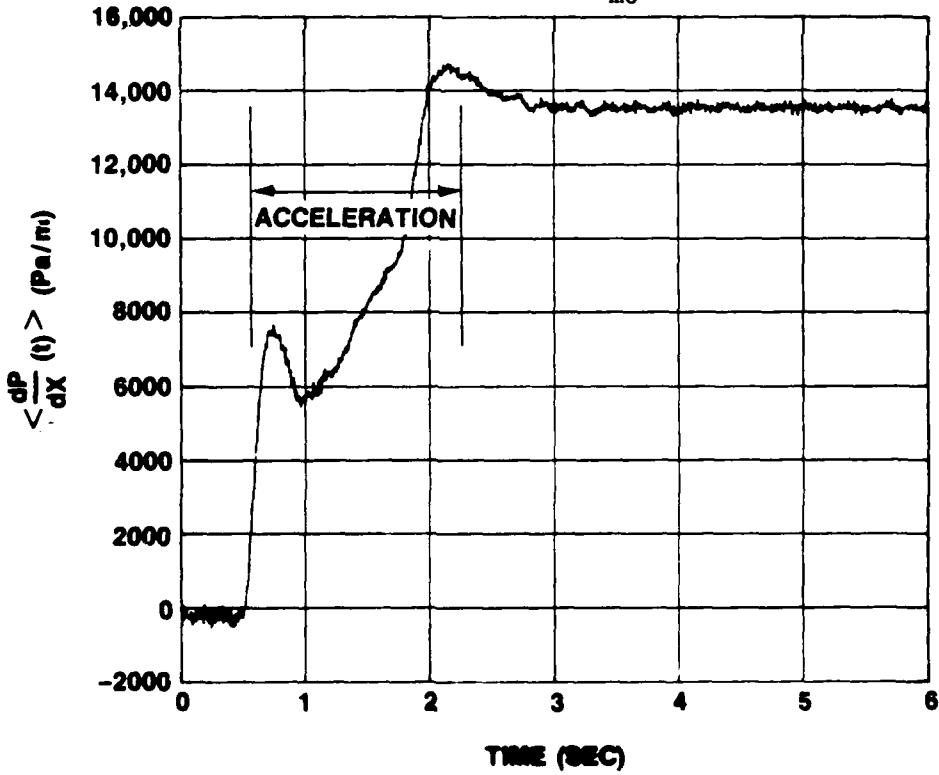
Figure IV-99. $\langle dp/dx\ (t)\rangle$ vs t for Ensemble Average of 20 runs at $\ddot{X} = 6.1\ m/s^2$ and $\bar{U}_{m0} = 0$
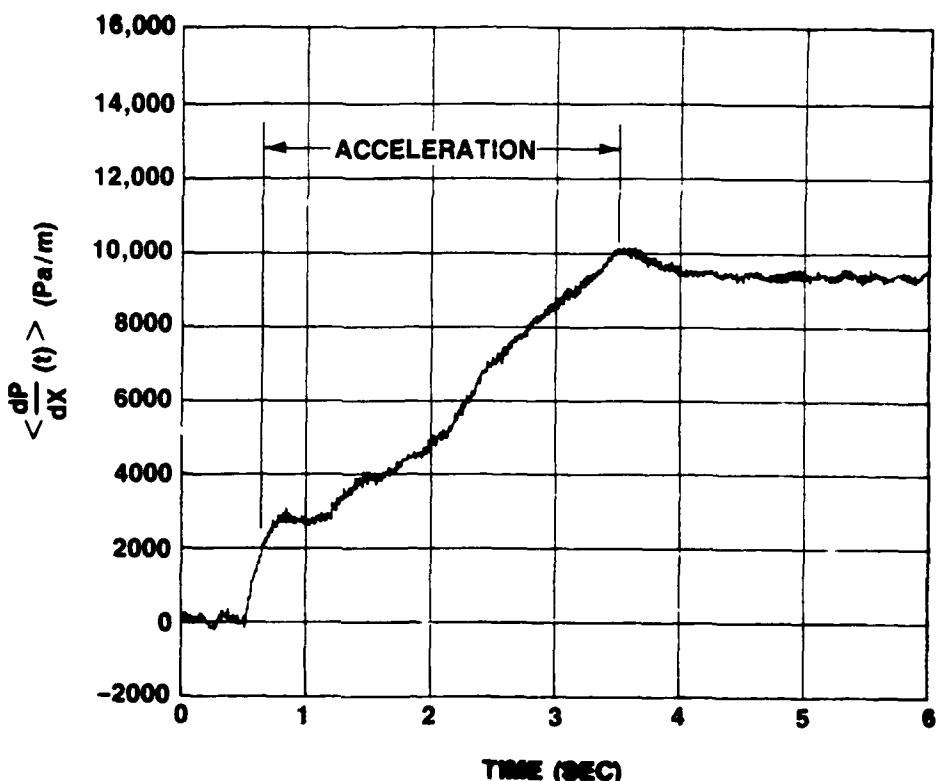
Figure IV-100. $\langle dp/dx\ (t)\rangle$ vs t for Ensemble Average of 20 runs at $\ddot{X} = 2.4\ \mathrm{m/s}^2$ and $\overline{U}_{m0} = 1\ \mathrm{m/s}$
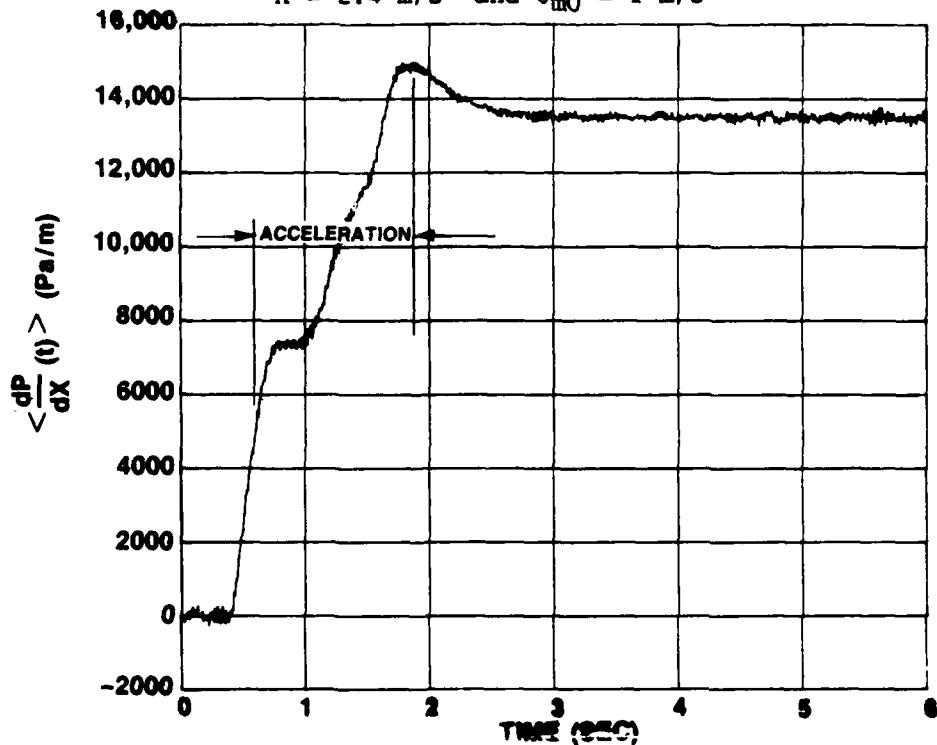
Figure IV-101. $\langle dp/dx\ (t)\rangle$ vs t for Ensemble Average of 20 runs at $\ddot{X} = 6.1\ \mathrm{m/s}^2$ and $\overline{U}_{m0} = 1\ \mathrm{m/s}$

177

the run. From that point on, the pressure gradient increased fairly linearly. In each case, transition occurred well within the linear portion of the pressure gradient curve.

For the last two cases, which started from an initially turbulent flow, the gradient was fairly linear throughout the range of constant acceleration.

The pressure gradient data, along with the τ_w and U_m data, are used in the following section to evaluate the assumption that the wall shear stress sensors can respond accurately to transient flows.

Wall Shear Stress Sensor Transient Response

Until the present study, researchers have only assumed that hot-film wall shear stress sensors, similar to those used in the present study, could accurately respond to and measure wall shear stress in transient flows. To the author's knowledge, there has not been available any method or facility by which this assumption could be evaluated.

The unique capabilities of the NUSC Flow Loop Facility can be conveniently incorporated into a method using constant acceleration along with the integral form of the the linear momentum equation for a control volume to achieve a suitable means of evaluating the assumption. This method, which uses the data already presented, is explained in detail in the following paragraphs.

The linear momentum equation for an incompressible flow can be expressed as

178

$$\Sigma F = \int\int_{cs} \vec{V}(\rho\vec{V} \cdot d\vec{a}) + \frac{\partial}{\partial t} \int\int\int_{V} \vec{V}\rho d V \,, \qquad (IV-11)$$

where $\vec{V}$ is the three-dimensional velocity vector, V is the volume of the control volume and ΣF is the sum of the forces acting on the control volume.

Applying the X-component of this equation to the control volume of figure IV-102 (which is for a constant diameter pipe) results in

$$-\int\int_{cs} P \; d\vec{a} + \int\int_{cs} \tau_w dX = \int\int_{cs} U(\rho U \cdot d\vec{a}) + \frac{\partial}{\partial t} \int\int\int_{V} \rho U d V, \; (IV-12)$$
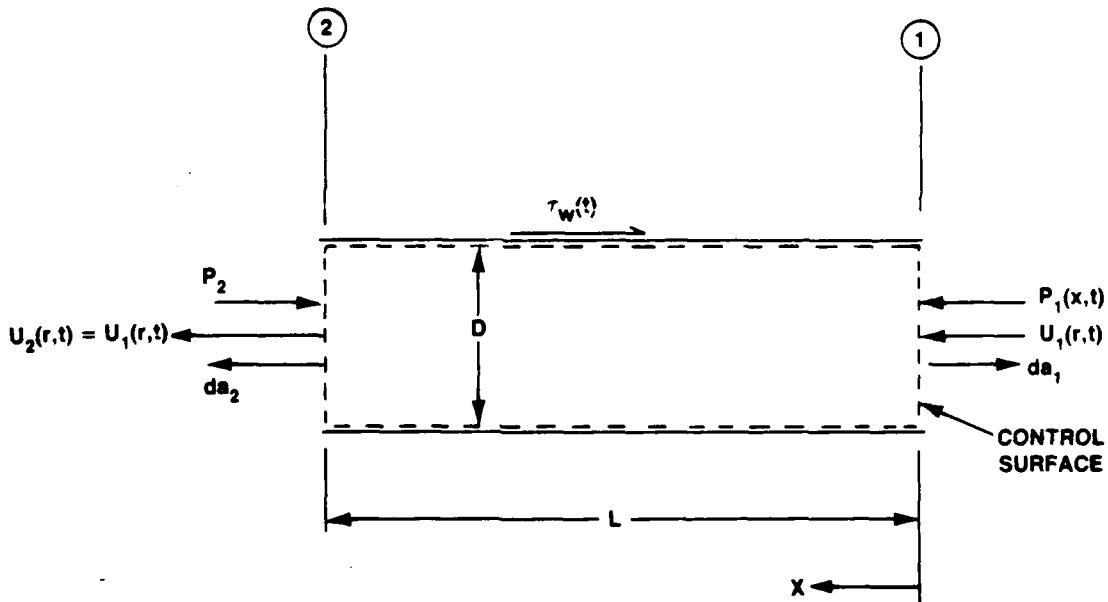
Figure IV-102. Control Volume

Based on the previously presented results, the velocity profile and τ_w are taken to be uniform or independent of axial location,

179

X. Because the instantaneous τ_w is constant along the length of the control volume, the second term on the left-hand side of equation (IV-12) becomes simply $\tau_w(\pi DL)$. Also, since there is no net transverse acceleration, the first term on the left-hand side becomes $-\Delta P \pi D^2/4$, where $\Delta P = P_2 - P_1$.

Since the difference in momentum flux through the ends of the control volume is zero for uniform incompressible flow, the first term on the right-hand side of equation (IV-12) is zero. Using the fact that the velocity profile is not a function of X and assuming the contribution of the turbulent fluctuations to the rate of change momentum within the control volume is negligible, the second term on the right-hand side of equation (IV-12) becomes

$$\frac{\partial}{\partial t}\iiint_{\Psi}\rho U d\Psi = \frac{\partial}{\partial t}\left[\int_a \rho U da\right] L = \rho\frac{dQ}{dt}L = \rho\,\frac{\pi D^2}{4}\,L\ddot{X} , \qquad (IV-13)$$

where Q is the volumetric flow rate and X is accurately known.

Incorporating the above into equation (IV-12) results in the following:

$$-\Delta P\left(\frac{\pi D^2}{4}\right) + \tau_w(\pi DL) = \rho L\left(\frac{\pi D^2}{4}\right)\ddot{X} . \qquad (IV-14)$$

Rearranging this gives the instantaneous time-dependent value for τ_w as

$$\tau_w = \frac{D}{4}\left[\rho\ddot{X} + \frac{\Delta P}{L}\right]. \qquad (IV-15)$$

The above calculation for the instantaneous value of τ_w can be used as a parameter by which the measured instantaneous τ_w from a transient run can be nondimensionalized. If the above assumptions

180

are valid and if the hot-film wall shear stress sensor accurately responds to the transient, then the ratio of the two parameters should be equal to one.

The previous analysis was applied to the ensemble-averaged data of 20 runs from case 3 of the second series of transient tests. The acceleration was 2.4 m/s^2 from an initially turbulent flow at 1 m/s^2. The resulting curve is shown in figure IV-103. The range of time over which the flow experienced approximately constant acceleration is designated on the figure and occurred between approximately 0.6 and 3.5 seconds. Outside that range, the calculations and resulting data are meaningless since the calculations over the total time of the run were based on having an acceleration of 2.4 m/s^2.

Over the major portion of the transient, the ratio is approximately equal to 1 which validates the accuracy of the τ_w sensors during the transient. However, at approximately 1.2 second, the ratio decreases until, at time 1.3 second, the ratio is 0.6. The ratio then increases almost linearly to 1 at 1.9 seconds. When comparing figure IV-103 with the curve of the centerline turbulence intensity (RMS) shown in figure IV-66, a striking resemblance in the shape of the curve is evident. For the times when the ratio was below 1, the turbulence intensity also decreased. This again tends to confirm the hypothesis made throughout this report that the acceleration tends to stabilize the flow at the beginning of the transient where the acceleration parameter, K_a, is its largest at a value of 2×10^{-6}. This can be compared to the value for relaminarization of a convectively accelerated flow of $K = 3 \times 10^{-6}$.

181
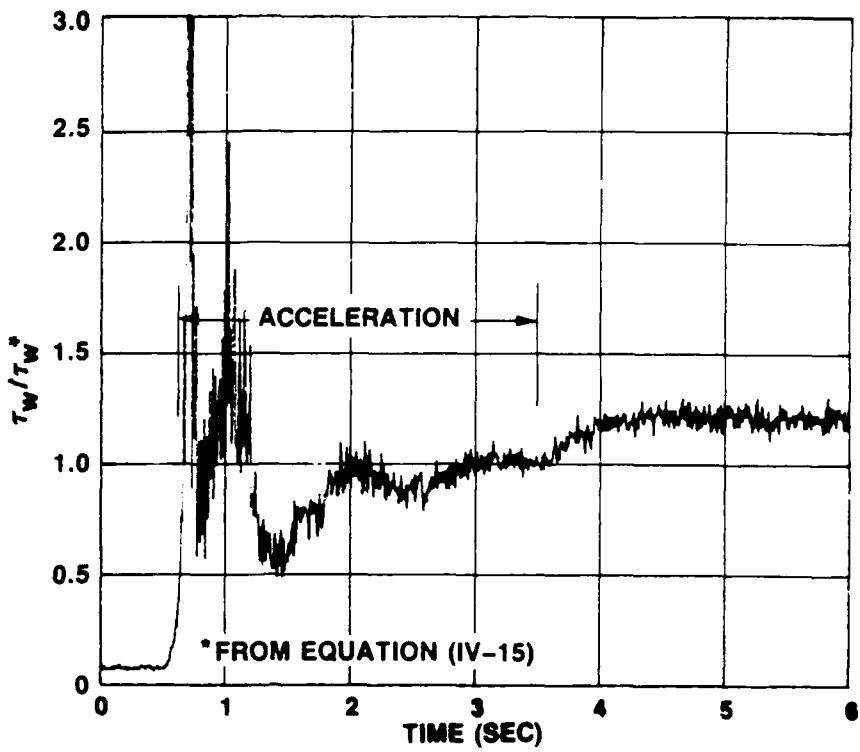
Figure IV-103. τ_w Nondimensionalized by Equation (IV-15) for $\ddot{X} = 2.4$ m/s^2 and $\bar{U}_{m0} = 1$ m/s

Since the rate of change of momentum inside the control volume due to the turbulent fluctuations was neglected in the previous analysis, the ratio would be expected to be lower than one for the portion of the transient when energy was expended in reducing the turbulence intensity and, hence, stabilizing the flow.

This analysis was also applied to the data of case 4, which had an acceleration of 6.1 m/s^2 from an initially turbulent flow at 1 m/s. Results are shown in figure IV-104. For this case, the constant acceler ation occurred between times of 0.5 and 1.8 seconds. As with case 3, the ratio was below 1 at the outset of the transient when K_a was equal to 5 x 10^{-6}. As observed by comparison with figure IV-71 for the centerline turbulence intensity, the turbulence intensity also decreased

during the time at which the ratio was below 1. This again supported
the contention that the acceleration stabilizes the flow.
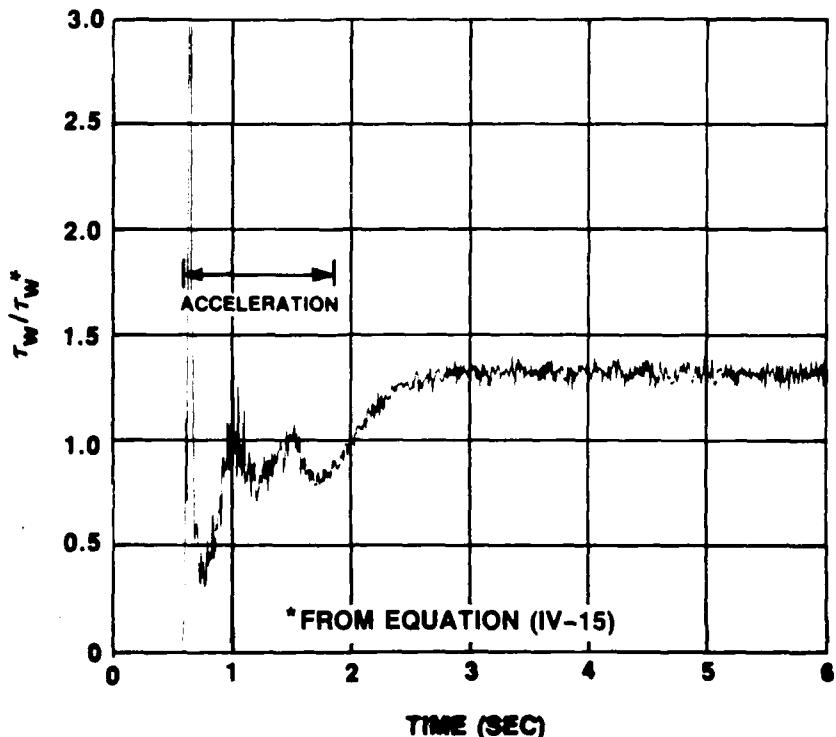
Figure IV-104. τ_w Nondimensionalized by Equation (IV-15) for
$\ddot{X} = 6.1$ m/s^2 and $\bar{U}_{m0} = 1$ m/s

From 0.9 seconds to the end of the constant acceleration at 1.8
seconds, the ratio was approximately equal to 1. This again confirms
the accuracy of hot-film wall shear stress sensors during transients
having accelerations up to at least 6.1 m/s^2.

In addition to the above analysis, the previous reported τ_w
data, which showed an abrupt change at transition to the quasi-steady
turbulent value, gives considerable support to the accuracy of the hot-
film wall shear stress sensors in transient flows.

V. CONCLUSIONS

A unique series of experiments on accelerating pipe flow have been conducted under the present study. Since these experiments differ substantially from those of previous investigators, they have resulted in many new observations and insights into the effect of accelerations on the physics of fluid flow.

To provide the capabilities required of the test facility and the associated instrumentation, a novel facility, the NUSC Flow Loop Facility, was designed and built. Much of the instrumentation used for transient measurements was either developed or validated for transient applications.

The major conclusions regarding the facility and instrumentation are:

1. A unique pipe flow facility was designed and built to provide programmed acceleration. The tests conducted under the present study utilized constant acceleration (up to 11.8 m/s^2) over a wide velocity range (to 11.3 m/s). The facility's ability to repeat a given transient was shown to be within ±0.5 percent (95 percent confidence level and relative to the instantaneous velocity).

2. A flowmeter capable of measuring transient volumetric flowrates with an accuracy of at least ±1.0 percent of reading and a data rate of 60 Hz was developed. To the author's knowledge, no other true transient flowmeter is commercially available.

184

3. An LDV technique was developed that could measure coincident axial and radial velocity components across the complete diameter in small diameter circular pipes. This method circumvents the problems of pipe curvature and index of refraction usually encountered in making coincident measurements in curved cross-sections. This provided the capability of measuring the complete Reynolds stress profile across small diameter pipes. Additionally, a forward scattering technique was utilized, which resulted in a valid data rate for the axial velocity component of up to 50,000 Hz. This rate can be compared to the data rate of approximately 500 Hz normally associated with back scattering techniques. The high data rate was found to be necessary for accurate transient measurements.

4. Based on a linear momentum analysis that used the data collected during the transient tests, it was shown that the hot-film wall shear stress sensors are accurate in transient flow applications of up to at least 1 g acceleration.

For the present study, 1016 transient test runs were conducted under constant accelerations between 1.8 and 11.8 m/s^2. Initial mean cross-sectional averaged velocity was either zero or 1 m/s which resulted in an initially turbulent flow. Tests were configured to investigate transition to turbulence, relaminarization of an initially turbulent flow, and the details of many of the flow phenomena during the transient.

Conclusions regarding the occurrence of transition and relaminarization are as follow:

185

1. Over the length of the test section (approximately 600 pipe diameters), transition was essentially global occurring at practically the same instance along the pipe and across the cross-section. However, for the higher accelerations, it was observed that at some sensor stations, transition did occur up to 32 percent earlier (from the start of the run) than that occurring over the major portion of the test section. This indicates that some local instability may be responsible for locally tripping the flow to turbulence (i.e., a protruding sensor). For these locations, the time of transition also fluctuated by 32 percent between repeat runs. Conversely, the remaining sensor locations, including the local velocity measurements across the pipe diameter, showed transition always at the same time (within the 1/60 second between samples) for each of the 20 repeat runs used in ensemble averaging.

2. Re_D at transition increased with acceleration and ranged between 2.4×10^5 to 5.24×10^5. No unique or critical value of transition Re_D was observed.

3. Two correlations that show promise for predicting transition were developed. Probably the most reliable estimate is the instantaneous boundary layer thickness Reynolds number Re_δ 24300 ± 14 percent, which accounts for size effects. The second parameter, K_a $1.53 \times 10^{-8} \pm 34$ percent is the local acceleration analog of a similar parameter normally used in relaminarization of convectively accelerated flows, K. Neither K_a or K account for size effects. The above values for Re_δ and K_a are for the mean value

186

of all the data. It should be noted that the data did follow a trend about which data scatter was considerably lower than that indicated.

4. On the basis of the single data point of van de Sande et al.[19], it is thought that the mean values of Re_δ and K_a given above might not be valid for accelerations less than 1 m/s^2 or in dimensionless terms, for $R^2(dU_m/dt)/(\nu U_m)$ less than about 200.

5. For all accelerations tested, the value of wall shear stress at transition was 5.13 Pa $\pm$ 37 percent. This approximately constant value is interesting considering the relatively large range of U_m observed at transition. Future experiments are being planned to investigate this further.

6. When the transient was started from an initially turbulent flow, no relaminarization was observed. The largest value of K_a occurred at the beginning of the transient and ranged from 1.57×10^{-6} for the lowest acceleration of 1.8 m/s^2 to a value of 8.52×10^{-6} for the highest acceleration of these tests at 9.64 m/s^2. These values can be compared to $K = 3 \times 10^{-6}$ normally associated with relaminarization of convectively accelerated flows. If a direct correlation between K_a and K can be made, then relaminarization during the present tests would have been expected. Even though relaminarization was not observed, the time histories of the τ_w and the local turbulence intensity for locations across the pipe diameter indicate that the acceleration had tended to stabilize the turbulence at the outset of the transient. If the flow could have been stabilized further through higher accelerations or lower initial

velocities, then relaminarization might have occurred. Future tests
will investigate this further.

Conclusions related to the general physics of the flow under a
constant acceleration are based on ensemble averaged data of 20 repeat
runs for each LDV measurement location across the pipe diameter. The
major conclusions are:

1. For an acceleration from rest, the velocity profile
(0.05 < Y/R < 1.0) prior to transition agrees with that given by
Szymanski's exact laminar solution for a suddenly applied constant
pressure gradient. Note that for the dimensionless times observed
during the present tests (t* $\leq$ 0.00327), Szymanski's flow exhibits
constant acceleration. Following transition, the profile is the
quasi-steady turbulent one based on the universal law-of-the-wall.

2. For accelerations less than 2.4 m/s^2, τ_w prior to
transition can be calculated from Szymanski's exact solution. At the
acceleration of 6.1 m/s^2, τ_w remained at a constant value of
approximately 5 pascals for a large range of velocities prior to
transition and hence deviated considerably from that calculated via
Szymanski's equation. Obviously, here the velocity profile near the
wall must deviate from Szymanski's solution. This apparent anomaly
requires further research. Following transition, τ_w follows the
quasi-steady turbulent value for all accelerations tested.

3. At transition, the velocity profile and the wall shear stress
change almost instantaneously (generally within 0.017 seconds) to the
quasi-steady turbulent values.

188

4. For the tests which started from an initially turbulent flow at 1 m/s, the velocity profile followed the quasi-steady turbulent profile throughout the transient. The turbulence intensity profile, as calculated using the ensemble averaged data, also followed that of the quasi-steady values for most of the transient. However, an interesting observation was made in that at the outset of the transient, the turbulence intensity decreased below the quasi-steady value for a short duration lasting up to approximately 1.0 second. This phenomenon was attributed to the stabilizing effect the acceleration has on the flow which tends to approach relaminarization. At the outset of runs with an acceleration of 2.4 m/s^2, K_a was approximately 2×10^{-6} while for the acceleration of 6.1 m/s^2 K_a was 5×10^{-6}.

5. Also observed during the initially turbulent runs was that τ_w was also equal to the quasi-steady value for most of the transient. As with the turbulence intensity data, however, the measured τ_w was lower than the quasi-steady value at the outset. In fact, the shape of the centerline turbulence intensity time history was almost identical to that of the wall shear stress. This was further evidence that the acceleration tended to stabilize the flow.

6. Based on the correlation of the turbulence intensity data with the wall shear stress data and a momentum analysis, it seems reasonable to conclude that the turbulence intensity, as calculated here using ensemble averaging, is a suitable means of evaluating turbulence intensity in transient flows. This is especially evident during the portion of the initially turbulent runs where the flow appeared to be

somewhat stabilized. This calculation of turbulence intensity would not be possible if the facility couldn't provide the high repeatability of the transient between repeat runs.

7. No Reynolds stress measurements were made since the 20 repeat runs used in the ensemble averaging was insufficient to assure reasonable accuracy. However, since the velocity profile, the turbulence intensity, and the wall shear stress all followed the respective quasi-steady turbulent values during most of the turbulent portion of the transient, the Reynolds stress can be considered to also follow its quasi-steady value.

VI. RECOMMENDATIONS

The results of the present study have answered many questions that existed at the outset of the project. However, since very little was known about the effect of accelerations, many questions remain and many were also generated as a result of this study.

Therefore, several recommendations for future work can be made:

1. Experiments are required to determine the effect of low accelerations on transition.

2. Experiments on different size pipes are needed to validate the transition correlation parameters.

3. The theory of stability of a shear layer should be extended to a constant acceleration flow.

4. An experimental investigation should be conducted to determine why some axial locations transitioned to turbulence early relative to the major portion of the test section and why only at these locations did the time of transition change considerably between repeat runs (i.e., is there a surface irregularity tending to trip the flow?).

5. An experimental investigation should be conducted to determine why the wall shear stress remained constant over a large velocity range at the outset of the high acceleration transients from rest. This was an apparent anomaly when comparing results to the exact solution. Also investigate why the wall shear stress at transition was virtually the same value for all accelerations tested.

6. Experiments should be conducted with higher K_a at the outset of an initially turbulent flow to determine if and under which conditions relaminarization occurs. This would be accomplished by either higher accelerations or starting the acceleration at lower velocities.

7. An experimental investigation should be conducted to determine the details of transition by repeating the experiments of the present study using one highly instrumented test station including τ_w and pressure sensors and the LDV, all with a much higher data sampling rate. This will further refine the time associated with the redistribution of the velocity profile and whether the turbulence propagates from the wall to the core of the pipe or vice versa. This information would also aid in the understanding of the physics of turbulence in general.

8. Additional experiments similar to those of the present investigation should be conducted but with other types of acceleration such as constant rate of change of acceleration. This will also increase the basic understanding of the various effects acceleration has on fluid flow.

LIST OF REFERENCES

1. P. Szymanski, "Some Exact Solutions of the Hydro-dynamic Equations of a Viscous Fluid in the Case of a Cylindrical Tube," J. Math. Pures et Appl., vol.11, pp. 67-107, 1932.

2. P.L. Chambre, V.E. Schrock, and A. Gopalakrishnan, "Reversal of Laminar Flow in a Circular Pipe," Nucl. Eng. Design, vol. 47, pp. 239-250, 1978.

3. W. Zielke, "Frequency-Dependent Friction in Transient Pipe Flow," Journal of Basic Engineering, vol. 90, pp. 109-115, March 1968.

4. J.K. Tapply, M. Faghri, and F.M. White, "Unsteady Laminar Fluid Flow in the Entrance Region of a Cylindrical Pipe With a Step Change in Pumping Pressure," AIAA Paper No. AIAA-86-1039, American Institute of Aeronautics and Astronautics, December 1985.

5. H. Kawamura, "Transient Hydraulics and Heat Transfer in Turbulent Flow," Nucl. Techn., vol. 30, pp.246-255, September 1976.

6. M. Ohmi, S. Kyomen, and T. Usui, "Analysis of Velocity Distribution in Pulsating Turbulent Pipe Flow With Time-Dependent Friction Velocity," Bull. JSME, vol. 21, pp. 1137-1143, July 1978.

7. E.G. Richardson and E. Tyler, "The Transitional Velocity Gradient Near The Mouths of Pipes in Which an Alternating or Continuous Flow of Air is Established," Proceedings of the Physical Society of London, vol. 43, pp. 1-15, 1929.

8. R.G. Linford and N.W. Ryan, "Pulsatile Flow in Rigid Tubes," Journal of Applied Physiology, vol. 20, 1965.

9. E.B. Denison, "Pulsating Laminar Flow Measurements with a Directionally Sensitive Laser Velocimeter," Ph.D. Thesis, Mechanical Engineering Dept., Purdue University, West Lafayette, Indiana, 1970.

10. Schultz-Grunow, "Pulsierender Durchfluss Durch Rohre," Porschung 11, vol. 4, 1940, pp. 170-187; also NASA Technical Translation, NASA-IT-F-14881, 1973.

11. T. Mizushina, T. Maruyama, and Y. Shiozaki, "Pulsating Turbulent Flow in a Tube," Journal of Chemical Engineering of Japan, vol. 6, no. 6, pp. 487-494, 1973.

12. T. Mizushina, T. Maruyama, and H. Hirasawa, "Structure of the
    Turbulence in Pulsating Pipe Flows," Journal of of Chemical
    Engineering of Japan, vol. 8, no. 3, pp. 210-216, 1975.

13. B.R. Ramaprian, and S.W. Tu, "Study of Periodic Turbulent Pipe
    Flow," IIHR Report No. 238, Iowa Institute of Hydraulic Research,
    1982.

14. J.W. Daily, W.L. Hankey, R.W. Olive, and J.M. Jordaan,
    "Resistance Coefficients for Accelerated and Decelerated Flows
    Through Smooth Tubes and Orifices," Transactions of ASME, vol.
    78, pp. 1071-1077, July 1956.

15. R. Carsten, and J.E Roller, "Boundary-Shear Stress in Unsteady
    Turbulent Pipe Flow," Journal of Hydr. Division, vol. 2, pp.
    67-81, February 1959.

16. S.V. Denisov, "The Friction Coefficient in Non-Stationary Flows,"
    Journal of Engineering Physics, vol. 18, part 1, pp. 88-92,
    January 1970.

17. K. Kataoka, T. Kawabata, and K. Miki, "The Start-Up Response of
    Pipe Flow to a Step Change in Flow Rate," Journal of Chemical
    Engineering of Japan, vol 8, no. 4, pp. 266-271, 1975.

18. T. Marayama, T. Kuribayashi, and T. Mizushina, "The Structure of
    Turbulence in Transient Pipe Flows," Journal of Chemical
    Engineering of Japan, vol. 9, no. 6, pp. 431-439, 1975.

19. E. van de Sande, A.P. Belde, B.J.G. Hamer, and W. Hiemstra,
    "Velocity Profiles in Accelerating Pipe Flows Started From Rest,"
    Third International Conference on Pressure Surges, Canterbury,
    England, March 1980.

20. P.J. Lefebvre, "Design and Evaluation of NUSC's Flow Loop
    Facility," NUSC Technical Document No. 6512, Naval Underwater
    Systems Center, Newport, RI, May 1986.

21. K.M. LaPointe and P.J. Lefebvre, "Flow Loop Facility Flow Control
    System," NUSC TM No. 85-2076, Naval Underwater Systems Center,
    Newport, RI, November 1985.

22. P.J. Lefebvre and W.W. Durgin, "A Transient Electromagnetic
    Flowmeter," Measuring and Metering of Unsteady Flows, ASME-FED,
    vol. 40, December 1986.

23. B.J. Bellhouse and D.L. Schultz, "Determination of Mean and Dynamic Skin Friction, Separation and Transition in Low-Speed Flow with a Thin-Film Heated Element," Journal of Fluid Mechanics, vol.24, part 2, 1966.

24. G.L. Brown, "Theory and applications of Heated Films for Skin Friction Measurement," Proceedings of the 1967 Heat Transfer and Fluid Mechanics Institute, Stanford University Press, Stanford University, CA, 1967.

25. J.O. Geremia, "An Experimental Investigation of Turbulence Effects at the Solid Boundary Using Flush-Mounted Hot Film Sensors," Ph.D. Thesis, George Washington University, Washington, DC, 1970.

26. V.A. Sandborn, "Evaluation of the Time Dependent Surface Shear Stress in Turbulent Flows," Proceedings of the ASME Winter Annual Meeting, Paper No. 79-WA/FE-17, 1979.

27. B.R. Ramaprian, and S.W. Tu, "Calibration of a Heat Flux Gage for Skin Friction Measurements," Journal of Fluids Engineering, vol. 105, December 1983.

28. F.M. White, Viscous Fluid Flow, McGraw-Hill Book Company, New York, NY, 1972.

29. S.J. Kline and F.A. McClintock, "Describing Uncertainties in Single Sample Experiments," Mechanical Engineering, January 1953.

30. P.J. Lefebvre and K.M. LaPointe, "The Effect of Mounting Position on Hot-Film Wall Shear Stress Sensors," Proceedings of the AIAA/ASME 4th Fluid Mechanics, Plasma Dynamics, and Lasers Conference, paper no. AIAA-86-1101, May 1986.

31. U. Arnold, U. Stein, and E. Pasche, "First Experience with an On-Axis LDV-System in Spectral Applications to Open-Channel Flow," Proceedings of the Symposium on Laser Anemometry, 1985 ASME Winter Annual Meeting, November 1985.

32. TSI Inc., "System 9100-11 Five Beam, Three Component Laser Doppler Velocimeter Instruction Manual," 1982.

33. J. Laufer, "The Structure of Turbulence in Fully Developed Pipe Flow," NACA Technical Note 2954, National Advisory Committee for Aeronautics, June 1953.

34. W.P. Jones, and B.E. Launder, "Some Properties of Sink-Flow Turbulent Layers," _Journal of Fluid Mechanics_, vol.56, part 2, 1972, pp 337-351.

35. V.C. Patel and M.R. Head, "Reversion of Turbulent to Laminar Flow," _Journal of Fluid Mechanics_, vol 34, part 2, 1968, pp 371-392.

36. R. Narasimha and K.R. Sreenivasan, "Relaminarization in Highly Accelerated Turbulent Boundary Layers," _Journal of Fluid Mechanics_, vol.61, part 3, 1973, pp 417-447.

37 J. Laufer, "The Structure of Turbulence in Fully Developed Pipe Flow," NACA Report No. 1174, National Advisory Committee for Aeronautics, 1954.

APPENDIX A

FLOW LOOP FACILITY PHOTOGRAPHS
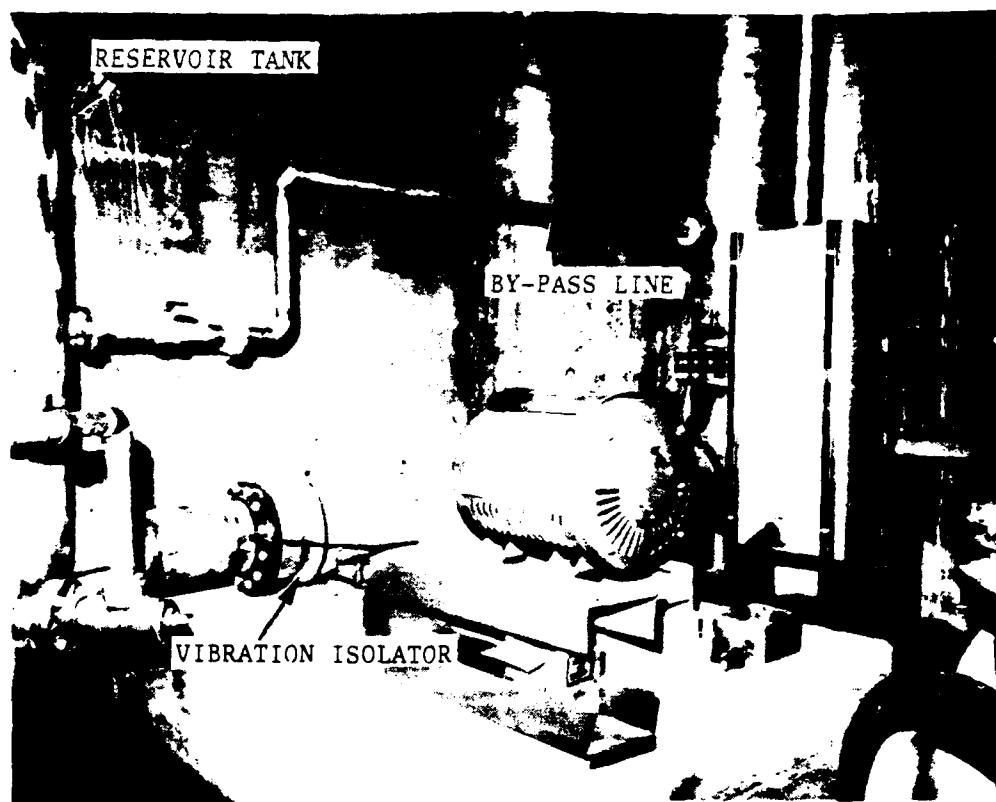
Figure A-1. 150-hp Pump
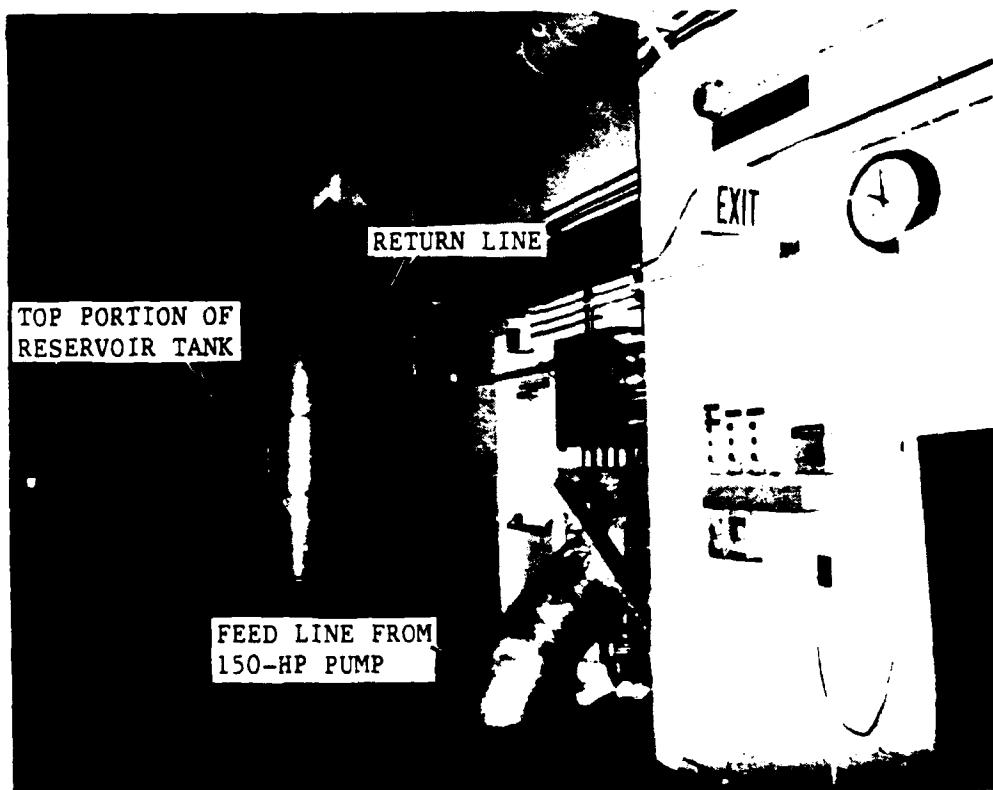
Figure A-2. Reservoir Tank
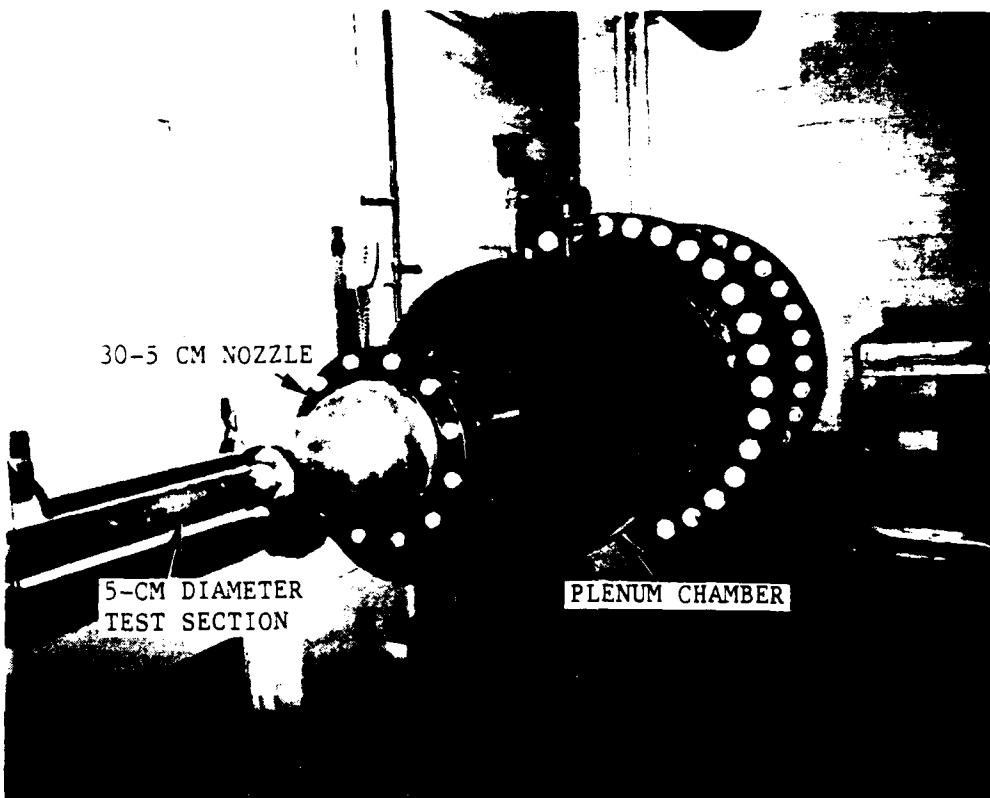
Figure A-3. Plenum Chamber
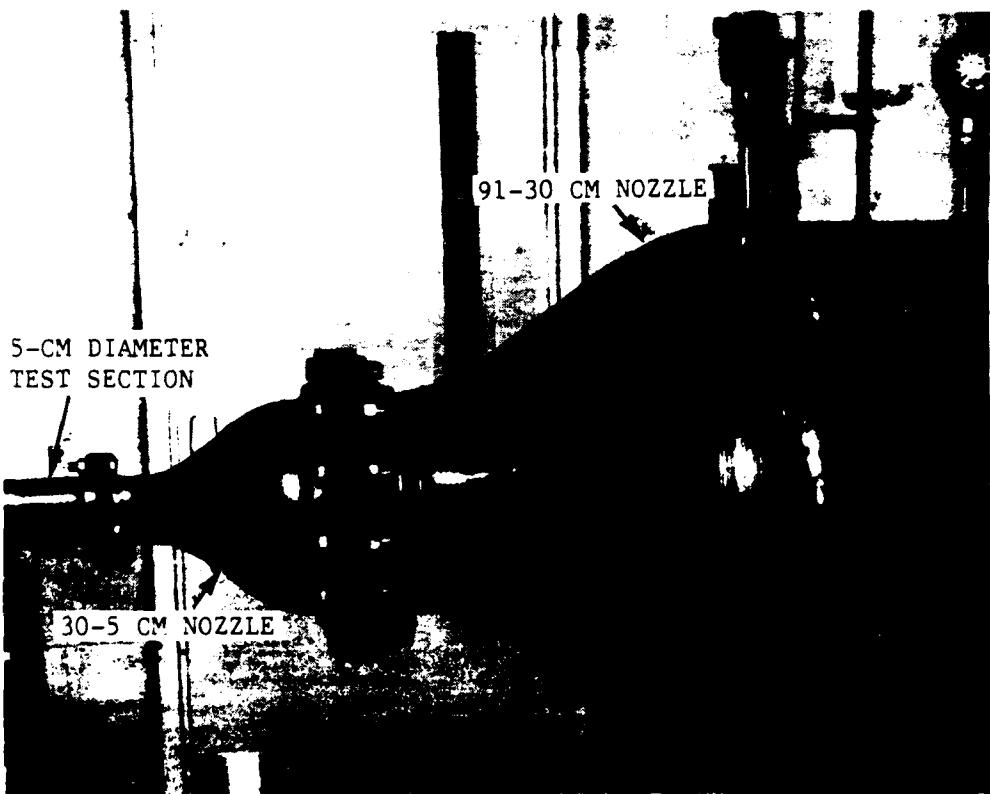
Figure A-4. Plenum Chamber Nozzles

199
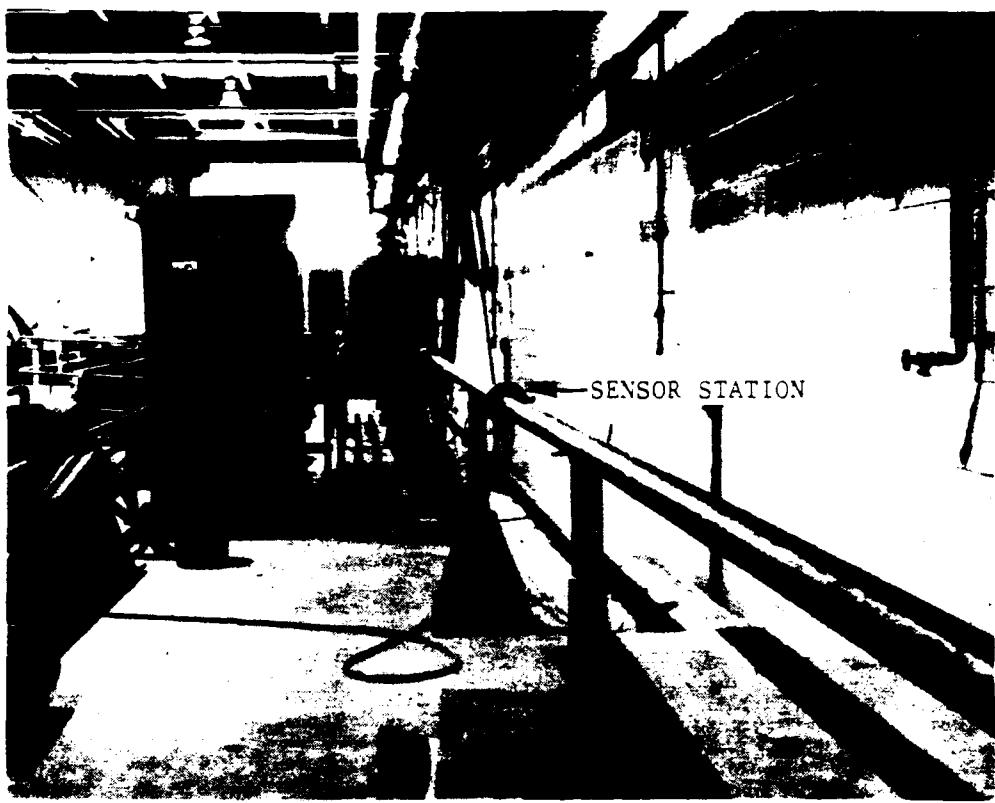
Figure A-5. 5-cm Diameter Test Section
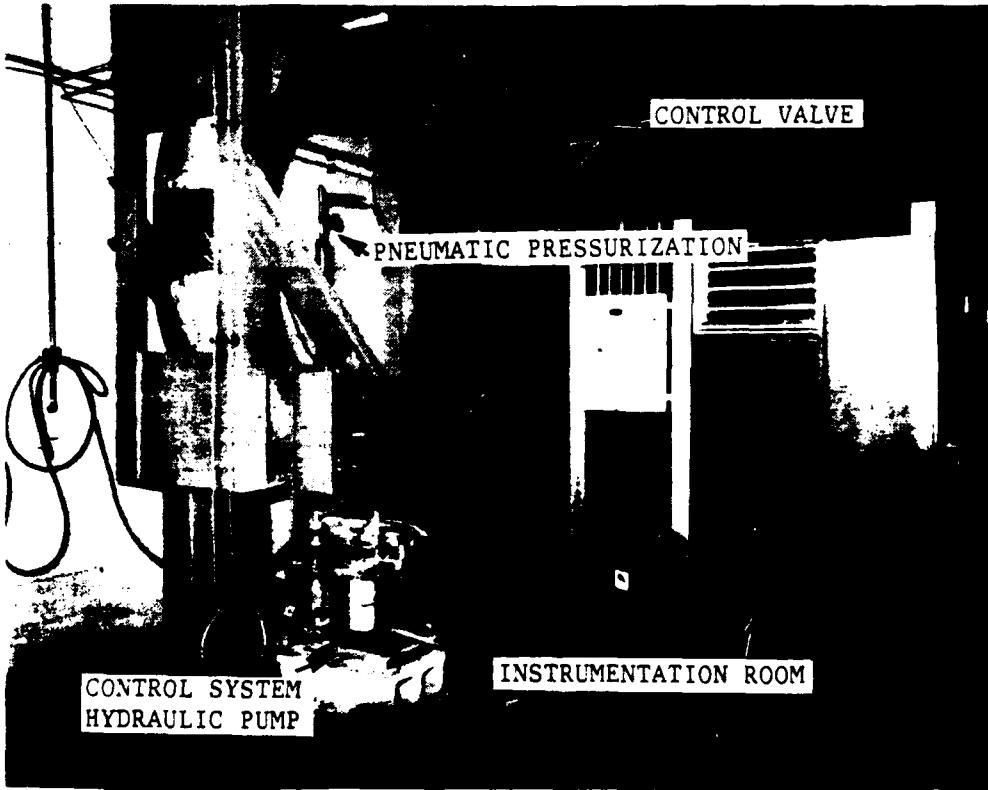
Figure A-6. Return Line
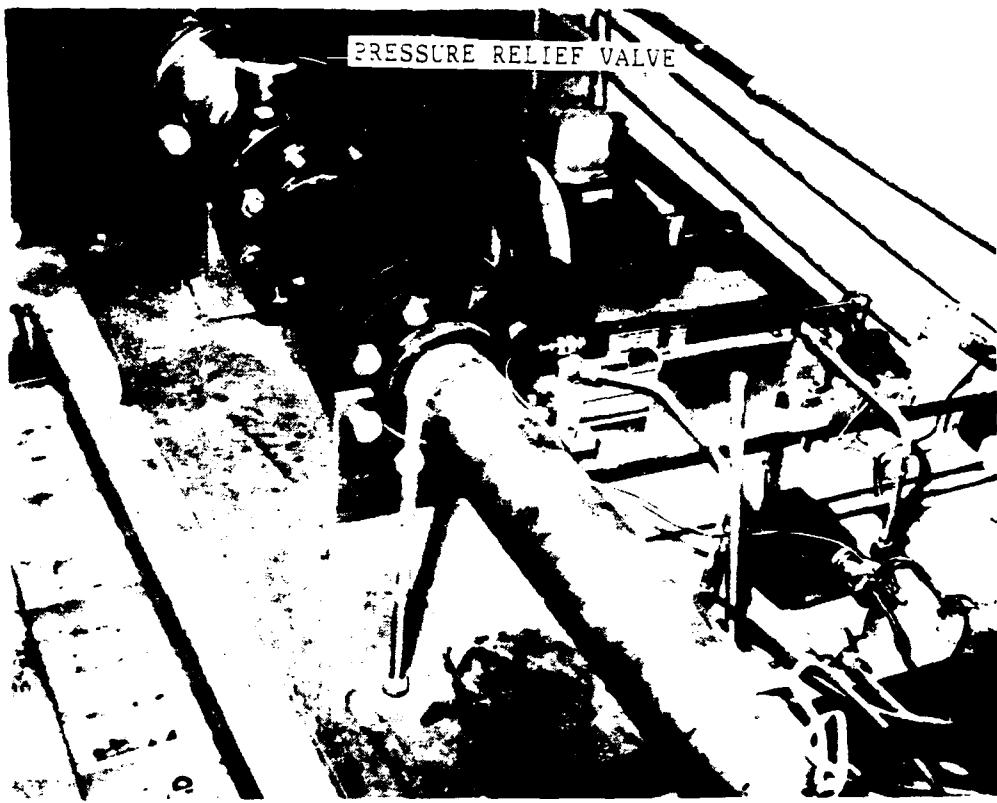
Figure A-7.   Control Valve
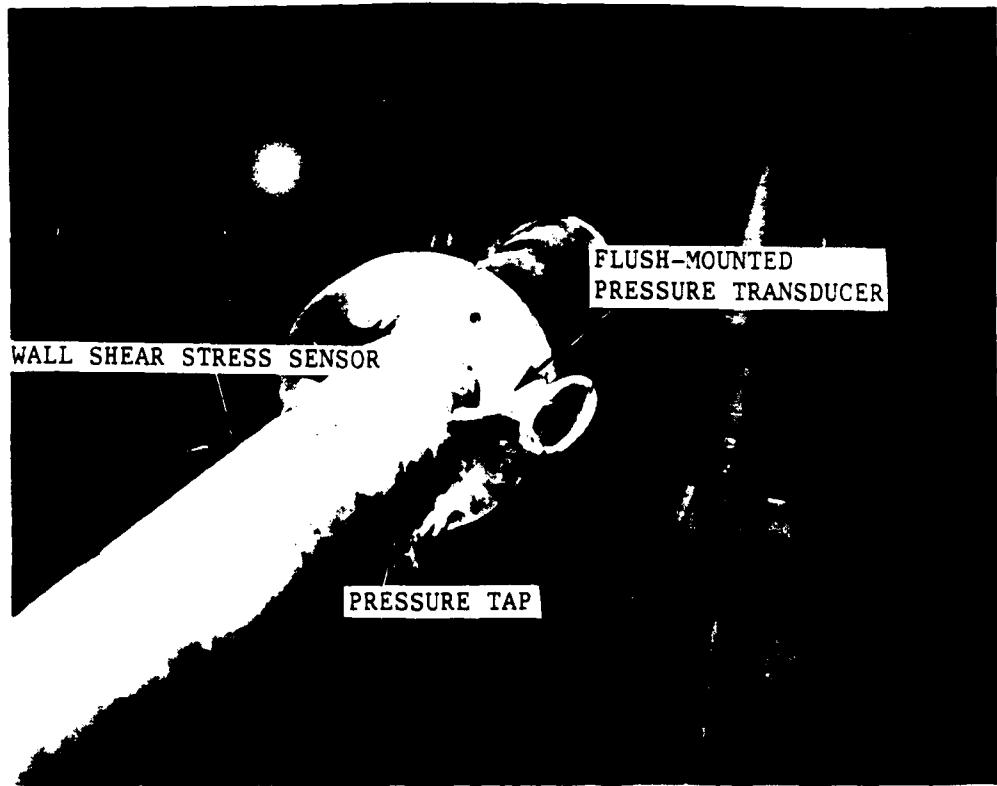
Figure A-8.   Pressure Transducer Mounting
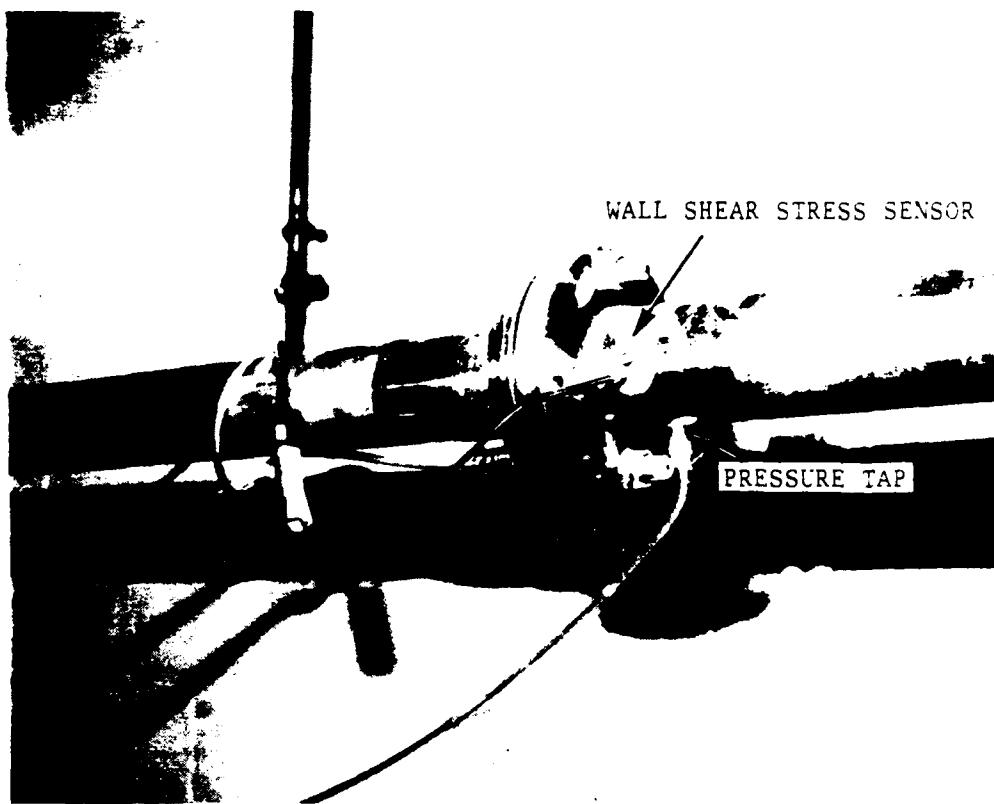
Figure A-9. Wall Shear Stress Sensor Mounting
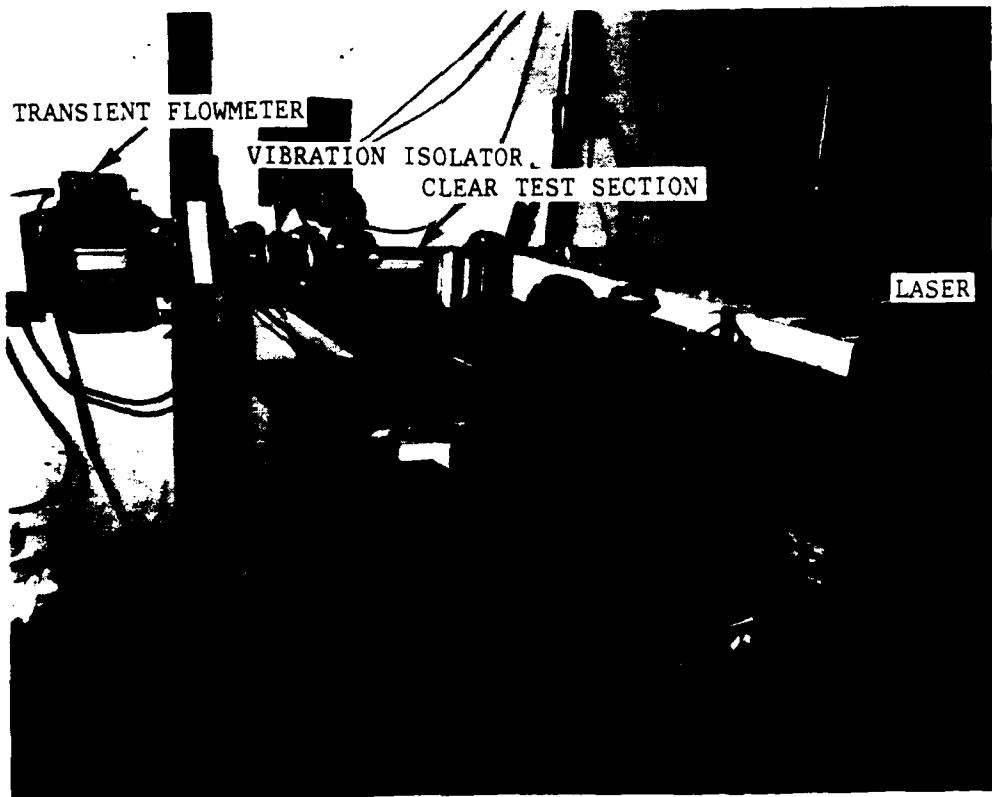
Figure A-10. Laser Doppler Velocimeter

Figure A-11.   Instrumentation

APPENDIX B

LASER DOPPLER VELOCIMETER CALCULATIONS

DEFINTIONS

Burst Density   Number of particles in the measuring volume (high

burst density has many particles in volume at any

one time and results in phase noise; no phase noise

with low burst density) (see table B-1)

Data Density   Time between successive, measurable signal bursts

compared with the time scale of the velocity

fluctuations

High data density: often sufficient to use analog

output, standard averaging, and RMS meters

(amplitude probability, etc.); also can data

average if data are digitized at equal time

increments; lowpass filter allows frequencies of

interest to pass while filtering steps caused by

"sample and hold"

Low data density: must correct for velocity bias

via weighting with time between data points

204

| Phase Noise: | Looks like turbulence; occurs with high burst density; also called Doppler ambiguity and transit time broadening (see table B-1) |

Particles entering and leaving volume are out of phase and therefore cause a phase shift in the signal (summed frequency is frequency modulated)

If each Doppler burst looks clean (i.e., only one particle in measuring volume), then there is no phase noise

Phase noise appears as white noise in power spectrum

$\beta_D = 1.8/N_{fR}$ = estimate of Doppler signal spectrum bandwidth

Equivalent turbulence intensity =

$$\sqrt{\overline{\Delta f_D f_C}}/f_D = \sqrt{\overline{\beta_D f_D f_C}}/f_D$$

where f_C is the lowpass cutoff frequency (at output of signal processor), and f_D is the Doppler frequency (assumes 1.1 particles in measuring volume at any one time)

Example: If RMS_u = 10%, RMS phase noise = 2%, and correction to $RMS_u = (\sqrt{10^2-2^2})//\sqrt{10^2} = 0.98$

Velocity Bias: Probability (per unit time) of a particle entering the measuring volume depends on the fluid velocity (more data points at high velocity relative to low velocity)

Velocity bias is actually a very small error if turbulence intensity is less than 15% (most people do not account for velocity bias)

For high data density and low burst density: (1) time average of analog output gives correct mean value; (2) accurate time averages are obtained if digital data are sampled at uniform time increments; (3) for random data sampling (as data points are obtained), each point should be time weighted for accurate time averages (must measure each particle or other errors will result)

For low data density: (1) weight data with time between data points; (2) for flows greater than 1-dimensional, a 1-D velocity correction over-corrects; must use total velocity vector correction

Fringe Bias: For particles entering at different angles, bias

                        is in direction of greatest probability of

                        particle travel (affects accuracy of individual

                        velocity components); correct with frequency

                        shifting

Velocity

Gradient Bias: Caused by insufficient space resolution of measur-

                        ing volume; average velocity over volume is

                        measured

u'v' Coincidence

Window$_{(max)}$:   1.0 times particle transit time across measuring

                        volume; therefore, window time = 1.0(measuring

                        volume length/transit velocity)

Processor Accuracy: Clock resolution:

                        Accuracy = $\pm$clock resolution/t = $\pm(2 \times 10^{-9})/t$,

                        where t is the transit time over N cycles

                        (N/f_D)

                        12-bit digital output (4096 counts) resolution:

                        With counter in autorange mode, output stays

                        within 2 to 8 volts (exponent changes automat-

                        ically); 5 volts$_{avg}$ $\simeq$ 2000 counts; therefore,

                        error $\simeq$ $\pm 1/2000$ = $\pm 0.05\%$

207

Table B-1. Phase Noise and Velocity Bias Effects

		Phase Noise	Velocity Bias
High data density	Low burst density	No	Corrected by sampling at equal time increments
	High burst density	Yes	Same as above
Low data density	Low burst density	No	Weight with time between consecutive data points
	High burst density	Yes	Same as above

CALCULATIONS

Calculations for LDV Measuring Volume Geometry

$f = 290.4$ mm
(focal length)

$\kappa = 9.77°$
(lens half-angle)

$\lambda_{green} = 514.5$ nm
(wavelength)
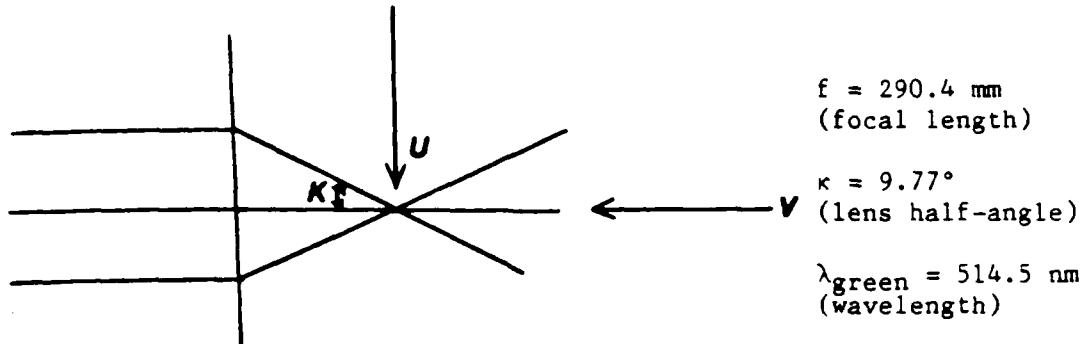
Figure B-1.   Three-Beam (One-Color)/Two-Component (Axial and Radial)
LDV Beam Pattern

Calculations with No Beam Expander (Beam Diameter D_{e-2} = 1.2 mm)

1. ### Radial (V) Component:

$d_Z = \lambda/[4 \sin^2(\kappa/2)]$ (virtual radial
                                                            fringe spacing)

$\quad = (514.5 \times 10^{-9})/[4 \sin^2(4.885°)]$

$\quad = 17.74$ μm

$d_m = (4f\lambda)/(\pi D_{e-2})$ (volume diameter)
                                                     (see Notes 1 and
$\quad = [4(0.2904)(514.5 \times 10^{-9})]/[\pi(0.0012)]$ and 2 on next page)

$\quad = 0.158$ mm $= 0.0062$ in.

$l_m = d_m/\sin \kappa$ (volume length)

$\quad = (0.158 \times 10^{-3})/\sin(9.77°)$

$\quad = 0.931$ mm $= 0.037$ in.

$$N_{fR} = 1_m/d_Z \qquad \text{(number of fringes)}$$

$$= (0.931 \times 10^{-3})/(17.74 \times 10^{-6})$$

$$= 52.5$$

$$\beta_D = 1.8/N_{fR} \qquad \text{(bandwidth)}$$

$$= 1.8/52.5$$

$$= 3.43\%$$

Notes: 1. d_m and 1_m are in same direction for each component

(1_m is in V-direction; d_m is in U-direction).

2. Cos κ is not in denominator of d_m since d_m is a function of center beam diameter at focal point.

2. <u>Axial (U) Component</u>:

$$d_f = \lambda/(2 \sin \kappa)$$

$$= (514.5 \times 10^{-9})/(2 \sin 9.77°)$$

$$= 1.516 \ \mu m$$

$$d_m = (4f\lambda)/(\pi D_{e-2} \cos \kappa)$$

$$= [4(0.2904)(514.5 \times 10^{-9})]/[\pi(0.0012) \cos(9.77°)]$$

$$= 0.161 \ mm = 0.0063 \ in.$$

$$1_m = d_m/\tan \kappa = (0.161 \times 10^{-3})/\tan(9.77°)$$

$$= 0.935 \ mm = 0.037 \ in.$$

210

$$N_{fR} = d_m/d_f$$

$$= (0.161 \times 10^{-3})/(1.516 \times 10^{-6})$$

$$= 106.2$$

$$\beta_D = 1.8/N_{fR}$$

$$= 1.8/106$$

$$= 1.7\%$$

Calculations with 2.27X Beam Expander (Beam Diameter D_{e-2} = 2.724 mm)

1. Radial (V) Component:

$$d_Z = 17.74 \ \mu m$$

$$d_m = (4f\lambda)/(\pi D_{e-2})$$

$$= [4(0.2904)(514.5 \times 10^{-9})]/[\pi(0.002724)]$$

$$= 0.070 \ mm \approx 0.0027 \ in.$$

$$l_m = d_m/\sin \kappa$$

$$= 0.070/\sin(9.77°)$$

$$= 0.412 \ mm \approx 0.016 \ in.$$

$$N_{fR} = l_m/d_Z$$

$$= (0.412 \times 10^{-3})/(17.74 \times 10^{-6})$$

$$= 23.2$$

$$\beta_D = 1.8/N_{fR}$$

$$= 1.8/23.2$$

$$= 7.8\%$$

2. <u>Axial (U) Component:</u>

$$d_f = 1.516 \ \mu m$$

$$d_m = (4f\lambda)/(\pi D_{e-2} \cos \kappa)$$

$$= [4(0.2904)(514.5 \times 10^{-9})]/[\pi(0.002724) \cos(9.77°)]$$

$$= 0.0709 \ mm = 0.0028 \ in.$$

$$l_m = d_m/\tan \kappa = (0.0709)/\tan(9.77°)$$

$$= 0.412 \ mm = 0.016 \ in.$$

$$N_{fR} = d_m/d_f$$

$$= 0.0709 \times 10^{-3}/(1.516 \times 10^{-6})$$

$$= 46.8$$

$$\beta_D = 1.8/N_{fR}$$

$$= 1.8/46.8$$

$$= 3.85\%$$

Calculations for Counter Processor Settings (No Beam Expander)

LDV settings with no beam expander are summarized in table B-2. In the calculations, U is the axial component of velocity and V is the radial component.

Table B-2. Summary of LDV Settings with No Beam Expander

Vel (m/s)	f_{ped} (kHz)	f_{du} (MHz)	Transit Time t^* (μsec)	β_D $(1.8/N_{f_R})$	Equivalent Turbulence Int'sity**	$f_{so}min$ (kHz)	$f_{dv}max$ (kHz)	$f_{sv}min$ (kHz)
0.3	1.9	0.2	526	0.017	0.0086	15	3.4	18.4
1.5	9.5	1.0	105	0.017	0.0038	76	17	93
3.0	19	2.0	52	0.017	0.0027	154	34	188
6.1	38	4.0	26	0.017	0.0019	308	69	377
9.1	57	6.0	18	0.017	0.0015	444	103	547

*Transit time t = coincidence window.
**Equivalent turbulence intensity $= \pm\sqrt{\beta_D f_D f_C}/f_D$ with $f_C = 1$ kHz.

$$f_{pedestal} = \text{U velocity/U volume transit distance} \qquad \text{(assume only one particle in}$$

$$= V/d_m = V/(5.2 \times 10^{-4} \text{ ft}) \qquad \text{volume at all t)}$$

$$f_{du} = V/d_f \qquad \text{(Doppler freq, U-component)}$$

$$= V/1.516 \ \mu m = V/(4.97 \times 10^{-6} \text{ ft})$$

$$f_{dv} = V/d_Z \qquad \text{(Doppler freq, V-component)}$$

$$= V/17.74 \ \mu m = V/(5.82 \times 10^{-5} \text{ ft})$$

213

$$t = d_m/V \qquad \text{(transit time)}$$

$$= 1/f_{pedestal}$$

$$= (4.5 \times 10^{-4} \text{ ft})/V$$

Turbulence (for V-Component)

$$f_{so} = N/t \qquad \text{(minimum frequency shift when } V = 0)$$

$$= 8/t \qquad \text{(assures N radial fringes are crossed by each particle)}$$

Assume $V_{max} = 0.2U$; therefore,

$$f_{sv} = f_{so} + f_d \qquad \text{(minimum frequency shift for V-component)}$$

Add f_d to f_{so} since V may be positive or negative.

Calculations for Counter Processor Settings with 2.27X Beam Expander

LDV settings with a 2.27X beam expander are summarized in table B-3. U is the axial component of velocity and V is the radial component.

Table B-3. Summary of LDV Settings with 2.27X Beam Expander

Vel (m/s)	f_{ped} (kHz)	f_{du} (MHz)	Transit Time t* (µsec)	β_D (1.8/N_{FR})	Equivalent Turbulence Int'sity**	f_{so}min (kHz)	f_{dv}max (kHz)	f_{sv}min (kHz)
0.3	4.3	0.2	232	0.0385	0.0129	34	3.4	37.4
1.5	22	1.0	45	0.0385	0.0057	177	17	194
3.0	43	2.0	23	0.0385	0.0041	348	34	382
6.1	87	4.0	11	0.0385	0.0029	727	69	796
9.1	130	6.0	7.7	0.0385	0.0023	1039	103	1142

*Transit time t = coincidence window.
**Equivalent turbulence intensity = $\pm\sqrt{\beta_D f_D f_C}/f_D$ with f_C = 1 kHz.

$f_{pedestal}$ = U velocity/U volume transit distance   (assume only one particle in volume at all t)

$\quad\quad\quad$ = V/dm = V/(2.3 x 10^{-4} ft)

$f_{du}\quad\quad$ = V/d_f (Doppler freq, U-component)

$\quad\quad\quad$ = V/1.516 µm = V/(4.97 x 10^{-6} ft)

$f_{dv}\quad\quad$ = V/d_Z (Doppler freq, V component)

$\quad\quad\quad$ = V/17.74 µm = V/(5.82 x 10^{-5} ft)

$$t = d_m/V \qquad \text{(transit time)}$$

$$= 1/f_{pedestal}$$

$$= (4.5 \times 10^{-4} \text{ ft})/V$$

Turbulence (for V-Component)

$$f_{so} = N/t \qquad \text{(minimum frequency shift when } V = 0\text{)}$$

$$= 8/t \qquad \text{(assures N radial fringes are crossed by each particle)}$$

Assume $V_{max} = 0.2U$; therefore,

$$f_{sv} = f_{so} + f_d \qquad \text{(minimum frequency shift for V-component)}$$

Add f_d to f_{so} since V may be positive or negative.

216

SUMMARY OF LDV SETUP AND OPERATING CONDITIONS

d_f (X-axis) = 1.516 μm

d_z (R-axis) = 17.74 μm

U and V Components

Number of cycles = 4 for transient (better velocity resolution)

Number of cycles = 8 for steady state

Frequency shift = 0.5 MHz

Coincidence time = 7 μsec

Comparison = 1%

For U-component:

  highpass filter = 300 kHz

  lowpass filter = 10 MHz

For V-component:

  highpass filter = 300 kHz

  lowpass filter = 3 MHz

Accuracy

Assume no phase noise or velocity bias (only one particle in the measuring volume at any one time and a high data rate)

217

BIBLIOGRAPHY

Arnold U.; Stein, U.; and Pasche, E. "First Experience with an On-Axis
    LDV-System in Spectral Applications to Open-Channel Flow,"
    Proceedings of the Symposium on Laser Anemometry, 1985 ASME
    Winter Annual Meeting: November 1985.

Bellhouse, B.J., and Schultz, D.L. "Determination of Mean and Dynamic
    Skin Friction, Separation and Transition in Low-Speed Flow with
    a Thin-Film Heated Element," Journal of Fluid Mechanics 24, part
    2: 1966.

Brown, G.L. "Theory and Applications of Heated Films for Skin Friction
    Measurement," Proceedings of the 1967 Heat Transfer and Fluid
    Mechanics Institute, Stanford University, CA: Stanford
    University Press, 1967.

Carsten, R., and Roller, J.E. "Boundary-Shear Stress in Unsteady
    Turbulent Pipe Flow," Journal of Hydr. Division 2, (February
    1959): 67-81

Chambre, P.L.; Schrock, V.E.; and Gopalakrishnan, A. "Reversal of
    Laminar Flow in a Circular Pipe," Nucl. Eng. Design 47, (1978):
    pp. 239-250.

Daily, J.W.; Hankey, W.L.; Olive, R.W.; and Jordan, J.M. "Resistance
    Coefficients for Accelerated and Decelerated Flows Through
    Smooth Tubes and Orifices," Transactions of ASME 78, (July 1956):
    pp. 1071-1077, .

Denison, E.B. "Pulsating Laminar Flow Measurements with a Directionally
    Sensitive Laser Velocimeter," Ph.D. Dissertation, Purdue
    University, West Lafayette, Indiana, 1970.

Denisov, S.V. "The Friction Coefficient in Non-Stationary Flows,"
    Journal of Engineering Physics 18, part 1 (January 1970):
    pp. 88-92, .

Geremia, J.O. "An Experimental Investigation of Turbulence Effects at
    the Solid Boundary Using Flush-Mounted Hot Film Sensors," Ph.D.
    Dissertation, George Washington University, Washington, DC, 1970.

Jones, W.P., and Launder, B.E. "Some Properties of Sink-Flow Turbulent
    Layers," Journal of Fluid Mechanics 56, part 2 (1972): pp
    337-351.

Kataoka, K.; Kawabata, T.; and Miki, K. "The Start-Up Response of Pipe
    Flow to a Step Change in Flow Rate," Journal of Chemical
    Engineering of Japan 8, no. 4 (1975): pp. 266-271.

Kawamura, H. "Transient Hydraulics and Heat Transfer in Turbulent
    Flow," Nucl. Techn. 30, (September 1976): pp.246-255.

Kline, S.J., and McClintock, F.A. "Describing Uncertainties in Single
    Sample Experiments," Mechanical Engineering, January 1953.

LaPointe, K.M., and Lefebvre, P.J. Flow Loop Facility Flow Control
    System. Newport, RI, Naval Underwater Systems Center Technical
    Memorandum No. 85-2076 [November 1985].

Laufer, J. "The Structure of Turbulence in Fully Developed Pipe Flow,"
    NACA Technical Note 2954, National Advisory Committee for
    Aeronautics, June 1953.

Laufer, J. "The Structure of Turbulence in Fully Developed Pipe Flow,"
    NACA Report No. 1174, National Advisory Committee for
    Aeronautics, 1954.

Lefebvre, P.J. "Design and Evaluation of NUSC's Flow Loop Facility,"
    NUSC Technical Document No. 6512, Naval Underwater Systems
    Center, Newport, RI, May 1986.

Lefebvre, P.J., and Durgin, W.W. "A Transient Electromagnetic
    Flowmeter," Measuring and Metering of Unsteady Flows, ASME-FED
    40 (December 1986).

Lefebvre, P.J., and LaPointe, K.M. "The Effect of Mounting Position on
    Hot-Film Wall Shear Stress Sensors," Proceedings of the
    AIAA/ASME 4th Fluid Mechanics, Plasma Dynamics, and Lasers
    Conference, paper no. AIAA-86-1101, May 1986.

Linford, R.G., and Ryan, N.W. "Pulsatile Flow in Rigid Tubes," Journal
    of Applied Physiology 20 (1965).

Marayama, T.; Kuribayashi, T.; and Mizushina, T. "The Structure of
    Turbulence in Transient Pipe Flows," Journal of Chemical
    Engineering of Japan 9, no. 6 (1975): pp. 431-439.

Mizushina, T.; Maruyama, T.; and Hirasawa, H. "Structure of the
    Turbulence in Pulsating Pipe Flows," Journal of of Chemical
    Engineering of Japan 8, no. 3 (1975): pp. 210-216.

Mizushina, T.; Maruyama, T.; and Shiozaki, Y. "Pulsating Turbulent Flow
    in a Tube," Journal of Chemical Engineering of Japan 6, no. 6
    (1973): pp. 487-494.

Narasimha, R., and Sreenivasan, K.R. "Relaminarization in Highly
    Accelerated Turbulent Boundary Layers," Journal of Fluid
    Mechanics 61, part 3 (1973): pp 417-447.

Ohmi, M.; Kyomen, S.; and Usui, T. "Analysis of Velocity Distribution in Pulsating Turbulent Pipe Flow With Time-Dependent Friction Velocity," Bull. JSME, vol. 21, pp. 1137-1143, July 1978.

Patel, V.C., and Head, M.R. "Reversion of Turbulent to Laminar Flow," Journal of Fluid Mechanics 34, part 2 (1968): pp 371-392.

Ramaprian, B.R., and Tu, S.W. "Calibration of a Heat Flux Gage for Skin Friction Measurements," Journal of Fluids Engineering 105 (December 1983).

Ramaprian, B.R., and Tu, S.W. "Study of Periodic Turbulent Pipe Flow," IIHR Report No. 238, Iowa Institute of Hydraulic Research, 1982.

Richardson, E.G., and Tyler, E. "The Transitional Velocity Gradient Near The Mouths of Pipes in Which an Alternating or Continuous Flow of Air is Established," Proceedings of the Physical Society of London 43, pp. 1-15, 1929.

Sandborn, V.A. "Evaluation of the Time Dependent Surface Shear Stress in Turbulent Flows," Proceedings of the ASME Winter Annual Meeting, paper no. 79-WA/FE-17, 1979.

Schultz-Grunow, "Pulsierender Durchfluss Durch Rohre," Porschung 11, vol. 4, 1940, pp. 170-187; also NASA Technical Translation, NASA-IT-F-14881,1973.

Szymanski, P. "Some Exact Solutions of the Hydro-dynamic Equations of a Viscous Fluid in the Case of a Cylindrical Tube," J. Math. Pures et Appl., vol.11, pp. 67-107, 1932.

Tapply, J.K.; Faghri, M.; and White, F.M. "Unsteady Laminar Fluid Flow in the Entrance Region of a Cylindrical Pipe With a Step Change in Pumping Pressure," AIAA Paper No. AIAA-86-1039, American Institute of Aeronautics and Astronautics, December 1985.

TSI Inc., "System 9100-11 Five Beam, Three Component Laser Doppler Velocimeter Instruction Manual," 1982.

van de Sande, E.; Belde, A.P.; Hamer, B.J.G.; and Hiemstra, W. "Velocity Profiles in Accelerating Pipe Flows Started From Rest," Third International Conference on Pressure Surges, Canterbury, England, March 1980.

White, F.M. Viscous Fluid Flow, New York: McGraw-Hill Book Company, 1972.

Zielke, W. "Frequency-Dependent Friction in Transient Pipe Flow," Journal of Basic Engineering 90, (March 1968): pp. 109-115.

INITIAL DISTRIBUTION LIST

Addressee	No. of Copies
DTIC	12
DARPA	1
CNO (NOP–02, NOP–62)	2
CNR (OCNR–10, OCNR–11, OCNR–12 (Hansen), OCNR–1215 (Fein), OCNR–20, OCNR–432 (Whitehead, Reischman, Lekoudis))	8
ONR Detachment, Boston	1
NAVSEA (SEA–56W, SEA–55W31 (Lewis), SEA–56W13 (Crabb – 2 copies), SEA–5021 (Leadman), SEA–05R32 (Smookler), PMS–350 (Nelson), PMS–402)	8
NCSC	1
DTRC, Carderock (Code 1556 (Coder, Purtell))	2
Alden Research Laboratory (Hecker)	1
Colorado State University (Sandborn)	1
Worcester Polytechnic Institute (Durgin)	1

END

DATE

FILMED

DTIC

JULY 88